Abstract

Measuring the Knot of Non-Hermitian Degeneracies and Non-Abelian braids

Parker A. Henry

2022

There has been much interest in physical systems that can be described as linear dynamical systems which incorporate gain, loss, and non-reciprocity. Such systems can serve as novel devices in sensing and control applications. They can be realized in any physical domain, including optics, acoustics, electronics, and optomechanics. Systems that incorporate gain, loss, and non-reciprocity are known as "non-Hermitian," and are distinguished from Hermitian systems by their complex eigenvalues, mode nonorthogonality, and a class of degeneracy known as an exceptional point, for which the dynamical matrix $\mathcal{H}$ is nondiagonalizable. Spectral flow presents another distinction between non-Hermitian and Hermitian systems.

Spectral flow is a topological property of the path which the system eigenvalues take in the complex plane $\mathbb{C}$ when the system's parameters are varied around a closed loop. For a Hermitian system, the spectral flow is trivial, since the eigenvalues must return to themselves; for a non-Hermitian system, eigenvalues need not return to the original values.

Optomechanics has been used to explore the spectral flow of systems near exceptional points (EPs) for 2-mode systems, for which it is well-understood that spectral flow is determined by how the loop encircles an EP degeneracy. In this thesis, we discuss spectral flow for n-mode systems, and, in an optomechanical platform, experimentally demonstrate the $n = 3$ case. This case is of interest because the corresponding exceptional point space is a trefoil knot, as opposed to a single point, and because the braid group formed by the spectral flow is non-Abelian.

We begin with a pedagogical introduction to exceptional point degeneracies and spectral flow. This introduces the braid group of spectral flow for control loops encircling the exceptional point space. Next, we employ the optomechanical interaction to define a three-mode non-Hermitian system of mechanical modes, for which we have full control over the parameters that determine the eigenvalues. We describe the optomechanical non-Hermitian platform used in our experiment, which consists of an Si_3N_4 membrane coupled to a Fabry-Pérot cavity in a cryostat, which is driven by two lasers. We show that this system can be brought to a triply degenerate exceptional point (EP_3). Around this EP_3 point, we raster the doubly degenerate exceptional point (EP_2) subspace on a hypersurface which encloses the EP_3 point, and show that this EP_2 subspace forms a trefoil knot. Near this EP_2 trefoil knot, we execute control loops which achieve spectral flow. We show that these spectral flows realize the non-Abelian braid group B_3. Finally, we conclude with a discussion on topological energy transfer between these three modes in a future experiment.

Measuring the Knot of Non-Hermitian Degeneracies and Non-Abelian braids

A Dissertation
Presented to the Faculty of the Graduate School
of
Yale University
in Candidacy for the Degree of
Doctor of Philosophy

by
Parker A. Henry

Dissertation Director: Jack G. E. Harris

May 2022

© 2022 by Parker Alexander Henry
All rights reserved.

Contents

List of Figures **vii**

1 Introduction **1**

1.1 Overview 1

1.2 Thesis Outline 3

2 Spectral Flow near Exceptional Points **6**

2.1 Overview of Exceptional Points 6

2.2 Spectral Theory 8

2.2.1 Linear Maps 8

2.2.2 Eigenvalues and Eigenvectors 14

2.2.3 Generalized Eigenspaces and Jordan Normal Form 16

2.2.4 Characteristic Polynomial 22

2.2.5 Trace, Determinant, and Discriminant 24

2.3 n-Mode Spectral Flow 25

2.3.1 Control Space $\mathcal{L}_n$ of Spectra 25

2.3.2 $\mathcal{L}_n$ Path Homotopy and Fundamental Group 27

2.3.3 Degenerate and Nondegenerate Subspaces of $\mathcal{L}_n$ 28

2.4 2-Mode System 29

2.4.1 2 Coupled Oscillators 30

2.4.2 2-Mode Toy System 31

2.4.3 2-Mode Jordan-Arnol'd Form 35

2.4.4 $\pi_1(\mathcal{G}_2) \cong B_2 \cong \mathbb{Z}$ 38

2.5 3-Mode System 39

2.5.1 3-Mode Control Space 39

2.5.2 The Knotted Topology of EP_2 in a 3-Mode System 41

2.5.3 EP_2 Manifold 42

2.5.4 Braid Group B_3 44

3 Optomechanics Theory **45**

3.1 Overview of Optomechanics 45

3.2 Mechanical Oscillator 46

3.2.1 Linear Response: the Mechanical Transfer Function 46

3.2.2 The High-Q Regime: Reducing the 2nd Order ODE to a 1st Order ODE . 47

3.2.3 Hamiltonian of the Mechanical Oscillator 49

3.3 Fabry-Pérot Cavity 50

3.3.1 Fabry-Pérot Cavity Fields and Hamiltonian 50

3.3.2 Input-Output Theory 53

3.3.3 Cavity Equation of Motion via Input-Output Theory 58

3.3.4 Cavity Spectrum 60

3.4 Optomechanical Coupling 61

3.4.1 Effect of the Mechanics on the Optics 62

3.4.2 Effect of the Optics on the Mechanics 63

3.4.3 Optomechanical Equations of Motion: An Alternate Derivation from Input-Output Theory 65

3.4.4 Linearizing the Optomechanical E.O.M.'s 66

3.4.5 Optomechanical Spring: Solution to the Linearized E.O.M.'s 68

3.5 Two-Mode Optomechanics 72

3.5.1 Nearly Degenerate Two-Mode Optomechanical Coupling 72

3.5.2 Nondegenerate Two-Mode Coupling via Floquet Theory: Writing the Hamiltonian 76

3.5.3 Nondegenerate Two-Mode Coupling: Equations of Motion 80

3.5.4 Nondegenerate Two-Mode Coupling: Solving the Equations of Motion . . 82

3.5.5 Nondegenerate Two-Mode Coupling: Time-Independent Floquet Frame . 85

3.6 Three-Mode Hamiltonian 87

4 Membrane-in-the-Middle Platform **91**

4.1 Membrane 91

4.1.1 Membrane Mechanical Modes 91

4.1.2 Experimental Membrane and Mount 92

4.1.3 Membrane Mechanical Ringdowns 94

4.2 Optical Cavity 96

4.2.1 Description of the Optical Cavity 96

4.2.2 Characterizing the Cavity with a Cavity Scan 97

4.3 Cryostat 101

4.3.1 Description of the Cryostat . . . 101
4.3.2 ^{4}He Recovery in the "Wet" Fridge . . . 103
4.4 History of the MIM Experiment . . . 104

5 Data Acquisition 106
5.1 Optical Table . . . 106
5.1.1 Optical Paths . . . 106
5.2 Laser Locking Methods . . . 109
5.2.1 PDH Locking the Probe Laser . . . 109
5.2.2 Shifted Locking ("Slocking") the Control Laser . . . 111
5.2.3 Sweetspot Measurement . . . 112
5.2.4 Control Laser Power Stabilization . . . 114
5.3 Electronic Setup . . . 115
5.3.1 Heterodyne Measurement Electronics . . . 115
5.3.2 Optomechanical Control Electronics . . . 116
5.3.3 Calibration of Laser Powers . . . 118
5.4 Measurement of Exceptional Points . . . 119
5.4.1 Dataset Acquisition . . . 120
5.4.2 Zurich HF2 LIA and Drive Settings . . . 121
5.4.3 Dataset Shape . . . 122

6 Data Analysis 123
6.1 Spectroscopy of Exceptional Points from Driven Response Measurements . . . 123
6.1.1 Mechanical Displacement in Driven Measurements . . . 123
6.1.2 Quadrature Measurements . . . 127
6.1.3 Extracting Eigenvalues from Spectra . . . 129
6.2 Finding an EP_3 Point in a 4D Space . . . 130
6.2.1 Slices with 2D Sheets . . . 131
6.2.2 Slices with 1D "Whirlpool" Sweeps . . . 132
6.2.3 Sparse 4D Sweeps: A Topological Quantification of Proximity to EP_3 . . . 134
6.2.4 Noise Limits on d_3 . . . 138
6.3 Obtaining EP_2 Points . . . 140
6.3.1 Quantifying Proximity to EP_2 . . . 140
6.3.2 Choosing a Hypersurface: The 3D Hyperrectangular Surface . . . 142
6.3.3 Discretization and Scanning of 3D Rectangles . . . 144
6.4 Analysis of EP_2 Slices . . . 146

6.4.1 Filtering of EP_2 Slices . . . 148
6.4.2 Algorithmically Finding EP_2 Points . . . 155
6.5 Measuring the EP_2 Trefoil Knot . . . 158
6.5.1 Rectilinear Stereographic Projection . . . 159
6.5.2 Stereographic Projection . . . 161
6.6 Eigenvalue Braiding . . . 166

7 Future: Real-Time Control Loops 170
7.1 Non-Hermitian Berry Phase . . . 170
7.1.1 The Adiabatic Theorem . . . 170
7.1.2 Proof of the Adiabatic Theorem for Hermitian Systems . . . 172
7.1.3 Berry Phase . . . 175
7.1.4 Considerations for Non-Hermiticity . . . 175
7.2 Ringdown Train Electronics . . . 177
7.2.1 Modifications for Dynamics . . . 178
7.2.2 AWG and Burst . . . 181
7.3 Complex Ringdown Trains . . . 184
7.3.1 Complex Ringdown Response . . . 184
7.3.2 Complex-Averaged Ringdowns . . . 185
7.4 Sample Dynamical Loop . . . 190

8 Conclusion and Outlook 193
8.1 Summary . . . 193
8.2 Outlook . . . 194

A Derivation: Dropping the Counter-Rotating Term in the High-Q Limit 196

B Rectangular Membrane Frequency Derivation 199

C Optomechanical Measurements 203
C.1 Extracting Optomechanical Coupling Constants . . . 203
C.2 Cavity Measurements . . . 206

D Pound-Drever-Hall (PDH) Frequency Locking 208

E Metric Expansions near EP's 212
E.1 Expansions near EP_2 . . . 212
E.2 Expansions near EP_3 . . . 216

F Outlier Filter Implementation **218**

G Braid Coloring Algorithm **220**

References **222**

List of Figures

1.1 a: a Möbius strip of 2×2 spectral flow. b: a trefoil knot of 3×3 eigenvalue degeneracies. 2

2.1 a: a path $f : [0,1] \to X$ in the topological space X. b: a path homotopy $F : [0,1] \times [0,1] \to X$ between the paths $f(s)$ and $g(s)$ in X. 26

2.2 Two distinct loop homotopy classes of the complex plane $\mathbb{C}$, minus a single point (marked by the $\times$). The loop homotopies in $[\tilde{f}]$ are marked with solid lines, and the loop homotopies in $[\tilde{g}]$ are marked with dashed lines. 28

2.3 Eigenvalue braids in the 2-mode system. z wraps around itself from 0 to 2π once in all plots. LHS shows z and the two eigenvalues in the complex plane, as well as the arguments of z and the eigenvalues versus the parameter $s \in [0,1]$. RHS shows the eigenvalues as a function of $s \in [0,1]$. Black x's denote the base points of the control loop z (green), as well as the eigenvalues (blue and orange). z does not enclose $z = 0$ in a and b, and z does enclose $z = 0$ in c and d. In a and b, $r_0 = 0.25$. In c and d, $r_0 = 0.75$. In all plots, $g_0 = 1$, $\gamma = 1$. 32

2.4 Eigenvalue braids in the 2-mode system. z wraps around itself from 0 to 4π once in all plots ($n = 2$ in Equation (2.77)). LHS shows z and the two eigenvalues in the complex plane, as well as the arguments of z and the eigenvalues versus the parameter $s \in [0,1]$. RHS shows the eigenvalues as a function of $s \in [0,1]$. Black x's denote the base points of the control loop z (green), as well as the eigenvalues (blue and orange). z does not enclose $z = 0$ in a and b, and z does enclose $z = 0$ in c and d. In a and b, $r_0 = 0.25$. In c and d, $r_0 = 0.75$. In all plots, $g_0 = 1$, $\gamma = 1$. 34

2.5 The trefoil knot (green), parameterized by Equations (2.112) and (2.113). The trefoil knot is wound around a torus of radii r and ρ (blue). The coordinates t and ϕ parameterize the circles of radii r and ρ, respectively. 41

2.6 A: A depiction of the EP_2 manifold in the $\mathcal{L}_3$ control space (gold), which contains EP_3 (blue). $\mathcal{L}_3$ is depicted here as $\mathbb{R}^4 \cong \mathbb{C}^2$. We look at the S^3 hypersurface (green), on which the EP_2 manifold is a trefoil knot. B: three loops in the control space $\mathcal{G}_3$, which realize three braids in distinct braid isotopy classes in B_3. Left: the braid exchanges zero eigenvalues; middle: the braid exchanges two eigenvalues; right: the braid exchanges three eigenvalues. 44

3.1 A plot of the ratio of output to input field amplitude, as the laser detuning Δ is swept. This is plotted for multiple values of $\kappa_{\mathrm{in}}/\kappa$. Left: the absolute value of the amplitude. Right: the real and imaginary parts in the complex plane. 59

3.2 The cavity reflection coefficient, equation (3.100), as a function of the laser frequency, in units of the free spectral range $\Delta\nu_{\mathrm{fsr}}$. For this simulation, $r_1 = 0.8$, and $r_2 = 0.85$. 62

3.3 The optomechanical interaction plotted in the resolved sideband and the unresolved sideband regimes. The left-hand sides show the optomechanical frequency and damping shifts versus the swept laser detuning Δ, and the right-hand sides show these shifts in the complex plane, defined by the frequency and damping shifts. In each plot, $\omega_m = 1\,\mathrm{kHz}$, $\sqrt{\kappa_{\mathrm{in}}}\,|a_{\mathrm{in}}| = 100\,\mathrm{kHz}$, $g_0 = 1\,\mathrm{Hz}$. 71

3.4 Two highly nondegenerate mechanical modes, coupled by two laser tones. A mechanical drive is applied at frequency $\omega = \omega_1$ (red Lorentzian). The motion at ω_1 creates a motional sideband (red-white Lorentzian) with the red laser tone (rightmost red arrow), which is detuned from the cavity resonance ω_c by $-\omega_1$. The motional sideband beats with the blue laser tone (blue arrow), which is detuned by $-\omega_2$ from the same cavity resonance. This beatnote is at $\omega = \omega_2$ (leftmost red arrow), and drives the membrane at $\omega = \omega_2$. 77

3.5 The three lasers used to optomechanically control three mechanical modes, plotted as intensity versus laser frequency. The laser frequency axis is set to zero at the cavity resonance for the control laser. The blue Lorentzian represents the cavity linewidth. 87

4.1 The vibrational modes of the square membrane (Equation 4.4). The blue color is the high value, the red color is the low value, and the white color is the zero. . . 92

4.2 The membrane, mounted on its membrane mount. 93

4.3 Left: a ringdown train of the 557.4 kHz mode. The sampling rate is 1800 samples per second, and the bandwidth on the lock-in amplifier is 100 Hz. The blue lines are the membrane mode motion. The orange vertical lines are where the drive was turned off. The green vertical lines are where the drive was turned on. These aid in the analysis. Right: a fit of the averaged motion over all of these ringdowns to the fit function (4.6). A value of $\gamma = 2\pi \times 2.0\,\text{Hz}$ is extracted from this fit. . . 94
4.4 Ringdown trains for four mechanical modes. 95
4.5 The optical cavity, with the membrane "bridge" (Figure 4.2) mounted inside. . . 96
4.6 A batch of the mirrors used in the optical cavity of this experiment. Purchased from ATFilms. 97
4.7 The control laser frequency versus the control laser temperature. 98
4.8 A cavity scan measurement. a) the reflection is measured both while the temperature is ramped up and down. b) the reflection is measured only while the temperature is ramped up. 98
4.9 The scan of our cavity modes. The color axis shows the cavity reflection. The piezo voltage sweeps the membrane ring piezo voltage, which sweeps the membrane piezo position on a 1D axis. The laser frequency is swept by sweeping the laser temperature via an applied DC voltage. 99
4.10 a) an image of our cryostat. b) a schematic of the ^{3}He cryostatic environment. Figure b from [33, p.33, Figure 2.1] and [70, p.54, Figure 3.5]. 101
4.11 The cryogenic platform used for this experiment. a. Schematic of the platform. b. Photo of the platform. Figure adapted from [33, p.34, Figure 2.2] and [70, p.56, Figure 3.6]. 102
4.12 The springs, the collimator, and the optical cavity, removed from the helium insert. These were removed when the setup was disassembled and moved from SPL to YSB. 103

5.1 Detailed optical diagram. The red path is the probe laser path. The blue path is the control laser path. The purple path is the probe and control laser paths combined. Black lines denote electronics. 106

5.2 A: A simplified diagram of the experimental setup. B (upper): The control laser tones used in this experiment. The horizontal axis gives the detuning with respect to the cavity mode addressed by the control laser. The AOM produces three optical tones which optomechanically control the membrane mechanical modes. B (lower): The probe laser tones. The probe laser is approximately two FSR's red-shifted from the control laser frequency. The LO (grey) is $-79.5\,\mathrm{MHz}$ away from the mechanical drive. The mechanical drive is produced by an AOM. The 15 MHz sidebands are produced by an EOM, and are used for PDH locking. . . 107

5.3 A simulation of sweeping the control laser frequency to find the cavity resonance. Top: the blue ramp is the frequency of the control laser (dashed blue line is the mean of the ramp), and orange is the cavity resonance. Bottom: cavity reflection in red. The reflection dips to minima whenever the ramped control laser frequency matches the cavity resonance (simulation done with cavity mirror reflections $r_1 = .9$, $r_2 = .95$). 112

5.4 Sweetspot search after a helium transfer. The applied piezo voltage is swept, and the resonant Rohde-Schwartz (RS) frequency is plotted on the y-axis. The red points are the data taken after the transfer of 2021/11/07, and the blue points are the data taken from the previous transfer. The red points are fit to a parabola (red line), and the applied voltage and matching RS frequency are chosen. 113

5.5 The effect of the control laser power stabilization. Left: the voltage vs time without the VOA power stabilization, taken over 2.5 hours. The value of (max-min)/min at the final tapoff before the cavity is 3.5%. Right: the voltage vs time with the VOA power stabilization, taken over 8 hours. The value of (max-min)/min is 1.8%. 114

5.6 The measurement electronics that digitize the cavity signal. The cavity reflection is monitored on the oscilloscope in the top path. The membrane motion is measured with a Zurich HF2 LIA in the middle path. The probe laser is locked to a cavity mode in the bottom path (see Figure 5.1 and Section 5.2.1). Adapted from [33, Figure 2.8] and [70, Figure 3.9]. 116

5.7 Calibration of the power of the control tone that addresses the 705 kHz mechanical mode, as a function of the RF input voltage. The RF frequency is set to 79.5 MHz. Blue points are data taken at each RF voltage from a Rigol function generator. The orange is a fit to a parabola of the form $aV^2 + bV + c$. Units are volts on both axes. 118

5.8 Driven response spectra for each of the three mechanical modes. The amplitudes of the spectra are plotted in the left-hand plots, and the same three spectra are plotted in the complex plane on the right-hand side. The red-to-blue coloring represents the drive frequency. This coloring serves to identify frequency values between the left- and right-hand plots. The black curves are fits to sums of nine Lorentzians (the fit is detailed in Chapter 6), and the blue, orange, and green curves are the individual Lorentzians extracted from these fits. 121

5.9 Driven response for several driving amplitudes, at a modulation depth of 10% and a drive of 15.0 dBm RF power. The drive we do in most of the exceptional point measurements is 400 mV, which is well within the linear regime when three control tones are applied. 122

6.1 Three 2-parameter slices through the 4-dimensional control space. These slices sweep two out of three of P_i, $i = 1, 2, 3$, with δ fixed at $\delta = 2\pi \times 49.7\,\mathrm{kHz}$. The 3D plot shows the slices intersecting. The bottom row shows the individual slices. The colorbar is the d_3 metric (Equation (6.34)). Plot (a) represents raw data. Plot (b) represents theoretical estimates of d_3, based on our optomechanical model. . 131

6.2 All $\binom{42}{} = 6$ slices of the 4-dimensional space to find EP3, laid out in 6 columns. Data are plotted as colormaps, against the two free parameters. The colorbar is the metric d_3 (Equation (6.34)). The fixed parameters are captioned above each slice. The top row is raw data. The middle row is the filtered d_3 data (Section section:filtering). Note that the smoothed data have higher minima than the raw data, because the extrema are averaged by the filtering. The black dots are algorithmically chosen minima in the filtered d_3, which represent estimates of EP_3 points. The bottom row is theoretically calculated d_3 values, from our optomechanical model. 132

6.3 A series of 1-dimensional sweeps to minimize d_3 (Equation (6.34)). On the first one, initial parameters are set in P_1, P_3, and δ that are estimated to reach EP_3. P_2 is swept. The minimum value of P_2 found in this sweep is used as the fixed value of P_2 in the next measurement, and P_3 is swept for a minimum. This process is done iteratively to iteratively find a point in parameter space that best minimizes d_3. 133

6.4 Simulation: the Hopf Invariant, as a function of the finite mesh size n for a mesh of size (n, n, n, n). 136

6.5 The Hopf Invariant swept across EP_3 in P_B. 137

6.6 Simulated dependence of χ on the other experimental parameters. 137

6.7 d_3 dependence on the (δ, P_1, P_2, P_3) parameters, for simulated lines that reach the numerically estimated EP_3 138

6.8 A Monte Carlo simulation of the minimum value of d_3 of a 4D hyperrectangle centered about EP_3 . The simulation perturbs the parameters in the perfect hyperrectangle by Gaussian fluctuations parametrized by Equation 6.47. 139

6.9 A plot of Abs(z) and Arg(z), against the real and imaginary parts of $z = x + iy$, in the left- and right-hand plots, respectively. There is a minimum at $x = 0$ and $y = 0$ (left), as well as a vortex at $x = 0$ and $y = 0$ (right). 140

6.10 One of the eight faces of the 4D hyperrectangle over which data is taken. This particular face is the $\delta_{\max}$ face. 142

6.11 a: The surface of a 3D cube, unfolded into six 2D squares. b: Folding the six squares back up into the surface of a 3D cube. c: The folded squares, which now make up the surface of a 3D cube. Figures a and b are from [82]. 143

6.12 a: the eight 3D cubes which are the faces of the 4D hyperrectangle joined together by identifying the faces of the 3D cubes. b and c: folding the eight 3D cubes together to represent the data as a tesseract. 144

6.13 Plots of several 3D rasters of the $\delta_{\max}$ face, with each dataset aggregated into one here. (a) is all data, colored by min-diff. (b) is those points with measured min diff below a gradient threshold of 20 Hz at $P_3 = 78\,\mu W$, and 25 Hz at $P_3 = 702\,\mu W$. (c) is theoretical calculations of those points, with min diff below 30 Hz. 145

6.14 A slice taken to measure EP_2. The left two columns are the magnitude and phase of the discriminant D, respectively. The right two columns are the magnitude and phase of the eigenvector indicator E, respectively. The first row is raw data. The second row is filtered data (as described in Section 6.4.1). The black and cyan points in the magnitude and phase plots, respectively, are algorithmically chosen minima and vortices, which represent our estimates of EP_2 points (as described in Section 6.4.2). The third row is theoretically predicted data. 146

6.15 The sixty-one 2D slices performed over the hypersurface described in Section 6.3.2. a: the 61 slices on each of the eight faces of the hypersurface. b: the 61 slices, assembled in the "rectilinear stereographic" projection of the hypersurface (detailed in Section 6.5.1). c: the 61 slices, assembled in the 3D stereographic projection of the hypersurface (detailed in Section 6.5.2). 147

6.16 Kernels that can be convolved with a data to get a "moving average" of a pixel with its nearest neighbors, so as to reduce noise in data. Left is the boxcar kernel, with a width of 3 units, and right is a Gaussian kernel, with a FWHM of 3 units, chosen to match the width of the boxcar on the left ($\sigma = 1.2740$, from Eq. (6.57)) 150

6.17 The results of Gaussian-filtering an image (showing the cryostat in which these experiments were performed). Higher values of σ correspond to a stronger pixel blurring, i.e. a stronger pixel smoothing. 151

6.18 The results of filtering our discriminant data with our filtering procedure. First, we outlier-filter the raw data (top row), by replacing outlier pixels (in circles; top) with median-filtered pixels (middle row). Next, we Gaussian-filter the outlier-filtered data to smooth the data (bottom row), with Gaussian standard deviation $\sigma = 10/(2\pi)$. These filters are applied to the real and imaginary components of the discriminant (left two columns). The corresponding magnitude and phases are plotted alongside them (right two columns). The gaussian filter is implemented in [94] [92]. 152

6.19 The results of Gaussian-filtering the real and imaginary components of the discriminant data without first outlier-filtering the data. Convolving the non-outlier pixels with the outlier salt and pepper pixels with the non-outlier pixels spreads the outlier values over the rest of the data. 153

6.20 The result of applying a median filter of size $= (3, 3)$ to the real and imaginary discriminant data. It replaces outlier salt and pepper noise pixels with less noisy pixels, as well as smoothes out the data, by itself. 154

6.21 The computation of the second derivative test determinant (b) for the function $f(x, y) = \sqrt{x^2 + y^2}$ (a). The determinant has a singularity at $(x, y) = (0, 0)$. This singularity motivates our minimum finding algorithm for the discriminant (6.48) and the eigenvector indicator (6.50). 157

6.22 All of the EP_2 points that were algorithmically found from all of the 61 datasets in this experiment, via all four methods in Section 6.4.2. The columns represent each of the four methods. The top row is the tesseract representation of the 3D hypersurface. The bottom row is the stereographic projection of the 4D data. The circles represent the algorithmically obtained EP_2 points, and the line represents a theoretically estimated EP_2 curve. The points are colored by θ (Equation 2.115; upper right corner). 159

6.23 A stereographic projection of the unit circle ($|x|^2 + |y|^2 = 1$) onto the real line (x-axis). The north pole is chosen as $(0, 1)$ (blue). The points (x, y) and (x', y') on the circle (red) are mapped onto the points $x/(1-y)$ and $x'/(1-y')$ on the real line (purple). 162

6.24 A stereographic projection of the unit circle ($|x|^2 + |y|^2 = 1$) onto the real line (x-axis). The north pole is chosen as (p, q) (blue), so we rotate the coordinate system to one in which (p, q) is at the origin. 163

6.25 The datasets over which closed loops were realized in order to demonstrate eigenvalue braiding (Figure 6.26). The axes denote the swept parameters, and the legend to the right denotes the fixed parameters. Top (bottom) sheet: P_1 and P_2 (P_3) were the swept parameters in these sheets, while δ and P_3 (P_2) were the fixed parameters. The black circular dot denotes the common start and end point of these rectangular loops. Black crosses denote the measured EP_2 points. The cyan, light-blue and dark-blue loops correspond to the A, B, and C columns of Figure 6.26, respectivey. 166

6.26 The eigenvalue trajectories of the loops in Figure 6.25. Columns A, B and C correspond to the cyan, light-blue and dark-blue loops of Figure 6.25, respectively. The top row is the rectangular loop (dark blue), with its start/end (black dot). The yellow points are the EP_2 points, as obtained in Section 6.4, and the yellow curve is the estimated EP_2 curve. Middle row is the extracted eigenvalue data along the loop. i traces out the loop from its beginning to end. Bottom row is theoretically estimated eigenvalues. 167

6.27 A collection of loops (a-c) and eigenvalue spectra trajectories (d-f). The three loops are each from a different loop homotopy class. The three loops realize the braids σ_1^2, σ_1^3, and $\sigma_1\sigma_2\sigma_1$, respectively. 168

6.28 A demonstration of the noncommutativity of the eigenvalue braid group B_3 (b-c), via noncommutation of the control loops (a). Performing the red loop, then blue loop, produces (b); performing the blue loop, then red loop, produces (c). 169

7.1 A ringdown train. The clock voltage is in the top row, the response voltage is in the middle, and the response phase is in the bottom row. 178

7.2 The HP8642B signal generator used to generate control tones in the 2016 experiment (used to generate the AM modulation in the probe in this experiment). AM and FM inputs are on the left-hand side, and the output is on the right-hand side. 178

7.3 The result of applying two trapezoids (a) and two sines (b) for AM and FM modulation, via an external modulation input port and a variable RF attenuator, respectively. The output waveform (green), is frequency-modulated from 200 kHz to 1.2 MHz. The amplitude is a complicated function of the attenuator transfer function. The red waveform creates FM modulation, and the yellow waveform creates AM modulation. 179

7.4 The result (green) of applying a low voltage and a high voltage to the FM port (both red). The low voltage (a) sets the frequency to 200 kHz, and the high voltage (b) sets the frequency to 1.2 MHz. The yellow voltage is an AM input to the RF attenuator, and is held constant for these traces. 179

7.5 The output of the variable RF attenuator (green), with a 200 Hz AM input (yellow), and a 10 kHz RF tone (blue), when no DC block is applied to the output. . 180

7.6 Arbitrary waveforms generated on a function generator. Green is an AM modulated waveform, and yellow is the modulation input. a: a train of arbitrary waveforms. b: a pulsed waveform. In both of these, the rise time is 250 µs, the fall time is 500 µs, the high time is 500 µs, and the low time is 250 µs. 181

7.7 Two burst-mode ellipsoids applied via a function generator, which is calibrated to create a sine wave in the control tone power. The clock is in purple, and the two function generator outputs are blue and yellow. 183

7.8 A series of ringdown measurements of the $\omega_d/2\pi = 705\,\text{kHz}$ mode. The ringdowns are shown in (a), and they are averaged in (b) and (c). The top row of (a) shows the clock, the middle row shows the norm, and the bottom row shows the phase. (b) shows a fit of the average norm to an exponential decay, and (c) shows a linear fit of the average phase. 186

7.9 A ringdown train measurement of 100 ringdowns, in which the drive is at $\omega_d/2\pi = 705\,\text{kHz}$, and read-out frequency is $\omega_{\text{read}}/2\pi = 352\,\text{kHz}$. a: seven of the ringdowns are shown. The ringup period is $T = 1.7\,\text{s}$. Top row is the clock, middle row is the response amplitude, and bottom row is the response phase. b: one individual driving interval. Note that the response phase is shifted by the drive. c: the complex average (Equation (7.50)). 187

7.10 Driven motion of mechanical mode 3 ($\omega_d/2\pi = 705\,\text{kHz}$), while reading mode 1 ($\omega_{\text{read}}/2\pi = 352\,\text{kHz}$), with control tones applied, so that motion at mode 3 drives mode 1 (as in Sections 3.6 and 5.3.2). a: the clock is high in the top row, the amplitude of the response is in the middle row, and the phase is shown in the bottom row. b: a linear fit of $\theta/(2\pi) = \Delta f \times t$. $\Delta f = 19.318\,\text{Hz}$ is extracted. . . 188

7.11 A ringdown train of 100 ringdowns, with the ringup time $T_m = 1.6565\,\mathrm{s}$ (satisfying Equation (7.53)), which drives at $\omega_d/2\pi = 705\,\mathrm{kHz}$ and reads at $\omega_{\mathrm{read}}/2\pi = 352.3\,\mathrm{kHz}$. a: four of the 100 ringdowns. b: the complex average (Equation (7.50)). c: zoom-in of four averages over four 100-ringdown measurements. 189

7.12 The response of a ringdown train in which the 705 kHz mode is driven, and the membrane amplitude of motion is read at each of the frequencies. Blue shows the ringdowns when the control loop is not applied, and orange shows the ringdowns when the control loop is applied. 191

7.13 Complex averages of 100-ringdown ringdown trains, in which either the control loop is executed or not executed. The 705 kHz mode is driven, and the motion is read at 352.3 kHz. The plots show amplitude and phase. 191

A.1 The magnitude of the mechanical transfer function of a mechanical oscillator at various Q. The y-axis is made dimensionless by dividing by the approximate maximum values at resonance, $Q/(m\omega_m^2)$. This also puts the curves on the same scale to aid in the visual comparison across different Q values. We see that, even at modest Q, that the response peaks very sharply at ω near $\omega = \pm\omega_m$. 197

B.1 A rectangular membrane with length L_x and width L_y. 199

C.1 A fit of the mechanical frequency and damping versus the control laser detuning, to determine the optomechanical coupling constant. The extracted g is $g = 0.320(1)\,\mathrm{Hz}$, the extracted $\omega_m^{(0)}/2\pi = 704\,793.78(5)\,\mathrm{Hz}$, the extracted $\gamma_m^{(0)}$ is $\gamma_m^{(0)}/2\pi = 0.85(4)\,\mathrm{Hz}$, the extracted Δ_0 is $\Delta_0/2\pi = -1700(400)\,\mathrm{Hz}$, the extracted κ is $\kappa/2\pi = 189\,700(1400)\,\mathrm{Hz}$. The value of κ_{in} is fixed at $\kappa_{\mathrm{in}}/2\pi = 48\,\mathrm{kHz}$. . . . 204

C.2 A fit of the driven response to a single Lorentzian. The upper-left is the absolute value of the response, the lower-left is the quadratures of the response, and the right is the response in the complex plane. Dots are data, and lines are fits. . . . 204

C.3 A three-tone g measurement, with common κ and Δ_0 values, for the three modes in this experiment. 205

C.4 A fit of the cavity linewidth. 207

D.1 Pound-Drever-Hall error signal. Simulated from the reflectivity coefficient, with $r_1 = .9997$ and $r_2 = .99998$, from $\Omega = 0.005\omega_c$, and from the imaginary part of Equation (D.9). 211

G.1 The results of applying the coloring algorithm to sort the eigenvalues along their braids. 221

Chapter 1

Introduction

The goal of this dissertation was to experimentally investigate the generic physics of spectral flow associated with a system of three non-Hermitian coupled harmonic oscillators. We sought to explore the parameter space around a triple degeneracy of the three-mode system. We also wished to demonstrate the eigenvalue spectral flow produced by parameter loops, which are determined by how the loop encloses the subspace of double degeneracies. We used an optomechanical platform to demonstrate these goals, though essentially any three-mode, non-Hermitian system could have been used. In this dissertation, I describe the work that my colleagues and I have done to realize these goals [1].

1.1 Overview

Many systems in the physical sciences can be described by first-order differential equations of the form

$$i\frac{\partial}{\partial t}\mathbf{c} = \mathcal{H}\mathbf{c} \tag{1.1}$$

where $\mathcal{H}$ is an $n \times n$ dynamical matrix, and $\mathbf{c}$ is a vector in an n-dimensional complex vector space. For example, $\mathcal{H}$ in quantum mechanics, $\mathcal{H}$ can be an $n \times n$ Hamiltonian which determines the time-evolution of an n-level system. In classical mechanics, $\mathcal{H}$ can describe n coupled harmonic oscillators. Much of classical mechanics [2] [3], classical electrodynamics [4], and (closed) quantum mechanics [5] assume that $\mathcal{H}$ is Hermitian (i.e., the adjoint $H^\dagger$ satisfies $H^\dagger = H$). However, classical mechanics and electromagnetism can also readily introduce non-Hermiticity, via gain and loss (dampers or resistors), and nonreciprocity (gyrators).

There is much rich physics that lies beyond Hermitian systems. For instance, we can consider *spectral flow*, or the paths that eigenvalues of the dynamical matrix $\mathcal{H}(\Psi)$ take in the complex plane $\mathbb{C}$, when the control parameters Ψ of $\mathcal{H}(\Psi)$ are varied. These spectral flows produce unique

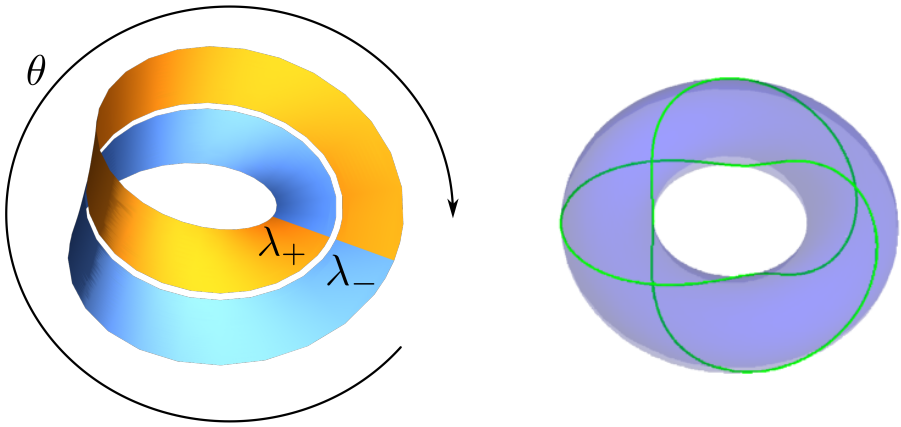

(a) (b)

Figure 1.1: a: a Möbius strip of 2×2 spectral flow. b: a trefoil knot of 3×3 eigenvalue degeneracies.

topological structures. For a toy 2×2 dynamical matrix[1]

$$\mathcal{H}(z) = \begin{pmatrix} 0 & 1 \\ z & 0 \end{pmatrix}, \tag{1.2}$$

which has eigenvalues

$$\lambda_{\pm} = \pm\sqrt{z}, \tag{1.3}$$

we can vary the parameter z as $z = e^{i\theta}$, for θ from 0 to 2π. Then the eigenvalues of $\mathcal{H}(\theta = 0)$ – $+1$ and -1 – switch to -1 and $+1$, respectively, for $\mathcal{H}(\theta = 2\pi)$. Together, these paths trace out a Möbius strip (Figure 1.1a). It turns out that this Möbius strip structure is intrinsically related to a feature of non-Hermitian systems called an *exceptional point*, which is when $\mathcal{H}(z)$ is not diagonalizable. The exceptional point of this toy $\mathcal{H}(z)$ is at $z = 0$, and the Möbius strip appears if and only if the loop varying z encloses $z = 0$. This structure was observed in [6] [7] [8] (it is also an important part of the story for "quasiadiabatic" time-evolution of the 2×2 system, as [6] demonstrates).

For an 3×3 non-Hermitian system, the topological structure involved is even richer. For the 2×2 system, the exceptional point which determines the classes of spectral flows was one point in the space; for the 3×3 system, the exceptional point space which determines the spectral flow is instead a trefoil knot (Figure 1.1b). The spectral flows thus form an even richer topological structure. A simple algebraic argument which lays this out is given in [9], yet this algebraic result can have wide-ranging applications in generic 3×3 non-Hermitian systems. This thesis

[1] Any nonzero 2×2 dynamical matrix can be brought to this form – the Jordan-Arnol'd form – with a similarity transformation, as shown in Chapter 2.

experimentally measures this trefoil knot degeneracy structure in a non-Hermitian system of three coupled modes, and measures the structures formed by its spectral flows.

The physical system used in this thesis is an optomechanical system. Fundamentally, light and a mechanical resonator couple because the phonons of light impart momentum onto the resonator, via the particle-like nature of photons. But phonons are also wavelike, and the resonator can change its wavelength in response to this momentum, which alters the wavelength of the photons. Optomechanics is a very productive platform to study a wide range of physical phenomena. We use optomechanics in this work to create a platform in which we experimentally study the topological structures associated with spectral flow in a non-Hermitian system of three coupled harmonic oscillators.

This thesis reports on the results of the MIM experiment since 2018 [1]. We design a non-Hermitian system of three coupled modes with three vibrational modes of a Si_3N_4 square membrane, coupled to a Fabry-Pérot cavity via the optomechanical interaction. We measure spectra in this parameter space by sweeping the parameters Ψ, and bring the system to the triply-degenerate EP_3 point that this system possesses. We then measure EP_2 points in a manifold surrounding this EP_3 point, and show that they form a trefoil knot. We also demonstrate that varying Ψ around a closed loop produces distinct eigenvalue braids, depending on how the loop encloses the EP_2 knot, and that concatenating these braids produces any braid in the braid group B_3.

1.2 Thesis Outline

In Chapter 2, we discuss the spectral flow of a non-Hermitian dynamical system, in the presence of exceptional points. Specifically, we discuss the dynamical matrix both at and near exceptional points with the Jordan Normal Form and the closely related Jordan-Arnol'd Form, respectively. We then discuss the connection between control loop homotopy classes in the non-degenerate parameter space and the braid group of eigenvalue spectra of the dynamical matrix. We then consider two- and three-mode systems: the eigenvalue braiding is determined by one doubly degenerate exceptional point in the two-mode case, and by a trefoil knot of doubly degenerate exceptional points (EP_2) in the three-mode case. All of this is discussed for generic non-Hermitian systems of damped coupled oscillators.

In Chapter 3, we describe the specific system of coupled oscillators used in this thesis: the modes of a mechanical membrane which are coupled to the optical modes of a cavity via dynamical backaction in optomechanics. We review the natural independent harmonic oscillators in the collection of vibrational modes of a membrane, as well as those of a Fabry-Pérot cavity.

We then review their coupling via dynamical backaction. In particular, we use this light-matter coupling to achieve a non-Hermitian system of three coupled modes, of which we realize full control of the eigenspectrum. We tune this eigenspectrum to EP_2 and EP_3 degeneracies.

In Chapter 4, we describe the membrane-in-the-middle (MIM) platform used in this experiment. Namely, we describe the membrane chosen to realize our mechanical modes, the Fabry-Pérot cavity which the membrane lives in, and the ^{3}He cryostat which contains the cavity-membrane system.

In Chapter 5, we describe the process of driving and reading out the membrane, while applying optical tones to tune the mode frequencies and dampings in the vicinity of EP_2 and EP_3 degeneracies. We outline the optical table configuration, which drives the membrane with one laser, and optomechanically controls the mechanical modes with an additional laser (as described in Chapter 3). We also describe the processes by which we lock the two lasers to two cavity modes. We then describe the electronic portion of the setup. Finally, we summarize practical aspects of dataset acquisition via lock-in detection.

In Chapter 6, we analyze the data taken in Chapter 5. We describe the response of the membrane to our drive, spectroscopy of the data, and the 9-Lorentzian fit model. We then find an EP_3 point in our 4-parameter system. After finding this EP_3 point, we describe the collection of datasets on the hypersurface on which we find EP_2 points (as in Chapter 2). We next outline the data analysis that we perform to algorithmically find EP_2 points in our datasets. Having found these EP_2 points, we represent them on our complete hypersurface with two stereographic projections, and see that they form a trefoil knot (as promised in Chapter 2). Finally, we realize generators of the braid group B_3, using control loops in the complement of the knot in our control space.

In Chapter 7, we discuss steps toward a future experiment in which we apply dynamical loops around the EP_2 knot near the triple degeneracy. The purpose of the dynamical loops is to demonstrate topological energy transfer between the three modes. We introduce the adiabatic theorem for Hermitian systems and the Berry phase (i.e., the geometric phase). Even though the adiabatic theorem does not hold for non-Hermitian systems in general, we also discuss quasiadiabatic and adiabatic processes for which the adiabatic theorem does hold, as well as the role that loss and gain modes play in diabatic (sudden) transitions in the non-Hermitian case. We show simple modifications to the electronic setup of Chapter 5 which enable dynamical loops. Additionally, we describe how complex ringdown measurements can be used to measure the phase as well as the amplitude of the excited modes. Finally, we show preliminary measurements in which we initialize one eigenmode and transfer its energy to a different eigenmode with a quasiadiabatic loop, and measure the amplitude and phase of the ringdown signal. We believe

this will be a key step in measuring the geometric phase introduced by the loop in a future experiment.

In Chapter 8, we first summarize the results of this thesis. We then describe a future, more powerful experimental setup, which will enable faster data-taking, control over the entire control space of eigenmodes around the EP_3 point, and reciprocal energy transfer between modes via "shortcuts to adiabaticity."

Chapter 2

Spectral Flow near Exceptional Points

In this chapter, we discuss exceptional points as they apply to spectral flow in this experiment. We first provide a review of exceptional points and their applications in Section 2.1. We next review spectral theory and generalized eigenspaces in Section 2.2, as nondiagonalizability of the dynamical matrix is a hallmark of exceptional points. We then examine spectral flow of an n-mode system, the braid group B_n of eigenvalue braids in Section 2.3, and these braids' connection to exceptional points. We explore spectral flow further for 2-mode (Section 2.4) and 3-mode systems (Section 2.5).

2.1 Overview of Exceptional Points

In the past decade, there has been high interest in non-Hermitian physics. In particular, non-Hermitian systems possess features absent from Hermitian systems, such as complex eigenvalues [10] [11], non-orthogonal eigenvectors, and exceptional point degeneracies (EPs) [12] [11]. Given a system whose time evolution is generated by an $n \times n$ dynamical matrix $\mathcal{H}$, exceptional point degeneracies are points in the system's parameter space for which $\mathcal{H}$ is nondiagonalizable [13] [14] [12]. Near EPs, $\mathcal{H}$ responds much more sharply to changes in parameters than they do away from EPs [13] [14] [15].

The novel features of non-Hermitian systems enable the development of new forms of sensing and control. Specifically, advances in fabrication technologies allow one to use gain and loss as new degrees of freedom [16], rather than as deviations from the theories that predominantly assume Hermitian dynamics, and which only permit real eigenvalues [5] [2] [4]. An application in the realm of sensing is that the eigenvalues λ of systems at an exceptional point are more

sensitive to perturbations (ϵ) than conventional sensors. This is because, near an exceptional point, $\delta\lambda(\epsilon) \sim \epsilon^{1/n}$, which is sharper than a Hermitian sensor, in which $\delta\lambda(\epsilon) \sim \epsilon$. This was demonstrated with a whispering-gallery-mode micro-toroid cavity [17] [18]. Additionally, this was used to enhance the sensitivity of *in vivo* microsensors in rats by a factor of 3.2 times the limit of conventional sensing methods [19]. More generally, sensors which have nonreciprocity (which requires non-Hermiticity) can exceed fundamental bounds on any reciprocal (and, hence, Hermitian) sensor [18] [20].

Non-Hermitian systems are fundamental to topological photonics [16]. In one experiment, at an exceptional point, the eigenstates undergo a transition from distributed modes to localized modes, as a function of lattice spacing [21]. This is a PT-symmetry-breaking phase transition, as discussed in detail in [22] [23] (PT-symmetry is defined here as spacetime reflection symmetry). For example, nonreciprocal lasing is found in a 1D chiral edge mode by breaking time-reversal symmetry in topological cavities [24]. Additionally, non-Hermiticity has implications to other symmetries besides PT-symmetry: the Altland-Zirnbauer symmetry classication for insulators and superconductors gets 38 symmetry classes instead of 10, because non-Hermiticity makes chiral symmetry distinct from sublattice symmetry [25] [21].

Non-Hermiticity even appears in quantum systems. In a three-level transmon in which the dynamics of a two-level subsystem can be approximately described using a non-Hermitian Hamiltonian, quantum state tomography is performed near the transmon's exceptional point [26]. A more recent work shows non-reciprocal state transfer by tuning the transmon qubit parameters in a control loop that encircles the exceptional point, as well as chiral geometric phases accumulated in this state transfer [27]. These works provide a route toward using non-Hermiticity in topological quantum information processing.

Exceptional points are also useful for amplifiers and for non-Hermitian power transfer. A fundamental limit in the gain-bandwidth ratio of optical amplifiers can be surpassed with exceptional points (e.g., with a microring resonator at an EP) [28]. A 2019 experiment uses EPs to achieve wireless power transfer between a source and a receiver resonator under robust operating conditions [29]; this improves on a 2007 experiment with energy transfer between coupled resonators, which needs to tune the coupling frequency as the source-receiver distance increases [30].

As detailed further in Section 4.4, the Harris group has experimentally explored nonreciprocal energy transfer in a two-mode optomechanical system by encircling an exceptional point, and experimentally demonstrated energy transfer which depends on whether a control loop encloses the exceptional point, and whether the state is in the "gainful" mode for most of the duration of the control loop [6] [31] [32] [33, pp.59-67]. Additionally, adiabatic transport is explored further

for an $n \times n$ system in a theoretical paper [34], which finds that, for certain initial states and closed control loops of time $T = 1/\epsilon$, the state returns to itself and gains a complex phase of ϵ^{-1} times a Puisseux expansion in powers of $\epsilon^{1/n}$; in particular, the nth order term is independent of T, and only depends on the loop homotopy class.

This has been a short review of the applications of non-Hermiticity in modern research. For more in-depth reviews, one can read [16] and [11].

2.2 Spectral Theory

To discuss exceptional points in a physical system, we first review basic notions of linear algebra. Specifically, we review generalized eigenspaces in vector spaces, since a dynamical matrix cannot be diagonalized at an exceptional point. We also review the Jordan canonical form, on which we will use perturbation theory to examine exceptional points in Sections 2.4.3 and 2.5.1. This discussion on generalized eigenspaces largely follows [35].

2.2.1 Linear Maps

Vector Spaces

Let us briefly define vector spaces and review basic notions of vector spaces.

A **vector space** is a set V with elements $v \in V$ for which the two operations *vector addition* and *scalar multiplication* (by elements of a field $\mathbb{F}$) are defined:

$$\begin{gathered} \text{Given any } v_1, v_2 \in V : \text{ define } v_1 + v_2 \in V \\ \text{Given any } v \in V,\, c \in \mathbb{F} : \text{ define } cv \in V \end{gathered} \tag{2.1}$$

The elements $v \in V$ are said to be **vectors** in the vector space.

The vector addition is commutative and associative. The vector addition also has a zero-identity $\mathbf{0} \in V$ such that for any $v \in V$, $\mathbf{0} + v = v$. Any $v \in V$ also has an additive inverse $-v \in V$, where $v + (-v) = \mathbf{0}$. [35, pp.12-13] [36, pp.1-2] [37, Section 2].

The scalar multiplication has a one-identity $1 \in \mathbb{F}$ where, for any $v \in V$, $1 \cdot v = v$. Furthermore, scalar multiplication satisfies the distributive property over vector addition:

$$\begin{gathered} v_1, v_2 \in V,\, a \in \mathbb{F} : \, a(v_1 + v_2) = av_1 + av_2 \\ v \in V,\, a, b \in \mathbb{F} : \, (a + b)v = av + bv \end{gathered} \tag{2.2}$$

The field $\mathbb{F}$ is most often taken to be the real or complex numbers, $\mathbb{R}$ or $\mathbb{C}$. In this thesis, we

primarily concern ourselves with vector spaces over $\mathbb{C}$.[1] Throughout this discussion, we will assume that V is a nonzero vector space (i.e., $V \neq \{\mathbf{0}\}$).

Subspaces

In discussing exceptional points of a physical system defined by a dynamical matrix M, we will frequently be interested in subsets U of vector spaces V which are vector spaces in their own right. These are called **vector subspaces**, or simply **subspaces**. In this discussion, we will decompose the vector space V into subspaces which are characterized by the eigenvalues and eigenvectors of M (Sections 2.2.2 and 2.2.3).

To state that a subset $U \subseteq V$ is a subspace of the vector space V, it suffices to check that the additive identity $\mathbf{0}_V \in V$ is in U (i.e. $\mathbf{0}_V \in U$), that U is closed under vector addition (i.e. if $u, w \in U$, then $u + w \in U$), and that U is closed under scalar multiplication (i.e. if $u \in U$, and $c \in \mathbb{F}$, then $cu \in \mathbb{F}$).

We now look at the addition of subspaces of V in this discussion. Suppose that $U_1, U_2, \ldots U_m$ are subspaces of V. Then the set

$$U_1 + U_2 + \cdots + U_m = \{u_1 + u_2 + \cdots + u_m \,:\, u_1 \in U_1, u_2 \in U_2, \ldots u_m \in U_m\} \tag{2.3}$$

is a subspace of V. Furthermore, this sum of subspaces is the smallest subspace of V that contains all of $U_1, U_2, \ldots, U_m$, in the sense that if another subspace $W \subseteq V$ contains all U_k, $k = 1, \ldots, m$, then $U_1 + \ldots U_m \subseteq W$ [35, Thm. 1.39, pp.20-1].

A noteworthy type of sum of vector subspaces is a **direct sum**

$$U = U_1 \bigoplus \cdots \bigoplus U_m, \tag{2.4}$$

which is the set in Equation 2.3, with the additional property that for any element $u \in U_1 + \cdots + U_m$, there is exactly one way to write $u = u_1 + \cdots + u_m$, where $u_k \in U_k$, $k = 1, \ldots, m$. It can be proven that (2.3) is a direct sum if and only if $\mathbf{0}_U \in U$ can be uniquely written as the sum $\mathbf{0}_U = \mathbf{0}_1 + \cdots + \mathbf{0}_m$, for $\mathbf{0}_k \in U_k$ [35, Thm. 1.44, p.23].

[1] A field is an algebraic structure over which addition and multiplication operations are defined, and both have additive and multiplicative inverses [37, Section 1]. There are many other fields relevant in number theory, algebraic geometry, and cryptography. [38, pp.176-7].

Linear Combinations and Bases

Consider a vector space V and a list of vectors $L = [v_\alpha]_\alpha$ (where the v_α are allowed to be repeated). We can write **linear combinations** of the vectors in L:

$$v = \sum_\alpha a_\alpha v_\alpha \tag{2.5}$$

for some coefficients $a_\alpha \in \mathbb{F}$. We call L a **basis** of V if, for every $v \in V$, *there exists a unique* representation of v as a linear combination of elements of L [36, p.6, Ch.1.2]. For example, if we consider $\mathbb{R}^3$ as a vector space over $\mathbb{R}$, then the list of vectors $L = [(1,0,0),(0,1,0),(0,0,1)]$ is a basis of $\mathbb{R}^3$. For a list of vectors in V to be a basis, it must satisfy two criteria: that the elements span V, and that they are linearly independent.

The span of L is the set of all vectors that can be written as linear combinations of elements of L:

$$\text{span}(L) = \{v \in V : v = \sum_\alpha a_\alpha v_\alpha,\ a_\alpha \in \mathbb{F}, v_\alpha \in L\} \tag{2.6}$$

We say that L **spans** V or L **generates** V if $\text{span}(L) = V$. In practice, $\text{span}(L) \subseteq V$ always holds, so one would prove that $V \subseteq \text{span}(L)$ holds to show that L spans V. For example, in $\mathbb{R}^3$, the list $\{(0,1,0),(0,0,1)\}$ does not span $\mathbb{R}^3$, but the list $\{(1,0,0),(0,1,0),(1,1,0),(0,0,1)\}$ spans $\mathbb{R}^3$ (but is not a basis).

The vectors in L are said to be **linearly independent** if, given a linear combination $\mathbf{0} = \sum_\alpha a_\alpha v_\alpha$ of vectors $v_\alpha \in L$, the only possible representation is with the linear combination $a_\alpha = 0$, for all indices α. If there is a way to write $\mathbf{0} = \sum_\alpha a_\alpha v_\alpha$ where not all a_α are 0, then L is **linearly dependent** [36, p.8, Ch.1.2] [35, p.33, Ch.2.A]. For instance, in $\mathbb{R}^3$, the list $\{(1,0,0),(0,1,0),(1,1,0)\}$ is not linearly independent (as $(0,0,0) = (1,0,0)+(0,1,0)-(1,1,0)$), whereas the list $\{(1,0,0),(0,1,0)\}$ is linearly independent (but not a basis for $\mathbb{R}^3$).

In discussing bases, one discusses the dimension of a vector space. There are two kinds of vector spaces in a discussion on dimension: those that admit a finite-length basis, and those that do not. A vector space with a finite-length basis is **finite-dimensional**. In this thesis, we concern ourselves almost entirely with vector spaces that have a finite dimension.

The relationship between a spanning list and a basis is as follows:

Theorem 2.2.1. *Let L be a spanning list of length n of a finite-dimensional vector space V. L can be reduced to a basis B of V by removing at most $n-1$ elements from L. [36, p.10, Ch.1.2] [35, pp.41-2, Ch.2.B]*

Proof. To prove this, suppose that a list of vectors L spans the vector space V. If the vectors of L are linearly dependent, it is easy to see that at least one element v_α of L can be written

in terms of the other members of L: $v_\alpha = \sum_{\beta \neq \alpha} a_\beta v_\beta$ [35, p.34, Ch.2.A]. Thus, if L is linearly dependent, we can identify an element $v_m \in L$ that can be written as a linear combination of other element of L, remove v_m from L, and still have $\text{span}(L - [v_m]) = \text{span}(L)$. This process is repeated until the list is linearly independent and still spans V. It is repeated at most $n-1$ times, until the final list B is linearly independent and spans V (and is nonempty). Thus, any finite-length spanning list L contains a basis of length at most that of L. ■

We also see the relationship between any linearly independent list and a basis:

Theorem 2.2.2. *Any linearly independent list L of a finite-dimensional vector space V can be extended to a basis B of V. If V has a basis with length n, and L has length m, then this can be done in finitely many operations [35, p.41, Ch.2.B].*

Proof. The proof is similar to the proof of Theorem 2.2.1: if L spans V, we are done. If not, let B be a finite-length basis of V. B spans V, so $L \cup B$ spans V. Take the combined list $L \cup B$, and remove elements of B from $L \cup B$ until the list L' is linearly independent and still spans B. ■

We may set a constraint on the lengths of any linearly independent list and any spanning list:

Theorem 2.2.3. *In a finite-dimensional vector space V, any linearly independent list L_1 has a length which is at least the length of any spanning list L_2 [35, p.35, Ch.2.A].*

Proof. This is proven combinatorially, where let $u_1, \ldots, u_m$ be the items in L_1, and $w_1, \ldots, w_n$ be the elements of L_2. n can be taken to be finite, since V is finite-dimensional. We can remove u_1 from L_1 and prepend it to L_2: $L_2^1 = [u_1, w_1, \ldots, w_n]$. Then L_2 is linearly dependent, so we can write one of the w_k elements, designated as w_1 (reordering the elements of L_2 if necessary), as $w_1 = a_1 u_1 + \sum_{k=2}^{n} b_k w_k$. Then remove w_1 to get $L_2^{1'} = [u_1, w_2, \ldots, w_n]$, which has length n and spans V. The list $L_1^1 = [u_2, \ldots, u_m]$ has length $m-1$, and is linearly independent. This procedure is continued inductively, where we remove u_k from L_1^{k-1}, prepend it to $L_2^{k-1'}$ to get L_2^k, and remove w_k from L_2^k to get $L_2^{k'}$ (again, having reordered the w_k if necessary). $L_2^{k'}$ spans V, is of length n, and L_1^k is linearly independent and has length $m-k$. This process terminates on $k = m$: L_1^m is empty, $L_2^{m'}$ has length n, and $L_2^{m'}$ still spans V, so we conclude $m \leq n$. ■

A corollary to the above result for bases is that

Corollary 2.2.3.1. *Any two bases B_1 and B_2 of a finite-dimensional vector space V have the same length: B_1 has length of at most that of B_2 [35, p.35].*

Proof. This is seen when we consider B_1 as the linearly independent list and B_2 as the generating list in the above discussion; switching the roles of B_1 and B_2 shows that the length of B_1 is at least that of B_2. ■

Thus, we can define the **dimension of a vector space** as the length of any basis of the vector space.

An intuitive property of direct sums is that

Theorem 2.2.4. *Given a subspace U which has a direct sum decomposition (Equation (2.4)),*

$$\dim U = \dim U_1 + \cdots + \dim U_m \tag{2.7}$$

[35, p.49, Ex.16]

Proof. This is easily proven with the "principle of inclusion-exclusion" for the dimension of the sum of two subspaces U_1 and U_2:

$$\dim (U_1 + U_2) = \dim U_1 + \dim U_2 - \dim (U_1 \cap U_2) \tag{2.8}$$

[35, p.47, Thm.2.43], together with the definition of a direct sum. ■

One might ask about vector spaces that are not finite dimensional, which are vector spaces that do not admit a finite-length basis. It can be proven with Zorn's Lemma (the maximal principle) that every vector space has a basis; see [39, Ch. 1.7, pp.58-61] for a proof of this. Since vector spaces that do not have finite-length bases do have bases, we call these spaces **infinite dimensional**. For instance, the space of polynomial functions $\mathcal{P}(\mathbb{C})$, which are functions $f(x) = \sum_{k=0}^{n} a_k x^k$, for $a_k \in \mathbb{C}$ and for any $n \in \mathbb{N}$. n is the index of the polynomial (and a_n is taken to be nonzero). A finite-length basis does not exist for this set, since if one writes a list L of linearly independent polynomials, these polynomials will have a highest index N. Then the polynomial $f(x) = x^{N+1}$ cannot be spanned by the list L, so L is not a basis. However, we can write a basis $B = [x^k : k \in \mathbb{N}]$. B has length infinity[2], so $\mathcal{P}(\mathbb{C})$ is clearly an infinite-dimensional vector space.

Unless otherwise stated, we assume in this thesis that a given vector space V is finite-dimensional.

Linear Operators

Recall the definition of a **linear map** $T : V \to W$, for vector spaces V and W over a field $\mathbb{F}$: T maps an element $v \in V$ to an element $w \in W$, with $w = T(v)$. A linear map will satisfy linearity: given $v_1, v_2 \in V$, and scalars $a, b \in \mathbb{F}$, we have

$$T(av_1 + bv_2) = aT(v_1) + bT(v_2). \tag{2.9}$$

[2]More formally, B has the same cardinality as the natural numbers [40, Ch.10]

The set of linear maps of V into W can be denoted $\mathcal{L}(V, W)$ [35, p.52] [36, Ch.1].

A **linear operator** is simply a linear map $T : V \to V$, or a linear map of the vector space V into the same vector space V. The set of linear operators on V can be denoted by $\mathcal{L}(V)$.

In discussing the spaces of generalized eigenvectors, we will use the notion of null spaces and ranges of linear maps. The **null space**, or *kernel*, of a linear map $T : V \to W$ is the set of all vectors $v \in V$ such that $T(v) = 0$ [35, p.60]. This space is written as null(T). The **range** of T is the set of all vectors $w \in W$ such that $T(v) = w$, for some $v \in V$ [35, p.62]. This space is written as range(T). Both the null space and the rank are subspaces of V and W, respectively.

The null space and range of a linear map is closely related to injectivity and surjectivity. Recall that a function $f : X \to Y$ is injective if, for all $x_1, x_2 \in X$, $f(x_1) = f(x_2)$ implies that $x_1 = x_2$ [35, p.60]. Recall also that f is surjective if, for all $y \in Y$, there exists $x \in X$ such that $f(x) = y$ [35, p.62]. One can show that a linear map $T : V \to W$ is injective if and only if null(T) = $\{0\}$ [35, p.61]. One may also note that the definition of surjectivity is equivalent to range(T) = W. Finally, a function is invertible if and only if it is both injective and surjective.

A fundamental result about the null space and range of a linear operator is the *nullity-plus-rank theorem* for operators $T : V \to W$ on finite dimensional vector spaces V and W. It states

Theorem 2.2.5 (Nullity-Plus-Rank Theorem)**.** *Let V and W be finite-dimensional vector spaces. Let $T : V \to W$ be a linear map. Then [35, Thm.3.22, p.63]*

$$\dim V = \dim \text{null}(V) + \dim \text{range}(V) \tag{2.10}$$

Proof. Let $B_{\text{null}} = [v_1, \ldots, v_m]$ be a basis for null(V). By Theorem 2.2.2, we can extend B_{null} to a basis B of V: $B = [v_1, \ldots, v_m, w_1, \ldots, w_{n-m}]$. Thus, since $\dim \text{null}(V) = m$, and $\dim V = n$, we need to prove that $\dim \text{range}(V) = n - m$. Let $w \in \text{range}(V)$. Then $T(v) = w$, for some $v \in V$. Write $v = \sum_{k=1}^{m} a_k v_k + \sum_{k=1}^{n-m} b_k w_k$. Apply T to both sides:

$$w = T(v) = T\left(\sum_{k=1}^{m} a_k v_k + \sum_{k=1}^{n-m} b_k w_k\right) = \sum_{k=1}^{n-m} b_k T(w_k) \tag{2.11}$$

so $T(w_1), \ldots, T(w_{n-m})$ spans range(V). These are also linearly independent, since $w_1, \ldots, w_{n-m}$ is linearly independent (as $w_1, \ldots, w_{n-m}$ are part of a basis for V). Thus, $T(w_1), \ldots, T(w_{n-m})$ is a basis for range(V). ■

This powerful result has many corollaries in finite-dimensional linear algebra. For instance,

Corollary 2.2.5.1. *A map $T : V \to W$ on finite-dimensional V and W is injective if and only if it is surjective, and also if and only if it is invertible [35, Thm.3.69, p.87].*

Proof. If T is injective, $\dim \text{null}(T) = 0$. By the nullity-plus-rank theorem, $\dim V = \dim \text{range}(T)$, so T is surjective. The reverse is proven in the same way. Then, by the above, T is bijective if it is injective or surjective. ■

2.2.2 Eigenvalues and Eigenvectors

In this section, we discuss the eigenvalues and eigenvectors of a linear operator on a vector space.

First, we define an eigenvalue and eigenvector of a linear operator $T \in \mathcal{L}(V)$, on a vector space V. A scalar $\lambda \in V$ is an **eigenvalue** of T if, for some $v \in V$, $v \neq 0$, $Tv = \lambda v$. The vector v is an **eigenvector** [35, p.134].[3] Equivalent to the definition of an eigenvector, we say that λ is an eigenvalue of T if the operator $T - \lambda I$ is not injective (i.e. the nonzero eigenvector $v \in V$ is in $\text{null}(T - \lambda I)$). For T on a finite-dimensional vector space V, this is equivalent to $T - \lambda I$ not being surjective, and also to $T - \lambda I$ not being invertible (Theorem 2.2.5.1) [35, p.134].

The **eigenspace** of eigenvectors corresponding to an eigenvalue λ of the linear operator T over the vector space V is denoted $E(\lambda)$. This is the set of all vectors such that $(T - \lambda I)v = 0$. It is easy to see that $E(\lambda) = \text{null}(T - \lambda I)$. We define the **geometric multiplicity** of λ_k as $\dim E(\lambda_k)$ [35, p.255].

Theorem 2.2.6. *Any linear operator T on a finite-dimensional complex vector space V has an eigenvalue $\lambda \in \mathbb{C}$.*

Proof. To prove this assertion, take any nonzero vector $v \in V$. Let $n = \dim V$. Then we can construct a list of vectors $v, Tv, T^2v, \ldots, T^nv$. There are $n + 1$ vectors, so this list of vectors must be linearly dependent. Thus, there exist scalars $a_k \in \mathbb{C}$, $k = 0, \ldots, n$, where not all a_k are zero, such that

$$0 = a_0 v + a_1 Tv + \cdots + a_n T^n v \tag{2.12}$$

Consider the polynomial $p(z) = a_0 + a_1 z + \cdots + a_n z^n$. This polynomial can be naturally used to define a linear operator $p(T)$:

$$p(T) = a_0 I + a_1 T + \cdots + a_n T^n \tag{2.13}$$

Thus, $0 = p(T)v$. Note that $p(z)$ is a polynomial over a complex field, so by the fundamental theorem of algebra, $p(z) = (z - \lambda_n) \ldots (z - \lambda_1)$, where the scalars $\lambda_k \in \mathbb{C}$ need not be distinct. Then

$$0 = p(T)v = (T - \lambda_n I)(T - \lambda_{n-1} I) \ldots (T - \lambda_1 I)v \tag{2.14}$$

[3] This might be called an "ordinary" eigenvector, to distinguish from a generalized eigenvector (of order greater than one).

Then one of two statements is true: $(T - \lambda_1 I)v = 0$, or not. If yes, then v is an eigenvector corresponding to eigenvalue λ_1. If not, proceed inductively. It must hold that for some m from 1 to n, $0 = (T - \lambda_m)\left(\prod_{k=m-1}^{1}(T - \lambda_k I)v\right)$, or else $0 \neq p(T)v$, which contradicts Equation (2.12). Then λ_m is an eigenvalue with eigenvector $w = \left(\prod_{k=m-1}^{1}(T - \lambda_k I)v\right)$, thus proving the result. ■

We can remark that Theorem 2.2.6 does not hold for linear operators over real fields. For instance, $T(x, y) = (-y, +x)$, which has a matrix representation $M = \begin{pmatrix} 0 & -1 \\ 1 & 0 \end{pmatrix}$ has no real eigenvalues. If it is taken as an operator on $\mathbb{C}^2$, then it has eigenvalues $\pm i$. Additionally, Theorem 2.2.6 does not hold for infinite-dimensional spaces. For instance, in the full infinite-dimensional Fock basis of a harmonic oscilllator, the raising operator $a^\dagger |n\rangle = \sqrt{n+1}\,|n+1\rangle$ has no eigenvalue; the only vector for which $a^\dagger v = \lambda v$ for any $\lambda \in \mathbb{C}$ is the zero vector $v = 0$.

A well-known result is that eigenvectors that correspond to distinct eigenvalues are linearly independent [35, p.136]. Thus, if a linear operator T on an n-dimensional space V has n distinct eigenvalues, it has n linearly independent eigenvectors, so its eigenvectors are a basis for V. However, if T has less than n distinct eigenvalues, then its eigenvectors need not be a basis for V. For instance, the linear operator $M = \begin{pmatrix} \lambda & 1 \\ 0 & \lambda \end{pmatrix}$ has λ as its only eigenvalue, and the only eigenvectors corresponding to λ are scalar multiples of $(1, 0)^T$.

If T does have a basis that consists entirely of eigenvectors of T, then we say that T is **diagonalizable**. Equivalently, if T is diagonalizable, we can take a list of the eigenvalues of T, $\lambda_1, \ldots, \lambda_m$, and decompose V into a direct sum

$$V = E(\lambda_1) \bigoplus E(\lambda_2) \bigoplus \cdots \bigoplus E(\lambda_m) \tag{2.15}$$

If the dimension of V is n, then $m \leq n$, by Theorem 2.2.4. The inequality is allowed for diagonalizable T, so some of the eigenspaces may have a dimension greater than 1. If we take bases B_k of $E(\lambda_k)$, then $B_1 \cup \cdots \cup B_m$ is a basis of V. In this basis,

$$T = \begin{pmatrix} \lambda_1 & 0 & \ldots & & 0 \\ 0 & \ddots & 0 & \ldots & \vdots \\ \vdots & 0 & \lambda_k & \ddots & \\ & & \ddots & \ddots & 0 \\ 0 & \ldots & & 0 & \lambda_m \end{pmatrix} \tag{2.16}$$

In general, to find a list of vectors that correspond to the eigenvalues of a linear operator

$T \in \mathcal{L}(V)$ and write a basis of V entirely in terms of these vectors, we extend the notion of eigenvectors to generalized eigenvectors (Section 2.2.3).

2.2.3 Generalized Eigenspaces and Jordan Normal Form

Generalized Eigenspace Definitions

Here, we define generalized eigenvectors, and use the Jordan Normal Form to "almost diagonalize" matrices that cannot be diagonalized. A **generalized eigenvector** corresponding to an eigenvalue λ of a linear operator T on a vector space V is a nonzero vector $v \in V$ for which there exists some integer $m \geq 1$ such that

$$(T - \lambda I)^m v = 0 \tag{2.17}$$

We will refer to the smallest integer m for which (2.17) holds the *order of the generalized eigenvector*.

We can write the space of generalized eigenvectors corresponding to λ as

$$G(\lambda) = \{v \in V \mid \exists j \in \mathbb{Z}^+ : (T - \lambda I)^j v = 0\} \tag{2.18}$$

It can be proven that [35, p.246, Thm.8.11]

$$G(\lambda) = \text{null}(T - \lambda I)^{\dim V} \tag{2.19}$$

We now define the **(algebraic) multiplicity** of λ_k as $d_k = \dim G(\lambda_k)$ [35, p.255].

Generalized Eigenspace Example

As a toy example of finding generalized eigenvectors, consider the matrix

$$M = \begin{pmatrix} \lambda & 0 & 0 & 0 \\ 0 & \lambda & 1 & 0 \\ 0 & 0 & \lambda & 1 \\ 0 & 0 & 0 & \lambda \end{pmatrix} \tag{2.20}$$

over the vector space $\mathbb{C}^4$. If we solve the roots μ of the characteristic polynomial $\det(\mu I - M) = 0$ (Equation (2.48)), the only root is the eigenvalue $\mu = \lambda$. The eigenvectors are those vectors

$v = (a, b, c, d)^T$ which satisfy

$$(M - \lambda I) \begin{pmatrix} a \\ b \\ c \\ d \end{pmatrix} = \begin{pmatrix} \lambda - \lambda & 0 & 0 & 0 \\ 0 & \lambda - \lambda & 1 & 0 \\ 0 & 0 & \lambda - \lambda & 1 \\ 0 & 0 & 0 & \lambda - \lambda \end{pmatrix} \begin{pmatrix} a \\ b \\ c \\ d \end{pmatrix} = \begin{pmatrix} 0 & 0 & 0 & 0 \\ 0 & 0 & 1 & 0 \\ 0 & 0 & 0 & 1 \\ 0 & 0 & 0 & 0 \end{pmatrix} \begin{pmatrix} a \\ b \\ c \\ d \end{pmatrix} = \begin{pmatrix} 0 \\ 0 \\ 0 \\ 0 \end{pmatrix} \tag{2.21}$$

The eigenvectors are $v_1 = (1, 0, 0, 0)^T$ and $v_2 = (0, 1, 0, 0)^T$ (or linear combinations of these). To find generalized eigenvectors, we can find solutions of the vector equations $(M - \lambda I)^k v = 0$, for any integer k. One way to do this is to solve the vector equations $(M - \lambda I)v = v_1$ and $(M - \lambda I)v = v_2$. The first equation, written out for $v = (a, b, c, d)^T$, is

$$v_1 = (M - \lambda I) \begin{pmatrix} a \\ b \\ c \\ d \end{pmatrix} = \begin{pmatrix} \lambda - \lambda & 0 & 0 & 0 \\ 0 & \lambda - \lambda & 1 & 0 \\ 0 & 0 & \lambda - \lambda & 1 \\ 0 & 0 & 0 & \lambda - \lambda \end{pmatrix} \begin{pmatrix} a \\ b \\ c \\ d \end{pmatrix} = \begin{pmatrix} 0 & 0 & 0 & 0 \\ 0 & 0 & 1 & 0 \\ 0 & 0 & 0 & 1 \\ 0 & 0 & 0 & 0 \end{pmatrix} \begin{pmatrix} a \\ b \\ c \\ d \end{pmatrix} = \begin{pmatrix} 1 \\ 0 \\ 0 \\ 0 \end{pmatrix} \tag{2.22}$$

There are no a, b, c, d that satisfy the above equation. We now try solving $(M - \lambda I)v = v_2$:

$$v_2 = (M - \lambda I) \begin{pmatrix} a \\ b \\ c \\ d \end{pmatrix} = \begin{pmatrix} \lambda - \lambda & 0 & 0 & 0 \\ 0 & \lambda - \lambda & 1 & 0 \\ 0 & 0 & \lambda - \lambda & 1 \\ 0 & 0 & 0 & \lambda - \lambda \end{pmatrix} \begin{pmatrix} a \\ b \\ c \\ d \end{pmatrix} = \begin{pmatrix} 0 & 0 & 0 & 0 \\ 0 & 0 & 1 & 0 \\ 0 & 0 & 0 & 1 \\ 0 & 0 & 0 & 0 \end{pmatrix} \begin{pmatrix} a \\ b \\ c \\ d \end{pmatrix} = \begin{pmatrix} 0 \\ 1 \\ 0 \\ 0 \end{pmatrix} \tag{2.23}$$

This equation does have a solution: $v_3 = (0, 0, 1, 0)^T$. v_3 is a generalized eigenvector of order 2, since $(M - \lambda I)^2 v_3 = 0$. Finally, we can solve $(M - \lambda I)v = v_3$:

$$v_3 = (M - \lambda I) \begin{pmatrix} a \\ b \\ c \\ d \end{pmatrix} = \begin{pmatrix} \lambda - \lambda & 0 & 0 & 0 \\ 0 & \lambda - \lambda & 1 & 0 \\ 0 & 0 & \lambda - \lambda & 1 \\ 0 & 0 & 0 & \lambda - \lambda \end{pmatrix} \begin{pmatrix} a \\ b \\ c \\ d \end{pmatrix} = \begin{pmatrix} 0 & 0 & 0 & 0 \\ 0 & 0 & 1 & 0 \\ 0 & 0 & 0 & 1 \\ 0 & 0 & 0 & 0 \end{pmatrix} \begin{pmatrix} a \\ b \\ c \\ d \end{pmatrix} = \begin{pmatrix} 0 \\ 0 \\ 1 \\ 0 \end{pmatrix} \tag{2.24}$$

This equation has the solution $v_4 = (0, 0, 0, 1)^T$. It is a generalized eigenvector of order 3, since $(M - \lambda I)^3 v_4 = 0$. Hence, we have four linearly independent generalized eigenvectors – v_1, v_2, v_3, v_4 – that correspond to the eigenvalue λ. These span the whole vector space $\mathbb{C}^4$. One can also check that this chain ends with v_4 – there is no solution v to the equation $v_4 = (M - \lambda I)v$.

Generating Generalized Eigenspaces with Jordan Chains

In general, to find generalized eigenvectors which span an entire generalized eigenspace $G(\lambda)$ of a linear operator $T \in \mathcal{L}(V)$, one can find an eigenvector v_1 of T (at least one exists, by definition of an eigenvalue). Then, for the generalized eigenvector of order m, one recursively solves

$$v_{m-1} = (T - \lambda I)v_m \tag{2.25}$$

This is consistent with the definition of a generalized eigenvector of order m (Equation (2.17)).

In total, if $G(\lambda)$ is a generalized eigenspace of dimension d, then a spanning set of generalized eigenvectors is realized as a cycle of generalized eigenvectors, or a Jordan chain [36, p.266-7, Ch.9.4] [41]

$$\begin{aligned} 0 = (T - \lambda I)v_1 &= \cdots = (T - \lambda I)^d v_d \\ v_1 = (T - \lambda I)v_2 &= \cdots = (T - \lambda I)^{d-1} v_d \\ v_2 = (T - \lambda I)v_3 &= \cdots = (T - \lambda I)^{d-2} v_d \\ &\vdots \\ v_{d-1} = (T - \lambda I)v_d & \end{aligned} \tag{2.26}$$

Decomposition into Generalized Eigenspaces

In a result analogous to one for ordinary eigenvectors,

Theorem 2.2.7. *Let V be an n-dimensional vector space, and let $T \in \mathcal{L}(V)$ be a linear operator. Generalized eigenvectors corresponding to distinct eigenvalues λ_k are linearly independent [35, p.247, Thm.8.13]*

Proof. To prove this, take any generalized eigenvectors $v_1, \ldots, v_m$, corresponding to distinct $\lambda_1, \ldots, \lambda_m$. Write

$$0 = a_1 v_1 + \cdots + a_m v_m \tag{2.27}$$

To prove that $a_k = 0$, for a given k, note that, for some integer j, $(T - \lambda_k I)^j v_k = 0$. Let j_k be the largest integer for which $(T - \lambda_k I)^{j_k} v_k \neq 0$. Define $w = (T - \lambda_k I)^{j_k} v_k$. Then $(T - \lambda_k I)w = 0$. Furthermore, for any $\lambda \in \mathbb{C}$, $(T - \lambda I)^n w = (\lambda_k - \lambda)^n$. Now apply $(T - \lambda_1 I)^n \ldots (T - \lambda_k I)^{j_k} \ldots (T - \lambda_m I)^n$ to the linear combination. Now, for v_i, with $i \neq k$, $(T - \lambda_i)^n v_i = 0$, since

$G(\lambda_i) = \text{null}(T - \lambda_i I)^n$. Because $(T - \lambda_i I)$ and $(T - \lambda_j I)$ commute, we get

$$\begin{aligned} 0 &= (T-\lambda_1 I)^n \dots (T-\lambda_k I)^{j_k} \dots (T-\lambda_m I)^n (a_1 v_1 + \dots + a_m v_m) \\ &= \Big((T-\lambda_1 I)^n \dots (T-\lambda_m I)^n (T-\lambda_k I)^{j_k} a_k v_k\Big) + \\ &\quad \Big((T-\lambda_k I)^{j_k} (T-\lambda_1 I)^n \dots (T-\lambda_m I)^n \sum_{i \neq k} a_i v_i\Big) \\ &= a_k (T-\lambda_1 I)^n \dots (T-\lambda_m I)^n w \\ &= a_k (\lambda_k - \lambda_1 I)^n \dots (\lambda_k - \lambda_m)^n w \end{aligned} \tag{2.28}$$

Since the eigenvalues are distinct, then $a_k = 0$. ■

Unlike with ordinary eigenvectors (which are merely generalized eigenvectors of order $m = 1$), the set of generalized eigenvectors of a linear operator T on a finite-dimensional complex vector space V does span V [35, p.252]. That is,

Theorem 2.2.8. *Let T be a linear operator on a finite-dimensional vector space V. Let $\lambda_1, \dots, \lambda_m$ be the distinct eigenvalues of T. We can decompose V as a direct sum*

$$V = G(\lambda_1) \bigoplus \cdots \bigoplus G(\lambda_m) \tag{2.29}$$

Proof. This can be proven by induction on $\dim V$. For $n = 1$, then since T must have an eigenvalue λ, by Theorem 2.2.6, the result holds vacuously.

Now assume that the result holds for any vector space V with $\dim V < n$. For a vector space V with $\dim V = n$, and a linear operator T on V, let λ be an eigenvalue of T. We show that

$$V = \text{null}(T - \lambda I)^n \oplus \text{range}(T - \lambda I)^n \tag{2.30}$$

First, if $v \in \text{null}(T - \lambda I)^n \cap \text{range}(T - \lambda I)^n$, then since $v \in \text{range}(T - \lambda I)^n$, $(T - \lambda I)^n w = v$. Apply $(T - \lambda I)^n$ to w, to get $0 = (T - \lambda I)^{2n} w = 0$. Then w is a generalized eigenvector of T, with eigenvalue λ, so $0 = (T - \lambda I)^n w = v$, since $G(\lambda) = \text{null}(T - \lambda I)^n$. Thus,

$$\text{null}(T - \lambda I)^n \cap \text{range}(T - \lambda I)^n = \{0\}. \tag{2.31}$$

Second, the sum in Equation (2.30) holds by the nullity-plus-rank theorem (Theorem 2.2.5), thus proving Equation (2.30).

Now, since λ is an eigenvalue of T, there is at least one eigenvector v of T corresponding to λ. Thus, $(T - \lambda I)^n v = 0$, so $\dim \text{null}(T - \lambda I)^n > 0$. Then $\dim \text{range}(T - \lambda I)^n < n$, by the nullity-plus-rank theorem, so by the induction hypothesis, we can decompose both the null space

and the range of $(T-\lambda I)^n$ into direct sums of generalized eigenspaces of T, thus proving the result. ■

From this decomposition, we note that a basis for V in terms of the generalized eigenvectors can always be chosen; one merely chooses bases for each generalized eigenspace, then concatenates them together to get a basis for V.

On each $G(\lambda_k)$, $(T-\lambda_k I)$ is a *nilpotent operator*, which is an operator N such that $N^j = 0$, for some integer power j; from the definition of a generalized eigenvector, one sees immediately that $(T-\lambda_k I)$ is nilpotent on $G(\lambda_k)$. Then, since $(T-\lambda_k I)$ is nilpotent on $G(\lambda_k)$, we have $(T-\lambda_k I)^{d_k}\big|_{G(\lambda_k)} = 0$ [35, p.248, Thm.8.18, Ch.8A], where $d_k = \dim G(\lambda_k)$.

One also sees that each $G(\lambda_k)$ is invariant under T, since for any element $v \in G(\lambda_k)$, $(T-\lambda_k I)Tv = T(T-\lambda_k I)v = 0$, so $Tv \in G(\lambda_k)$. Thus, the decomposition of any $v \in V$ as $v = v_1 + \cdots + v_m$, for $v_k \in G(\lambda_k)$, is invariant under T.

We now write the **Jordan Normal Form** of the linear operator T on a complex finite-dimensional vector space V. First, we note that for T, we can always write a decomposition of V into a direct sum of generalized eigenspaces of T (Equation 2.29). Furthermore, these generalized eigenspaces of T are invariant under T, so T will not map the elements of one generalized eigenspace $G(\lambda_k)$ into another $G(\lambda_l)$, unless $l = k$. Thus, a matrix representation of T has the form

$$T = \begin{pmatrix} \left(A_1\right)\Big|_{G(\lambda_1)} & 0 & \dots & 0 \\ 0 & \left(A_2\right)\Big|_{G(\lambda_2)} & \dots & 0 \\ \vdots & & \ddots & \\ 0 & 0 & \dots & \left(A_m\right)\Big|_{G(\lambda_m)} \end{pmatrix} \tag{2.32}$$

where each A_k is a square matrix on the subspace $G(\lambda_k)$, and $\lambda_1, \dots, \lambda_m$ are the eigenvalues of T.

On each $G(\lambda_k)$, we can write T as

$$T|_{G(\lambda_k)} = \lambda_k I|_{G(\lambda_k)} + (T-\lambda_k I)|_{G(\lambda_k)} \tag{2.33}$$

The left term is simply the identity matrix times λ_k, so it will always have the same identity matrix form regardless of the choice of basis. Thus, we are left to choose a basis that makes the matrix form of $(T-\lambda_k I)|_{G(\lambda_k)}$ as simple as possible.

Recognizing that $(T-\lambda_k I)|_{G(\lambda_k)}$ is a nilpotent operator on $G(\lambda_k)$, we show that a nilpotent operator N on an n-dimensional vector space V has a matrix representation where it has 0 for all of its elements, except on the superdiagonal. On the superdiagonal, the entries will be 0 or

1. To write this explicitly in matrix form, the nilpotent operator N has the matrix form

$$N = \begin{pmatrix} \begin{pmatrix} N_1 \end{pmatrix} & 0 & \dots & 0 \\ 0 & \begin{pmatrix} N_2 \end{pmatrix} & \dots & 0 \\ \vdots & & \ddots & \\ 0 & 0 & \dots & \begin{pmatrix} N_l \end{pmatrix} \end{pmatrix} \tag{2.34}$$

where each N_j is a square matrix that has ones on the superdiagonal, and zero everywhere else, i.e.

$$N_j = \begin{pmatrix} 0 & 1 & 0 & \dots & 0 \\ 0 & 0 & 1 & \dots & 0 \\ \vdots & & \ddots & & \\ 0 & 0 & \dots & 0 & 1 \\ 0 & 0 & \dots & 0 & 0 \end{pmatrix} \tag{2.35}$$

For each of these N_j, we can see that the column vector $u_j = (0, 0, \dots, 0, 1)^T$, of length m_j, is sent by N_j to $N_j u_j = (0, 0, \dots, 1, 0)^T$. This cycle continues, up to $N_j^{m_j} = (1, 0, \dots, 0, 0)^T$, and terminates at $N_j^{m_j+1} u_j = 0$. Hence, N has this matrix form if there are vectors u_j, for $j = 1, \dots, l$, and integers m_j such that the list

$$N^{m_1} u_1, \dots \; N u_1, u_1, N^{m_2} u_2, \dots, N u_2, u_2, \dots, N^{m_l} u_l, \dots, N u_l, u_l \tag{2.36}$$

is a basis for V, and if, for all $j = 1, \dots, l$, $N^{m_l+1} u_l = 0$. This basis does exist for any nilpotent operator N on a finite-dimensional vector space, as proven in [35, Thm.8.55, p.271] and [36, Chapter 9.4, p.266-72]. In this basis, N has the form given in Equations 2.34 and 2.35.

Returning to Equation 2.33, $(T - \lambda_k I)|_{G(\lambda_k)}$ is nilpotent on $G(\lambda_k)$, so $(T - \lambda_k I)|_{G(\lambda_k)}$ can be written in the form of Equations 2.34 and 2.35, for some basis of $G(\lambda_k)$. This basis sets

$$T|_{G(\lambda_k)} = \begin{pmatrix} \lambda_k & t_{12} & 0 & \dots & 0 & 0 \\ 0 & \lambda_k & t_{23} & \dots & 0 & 0 \\ \vdots & & \ddots & & & \\ 0 & 0 & 0 & \dots & \lambda_k & t_{(n-1),n} \\ 0 & 0 & 0 & \dots & 0 & \lambda_k \end{pmatrix} \tag{2.37}$$

where t_{ij} is either 0 or 1; the superdiagonal consists of 0 and 1. We can then choose m bases, for each of the $G(\lambda_k)$, where T has the form of the Jordan block, and append them together to

get T into the Jordan Normal Form (c.f. Equation 2.32)

$$T = \begin{pmatrix} \begin{pmatrix} J_1 \end{pmatrix} & 0 & \dots & 0 \\ 0 & \begin{pmatrix} J_2 \end{pmatrix} & \dots & 0 \\ \vdots & & \ddots & \\ 0 & 0 & \dots & \begin{pmatrix} J_m \end{pmatrix} \end{pmatrix} \tag{2.38}$$

where each J_p has the **Jordan block** form

$$J_p = \begin{pmatrix} \lambda_p & 1 & 0 & \dots & 0 & 0 \\ 0 & \lambda_p & 1 & \dots & 0 & 0 \\ \vdots & & \ddots & & & \\ 0 & 0 & 0 & \dots & \lambda_p & 1 \\ 0 & 0 & 0 & \dots & 0 & \lambda_p \end{pmatrix} \tag{2.39}$$

2.2.4 Characteristic Polynomial

Here, we define the characteristic polynomial of a linear operator T. If $\lambda_1, \dots, \lambda_m$ are the distinct eigenvalues of T, with multiplicities $d_1, \dots, d_m$, then the **characteristic polynomial** is

$$p(z) = (z - \lambda_1)^{d_1} \dots (z - \lambda_m)^{d_m} \tag{2.40}$$

The characteristic polynomial has degree $n = \dim V$, since the multiplicities of the eigenvalues must sum to $\dim V$, which holds because V decomposes into a direct sum of $G(\lambda_k)$. Additionally, the zeros of p are the eigenvalues of T, by construction. The characteristic polynomial $p(z)$ can be expanded as[4]

$$p(z) = z^n - a_{n-1}z^{n-1} + \dots + (-1)^n a_0, \quad a_k \in \mathbb{C} \tag{2.41}$$

$p(z)$ is a monic polynomial, since the coefficient of the leading term z^n is 1.

A fundamental result about the characteristic polynomial is the Cayley-Hamilton theorem, which states

Theorem 2.2.9. *Let $p(z)$ be the characteristic polynomial of a linear operator $T : V \to V$ on a finite-dimensional vector space V. Then $p(T) = 0$ [35, p.261, Thm.8.37] [36, p.253, Ch.9.1].*

Proof. Let $\lambda_1, \dots, \lambda_m$ be the distinct eigenvalues of T. Let $v \in V$ arbitrary. V can be decomposed as a direct sum of the generalized eigenspaces $G(\lambda_k)$, so write $v = v_1 + \dots + v_m$, for

[4] We write the coefficients of z^{n-k} with factors of $(-1)^{n-k}$ to make the coefficients match the elementary symmetric polynomials of the eigenvalues λ_j [42].

$v_k \in G(\lambda_k)$. Since $(T-\lambda_k I)$ is nilpotent on $G(\lambda_k)$, and $\dim G(\lambda_k) = d_k$, $(T-\lambda_k I)^{d_k}\big|_{G(\lambda_k)} = 0$. Apply $p(T)$ to v (and use the pairwise commutativity of the $(T-\lambda_j I)$):

$$\begin{aligned} p(T)v &= \left(\prod_{k=1}^{m}(T-\lambda_k I)^{d_k}\right)\left(\sum_{l=1}^{m} v_l\right) \\ &= \sum_{l=1}^{m}\left(\prod_{k\neq l}(T-\lambda_k I)^{d_k}\right)(T-\lambda_l I)^{d_l} v_l \\ &= 0 \end{aligned} \tag{2.42}$$

■

The coefficients of the characteristic polynomial (Equation (2.41)) are the **elementary symmetric polynomials** in the eigenvalues $\mu_1, \ldots, \mu_n$, where the μ_k are allowed to be repeated in multiplicity. They are [42]

$$a_{n-1} = \sum_{k=1}^{n} \mu_k = \mathrm{Tr}(T) \tag{2.43a}$$

$$a_{n-2} = \sum_{i<j} \mu_i \mu_j \tag{2.43b}$$

$$\vdots$$

$$a_0 = \prod_{k=1}^{n} \mu_k = \det(T) \tag{2.43c}$$

A distinction that we should make is that, though the characteristic polynomial and the eigenvalues of a linear operator T are bijectively mapped, the characteristic polynomial and the eigenvalues do not uniquely determine the linear operator T. For instance, if we consider the operator $M_1 = \begin{pmatrix} \lambda & 0 \\ 0 & \lambda \end{pmatrix}$, it has λ as its only eigenvalue, and its characteristic polynomial is $p_1(z) = (z-\lambda)^2$. Another operator that has the same eigenvalue(s) and characteristic polynomial is $M_2 = \begin{pmatrix} \lambda & 1 \\ 0 & \lambda \end{pmatrix}$. However, M_1 and M_2 have different minimal polynomials. For a given operator T, the *minimal polynomial* $q(z)$ is the (monic) polynomial of smallest degree such that $q(T) = 0$. The minimal polynomial for M_1 is $q_1(z) = (z-\lambda)$, and the minimal polynomial for M_2 is $q_2(z) = (z-\lambda)^2$. The roots of the minimal polynomial are precisely the eigenvalues of the linear operator T [35, p.265, Thm.8.49]. It can be proven that the minimal polynomial divides the characteristic polynomial [35, p.264, Thm.8.64].

2.2.5 Trace, Determinant, and Discriminant

We can quickly define the **trace** of a linear operator T on a vector space V as the sum of all of the eigenvalues of T, with each eigenvalue repeated according to its algebraic multiplicity [35, p.299]:

$$\mathrm{Tr}(T) = \sum_{k=1}^{m} d_k \lambda_k \tag{2.44}$$

We can also define the **determinant** as the product of all of the eigenvalues, with each eigenvalue repeated according to (algebraic) multiplicity

$$\det(T) = \prod_{k=1}^{m} \lambda_k^{d_k} \tag{2.45}$$

We can relate the characteristic polynomial $p(z)$ of T to the trace and determinant of T via

$$\begin{aligned} p(z) &= (z-\lambda_1)^{d_1} \dots (z-\lambda_m)^{d_m} \\ &= \prod_{k=1}^{m} \left(z^{d_k} - d_k \lambda_k z^{d_k - 1} + \dots + (-1)^{d_k} \lambda_k^{d_k} \right) \\ &= z^n - (d_1\lambda_1 + \dots + d_m \lambda_m) z^{n-1} + \dots + (-1)^n \prod_{k=1}^{n} \lambda_k^{d_k} \\ &= z^n - a_{n-1} z^{n-1} + \dots + (-1)^{n-1} a_1 z + (-1)^n a_0 \end{aligned} \tag{2.46}$$

so [35, p.308]

$$\mathrm{Tr}(T) = a_{n-1} \tag{2.47a}$$

$$\det(T) = a_0 \tag{2.47b}$$

$$p(z) = z^n - \mathrm{Tr}(T) z^{n-1} + \dots + (-1)^n \det(T) \tag{2.47c}$$

We can also show that $p(z)$ is equal to $\det(zI - T)$ [35, p.309]. This is easy to show, since if λ is an eigenvalue of T, then $z - \lambda$ is an eigenvalue of $zI - T$. The determinant is the product of eigenvalues, so

$$\det(zI - T) = (z - \lambda_1) \dots (z - \lambda_m) = p(z) \tag{2.48}$$

This is the traditional definition of the characteristic polynomial [36, p.100, Ch.4]. Per this definition, the algebraic multiplicity of an eigenvalue λ_k is the multiplicity of the root of the polynomial $\det(zI - T)$. This is equivalent to the definition given in Section 2.2.3.

The **discriminant** is the product

$$D = \prod_{i<j} (\mu_i - \mu_j)^2 \tag{2.49}$$

where $\mu_1, \ldots, \mu_n$ are the n eigenvalues of T, repeated in multiplicity. $D = 0$ if and only if an eigenvalue has an algebraic multiplicity greater than 1 (i.e., $p(z)$ has a repeated root).

It can be shown that the determinant can be realized via the matrix [42]

$$\delta = \begin{pmatrix} 1 & 1 & \ldots & 1 \\ \mu_1 & \mu_2 & \ldots & \mu_n \\ \vdots & & \ddots & \\ \mu_1^{n-1} & \mu_2^{n-1} & \ldots & \mu_n^{n-1} \end{pmatrix} \tag{2.50}$$

It can also be shown that the discriminant $D = \det(\delta\delta^T)$, and that the entries of $\delta\delta^T$ can be expressed in terms of the elementary symmetric polynomials. Some discriminant values for vector spaces of dimension $n = 2$ and $n = 3$ are

$$D = a_1^2 - 4a_0, \qquad n = 2 \tag{2.51a}$$

$$D = -4a_2^3 a_0 + a_2^2 a_1^2 + 18 a_2 a_1 a_0 - 4a_1^3 - 27a_0^2, \qquad n = 3 \tag{2.51b}$$

Equations (2.52) can be simplified by subtracting $\mathrm{Tr}(T)/n$ from the eigenvalues $\mu_1, \ldots, \mu_n$ (or, equivalently, by subtracting $\frac{1}{n}\mathrm{Tr}(T)\, I_{n\times n}$ from the matrix T). Then the second leading coefficient of the characteristic polynomial $a_{n-1} = 0$, and the discriminant for $n = 2$ and $n = 3$ is

$$D = -4a_0, \qquad n = 2 \tag{2.52a}$$

$$D = -4a_1^3 - 27a_0^2, \qquad n = 3 \tag{2.52b}$$

2.3 n-Mode Spectral Flow

2.3.1 Control Space $\mathcal{L}_n$ of Spectra

In this section, we describe the central theoretical aspect of this thesis: the trajectory of the eigenvalue spectrum when the control parameters are varied around a closed loop. In particular, we are interested in examining which classes of control loops give rise to eigenvalue trajectories that are topologically equivalent (more precisely, trajectories that belong to a given isotopy

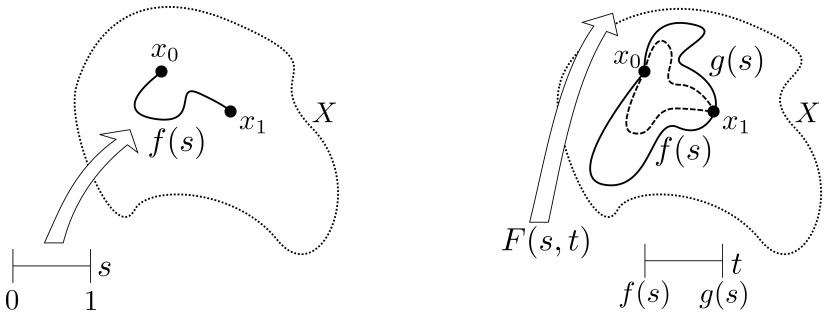

Figure 2.1: a: a path $f : [0,1] \to X$ in the topological space X.
b: a path homotopy $F : [0,1] \times [0,1] \to X$ between the paths $f(s)$ and $g(s)$ in X.

class). We use the term "spectral flow" to refer to these classes.

Given an $n \times n$ matrix $\mathcal{H}$, which represents the dynamical matrix of a system of n oscillators, we can consider the n eigenvalues $\lambda_1, \ldots, \lambda_n$ (where the λ_k may be repeated, according to multiplicity) as an unordered subset $\lambda = \{\lambda_1, \ldots, \lambda_n\}$, where $\lambda_k \in \mathbb{C}$. Per the discussion of characteristic polynomials in Section 2.2.4, the eigenvalues of $\mathcal{H}$ are determined by the ordered set of n coefficients $(a_0, \ldots, a_{n-1})$ of the characteristic polynomial (Equation (2.41)), as they are the roots of the characteristic polynomial (by the definition given in Section 2.2.4 from [35]). The coefficients $(a_0, \ldots, a_{n-1})$ are also determined from the eigenvalues $\{\lambda_1, \ldots, \lambda_n\}$ via the elementary symmetric polynomials (Equation (2.43)). Because we are interested in eigenvalue degeneracies (i.e., pairwise eigenvalue differences), we are only interested in the $n-1$ quantities $\lambda_1 - \lambda_2, \lambda_2 - \lambda_3, \ldots, \lambda_{n-1} - \lambda_n$. Any other eigenvalue difference $\lambda_i - \lambda_j$, $j \neq i$, can be obtained with a linear combination of these $n-1$ quantities. Thus, this problem only contains $n-1$ degrees of freedom. Without loss of generality, we may set the sum of the eigenvalues – the trace (Section 2.2.5) – to zero. Setting the trace to zero sets $a_{n-1} = 0$ in Equation (2.41), thus leaving $n-1$ free complex coefficients in the characteristic polynomial. This choice sets the characteristic polynomial to

$$p(z) = z^n + a_{n-2}z^{n-2} - \cdots + (-1)^{n-1}a_1 z + (-1)^n a_0, \tag{2.53}$$

We may take the $n-1$ complex coefficients of the characteristic polynomial (Equation (2.53)) as the *control space* $\mathcal{L}_n$ [1, p.2]. The isomorphism $\mathcal{L}_n \cong \mathbb{C}^{n-1}$ is obvious. $\mathcal{L}_n$ parametrizes the space of n traceless eigenvalue spectra, so there is also a natural bijective mapping between $\mathcal{L}_n$ and the unordered sets of n eigenvalues (which sum to 0, owing to the assumption of tracelessness) in $\mathbb{C}$.

2.3.2 $\mathcal{L}_n$ Path Homotopy and Fundamental Group

With this parametrization $\mathcal{L}_n$ of spectra, we impose the usual Euclidean metric topology on $\mathcal{L}_n$ [43, p.117, Ch.2, Section 20].[5] In addition, we consider paths $f : [0,1] \to X$, where $X = \mathcal{L}_n$ for now. The path f has an initial point x_0 and a final point x_1. That is,

$$\begin{aligned} f(0) &= x_0 \\ f(1) &= x_1 \end{aligned} \tag{2.54}$$

The path f in $\mathcal{L}_n$ smoothly varies the spectra along the path in the complex plane. A cartoon of the path f is shown in Figure 2.1a. We define an equivalence relation between these paths called **path homotopy**, in which two paths f_1 and f_2 in the space X with the same initial point $x_0 \in X$ and final point $x_1 \in X$ are homotopy equivalent if there is a continuous transformation $F : [0,1] \times [0,1] \to X$, called a *path homotopy*, such that [43, p.319, Ch.9, Section 51] [44, p.25, Ch.1.1]

$$F(s,0) = f_1(s) \quad \text{and} \quad F(s,1) = f_2(s) \tag{2.55a}$$

$$F(0,t) = x_0 \qquad \text{and} \quad F(1,t) = x_1 \tag{2.55b}$$

A cartoon of path homotopy is shown in Figure 2.1b. Path homotopy is an equivalence relation [43, p.320, Lemma 51.1, Ch.9, Section 51] [44, p.25, Ch.1.1]. We denote the set of paths equivalent to a path f as $[f]$, and call $[f]$ a path-homotopy class.

We define a product of paths, or **path concatenation**, of a path f_1 from x_0 to x_1 and another path f_2 from x_1 to x_2 as $(f_1 * f_2)$ [43, p.322, Ch.9, Section 51] [44, p.26, Ch.1.1]:

$$(f * g)(t) = \begin{cases} f(2t) & 0 \le t < 1/2 \\ g(2t-1) & 1/2 \le t \le 1 \end{cases} \tag{2.56}$$

The path concatenation is only defined when the end point of f_1 is the starting point of f_2. Path concatenation also induces a product on path homotopy classes $[f_1]$ and $[f_2]$ [43, p.322, Ch.9, Section 51]:

$$[f_1] * [f_2] = [f_1 * f_2] \tag{2.57}$$

We now define a group operation using path homotopy classes and path concatenation.

[5] A *topological space* is a set X with a subset $T \subseteq X$, called a *topology*, for which $\{\}, X \in T$, for which any union of elements of T is in T, and for which any finite intersection of elements of T is in T [43, p.74, Ch.2, Section 12]. The Euclidean metric $d(x,y) = |x-y|$ sets the topology on $\mathcal{L}_n$ where the open sets are generated by the balls $B(x,\varepsilon) = \{y : d(x,y) < \varepsilon\}$ [43, p.76, Ch.2, Section 13] [43, pp.117-8, Ch.2, Section 20]. We do not use the metric topology in any important way throughout the rest of this thesis, since the topological property of $\mathcal{L}_n$ we use is path homotopy.

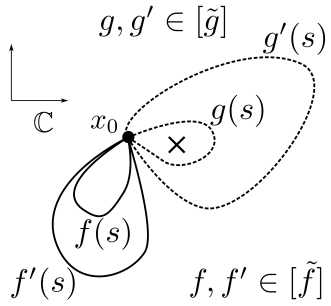

Figure 2.2: Two distinct loop homotopy classes of the complex plane $\mathbb{C}$, minus a single point (marked by the $\times$). The loop homotopies in $[\tilde{f}]$ are marked with solid lines, and the loop homotopies in $[\tilde{g}]$ are marked with dashed lines.

However, the concatenation $*$ is not defined for all path homotopy classes, since they might not have the same start or end points. To get around this and define a group operation, we can pick a common base point x_0 to serve as the start and end point of all paths that we consider. These paths are loops based at x_0. The set of all path homotopy classes of loops based at x_0, with the path concatenation operation $*$, forms the **fundamental group** $\pi_1(X, x_0)$ [43, p.327, Ch.9, Section 52] [44, p.26, Ch.1.1].[6] It is easy to check that $*$ is a group operation: $*$ is associative; there is an identity element $e \in \pi_1(X, x_0)$, defined by $e(t) = x_0$, $\forall t \in [0, 1]$; and every element has an inverse (i.e., the class $[f]$, defined by $f(t)$, has an inverse $[f^{-1}]$, defined by a reverse path $f^{-1}(t) = f(1-t)$).

$X = \mathcal{L}_n$ is topologically trivial, in the sense that for any base point x_0, any two loops f_1 and f_2 are path homotopy equivalent. That is, $\pi_1(\mathcal{L}_n, x_0) = 1$ (i.e., $\pi_1(\mathcal{L}_n, x_0)$ is the trivial group[7]), for all $x_0 \in \mathcal{L}_n$ [44, p.27, Ch.1.1, Example 1.4]. In fact, any loop f based at x_0 can be contracted to a fixed point $e(t) = x_0, \forall t \in [0, 1]$.

2.3.3 Degenerate and Nondegenerate Subspaces of $\mathcal{L}_n$

We partition the control space $\mathcal{L}_n$ into subspaces $\mathcal{G}_n$ and $\mathcal{V}_n$. $\mathcal{G}_n$ is the subspace of $\mathcal{L}_n$ in which the spectra are nondegenerate (i.e., the characteristic polynomial has no repeated roots), and $\mathcal{V}_n$ is the subspace in which the spectra are degenerate. Equivalently, $\mathcal{V}_n$ is the space where $D = 0$ (Equation (2.49)). $\mathcal{V}_n$ is determined from one complex constraint, so it has codimension 1 as a subspace of $\mathcal{L}_n$ (i.e., $\mathcal{V}_n$ is an $(n-2)$-dimensional subspace of the $(n-1)$-dimensional $\mathcal{L}_n$). When we say "codimension 1," we are counting by complex dimensions.

$\mathcal{G}_n$ and $\mathcal{V}_n$ need not have trivial fundamental groups. This is because loop homotopies in a space X, in addition to being continuous, must also keep the loops entirely within X. For

[6] The subscript 1 in $\pi_1(X, x_0)$ refers to the fact that $\pi_1(X, x_0)$ is the first homotopy group of X, with respect to x_0. There are other homotopy groups $\pi_n(X, x_0)$, for $n \in \mathbb{Z}^+$ [43, p.327, Ch.9]. A definition of $\pi_n(X, x_0)$ is given in [44, p.340, Ch.4.1].

[7] The trivial group is denoted 0 in Hatcher [44, p.27, Ch.1.1, Example 1.4]. It can be written as $\langle e \rangle$, where e is the single group element. It can also be written as 0 in the context of abelian groups, or 1 in the context of non-abelian groups [45] [46].

example, we consider the complex plane $\mathbb{C}$, with a single point removed from it (say, $0+0i$), as shown in Figure 2.2. A loop homotopy F cannot move a loop $f(s)$ to another loop $f'(s)$ unless F can avoid having the loop $f(s)$ intersect the removed point $0+0i$. Figure 2.2 shows two distinct loop homotopy classes. One of them – $[\tilde{f}]$ – is an identity element of the fundamental group, since concatenating an element of $[\tilde{f}]$ with any other loop $h(s)$ creates a loop which is loop homotopic to $h(s)$. The other – $[\tilde{g}]$ – is not an identity element, since concatenating two loops g_1 and g_2 in $[\tilde{g}]$ that wrap around the $\times$ once produces a loop $g_2 \circ g_1$ that wraps around the $\times$ twice. In fact, $[\tilde{g}]$ is a *generator* of the fundamental group of $X = \mathbb{C}\backslash\{0+0i\}$. An elementary result in algebraic topology is that, for any $x_0 \in X$, the fundamental group $\pi_1(X, x_0)$ is isomorphic to the integers $\mathbb{Z}$ [44, pp.29-31, Theorem 1.7] (i.e., any loop homotopy class $[\tilde{h}] \in \pi_1(X, x_0)$ can be written as the homotopy class of the generator $[\tilde{g}^n]$, where g is raised to some integer power n). The nontrivial $\pi_1(\mathbb{C}\backslash\{0+0i\}, x_0) \cong \mathbb{Z}$ arises from the removal of $\{0+0i\}$ from $\mathbb{C}$.

As with the subspace $\mathbb{C}\backslash\{0+0i\}$ of the complex plane $\mathbb{C}$, a loop homotopy in $\mathcal{G}_n$ cannot put a loop in $\mathcal{G}_n$ through the other subspace $\mathcal{V}_n$. We can identify the fundamental group of $\mathcal{G}_n$ by looking at the mapping between $\mathcal{G}_n$ and eigenvalue spectra of $\mathcal{H}$. As before, varying the control parameters in $\mathcal{G}_n$ via a smooth curve $\mathcal{C} \subset \mathcal{G}_n$ smoothly transports n eigenvalues $\lambda = \{\lambda_1, \ldots, \lambda_n\}$ in the complex plane. Throughout this thesis, we take $\mathcal{C}$ to be a loop with some basepoint at x_0. This causes the spectrum λ corresponding to x_0 to map back to itself along $\mathcal{C}$. This evolution of n points in $\mathcal{C}$ is a **braid** [47] [48] [49]. In analogy to path homotopy of loops in $\mathcal{G}_n$, we define **braid isotopy** for two braids: two braids are isotopic if the braids have the same basepoints, and if one can be continuously deformed into the other without the strands intersecting. Braid isotopy defines an equivalence relation. We now define **spectral flow** as the braid isotopy class b [1, p.3]. Again in analogy with path concatenation, we define a concatenation of braids with fixed endpoints, by sticking the start and endpoints of braids together. This forms the **braid group** B_n [47].

Let us take the mapping of the set $\mathcal{G}_n$ of coefficients of traceless, degree-n polynomials with nondegenerate spectra to the set of $n-1$ nondegenerate polynomial roots in $\mathbb{C}$ to be the function $\tilde{f} : \mathcal{G}_n \to \mathbb{C}^{n-1}$. Path homotopies in $\mathcal{G}_n$ correspond to braid isotopies in B_n via the mapping $\tilde{f}$. By this correspondence, the fundamental group $\pi_1(\mathcal{G}_n, x_0)$ for a point $x_0 \in \mathcal{G}_n$ is isomorphic to the braid group $B_n(\tilde{f}(x_0))$. $\pi_1(\mathcal{L}_n, x_0) = 0$, so the nontrivial $\pi_1(\mathcal{G}_n, x_0)$ arises from the structure of the degenerate subspace $\mathcal{V}_n$; this will be made more concrete for $n = 2$ in Section 2.4 and for $n = 3$ in Section 2.5.

2.4 2-Mode System

2.4.1 2 Coupled Oscillators

To make concrete the discussion of spectral flow, we consider the eigenvalue braids formed in a two-mode system. Let us consider two harmonic oscillators (discussed in more detail in Section 3.2). These oscillators have complex amplitudes c_1 and c_2. If they are uncoupled, they have independent equations of motion (c.f. Equation (3.19))

$$\begin{aligned} \dot{c}_1 &= -i\left(\omega_1 - i\gamma_1/2\right) c_1 \\ \dot{c}_2 &= -i\left(\omega_2 - i\gamma_2/2\right) c_2 \end{aligned} \tag{2.58}$$

These equations of motion are realized from the uncoupled Hamiltonian

$$\mathcal{H}_0 = \sum_{j=1}^{2} \hbar\omega_j \left(c_j^\dagger c_j + \frac{1}{2}\right) \tag{2.59}$$

Now, we add a coupling term $\hbar g(c_1 c_2^\dagger + c_1^\dagger c_2)$ to the Hamiltonian:

$$\mathcal{H} = \sum_{j=1}^{2} \hbar\omega_j \left(c_j^\dagger c_j + \frac{1}{2}\right) + \hbar g(c_1 c_2^\dagger + c_1^\dagger c_2) \tag{2.60}$$

Define the complex eigenvalues $\lambda_j = \omega_j - i\gamma_j/2$. The c_1 and c_2 equations of motion, as can be obtained from input-output theory (Section 3.3.2), are then

$$\begin{aligned} \dot{c}_1 &= -i(\lambda_1 c_1 + g c_2) \\ \dot{c}_2 &= -i(g c_1 + \lambda_2 c_2) \end{aligned} \tag{2.61}$$

As a vector equation, the equation of motion for $\mathbf{c}' = (c_1, c_2)^T$ is

$$\dot{\mathbf{c}}' = -i\mathcal{H}'_{\text{eff}}\mathbf{c}' \tag{2.62}$$

where

$$\mathcal{H}'_{\text{eff}} = \begin{pmatrix} \lambda_1 & g \\ g & \lambda_2 \end{pmatrix} \tag{2.63}$$

The solution to the equation of motion can be simplified by subtracting the trace from Equation (2.63):

$$\mathcal{H}'_{\text{eff}} = \begin{pmatrix} \bar{\lambda} & 0 \\ 0 & \bar{\lambda} \end{pmatrix} + \begin{pmatrix} \lambda & g \\ g & -\lambda \end{pmatrix} \tag{2.64}$$

where we define

$$\begin{aligned} \bar{\lambda} &= \frac{\lambda_1 + \lambda_2}{2} \\ \lambda &= \frac{\lambda_1 - \lambda_2}{2} \end{aligned} \tag{2.65}$$

If we multiply $\mathbf{c}$ by $U(t) = \begin{pmatrix} e^{i\bar{\lambda}t} & 0 \\ 0 & e^{i\bar{\lambda}t} \end{pmatrix}$, to get $\mathbf{c} = U(t)\mathbf{c}'$, then the equation of motion is

$$\dot{\mathbf{c}} = -i\mathcal{H}_{\text{eff}}\mathbf{c} \tag{2.66}$$

where $\mathcal{H}_{\text{eff}}$ is given by

$$\mathcal{H}_{\text{eff}} = \begin{pmatrix} \Delta - i\gamma/2 & g \\ g & -\Delta + i\gamma/2 \end{pmatrix} \tag{2.67}$$

with $\lambda = \Delta - i\gamma/2$. In studying spectral flow in Equation (2.67), we will treat Δ and g as free parameters with which to tune the eigenvalues of Equation (2.67).

2.4.2 2-Mode Toy System

The eigenvalues of Equation (2.67) are found from the roots of the characteristic polynomial (Equation (2.48)):

$$\begin{aligned} p(\mu) &= \det(\mu I_{2\times 2} - \mathcal{H}_{\text{eff}}) \\ &= (\mu - \lambda)(\mu + \lambda) - g^2 \\ &= \mu^2 - \lambda^2 - g^2 \end{aligned} \tag{2.68}$$

The roots are

$$\mu_\pm = \pm\sqrt{\lambda^2 + g^2} \tag{2.69}$$

The general form for the characteristic polynomial of a traceless 2×2 matrix is (c.f. Equation (2.41), with $a_1 = 0$, and $z = -a_0$)

$$p(\mu) = \mu^2 - z \tag{2.70}$$

Comparing Equations (2.68) and (2.70), we see that tuning the complex parameter $z = \lambda^2 + g^2$ tunes the eigenvalues $\mu_\pm = \pm\sqrt{z}$.

We find qualitatively different eigenvalue trajectories, depending on how we define $z(s)$ as a function of a parameter $s \in [0, 1]$, and if the curve defined by $z(s)$ encloses $z = 0$. Per the relation

$$\begin{aligned} z &= \lambda^2 + g^2 \\ &= \Delta^2 + g^2 - \gamma^2/4 - i\Delta\gamma, \end{aligned} \tag{2.71}$$

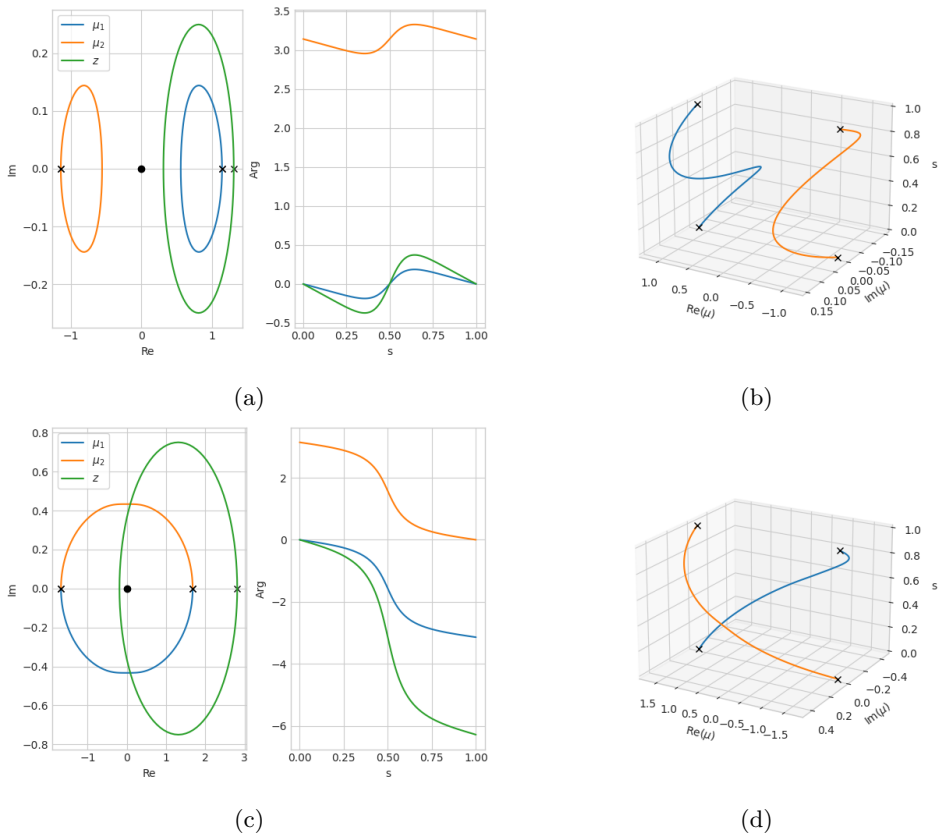

(a) (b)

(c) (d)

Figure 2.3: Eigenvalue braids in the 2-mode system. z wraps around itself from 0 to 2π once in all plots. LHS shows z and the two eigenvalues in the complex plane, as well as the arguments of z and the eigenvalues versus the parameter $s \in [0, 1]$. RHS shows the eigenvalues as a function of $s \in [0, 1]$. Black x's denote the base points of the control loop z (green), as well as the eigenvalues (blue and orange). z does not enclose $z = 0$ in a and b, and z does enclose $z = 0$ in c and d. In a and b, $r_0 = 0.25$. In c and d, $r_0 = 0.75$. In all plots, $g_0 = 1$, $\gamma = 1$.

$z = 0$ when

$$\gamma\Delta = 0, \quad \text{and} \tag{2.72a}$$

$$\Delta^2 + g^2 - \gamma^2/4 = 0. \tag{2.72b}$$

The choice that γ be a fixed parameter forces $\Delta = 0$, which then forces $g = \gamma/2$ at $z = 0$.

Now define curves $\Delta(s)$ and $g(s)$, by

$$\Delta(s) = r_0 \sin(2\pi s) \tag{2.73a}$$

$$g(s) = g_0 + r_0 \cos(2\pi s) \tag{2.73b}$$

For this section, let us assume that $z(0) \neq 0$ and $z(1) \neq 0$. The trajectories of the eigenvalues $\mu_\pm(s) = \pm\sqrt{z(s)} = \pm\sqrt{\lambda(s)^2 + g(s)^2}$ depends on how many times the trajectory of z encloses $z = 0$. For instance, in Figure 2.3, there are two loops performed in the parameter $z(s) =$

$\lambda(s)^2 + g(s)^2$. In a loop in which the curve defined by $z(s)$ does not enclose $z = 0$ (e.g., Figure 2.3 a and b), $\mu_\pm$ return to themselves;

$$\begin{aligned} \mu_+(0) &= \mu_+(1) \\ \mu_-(0) &= \mu_-(1) \end{aligned} \tag{2.74}$$

In a loop in which $z(s)$ does enclose $z = 0$ (e.g. Figure 2.3 c and d), even though $z(0) = z(1)$, the eigenvalues permute

$$\begin{aligned} \mu_+(0) &= \mu_-(1) \\ \mu_-(0) &= \mu_+(1) \end{aligned} \tag{2.75}$$

Somewhat more generally, for all choices of g_0 and r_0, the loops defined by Equation (2.73) which permute eigenvalues are path homotopic to one another, with the path homotopy realized by simply scaling r_0 to any value for which

$$|g_0 - r_0| < \gamma/2; \quad g_0 + r_0 > \gamma/2 \tag{2.76}$$

All of these loops which leave the eigenvalues fixed are also path homotopic with each other, so long as the complement of Equation (2.76) holds. In both of these cases, the homotopy does not have the loop pass through $z = 0$ (i.e., through $\mathcal{V}_2$). By the isomorphism between braids and control loops of the characteristic polynomial coefficients, two braid isotopy classes are formed from these: one class of braids which permute eigenvalues, and another which do not. Braids from the two isotopy classes cannot be deformed into one another without having the 2 strands pass through one another; this happens happen precisely when the loop passes through $z = 0$.

The toy example defined by the curves in Equations (2.73) has focused on the loops permuting the eigenvalues by winding around the exceptional point zero times or one time. However, permuting the eigenvalues is not the full story; more generally, control loops can wind around the exceptional point n times. For instance, we can define curves $\Delta_n(s)$ and $g_n(s)$ by

$$\Delta_n(s) = r_0 \sin(2\pi n \cdot s) \tag{2.77a}$$

$$g_n(s) = g_0 + r_0 \cos(2\pi n \cdot s) \tag{2.77b}$$

If this curve does not enclose $z = 0$, then the eigenvalues return to themselves again. However, if this curve does enclose $z = 0$, then the eigenvalues permute only if n is an odd integer. For instance, in Figure 2.4, with $n = 2$, in a and b, the loop does not enclose the exceptional point, so the eigenvalues return to themselves; in c and d, the loop does enclose the exceptional point, yet the eigenvalues returned to their initial values. However, the two braids formed by the

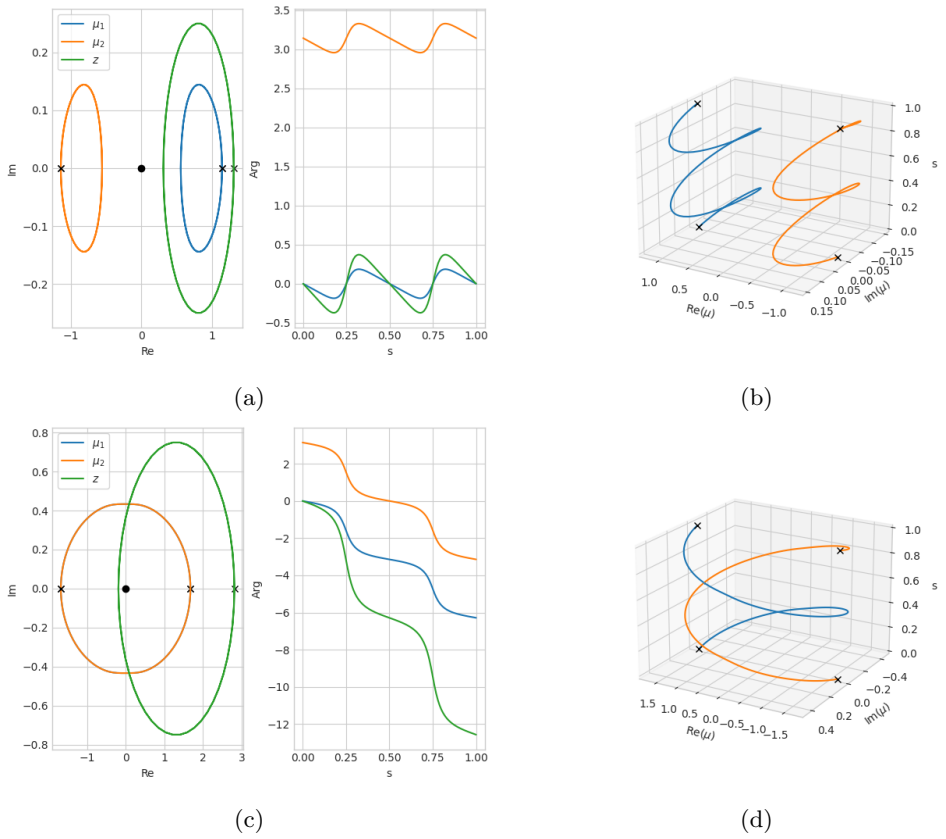

(a) (b)

(c) (d)

Figure 2.4: Eigenvalue braids in the 2-mode system. z wraps around itself from 0 to 4π once in all plots ($n = 2$ in Equation (2.77)). LHS shows z and the two eigenvalues in the complex plane, as well as the arguments of z and the eigenvalues versus the parameter $s \in [0, 1]$. RHS shows the eigenvalues as a function of $s \in [0, 1]$. Black x's denote the base points of the control loop z (green), as well as the eigenvalues (blue and orange). z does not enclose $z = 0$ in a and b, and z does enclose $z = 0$ in c and d. In a and b, $r_0 = 0.25$. In c and d, $r_0 = 0.75$. In all plots, $g_0 = 1$, $\gamma = 1$.

spectral flow are isotopically distinct from each other. This motivates the *winding number* of the control loop, or the number of times the loop encloses $z = 0$. The winding number of the loop uniquely determines the isotopy class of the braid formed from the loop. Thus, for the space $\mathcal{G}_2$ of nondegenerate spectra, the fundamental group $\pi_1(\mathcal{G}_2) \cong \mathbb{Z}$.

2.4.3 2-Mode Jordan-Arnol'd Form

We now find the eigenvector(s) of $\mathcal{H}_{\text{eff}}$ subject to $z = \lambda^2 + g^2$. For $z \neq 0$, the eigenvectors $\mathbf{v}_\pm = (a_\pm, b_\pm)^T$ are the solutions of

$$\mathcal{H}_{\text{eff}} \begin{pmatrix} a_\pm \\ b_\pm \end{pmatrix} = \begin{pmatrix} \lambda - \mu_\pm & g \\ g & -\lambda - \mu_\pm \end{pmatrix} \begin{pmatrix} a_\pm \\ b_\pm \end{pmatrix} = \begin{pmatrix} 0 \\ 0 \end{pmatrix} \tag{2.78}$$

A set of linearly independent eigenvectors are determined by the vector components

$$\begin{aligned} a_\pm &= (\lambda + \mu_\pm)/g \\ b_\pm &= 1 \end{aligned} \tag{2.79}$$

From the eigenvectors $v_\pm = ((\lambda + \mu_\pm)/g, 1)^T$, a change-of-basis matrix S_0 is constructed

$$S_0 = \begin{pmatrix} v_+ | v_- \end{pmatrix} = \begin{pmatrix} (\lambda + \mu_+)/g & (\lambda + \mu_-)/g \\ 1 & 1 \end{pmatrix} \tag{2.80}$$

The change-of-basis S_0 diagonalizes $\mathcal{H}_{\text{eff}}$:

$$S_0^{-1} \mathcal{H}_{\text{eff}} S_0 = \begin{pmatrix} \mu_+ & 0 \\ 0 & \mu_- \end{pmatrix} \tag{2.81}$$

When $z = 0$, the situation changes, in that $\mathcal{H}_{\text{eff}}$ cannot be diagonalized. Indeed, at $z = 0$, $\Delta = 0$, $g = \gamma/2$, and $\mu_+ = \mu_- = 0$. If we follow the prescription of Equation (2.78), the single eigenvector (up to multiplication by a scalar) is $a = g = 1$, $b = -\lambda = +i$. As discussed in Section 2.2.3, the eigenspace corresponding to $\mu = 0$ has dimension 1. If we wish to find a basis in which to write $\mathcal{H}_{\text{eff}}$ in terms of only its eigenvalue $\mu = 0$, we seek a generalized eigenvector of order 2 for $\mu = 0$. This is found with

$$\begin{pmatrix} -i\gamma/2 & \gamma/2 \\ \gamma/2 & +i\gamma/2 \end{pmatrix} \begin{pmatrix} a_2 \\ b_2 \end{pmatrix} = \begin{pmatrix} 1 \\ +i \end{pmatrix} \tag{2.82}$$

A solution is $a_2 = 0$ and $b_2 = 2/\gamma$. This vector satisfies $(\mathcal{H}_{\text{eff}} - 0I)^2 (a_2, b_2)^T = 0$ (see Section

2.2.3). Let us take $v_2' = (\gamma/2)v_2$, which is also a generalized eigenvector of order 2. We then write a similarity transformation

$$S = (v_1|v_2') = \begin{pmatrix} 1 & 0 \\ +i & 1 \end{pmatrix} \tag{2.83}$$

with which

$$S^{-1}\mathcal{H}_{\text{eff},z=0}S = \begin{pmatrix} 0 & 1 \\ 0 & 0 \end{pmatrix} \tag{2.84}$$

Equation (2.84) is a Jordan block, an "almost-diagonal" matrix.

In both cases, where the parameter $z = 0$ and $z \neq 0$, a matrix which has the same characteristic polynomial as Equation (2.67), is

$$J_2 + \delta J = \begin{pmatrix} 0 & 1 \\ z & 0 \end{pmatrix} \tag{2.85}$$

$J_2 + \delta J$ is a Jordan block, plus an additional z term. When $z \neq 0$, then the eigenvalues are $\pm\sqrt{z}$, and the eigenvectors are $\mathbf{v}_\pm(1, \pm\sqrt{z})^T$. A similarity transformation that diagonalizes $J_2 + \delta J$ is

$$T^{-1} = (\mathbf{v}_+|\mathbf{v}_-) = \begin{pmatrix} 1 & 1 \\ \sqrt{z} & -\sqrt{z} \end{pmatrix} \tag{2.86}$$

with inverse

$$T = \frac{1}{2}\begin{pmatrix} 1 & 1/\sqrt{z} \\ 1 & -1/\sqrt{z} \end{pmatrix} \tag{2.87}$$

Then $TJ_2T^{-1} = \text{Diag}(+\sqrt{z}, -\sqrt{z})$. Now we may bring $\mathcal{H}_{\text{eff}}$ into the form of $J_2 + \delta J$ with $S_2 = S_0T$ (Equations (2.80) and (2.87)):

$$S_2 = S_0T = \begin{pmatrix} \lambda/g & 1/g \\ 1 & 0 \end{pmatrix} \tag{2.88}$$

S_2 does not have a singularity at $z = 0$, unlike S and T. Then this transformation puts $\mathcal{H}_{\text{eff}}$ as a matrix in terms of its characteristic polynomial $p(\mu) = \mu^2 - z$, regardless of the value of z:

$$S_2^{-1}\mathcal{H}_{\text{eff}}S_2 = \begin{pmatrix} 0 & 1 \\ g^2 + \lambda^2 & 0 \end{pmatrix} = \begin{pmatrix} 0 & 1 \\ z & 0 \end{pmatrix} \tag{2.89}$$

The above is the **Jordan-Arnol'd form** for the 2×2 system [14] [15]. At $z = 0$, Equation

(2.89), and thus Equation (2.67), is not diagonalizable. $z = 0$ is an **exceptional point**, at which the eigenvalues and the eigenvectors become degenerate.[8]

The Jordan-Arnol'd form (Equation (2.89)) is the most general possible perturbation to the 2×2 Jordan block, up to a similarity transformation [14] [15]. To see this, we follow [14, p.355] and write a perturbation δJ to the Jordan block:

$$\delta J = \begin{pmatrix} \delta J_{11} & \delta J_{12} \\ \delta J_{21} & \delta J_{22} \end{pmatrix} \tag{2.90}$$

and we see which δJ can be written as a similarity transformation from $J = \begin{pmatrix} 0 & 1 \\ 0 & 0 \end{pmatrix}$. Under this assumption, we seek a similarity transformation $1 + \delta S$ near the identity. Then $(1+\delta S)^{-1} J (1+\delta S)^{-1} \approx J + \delta J$, or

$$\begin{aligned} (1+\delta S)^{-1} J (1+\delta S)^{-1} &\approx (1+\delta S)^{-1} J (1 - \delta S) \\ &= J + \delta S \cdot J - J \cdot \delta S \\ &= J + [\delta S, J] \end{aligned} \tag{2.91}$$

We identify those perturbations $\delta J_{\mathrm{i}} = [\delta S, J]$ as the perturbations which can be generated "internally" from a similarity transformation near the identity. Write δS as

$$\delta S = \begin{pmatrix} A & B \\ a & b \end{pmatrix} \tag{2.92}$$

Then

$$\begin{aligned} \delta J_{\mathrm{i}} &= [\delta S, J] \\ &= \begin{pmatrix} -a & A - b \\ 0 & a \end{pmatrix} \end{aligned} \tag{2.93}$$

In contrast, the perturbations δJ_{n} *cannot* be written in terms of a similarity transformation near the identity:

$$\delta J_{\mathrm{n}} = \begin{pmatrix} 0 & 0 \\ z & y \end{pmatrix} \tag{2.94}$$

The subscript n means "non-internally" generated. We can take $y = 0$, since we are considering

[8] In terms of algebraic and geometric multiplicities (Sections 2.2.2 and 2.2.3), an exceptional point is a point in parameter space at which the algebraic multiplicity is strictly greater than the geometric multiplicity. If the eigenvalues become degenerate, but the algebraic and geometric multiplicities remain equal, the system is instead at a *diabolic point*, where the eigenvectors remain nondegenerate.

traceless matrices. Adding δJ_{n} to the Jordan block, we have

$$J_2 + \delta J_{\mathrm{n}} = \begin{pmatrix} 0 & 1 \\ z & 0 \end{pmatrix} \tag{2.95}$$

Because the characteristic polynomial of a traceless 2×2 matrix is $p(\mu) = \mu^2 - z$, we can regard the perturbation z as a perturbation to the characteristic polynomial (as well as the minimal polynomial) of the Jordan block.

We conclude this discussion of the 2-mode exceptional point with three remarks. The first is that z spans the eigenvalue control space around the exceptional point at $z = 0$. Thus, one complex parameter, or two real parameters, are needed to realize full control of the eigenvalue control space for a 2-mode system. The second is that, for a general 2×2 *traceless* Hamiltonian $\mathcal{H}_{2\times 2}(\xi_1, \xi_2)$, for two real parameters ξ_1, ξ_2, one can calculate this Jordan-Arnol'd control parameter z with (c.f. Equation (2.47))

$$z = -\det\Big(\mathcal{H}_{2\times 2}(\xi_1, \xi_2)\Big) \tag{2.96}$$

Solving for values of ξ_1 and ξ_2 for which $z = 0$ determines where the exceptional point lies. The third is that, since the discriminant D is equal to $4z$, solving Equation (2.96) is equivalent to solving for zeros of the discriminant.

2.4.4 $\pi_1(\mathcal{G}_2) \cong B_2 \cong \mathbb{Z}$

In Section 2.4.2, we considered a system in which we realize two eigenvalue braids: one in which the eigenvalues permute, and one in which they do not. The braid isotopy classes which these two braids define are two elements of the infinite-dimensional braid group B_2.

Let the two braids in Section 2.4.2 be e and σ_1. e is just the identity braid. σ_1 is a generator of the braid group B_2, since any braid isotopy class in B_2 can be written as the braid isotopy $b = \sigma_1^j$, for $j \in \mathbb{Z}$. j is allowed to be a negative integer, signifying that the inverse element of σ_1 may generate the braid instead. Since j solely determines the braid isotopy class of b, we see that $B_2 \cong \mathbb{Z}$.

We compare the result that $B_2 \cong \mathbb{Z}$ with $\pi_1(\mathcal{G}_2)$. The loop homotopy class of a loop in $\mathcal{G}_2$ is determined by the integer number of times a loop wraps around $\mathcal{V}_2 = \{0\}$. Thus, $\mathcal{G}_2$ has the same fundamental group as the unit circle S^1. Then $\pi_1(S^1) = \mathbb{Z}$ [44, p.29-31], in agreement with $\pi(\mathcal{G}_2) \cong \mathbb{Z}$.

2.5 3-Mode System

2.5.1 3-Mode Control Space

In a manner similar to the 2-mode system, we consider three coupled modes c_1, c_2, and c_3, which are coupled by a Hamiltonian

$$\mathcal{H} = \sum_{j=1}^{3} \hbar\omega_j (c_j^\dagger c_j + 1/2) + \sum_{i \neq j} \hbar g_{ij} (c_i^\dagger c_j + c_i c_j^\dagger) \tag{2.97}$$

This leads to coupled equations of motion

$$\mathbf{c} = -i\mathcal{H}_{\text{eff}}\mathbf{c} \tag{2.98}$$

where (c.f., Equation (2.63))

$$\mathcal{H}_{\text{eff}} = \begin{pmatrix} \lambda_1 & g_{12} & g_{13} \\ g_{12} & \lambda_2 & g_{23} \\ g_{13} & g_{23} & \lambda_3 \end{pmatrix} \tag{2.99}$$

The characteristic polynomial of any traceless 3×3 matrix is (c.f. Equation (2.41))

$$p(\mu) = \mu^3 + a_1\mu - a_0 \tag{2.100}$$

Its discriminant is (from Equation (2.52))

$$D = -4a_1^3 - 27a_0^2 \tag{2.101}$$

The Jordan block for a traceless 3×3 matrix with exactly one eigenvalue $\lambda = 0$ and eigenvector is

$$J_3 = \begin{pmatrix} 0 & 1 & 0 \\ 0 & 0 & 1 \\ 0 & 0 & 0 \end{pmatrix} \tag{2.102}$$

It can be shown that the most general possible perturbation to the Jordan block (2.102) is given by [14, p.350-1]:

$$J + \delta J = \begin{pmatrix} 0 & 1 & 0 \\ 0 & 0 & 1 \\ x & y & z \end{pmatrix}; \, x, y, z \in \mathbb{C} \tag{2.103}$$

$J + \delta J$ in (2.103) has three complex parameters, so it has six real parameters. These six real numbers independently span the space of eigenspectra of a 3×3 complex matrix. For our

experiment, it suffices to consider $J + \delta J$ with an overall trace of zero, so we set $z = 0$. This yields the Jordan-Arnol'd form for a 3×3 traceless matrix:

$$J + \delta J = \begin{pmatrix} 0 & 1 & 0 \\ 0 & 0 & 1 \\ x & y & 0 \end{pmatrix}; x, y \in \mathbb{C} \tag{2.104}$$

We can remark that since x, y are two complex numbers that independently control the set of matrices $J + \delta J$ (2.104), the complex dimension of the set of $J + \delta J$ is two, and the real dimension is four. Thus, these $x, y \in \mathbb{C}$ parameters realize the entire control space of eigenvalues of 3×3 traceless complex matrices (which can be non-Hermitian).

We note some properties of $J + \delta J$ (2.104). Its characteristic polynomial is

$$p(\mu) = -\mu^3 + \mu y + x \tag{2.105}$$

Its discriminant polynomial is

$$d(x, y) = 4y^3 - 27x^2 \tag{2.106}$$

Per Equation (2.49), at least two of the three eigenvalues of $J + \delta J$ are equal if and only if $d(x, y) = 0$. A special case of this is when $x = y = 0$; then all three eigenvalues are equal.

We can also see that, at $d(x, y) = 0$, for $x \neq 0$, the three eigenvectors of the Jordan-Arnol'd form (Equation (2.104)) will not span the full 3D vector space. For $d(x, y) = 0$, the roots of the characteristic polynomial (Equation (2.105)) are (as found in in Appendix E):

$$\begin{aligned} \lambda_1 &= 2\left(\frac{x}{2}\right)^{1/3} \\ \lambda_2 = \lambda_3 &= -\left(\frac{x}{2}\right)^{1/3} \end{aligned} \tag{2.107}$$

An eigenvector corresponding to the nondegenerate λ_1 is $v_1 = ((x/2)^{1/3}, 0, 2x)^T$. The only eigenvector corresponding to $\lambda_2 = \lambda_3$ (up to a scalar multiple) is $v_2 = (2(x/2)^{2/3}, -x, (x^4/2)^{1/3})^T$. Thus, $J + \delta J$ is not diagonalizable when $d(x, y) = 0$. A generalized eigenvector of order 2 corresponding to $\lambda_2 = \lambda_3$ is $v_3 = (2(x/2)^{1/3}, 0, -x)^T$. These three vectors together define a change of basis $S = (v_1|v_2|v_3)$ that sets

$$J + \delta J \cong \begin{pmatrix} 0 & 0 & 0 \\ 0 & 0 & 1 \\ 0 & 0 & 0 \end{pmatrix} \tag{2.108}$$

Because $d(x, y) = 0$ makes the eigenvectors of the 3×3 matrix fail to span $\mathbb{C}^3$, the 3×3 matrix is at an **exceptional point** if and only if $d(x, y) = 0$. These points are EP_2 points, where

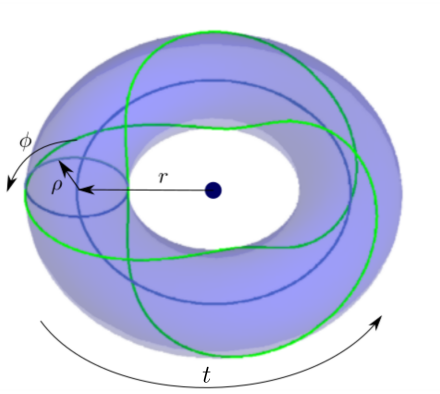

Figure 2.5: The trefoil knot (green), parameterized by Equations (2.112) and (2.113). The trefoil knot is wound around a torus of radii r and ρ (blue). The coordinates t and ϕ parameterize the circles of radii r and ρ, respectively.

the subscript 2 indicates a 2nd order degeneracy in the eigenvalues as well as the eigenvectors. A special case is when, in addition, $x = y = 0$. Then Equation (2.104) is already a Jordan block; it is an EP_3 point, or third-order exceptional point.

Because x and y are the only two complex parameters needed to fully parameterize the eigenvalue control space of a 3-mode system, we need only four real parameters in order to reach arbitrary control of this full space. Two useful relations for an arbitrary traceless $\mathcal{H}_{\text{eff}}$ arise from the similarity relation to Equation (2.104):

$$x = \det\left(\mathcal{H}_{\text{eff}}\right) \tag{2.109a}$$

$$y = \frac{1}{2}\,\mathrm{Tr}\left(\mathcal{H}_{\text{eff}}^2\right) \tag{2.109b}$$

Then, solving for $d(x, y) = 0$ yields EP_2 points, and solving for $x = y = 0$ yields the EP_3 point. Numerically solving these scalar equations is *far* simpler than directly finding the roots of the characteristic polynomial $p(\lambda) = \det(\mathcal{H}_{\text{eff}} - \lambda I)$ in the hopes of numerically finding exceptional points.

2.5.2 The Knotted Topology of EP_2 in a 3-Mode System

The subspace of the parameters x and y for which $d(x, y) = 0$ (2.106) possesses a trefoil knot structure. To see this, we follow an argument in [9]. We can write x, y in polar form:

$$\begin{aligned} x &= re^{it} \\ y &= \rho e^{i\phi} \end{aligned} \tag{2.110}$$

Then $d(x, y) = 0$ implies that

$$27r^2e^{i2t} = 4\rho^3 e^{i3\phi} \tag{2.111}$$

We can look at the magnitudes and the arguments of this equation:

$$\begin{aligned} 27r^2 &= 4\rho^3 \\ 2t &= 3\phi \end{aligned} \tag{2.112}$$

Thus, r, ρ, t, ϕ are four real parameters that, when they satisfy the constraints of Equation 2.112, realize the space of doubly degenerate eigenspectra of 3×3 complex matrices. Since there are two constraint equations, this space has real dimension 2.

Now, if we restrict our attention to a hypersurface in $\mathcal{L}_3$, which has real dimension 4, we set a constraint equation $F(r, \rho, t, \phi) = 0$. The intersection of this space with the space of doubly degenerate eigenspectra has three constraint equations, so it has real dimension 1.

For instance, if we restrict our attention to a hypersphere, we set a constraint equation

$$|x|^2 + |y|^2 = \varepsilon^2 \tag{2.113}$$

This sets $r^2 + \rho^2 = \varepsilon^2$. We can sweep this one-dimensional space with one parameter, $\theta \in [0, 2\pi)$, and setting

$$\begin{aligned} t &= 3\theta \\ \phi &= 2\theta \end{aligned} \tag{2.114}$$

Figure 2.5 shows the curve traced out by t, ϕ, r, ρ, as defined in Equations (2.114), (2.112), and (2.113). In Figure 2.5, we see that, as θ goes from 0 to 2π once, t goes from 0 to 6π, and ϕ goes from 0 to 4π. This (3,2) covering defines a trefoil knot.

We can remark that, from (2.114), $\theta = t - \phi$. Thus, θ can be obtained directly from the x and y control parameters:

$$\theta = \text{Arg}\left(\frac{x}{y}\right) \tag{2.115}$$

Because x and y are functions of the system eigenvalues, this relation is very useful in providing a single coordinate to parameterize the knot (c.f., Figure 6.22).

2.5.3 EP_2 Manifold

In Section 2.5.2, we took the EP_2 manifold and restricted it to a 3-sphere (Equation (2.113)). Here, we discuss considerations in the choice of hypersurface (which is delineated concretely in Section 6.3), as well as the full EP_2 manifold.

The solutions to $d(x, y) = 0$ form an algebraic variety [50]. $d(x, y)$ scales such that when

$$\begin{aligned} x &\mapsto ax \\ y &\mapsto by \end{aligned} \tag{2.116}$$

where $a^2 = b^3$, then

$$d(x, y) \mapsto a^2 d(ax, by) \tag{2.117}$$

so any root (x_0, y_0) of $d(x, y)$ corresponds to a root (ax_0, by_0) of $d(x, y)$. We see then that this algebraic variety is a cone $\mathcal{K} \times \mathbb{R}^{>0}$ in $\mathbb{C}^2$. $\mathcal{K}$ is the trefoil knot (Section 2.5.2), and $\mathbb{R}^{>0}$ is a "radial distance" from the $x = y = 0$ origin (the EP_3 point).

The EP_2 manifold is a 2-parameter algebraic variety in the full control space $\mathcal{L}_3 \cong \mathbb{C}^2$. The full control space has real dimension 4, so the algebraic variety has real codimension 2. Thus, we can loop around the 2-dimensional space of EPs. To make this easier to visualize, we can restrict the full EP_2 manifold to a hypersurface of our choosing; the space of EPs on this surface is then a 1-dimensional curve. One possible hypersurface – the 3-sphere – is considered in Section 2.5.2, which follows [9]. In practice, any cross-section of the EP_2 cone which is realized as the intersection of the EP_2 cone with a hypersurface will suffice, so long as [1, Supplement, Section 1]

1. The hypersurface encloses $x = y = 0$ (the EP_3 point). We require this because the theorem by [9] is stated for surfaces which enclose the origin $(0, 0)$ of the space $\mathbb{C}^2$.

2. The hypersurface does not intersect itself. This could cause the EP_2 curve to trace out something other than a trefoil knot.

3. Has the topology of the 3-sphere. Except perhaps on a set of measure zero, the hypersurface should locally "look like" a 3-sphere.

4. Is everywhere transverse to an infinitesimal scaling by $a \mapsto (1 + \varepsilon)a$. That is, the scaling should never "run parallel" to the surface.[9] A more mathematically rigorous description of transversality can be found in [51, pp.27-32, Chapter 1, Section 5].

These criteria are chosen so that the system eigenvalues are a one-to-one function of the position on the hypersurface. When these criteria are realized, then the $\mathbb{R}^{>0}$ part of the $\mathcal{K} \times \mathbb{R}^{>0}$ EP_2 manifold is sliced out, and we are left with the trefoil knot $\mathcal{K}$. Another choice which suffices

[9] The hypersurface which we choose in experimental space (described in Chapter 6) violates this condition in a few spots. The condition can be numerically approximated as: for any small continuous section of the hypersurface, there is only one continuous cluster of eigenvalues. A numerical check of the surface found that at least 99% of the surface satisfies this condition, and the points which violate this condition are away from the EP_2 points measured in Chapter 5.

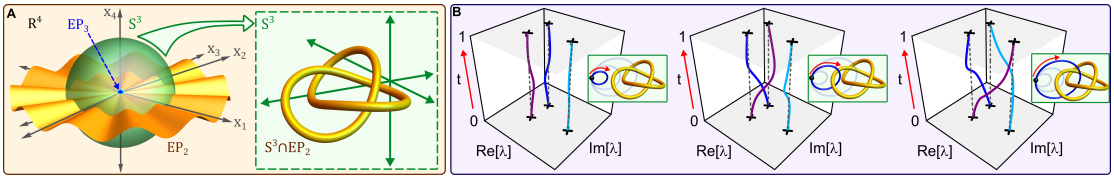

Figure 2.6: A: A depiction of the EP_2 manifold in the $\mathcal{L}_3$ control space (gold), which contains EP_3 (blue). $\mathcal{L}_3$ is depicted here as $\mathbb{R}^4 \cong \mathbb{C}^2$. We look at the S^3 hypersurface (green), on which the EP_2 manifold is a trefoil knot.
B: three loops in the control space $\mathcal{G}_3$, which realize three braids in distinct braid isotopy classes in B_3. Left: the braid exchanges zero eigenvalues; middle: the braid exchanges two eigenvalues; right: the braid exchanges three eigenvalues.

is a 4D hyperrectangle (see Section 6.3.2, which discusses the choice of hypersurface in the experiment).

2.5.4 Braid Group B_3

In Figure 2.6, we show a cartoon[10] of the full EP_2 manifold, intersecting with a hypersurface S in the $\mathcal{L}_3 \cong \mathbb{C}^2$ control space. On this hypersurface S – chosen to be a 3-sphere – the EP_2 surface is a trefoil knot, as guaranteed in Sections 2.5.2 and 2.5.3. We also show braids that arise from control loops on this hypersurface. These braids generate B_3.

Thus far, we have viewed the space $\mathcal{L}_3$ as a complex vector space isomorphic to $\mathbb{C}^2$, with complex dimension 2. If we instead view $\mathcal{L}_3$ as a real vector space $\mathbb{R}^4$, then it has a real dimension of 4. The hypersurface of a 4D control space, which has one real constraint, is a 3D space. Thus, a 1D control loop on the hypersurface can enclose the EP_2 curve, which has codimension 2 in real dimensions. As discussed more generally in Section 2.3, loop homotopy classes in $\mathcal{G}_3$ correspond to braid isotopy classes in B_3. Thus, the fundamental group of the complement of the knot $\mathcal{K}$ in $\mathcal{G}_3 \cap S$ is B_3.

We remark that B_3 is a nonabelian group, whereas B_2 is abelian (in fact, $B_2 \cong \mathbb{Z}$, while B_n is nonabelian for $n \geq 3$ [47]). Thus, control loops in the 3-mode system are noncommutative. We also remark that the system which we assume – a system of non-reciprocally coupled, damped harmonic oscillators – is quite ubiquitous, yet has the striking features of a trefoil knot topology, as well as noncommutative eigenvalue braids. To access $\mathcal{L}_n$ in a physical system, we require coupling, damping, and nonreciprocity. In Chapter 3, we discuss the theoretical details of the system of coupled oscillators that we choose for this experiment, yet there is nothing in this chapter that requires the choice to be an optomechanical platform; as discussed in this chapter, braids and knots are completely generic features of coupled harmonic oscillators.

[10] A mathematically poor, but nonetheless attractive cartoon.

Chapter 3

Optomechanics Theory

In this chapter, we discuss the physical system that we use to realize exceptional point physics. Namely, we describe the optomechanical interaction, which couples a mechanical oscillator to a cavity electromagnetic field. The optomechanical interaction is the workhorse that enables us to couple and tune three membrane mechanical modes.

3.1 Overview of Optomechanics

Cavity optomechanics couples an (optical or microwave) electromagnetic field in a cavity with a mechanical oscillator [52]. This coupling arises from the momentum carried by photons in the field as the radiation pressure force.

Applications of the radiation-pressure force can be found on the micro- and macroscale. On the atomic scale, the radiation-pressure force can be used for laser cooling, which is the basis for atomic clocks and ion traps[53] [54] [52]. For instance, laser cooling, combined with evaporative cooling of ^{87}Rb atoms, were used to obtain the first experimental observation of a Bose-Einstein condensate [55]. On the kg-scale, the radiation-pressure force can act on a movable cavity end-mirror and move it via the momentum that the photons impart (e.g., a microwave sapphire resonator coupled to a 1 kHz niobium membrane acoustic oscillator [56], bistability in a cavity induced by radiation-pressure force [57] [52]). The quantum fluctuations in the radiation-pressure force also impose limits on the sensitivity of interferometers [58], and these had to be taken into account in the measurement of gravitational waves by LIGO and VIRGO (with the first detection in September 2015 [59]) [60].

The Harris group uses optomechanics in a wide variety of domains. One recent experiment is the construction of a system of magnetically levitated drops of superfluid ^{4}He; the experiment probes the drop's optical and mechanical modes, its temperature, and its evaporation, as an

avenue toward creating an optomechanical system that can be used for quantum optomechanics [61] [62]. Another recent experiment is the measurement of high-order phonon correlations in a superfluid ^{4}He resonator by measuring the arrival of photons scattered by the resonator's acoustic modes [63]. The goals of these two experiments are quantum in nature, yet because of the diverse utility of optomechanics, we can probe other areas of physics, such as non-Hermitian physics, with essentially the same radiation-pressure-force mechanism. The experiments conducted with the membrane-in-the-middle experiment to explore topological transport in non-Hermitian physics since 2016 were completely classical (Section 4.4), and they all use radiation-pressure force to drive the modes of a square membrane inside its cavity.

3.2 Mechanical Oscillator

3.2.1 Linear Response: the Mechanical Transfer Function

In discussing the physical origin of the optomechanical interaction, the ubiquitous harmonic oscillator plays a fundamental role. Thus, we begin our discussion of the optomechanical interaction with a short discussion of the harmonic oscillator. Specifically, we discuss the mechanical transfer function of a harmonic oscillator.

Suppose we have a point mass m oscillating at a frequency ω_m, which suffers a mechanical damping γ_m. We drive it with an applied force F. The oscillation force is given by Hooke's law [2, Ch.5, p.161]:

$$F_{\text{spring}} = -kx \tag{3.1}$$

where the spring constant is $k = m\omega_m^2$. The damping force is proportional to $\dot{x}$:

$$F_{\text{damping}} = -m\gamma_m\dot{x} \tag{3.2}$$

The equation of motion follows from Newton's Second Law:

$$m\ddot{x} = \sum_i F_i = -m\omega_m^2 x - m\gamma_m\dot{x} + F \tag{3.3}$$

Equation (3.3) is easily solved by moving to the Fourier domain. The Fourier transform definition we use is such that for a time-domain function $f(t)$, the Fourier transform operator $\mathcal{F}[f(t)](\omega)$ performs

$$\mathcal{F}[f(t)](\omega) \triangleq \int_{-\infty}^{\infty} f(t)e^{i\omega t}dt \tag{3.4}$$

This functional mapping is often denoted

$$\tilde{f}[\omega] \triangleq \mathcal{F}[f(t)](\omega) \tag{3.5}$$

For our purpose of solving Equation (3.3), a useful property of the Fourier transform (Eq. (3.4)) is that a time derivative in the time domain corresponds to multiplication in the frequency domain:

$$\mathcal{F}\left[\frac{d}{dt}f(t)\right](\omega) = -i\omega\mathcal{F}[f(t)](\omega) \tag{3.6}$$

This turns the differential equation (3.3) into an algebraic equation

$$-m\omega^2\tilde{x}[\omega] = -m\omega_m^2\tilde{x}[\omega] + i\omega m\gamma_m\tilde{x}[\omega] + \tilde{F}[\omega] \tag{3.7}$$

Now we immediately have the displacement $\tilde{x}[\omega]$ as a function of the applied force $\mathcal{F}[\omega]$:

$$\tilde{x}[\omega] = \chi_x[\omega]\tilde{F}[\omega] \tag{3.8}$$

where the proportionality factor is the mechanical transfer function:

$$\chi_x[\omega] = \frac{1/m}{\omega_m^2 - \omega^2 - i\gamma_m\omega} \tag{3.9}$$

In the high-Q regime, we focus especially on frequencies ω near ω_m. Then we can approximate $\omega_m^2 - \omega^2 = (\omega_m + \omega)(\omega_m - \omega) \approx 2\omega_m(\omega_m - \omega)$ to get the **mechanical transfer function** [1] near resonance:

$$\boxed{\chi_x[\omega] \approx \frac{1/2m\omega_m}{\omega_m - \omega - i\gamma_m/2}} \tag{3.10}$$

3.2.2 The High-Q Regime: Reducing the 2nd Order ODE to a 1st Order ODE

The classic equation in Equation (3.3) is a second-order differential equation in x. In the limit where the quality factor Q, given by

$$Q = \omega_m/\gamma_m, \tag{3.11}$$

is very large, then Equation (3.3) can be reduced to a first-order differential equation, which considerably simplifies the dynamics. In the membrane-in-the-middle experiment considered in this thesis, when the membranes were first installed in the cryogenic system in 2013, the

[1] This is also called the mechanical susceptibility. However, to avoid confusion with the later definition of mechanical susceptibility (Equation (3.135b)) when we discuss optomechanics, we refer to this susceptibility factor as the mechanical transfer function.

mechanical oscillators had $Q \sim 10^6$ at room temperature, and $Q \sim 20 \times 10^6$ at cryogenic temperatures [33, p.35-6] [64, p.87]. More recently, the Q factors were $\sim 10^5$ in 2019 (Section 4.1.3). Thus, this thesis indeed operates in the high-Q regime.

Take the momentum $p = m\dot{x}$, and define the complex amplitude

$$c = \frac{1}{2x_{\text{ZPF}}}\left(x + \frac{ip}{m\omega_m}\right) \tag{3.12}$$

where x_{ZPF} is the zero-point fluctuation amplitude of a quantum mechanical oscillator:

$$x_{\text{ZPF}} \triangleq \sqrt{\frac{\hbar}{2m\omega_m}} \tag{3.13}$$

Admittedly, x_{ZPF} is merely a scaling factor which ensures that c is dimensionless. The choice could have been any quantity with dimensions of length. Though this thesis does not operate in any quantum mechanical regime, we nonetheless choose this scaling factor, as this is the convention in both classical and quantum optomechanics [52, pp. 8].

We can write x and p in terms of c:

$$x = x_{\text{ZPF}}(c + c^*) \tag{3.14}$$

$$p = -im\omega_m x_{\text{ZPF}}(c - c^*) \tag{3.15}$$

We can write Equation (3.3) and $p = m\dot{x}$ in terms of c and c^* to obtain

$$\begin{aligned} x_{\text{ZPF}}(\dot{c} + \dot{c}^*) &= -i\omega_m x_{\text{ZPF}}(c - c^*) \\ -im\omega_m x_{\text{ZPF}}(\dot{c} - \dot{c}^*) &= -m\omega_m^2 x_{\text{ZPF}}(c + c^*) + i\gamma_m m\omega_m x_{\text{ZPF}}(c - c^*) + F \end{aligned} \tag{3.16}$$

These equations can be solved in terms of c and c^* to obtain two equations:

$$\dot{c} = -i\omega_m c - \frac{\gamma_m}{2}(c - c^*) + c_{\text{in}} \tag{3.17}$$

and the complex conjugate of Equation (3.17), where we have defined

$$c_{\text{in}} \triangleq \frac{+iFx_{\text{ZPF}}}{\hbar} = \frac{+iF}{2m\omega_m x_{\text{ZPF}}} \tag{3.18}$$

We can simplify Equation 3.17 even further by using the high Q of the resonator; since the resonator is high-Q, for a drive $c_{\text{in}}[\omega]$ at a frequency ω which is near ω_m, plus or minus a few integer multiples of $\gamma_m/2$, $c^*[\omega]$ is very small, so it can be ignored. For a proof of this assertion, see Appendix A. Thus, by dropping the c^* term in Equation 3.17, we reduce the number of

coupled first-order differential equations from two to one:

$$\boxed{\dot{c} = -\left(i\omega_m + \frac{\gamma_m}{2}\right)c + c_{\text{in}}} \tag{3.19}$$

In the high-Q limit, we can take the Fourier transform of Equation (3.19) to get

$$-i\omega c[\omega] = -\left(\frac{\gamma_m}{2} + i\omega_m\right)c + c_{\text{in}}[\omega] \tag{3.20}$$

We then define the mechanical susceptibility

$$\chi_m[\omega] = \frac{1}{\gamma/2 + i(\omega_m - \omega)} \tag{3.21}$$

so that the frequency space solution is simply

$$c[\omega] = \chi_m[\omega]c_{\text{in}}[\omega] \tag{3.22}$$

3.2.3 Hamiltonian of the Mechanical Oscillator

The kinetic energy of the harmonic oscillator is

$$K = \frac{1}{2}mv^2 = \frac{1}{2}\frac{p^2}{m} \tag{3.23}$$

The potential energy is

$$U = \frac{1}{2}kx^2 = \frac{1}{2}m\omega^2x^2 \tag{3.24}$$

The total energy is simply

$$E = K + U = \frac{1}{2}\left(\frac{p^2}{m} + m\omega^2x^2\right) \tag{3.25}$$

This gives the Hamiltonian

$$\mathcal{H} = E = \frac{1}{2}\left(\frac{p^2}{m} + m\omega^2x^2\right) \tag{3.26}$$

In terms of the dimensionless mechanical oscillator amplitudes c and c^* (Equation (3.12)), it is a simple algebraic exercise to write the Hamiltonian as

$$\mathcal{H} = \hbar\omega\left(c^*c + \frac{1}{2}\right) \tag{3.27}$$

If we have multiple oscillators, where the jth oscillator has frequency ω_j, then the Hamiltonian for all of these oscillators is

$$\mathcal{H} = \sum_j \hbar\omega_j\left(c_j^*c_j + \frac{1}{2}\right) \tag{3.28}$$

3.3 Fabry-Pérot Cavity

3.3.1 Fabry-Pérot Cavity Fields and Hamiltonian

In this section, we review the electric and magnetic fields inside a Fabry-Pérot cavity. We follow an approach from [65, p.7-10] to derive the electromagnetic field as a harmonic oscillator.

Recall Maxwell's equations for the electric field $\mathbf{E}(\mathbf{r},t)$ and magnetic field $\mathbf{B}(\mathbf{r},t)$ in free space (i.e., with no charge or current densities $\rho(\mathbf{r},t)$ or $\mathbf{J}(\mathbf{r},t)$ present):

$$\nabla \cdot \mathbf{E}(\mathbf{r},t) = 0 \tag{3.29a}$$

$$\nabla \times \mathbf{E}(\mathbf{r},t) = -\frac{\partial \mathbf{B}(\mathbf{r},t)}{\partial t} \tag{3.29b}$$

$$\nabla \cdot \mathbf{B}(\mathbf{r},t) = 0 \tag{3.29c}$$

$$\nabla \times \mathbf{B}(\mathbf{r},t) = \frac{1}{c^2}\frac{\partial \mathbf{E}(\mathbf{r},t)}{\partial t} \tag{3.29d}$$

We also recall the magnetic vector potential $\mathbf{A}(\mathbf{r},t)$, which is defined such that it satisfies the equations

$$\mathbf{B}(\mathbf{r},t) = \nabla \times \mathbf{A}(\mathbf{r},t) \tag{3.30a}$$

$$\mathbf{E}(\mathbf{r},t) = -\frac{\partial \mathbf{A}(\mathbf{r},t)}{\partial t} - \nabla\phi(\mathbf{r},t) \tag{3.30b}$$

where $\phi(\mathbf{r},t)$ is the scalar potential. In the absence of an external field, $\phi(\mathbf{r},t)$ is constant.

We can plug the two defining equations of the vector potential, Equations (3.30a) and (3.30b), into Equation (3.29d) (known as the Ampère-Maxwell law) to get

$$\begin{aligned} \nabla \times \nabla \times \mathbf{A}(\mathbf{r},t) &= \nabla\left(\nabla \cdot \mathbf{A}(\mathbf{r},t)\right) - \nabla^2 \mathbf{A}(\mathbf{r},t) \\ &= \frac{1}{c^2}\left(-\frac{\partial^2 \mathbf{A}(\mathbf{r},t)}{\partial t^2} - \frac{\partial \nabla\phi(\mathbf{r},t)}{\partial t}\right) \end{aligned} \tag{3.31}$$

where we have utilized the vector identity $\nabla \times \nabla \times \mathbf{v} = \nabla(\nabla \cdot \mathbf{v}) - \nabla^2 \mathbf{v}$. [2]

We can simplify Equation (3.31) by choosing a gauge [3] that sets

$$\nabla \cdot \mathbf{A}(\mathbf{r},t) = 0 \tag{3.32}$$

[2] These vector calculus identities need not be memorized, if one instead remembers that the ith component of $\nabla \times \mathbf{v}$ is $(\nabla \times \mathbf{v})_i = \varepsilon_{ijk}\partial_j v_k$, where ε_{ijk} is the Levy-Civita symbol, and the identity $\varepsilon_{ijk}\varepsilon_{ilm} = \delta_{jl}\delta_{km} - \delta_{jm}\delta_{kl}$, one can derive $(\nabla \times \nabla \times \mathbf{v})_i = \varepsilon_{ijk}\partial_j\varepsilon_{klm}\partial_l v_m = \partial_i\partial_j v_j - \partial_j^2 v_i = \partial_i(\nabla \cdot \mathbf{v}) - \nabla^2 v_i$. Repeated indices are understood to indicate summation over the repeated index, as in the Einstein summation convention.

[3] $\mathbf{A}$ is not completely determined from Equations (3.30a) and (3.30b) alone. We can change $\mathbf{A}(\mathbf{r},t)$ and $\phi(\mathbf{r},t)$ via a scalar function $\psi(\mathbf{r},t)$ (where ψ is differentiable in space and time) via $\mathbf{A} \mapsto \mathbf{A} + \nabla\psi$; $\phi \mapsto \phi - \frac{\partial\psi}{\partial t}$. One can show that this does not change the values of $\mathbf{B}(\mathbf{r},t)$ or $\mathbf{E}(\mathbf{r},t)$ in Equations (3.30a) and (3.30b). We refer to this choice of A and ϕ that still satisfies Equations (3.30a) and (3.30b) as *choosing a gauge*.

Equation (3.32) is called the transversality condition. Since ϕ is constant, $\partial_t \nabla\phi = 0$, so $\mathbf{A}(\mathbf{r},t)$ satisfies the wave equation,

$$\nabla^2 \mathbf{A}(\mathbf{r},t) - \frac{1}{c^2}\frac{\partial^2 \mathbf{A}(\mathbf{r},t)}{\partial t^2} = 0 \tag{3.33}$$

We now proceed by considering the field in a cube of length L and volume $V = L^3$, and then Fourier expanding $\mathbf{A}(\mathbf{r},t)$[4]:

$$\mathbf{A}(\mathbf{r},t) = \sum_{\mathbf{k}} \left(\frac{\hbar}{2\omega_{\mathbf{k}}\varepsilon_0}\right)^{1/2} \left(a'_k \mathbf{u}_{\mathbf{k}}(\mathbf{r}) e^{-i\omega_{\mathbf{k}}t} + a_k^{*'} \mathbf{u}^*_{\mathbf{k}}(\mathbf{r}) e^{+i\omega_{\mathbf{k}}t}\right) \tag{3.34}$$

These vectors $\mathbf{k}$ are a discrete set of vectors. The functions $\mathbf{u}_{\mathbf{k}}(\mathbf{r})$ satisfy the wave equation

$$\left(\nabla^2 + \frac{\omega_{\mathbf{k}}^2}{c^2}\right) \mathbf{u}_{\mathbf{k}}(\mathbf{r}) = 0 \tag{3.35}$$

as well as the transversality condition

$$\nabla \cdot \mathbf{u}_{\mathbf{k}}(\mathbf{r}) = 0 \tag{3.36}$$

Furthermore, $\mathbf{u}_{\mathbf{k}}(\mathbf{r})$ are a complete orthogonal set of functions:

$$\int_V \mathbf{u}^*_{\mathbf{k}}(\mathbf{r}) \cdot \mathbf{u}_{\mathbf{k}'}(\mathbf{r})\, d^3r = \frac{1}{V}\,\delta_{\mathbf{k}\mathbf{k}'} \tag{3.37}$$

With reflective boundary conditions, the functions $\mathbf{u}_{\mathbf{k}}(\mathbf{r})$ take the form

$$\mathbf{u}_{\mathbf{k}}(\mathbf{r}) = V^{-1/2} \sum_{\mu=\pm 1} c_{\mathbf{k}}^{(\mu)} \exp(i\mathbf{k}\cdot\mathbf{r})\, \hat{\mathbf{e}}_{\mathbf{k}}^{(\mu)} \tag{3.38}$$

where $\hat{\mathbf{e}}_{\mathbf{k}}^{(\mu)}$ is a unit polarization vector, and $\mu = \pm 1$ is a polarization index. We see from the transversality condition (Equation (3.36)) that, for all $\mathbf{k}$,

$$\mathbf{k} \cdot \hat{\mathbf{e}}_{\mathbf{k}}^{(\mu)} = 0 \tag{3.39}$$

We also see that the orthogonality condition (Equation (3.37)) becomes an orthonormality condition

$$\hat{\mathbf{e}}_{\mathbf{k}}^{(\mu)*} \cdot \hat{\mathbf{e}}_{\mathbf{k}}^{(\mu)} = \delta_{\mathbf{k}\mathbf{k}'} \tag{3.40}$$

Because of the reflective boundary conditions, the components of $\mathbf{k} = (k_x, k_y, k_z)$ will all be of

[4]The coefficients $a'_{\mathbf{k}}$ are chosen, along with these factors $\left(\frac{\hbar}{2\omega_{\mathbf{k}}\varepsilon_0 V}\right)^{1/2}$, to agree with the conventions in quantum mechanics, even though $\hbar$ plays no fundamental role in this discussion.

the form

$$k_x = \frac{\pi}{L} n_x, \quad k_y = \frac{\pi}{L} n_y, \quad k_z = \frac{\pi}{L} n_z, \qquad n_x, n_y, n_z \in \mathbb{Z} \tag{3.41}$$

We also see from Equation (3.35) that the magnitude $|\mathbf{k}|$ satisfies

$$|\mathbf{k}| = \frac{\omega_k}{c} \tag{3.42}$$

Thus, the permissible values of ω_k are

$$\omega_k = \frac{\pi c}{L} n_k = \frac{2\pi c}{\lambda_k}, \quad n_k \in \mathbb{Z}^+ \tag{3.43}$$

where the wavelength λ_k is

$$\lambda_k = 2L/n_k, \quad n_k \in \mathbb{Z}^+ \tag{3.44}$$

We can rewrite Equation (3.34) as

$$\mathbf{A}(\mathbf{r}, t) = \sum_{\mathbf{k}} \sum_{\mu=\pm 1} \left(\frac{\hbar}{2\omega_{\mathbf{k}} \varepsilon_0 V} \right)^{1/2} \left(a_{\mathbf{k}}^{(\mu)} \hat{\mathbf{e}}_{\mathbf{k}}^{(\mu)} e^{+i\mathbf{k}\cdot\mathbf{r} - i\omega_{\mathbf{k}} t} + a_{\mathbf{k}}^{(\mu)*} \hat{\mathbf{e}}_{\mathbf{k}}^{(\mu)*} e^{-i\mathbf{k}\cdot\mathbf{r} + i\omega_{\mathbf{k}} t} \right) \tag{3.45}$$

and plug Equation (3.45) into Equation (3.30a) and (3.30b) to obtain $\mathbf{E}(\mathbf{r}, t)$ and $\mathbf{B}(\mathbf{r}, t)$:

$$\mathbf{E}(\mathbf{r}, t) = +i \sum_{\mathbf{k}} \sum_{\mu=\pm 1} \left(\frac{\hbar \omega_{\mathbf{k}}}{2\varepsilon_0 V} \right)^{1/2} \left(a_{\mathbf{k}}^{(\mu)} \hat{\mathbf{e}}_{\mathbf{k}}^{(\mu)} e^{+i\mathbf{k}\cdot\mathbf{r} - i\omega_{\mathbf{k}} t} - a_{\mathbf{k}}^{(\mu)*} \hat{\mathbf{e}}_{\mathbf{k}}^{(\mu)*} e^{-i\mathbf{k}\cdot\mathbf{r} + i\omega_{\mathbf{k}} t} \right) \tag{3.46a}$$

$$\mathbf{B}(\mathbf{r}, t) = +i \sum_{\mathbf{k}} \sum_{\mu=\pm 1} \left(\frac{\hbar \omega_{\mathbf{k}}}{2c^2 \varepsilon_0 V} \right)^{1/2} \left(a_{\mathbf{k}}^{(\mu)} \hat{\mathbf{k}} \times \hat{\mathbf{e}}_{\mathbf{k}}^{(\mu)} e^{-i\omega_{\mathbf{k}} t} - a_{\mathbf{k}}^{(\mu)*} \hat{\mathbf{k}} \times \hat{\mathbf{e}}_{\mathbf{k}}^{(\mu)*} e^{+i\omega_{\mathbf{k}} t} \right) \tag{3.46b}$$

The Hamiltonian of the electromagnetic field is given by

$$\mathcal{H} = \frac{\varepsilon_0}{2} \int_V dV \, \left(|\mathbf{E}|^2 + c^2 |\mathbf{B}|^2 \right) \tag{3.47}$$

Using the orthonormality relation (3.40) (and the vector identity $(\mathbf{a} \times \mathbf{b}) \cdot (\mathbf{a} \times \mathbf{c}) = k^2 \mathbf{a} \cdot \mathbf{b} - (\mathbf{a} \cdot \mathbf{b})(\mathbf{a} \cdot \mathbf{b})$), we can evaluate the integrals and inner products in the Hamiltonian to obtain

$$\mathcal{H} = \frac{1}{2} \sum_{\mathbf{k}, \mu} \hbar \omega_{\mathbf{k}} \left(a_{\mathbf{k}}^{(\mu)} a_{\mathbf{k}}^{(\mu)*} + a_{\mathbf{k}}^{(\mu)*} a_{\mathbf{k}}^{(\mu)} \right) \tag{3.48}$$

At this point, we may impose commutation relations on the complex amplitudes

$$[a_{\mathbf{k}}^{(\mu)}, a_{\mathbf{k}'}^{(\mu)}] = 0, \quad [a_{\mathbf{k}}^{(\mu)*}, a_{\mathbf{k}'}^{(\mu)*}] = 0, \quad [a_{\mathbf{k}}^{(\mu)}, a_{\mathbf{k}'}^{(\mu)*}] = 1, \tag{3.49}$$

in agreement with the bosonic commutation relations of quantum mechanics[5], and obtain the Hamiltonian in a form recognizable as the Hamiltonian of a simple harmonic oscillator

$$\mathcal{H} = \sum_{\mathbf{k},\mu} \hbar\omega_{\mathbf{k}} \left(a_{\mathbf{k}}^{(\mu)*} a_{\mathbf{k}}^{(\mu)} + \frac{1}{2} \right) \tag{3.50}$$

3.3.2 Input-Output Theory

In this subsection, we obtain the equation of motion for the interaction of a single cavity mode with an external multi-mode electromagnetic field.

We follow the treatment in [65, pp.93-9, Ch.6.1] and [65, pp.127-31, Ch.7.1], which follows [66] and [67].[6] For consistency with these sources, we interchangeably use a^* and $a^\dagger$ to denote the complex conjugate of the complex amplitude/operator a. This is fine, since this thesis does not consider quantum mechanics.

We assume that the cavity Hamiltonian is described by $\mathcal{H}_\mathrm{S}$, and the external electromagnetic field comprises a bath, described by $\mathcal{H}_\mathrm{B}$. For this section, we do not describe $\mathcal{H}_\mathrm{S}$; we discuss it in more detail in Section 3.3.3. $\mathcal{H}_\mathrm{B}$ can be modelled as a collection of bosonic modes. Finally, the interaction between the system and the bath is given by a time-varying potential $V(t)$. Let the single cavity mode be given by a time-varying complex amplitude $a(t)$, and the multi-mode electromagnetic field have complex amplitudes b_j that correspond to mode j of frequency ω_j. Thus, the total Hamiltonian is

$$\mathcal{H}(t) = \mathcal{H}_\mathrm{S} + \mathcal{H}_\mathrm{B} + V(t) \tag{3.51}$$

For this discussion, we assume that the external electromagnetic field propagates in the x-direction, and we consider only one polarization axis. For simplicity, we look at the positive frequency components of the electromagnetic field given in Equation (3.46a):

$$E^{(+)}(x,t) = +i \sum_j \left(\frac{\hbar\omega_j}{2\varepsilon_0 V} \right)^{1/2} b_j e^{+ik_j x - i\omega_j t} \tag{3.52}$$

where b_j is the complex amplitude for mode j, and $k_j = \omega_j/c$. We assume that the modes of the external electromagnetic field exist in a narrow band about a very large center carrier frequency Ω. This is always valid in quantum optics [66, p.30]. We shall assume that all modes are centered around a carrier frequency Ω, which is the cavity resonance frequency, and $\Omega \gg 1\,\mathrm{Hz}$.

[5] In a true quantum mechanical treatment, we would also promote the complex amplitudes $a_{\mathbf{k}}^{(\mu)}$ and $a_{\mathbf{k}}^{(\mu)*}$ to operators $\hat{a}_{\mathbf{k}}^{(\mu)}$ and $\hat{a}_{\mathbf{k}}^{(\mu)\dagger}$ that act on a bosonic Hilbert space of Fock states. However, since this thesis does not consider quantum mechanics, we opt not to do this, and content ourselves with the commutation relations in Equation (3.49). In particular, for a complex amplitude, or operator a, we do not distinguish between the complex conjugate a^* and the "dagger" $a^\dagger$.

[6] *Caveat lector*: there are numerous sign errors and missing square roots in the formulae of [65, pp.127-31, Ch.7.1].

This assumption renders Equation (3.52) as

$$E^{(+)}(x,t) = +i\left(\frac{\hbar\Omega}{2\pi\varepsilon_0 Ac}\right)^{1/2}\sqrt{\Delta\omega_{\mathrm{FSR}}}\sum_j b_j e^{-i\omega_j(t-x/c)} \tag{3.53}$$

where A is a transverse area of the cavity. Recall that the free-spectral range frequency is

$$\Delta\omega_{\mathrm{FSR}} = \frac{\pi c}{L}, \tag{3.54}$$

where L is the length of the cavity. Note that the prefactor of the sum in Equation (3.53) has dimensions of newtons per coulomb (i.e., an electric field).

The Hamiltonian corresponding to the bath electromagnetic field (3.53), rewritten here, is

$$\mathcal{H}_{\mathrm{B}} = \sum_j \hbar\omega_j\left(b_j^\dagger b_j + \frac{1}{2}\right) \tag{3.55}$$

The interaction potential $V(t)$ exchanges photons between the cavity and the environment. Equivalently, we destroy a photon in the environment to create one in the cavity, and vice versa. This Hamiltonian is given by [65, p.95]

$$V(t) = \hbar\left(a^\dagger\Gamma(t)e^{i\Omega t} + a\Gamma(t)^\dagger e^{-i\Omega t}\right) \tag{3.56}$$

where

$$\Gamma(t) = \sum_j g_j b_j e^{-i\omega_j t} \tag{3.57}$$

We now take the continuum limit. We do this by following the approach in [68, Appendix B], by using the conversion

$$\left(\Delta\omega\sum_\omega\right) \to \left(\int d\omega\right) \tag{3.58}$$

This sets Equations (3.53) and (3.50) to

$$E^{(+)}(x,t) = +i\left(\frac{\hbar\Omega}{2\pi\varepsilon_0 Ac}\right)^{1/2}\frac{\sqrt{\Delta\omega_{\mathrm{FSR}}}}{\Delta\omega}\int_0^\infty d\omega\, b(\omega)e^{-i\omega(t-x/c)} \tag{3.59a}$$

$$\mathcal{H}_{\mathrm{B}} = \frac{1}{\Delta\omega}\int_0^\infty d\omega\,\hbar\omega\left(b^\dagger(\omega)b(\omega) + \frac{1}{2}\right) \tag{3.59b}$$

In the equations of Equations (3.59), $b(\omega)$ and $b^\dagger(\omega)$ have units of unity. To simplify the formulae of Equations (3.59), we scale $b(\omega)$, similarly to [68, Appendix B], via

$$b(\omega) \to \tilde{b}(\omega) = e^{i\xi}\sqrt{\frac{1}{\Delta\omega}}\,b(\omega) \tag{3.60}$$

The phase ξ does not change $\mathcal{H}_{\mathrm{B}}$ (3.59b), and multiplies $E^{(+)}(x,t)$ (3.59a) by a phase factor $e^{-i\xi}$. The choice of ξ does not affect the dynamics qualitatively. We choose $\xi = \pi$ in Equation (3.60) to remove the $+i$ factor in Equation (3.59a), and obtain

$$E^{(+)}(x,t) = \left(\frac{\hbar\Omega}{2\pi\varepsilon_0 Ac}\right)^{1/2} \sqrt{\frac{\Delta\omega_{\mathrm{FSR}}}{\Delta\omega}} \int_0^\infty d\omega\, \tilde{b}(\omega) e^{-i\omega(t-x/c)} \tag{3.61a}$$

$$\mathcal{H}_{\mathrm{B}} = \int_0^\infty d\omega\, \hbar\omega \left(\tilde{b}^\dagger(\omega)\tilde{b}(\omega) + \frac{1}{2}\right) \tag{3.61b}$$

We remark that the units of $\tilde{b}(\omega)$ in Equation (3.60) are $(2\pi \times \mathrm{Hz})^{-1/2}$. For the rest of this section, we suppress the tilde in the $\tilde{b}(\omega)$, and simply write $b(\omega)$ in the continuum limit.

In analogy to the positive-frequency electric field amplitude in Equation (3.61a), and following [65, Ch.7.1], we define a field $b(x,t)$ with complex amplitude

$$\begin{aligned} b(x,t) &= \frac{1}{\sqrt{2\pi}} \int_0^\infty d\omega\, b(\omega) e^{-i\omega(t-x/c)} \\ &= e^{-i\Omega(t-x/c)} \frac{1}{\sqrt{2\pi}} \int_{-\infty}^\infty d\omega\, b(\omega) e^{-i\omega(t-x/c)} \end{aligned} \tag{3.62}$$

where we used the change of variables $\omega \to \omega + \Omega$, and set the lower limit of integration from $-\Omega$ to $-\infty$, since $\Omega \gg 1$. $b(\omega)$ has units of $(2\pi \times \mathrm{Hz})^{-1/2}$, so this gives $b(x,t)$ units of $\sqrt{\mathrm{Hz}}$. The moment $n(x,t) = \left\langle b^\dagger(x,t) b(x,t) \right\rangle$ has units of Hz, and it can be interpreted as the probability per unit time to detect a photon at point x and at time t [65, p.128, Ch.7.1].

In considering the time dynamics of the modes a and $b(\omega)$, we note that since the cavity can have matter inside of it (e.g. this experiment's square membrane), the cavity mode a can have a time dependence $a(t)$ that reflects the motion of the matter. Similarly, the external electromagnetic field amplitudes $b(\omega)$ can have a time dependence $b(t,\omega)$ which does not simply arise from the harmonic oscillator Hamiltonian $\mathcal{H}_{\mathrm{B}}$. Thus, we treat the equations of motion in an interaction picture, by changing the bath operators $b(x,t)$ and $b^\dagger(x,t)$ to a rotating frame $b(x,t)e^{+i\Omega t}$ and $b^\dagger(x,t)e^{-i\Omega t}$. We can take $V(t)$ (Equation (3.56)) in the continuum limit, with the prescription given in Equation (3.60), to get

$$V(t) = +i\hbar \int_{-\infty}^\infty d\omega\, g(\omega) \left(a(t) b^\dagger(\omega) - a^\dagger(t) b(\omega)\right) \tag{3.63}$$

To obtain the dynamics of $a(t)$ and $b(t,\omega)$, we use the coupled Heisenberg equations of motion

$$\dot{a}(t) = \frac{1}{i\hbar}[a, \mathcal{H}_{\mathrm{S}} + V(t)] \tag{3.64a}$$

$$\dot{b}(t,\omega) = \frac{1}{i\hbar}[b(\omega), \mathcal{H}_{\mathrm{B}} + V(t)] \tag{3.64b}$$

We can either solve Equations (3.64) based on the initial values at time t_0 (i.e., the *input*), and solve for $t_0 < t$, or based on the final values at time t_1 (i.e., the *output*), and solve for $t < t_1$. With Equations (3.61b) and (3.63), Equation (3.64b) becomes

$$\dot{b}(t,\omega) = -i\omega b(\omega) + g(\omega)a \tag{3.65}$$

which has an input solution

$$b(t,\omega) = e^{-i\omega(t-t_0)}b_0(\omega) + g(\omega)\int_{t_0}^{t} dt'\, e^{-i\omega(t-t')}a(t') \tag{3.66}$$

where $t_0 < t$ and $b_0(\omega) = b(t_0,\omega)$. The output solution is

$$b(t,\omega) = e^{-i\omega(t-t_1)}b_1(\omega) - g(\omega)\int_{t}^{t_1} dt'\, e^{-i\omega(t-t')}a(t') \tag{3.67}$$

for $t < t_1$ and $b_1(\omega) = b(t_1,\omega)$.

Equation (3.64a), in terms of the input at t_0, is

$$\begin{aligned}\dot{a} &= \frac{1}{i\hbar}[a,\mathcal{H}_{\mathrm{S}}] - \int_{-\infty}^{\infty} d\omega\, g(\omega)b(t,\omega) \\ &= \frac{1}{i\hbar}[a,\mathcal{H}_{\mathrm{S}}] - \int_{-\infty}^{\infty} d\omega\, g(\omega)e^{-i\omega(t-t_0)}b_0(\omega) - \int_{-\infty}^{\infty} d\omega\, g(\omega)^2\int_{t_0}^{t} dt'\, e^{-i\omega(t-t')}a(t')\end{aligned} \tag{3.68}$$

We now assume, as in [67] and [65, p.130, Ch.7.1], that the bath spectrum $g(\omega)$ is flat in frequency over a wide range centered around $\omega = \Omega$ in the lab frame (or $\omega = 0$ in the rotating frame we chose). Thus, we set

$$g(\omega)^2 = \frac{\gamma}{2\pi} \tag{3.69}$$

We now use the equation

$$\int_{-\infty}^{\infty} d\omega\, e^{-i\omega(t-t')} = 2\pi\delta(t-t') \tag{3.70}$$

as well as[7]

$$\int_{t_0}^{t} dt'\, \delta(t-t')f(t') = \frac{1}{2}f(t) \tag{3.71}$$

In Equation (3.68), we simplify the third term by interchanging the ω and t' integrals and using

[7] We can derive this Dirac delta equation by considering a small time $\delta t > 0$, and using the Dirac delta equations $\int_{t_0-\delta t}^{t}\delta(t-t')f(t') = f(t)$ and $\int_{t_0+\delta t}^{t}\delta(t-t')f(t') = 0$. We take the arithmetic mean of these equations, and use $\lim_{\delta t\to 0^+}\int_{t_0-\delta t}^{t}(.) = \lim_{\delta t\to 0^+}\int_{t_0+\delta t}^{t}(.) = \int_{t_0}^{t}(.)$ to arrive at Equation (3.71).

Equations (3.70) and (3.71). This yields

$$\int_{-\infty}^{\infty} d\omega\, g(\omega)^2 \int_{t_0}^{t} dt'\, e^{-i\omega(t-t')} a(t') = \frac{\gamma}{2} a(t) \tag{3.72}$$

We define the second term of Equation (3.68) as an *input field* operator

$$a_{\text{in}}(t) = -\frac{1}{\sqrt{2\pi}} \int_{-\infty}^{\infty} d\omega\, e^{-i\omega(t-t_0)} b_0(\omega) \tag{3.73}$$

The minus sign is a phase convention that [65, p.130, Ch.7.1] follows, such that left-going fields are negative, and right-going fields are positive. $a_{\text{in}}(t)$ has units of $\sqrt{\text{Hz}}$, since $b_0(\omega)$ has units of $(2\pi \times \text{Hz})^{-1/2}$. From Equations (3.68), (3.72), (3.73), we finally arrive at the *input equation of motion*

$$\boxed{\dot{a}(t) = \frac{1}{i\hbar}[a, \mathcal{H}_{\text{S}}] + \sqrt{\gamma}\, a_{\text{in}}(t) - \frac{\gamma}{2} a(t)} \tag{3.74}$$

If we choose instead to solve Equation (3.64a) in terms of the *output* for $t < t_1$, we find

$$\dot{a} = \frac{1}{i\hbar}[a, \mathcal{H}_{\text{S}}] - \int_{-\infty}^{\infty} d\omega\, g(\omega) e^{-i\omega(t-t_1)} b_1(\omega) + \int_{-\infty}^{\infty} d\omega\, g(\omega)^2 \int_{t}^{t_1} dt'\, e^{-i\omega(t-t')} a(t') \tag{3.75}$$

When we define the *output field* operator

$$a_{\text{out}}(t) = +\frac{1}{\sqrt{2\pi}} \int_{-\infty}^{\infty} d\omega\, e^{-i\omega(t-t_1)} b_1(\omega) \tag{3.76}$$

we get, from Equation (3.75), the *output equation of motion*

$$\boxed{\dot{a}(t) = \frac{1}{i\hbar}[a, \mathcal{H}_{\text{S}}] - \sqrt{\gamma}\, a_{\text{out}}(t) + \frac{\gamma}{2} a(t)} \tag{3.77}$$

Lastly, we can obtain a *boundary condition* on the input and output fields $a_{\text{in}}(t)$ and $a_{\text{out}}(t)$ by subtracting Equations (3.74) and (3.77):

$$\boxed{a_{\text{in}}(t) + a_{\text{out}}(t) = \sqrt{\gamma}\, a(t)} \tag{3.78}$$

In closing this section, we remark that this theory was largely developed in the papers by Collett and Gardiner [66] and [67], in 1984 and 1985, respectively. For a more in depth discussion of input-output theory and stochastic mechods in quantum optics, the reader may consult the 2004 textbook by Gardiner and Zoller [69].

3.3.3 Cavity Equation of Motion via Input-Output Theory

In this section, we treat the Fabry-Pérot cavity with input-output theory and find the equation of motion for an optical cavity mode. We find essentially the same equation of motion as Equation (3.19) for the mechanical resonator.

We begin with the input-output theory formalism discussed in Section 3.3.2. Now, we assume that the cavity is coupled to a mechanical resonator, placed inside the cavity. We assume for now that the system Hamiltonian has a form

$$\mathcal{H}_{\mathrm{S}} = \mathcal{H}_{\mathrm{cavity}} + \mathcal{H}_{\mathrm{mechanics}} + V \tag{3.79}$$

where the cavity and mechanical oscillators have Hamiltonians (as motivated in Sections 3.2 and 3.3):

$$\mathcal{H}_{\mathrm{cavity}} = \sum_j \hbar\omega_j \left(a_j^\dagger a_j + \frac{1}{2}\right) \tag{3.80}$$

$$\mathcal{H}_{\mathrm{mechanics}} = \sum_j \hbar\omega_j \left(c_j^\dagger c_j + \frac{1}{2}\right) \tag{3.81}$$

and the potential $V = V(a_j, a_j^\dagger, c_j, c_j^\dagger)$ couples the mechanics and the cavity field. Here, we focus on one cavity mode $a_j = a$, and treat the cavity mode in zeroth order of the mechanical modes. Thus, we take

$$\mathcal{H}_{\mathrm{S}} \approx \mathcal{H}_{\mathrm{cavity}}|_{\text{single-mode}} = \hbar\omega_c \left(a^\dagger a + \frac{1}{2}\right) \tag{3.82}$$

and plug Equation (3.82) into Equation (3.74):

$$\begin{aligned} \dot{a}(t) &= \frac{1}{i\hbar}\left[a, \hbar\omega_c\left(a^\dagger a + \frac{1}{2}\right)\right] - \frac{\kappa}{2}\,a + \sqrt{\kappa_{\mathrm{in}}}\,a_{\mathrm{in}} \\ &= -\left(i\omega_c + \frac{\kappa}{2}\right) a + \sqrt{\kappa_{\mathrm{in}}}\,a_{\mathrm{in}} \end{aligned} \tag{3.83}$$

where we have taken κ as the total loss rate of the cavity, and κ_{in} as the input coupling rate of the cavity to an external electromagnetic field. a_{in} is the complex amplitude of the light incident on the cavity. We can immediately see that Equation (3.83) is nearly identical to Equation (3.19) for the mechanical resonator.

We typically supply a_{in} via a laser of some power P. These are related by

$$P = \hbar\omega_c \left\langle a_{\mathrm{in}}^\dagger a_{\mathrm{in}} \right\rangle \tag{3.84}$$

a_{in} has units of $\sqrt{\mathrm{photons/Hz}}$, so P has units of joules per second, as expected.

To solve the differential equation of motion (Equation (3.83)), we will assume that the input

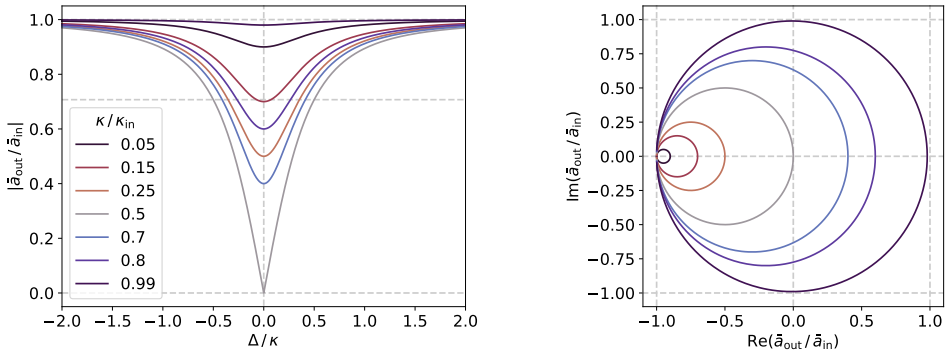

(a) (b)

Figure 3.1: A plot of the ratio of output to input field amplitude, as the laser detuning Δ is swept. This is plotted for multiple values of $\kappa_{\mathrm{in}}/\kappa$. Left: the absolute value of the amplitude. Right: the real and imaginary parts in the complex plane.

light field is monochromatic with frequency ω_{L}, applied by a laser. Hence, $a_{\mathrm{in}}(t)$ is given by

$$a_{\mathrm{in}}(t) = \bar{a}_{\mathrm{in}} e^{-i\omega_{\mathrm{L}} t} \tag{3.85}$$

We now seek solutions of the form

$$a(t) = \bar{a} e^{-i\omega t} \tag{3.86}$$

We plug Equations (3.85) and (3.86) into Equation (3.83):

$$-i\omega\bar{a} = -\left(i\omega_c + \frac{\kappa}{2}\right)\bar{a} + \sqrt{\kappa_{\mathrm{in}}}\, a_{\mathrm{in}} e^{-i(\omega_{\mathrm{L}}-\omega)t} \tag{3.87}$$

We take the time average $\langle . \rangle_T$,

$$\langle f(t) \rangle_T = \frac{1}{T}\int_0^T dt\, f(t) \tag{3.88}$$

of Equation (3.87), where T is sufficiently large (at least many periods of ω and ω_{L}). If $\omega \neq \omega_L$, then Equation (3.87) becomes

$$-i\omega\bar{a} = -\left(i\omega_c + \frac{\kappa}{2}\right)\bar{a} \tag{3.89}$$

which has only the trivial solution $\bar{a} = 0$. If $\omega = \omega_L$, i.e., the cavity field frequency is exactly resonant with the input laser frequency, we find that

$$\boxed{\bar{a} = \frac{\sqrt{\kappa_{\mathrm{in}}}}{\kappa/2 - i\Delta}\bar{a}_{\mathrm{in}}} \tag{3.90}$$

where the cavity-laser detuning is

$$\Delta = \omega_{\mathrm{L}} - \omega_c \tag{3.91}$$

We can apply the boundary condition of input-output theory (Equation (3.78)) to obtain the reflected field amplitude:

$$\boxed{\bar{a}_{\text{out}} = -\left(1 - \frac{\kappa_{\text{in}}}{\kappa/2 - i\Delta}\right)\bar{a}_{\text{in}}} \tag{3.92}$$

Figure 3.1 shows the ratio of a_{out} to a_{in}, plotted as the laser detuning Δ is swept, and for multiple values of $\kappa_{\text{in}}/\kappa$. For $\kappa_{\text{in}} < \kappa/2$, the laser is **undercoupled** to the cavity; for $\kappa_{\text{in}} > \kappa/2$, the laser is **overcoupled** to the cavity; when $\kappa_{\text{in}} = \kappa/2$, the laser is **critically coupled** to the cavity. In this last case, at $\Delta = 0$, the ratio of output to input light is exactly zero. In fact, the minimum in the absolute value is given by

$$\left|\frac{\bar{a}_{\text{out}}}{\bar{a}_{\text{in}}}(\Delta = 0)\right| = \left|1 - \frac{\kappa_{\text{in}}}{\kappa/2}\right| \tag{3.93}$$

so the depth grows/shrinks linearly in κ_{in}. As Figure 3.1a shows, the absolute value of the reflection does not distinguish between an underdamped or an overdamped cavity-laser coupling. To distinguish the two, we also look at the phase information, and plot the ratio in the complex plane (Figure 3.1b). The underdamped curve in the complex plane does not enclose the origin, as Δ is swept; the overdamped curve does enclose the origin.

3.3.4 Cavity Spectrum

In this section, we describe the cavity spectrum. Instead of using input-output theory (Section 3.3.2), it suffices to use classical electromagnetism in this discussion.

The cavity in the experiment has two mirrors of reflectivities $r_1 = .9998$ and $r_2 = .99997$.[70, pp. 111]

To see how much light gets reflected from the cavity, suppose that the incident light has frequency ω. We seek an expression $F(\omega)$ that measures how much light gets reflected. The incident electric field E_{inc} can be represented with an electric field

$$E_{\text{inc}} = E_0 e^{-i\omega t} \tag{3.94}$$

where E_0 is a complex electric field amplitude.

When light of frequency ω reflects back, we must consider whether it reflects off of mirror 1 or mirror 2. It has an amplitude r_1 to reflect off the first mirror, so this contribution to the reflection is

$$-r_1 E_0 e^{-i\omega t} \tag{3.95}$$

where the π-phase shift comes from the fact that the cavity mirror has an index of refraction $n > 1$. In addition, the light can transmit through mirror 1 with amplitude $t_1 = \sqrt{1 - r_1^2}$, then

reflect off of mirror 2 with amplitude r_2, and then transmit back through mirror 1. The time it takes for this to happen is $2L/c$, which is $1/\Delta\nu_{\text{fsr}}$, where $\Delta\nu_{\text{fsr}}$ is the free-spectral range of the cavity. Then this contribution is

$$t_1 r_2 t_1 E_0 e^{-i\omega(t+1/\Delta\nu_{\text{fsr}})} = (1-r_1^2) r_2 E_0 e^{-i\omega(t+1/\Delta\nu_{\text{fsr}})} \tag{3.96}$$

In general, we can find that the light bounces k times back and forth inside the cavity before it gets transmitted back in the direction that the incident light came from. The time it takes for this to happen is $k/\Delta\nu_{\text{fsr}}$. This contribution is then

$$t_1 r_2^k r_1^{k-1} t_1 E_0 e^{-i\omega(t+k/\Delta\nu_{\text{fsr}})} = (1-r_1^2) r_2^k r_1^{k-1} E_0 e^{-i\omega(t+k/\Delta\nu_{\text{fsr}})} \tag{3.97}$$

Superimposing the above contributions together, we find an expression for the total reflected field:

$$\begin{aligned} E_{\text{ref}} &= -r_1 E_0 e^{-i\omega t} + (1-r_1^2) E_0 e^{-i\omega t} \sum_{k=1}^{\infty} r_2^k r_1^{k-1} e^{-i\omega k/\Delta\nu_{\text{fsr}}} \\ &= r_1 E_0 e^{-i\omega t} + (1-r_1^2) r_2 E_0 e^{-i\omega(t+1/\Delta\nu_{\text{fsr}})} \sum_{k=0}^{\infty} (r_2 r_1)^k e^{-i\omega k/\Delta\nu_{\text{fsr}}} \end{aligned} \tag{3.98}$$

Recognizing the geometric series $\sum_{k=0}^{\infty} ar^k = a/(1-r)$, for $|r| < 1$, we get

$$E_{\text{ref}} = \frac{E_0 e^{-i\omega t}\left(-r_1 + r_2 e^{-i\omega/\Delta\nu_{\text{fsr}}}\right)}{1 - r_2 r_1 e^{-i\omega/\Delta\nu_{\text{fsr}}}} \tag{3.99}$$

We then get an expression $F(\omega) = E_{\text{ref}}/E_{\text{inc}}$:

$$F(\omega) = \frac{-r_1 + r_2 e^{-i\omega/\Delta\nu_{\text{fsr}}}}{1 - r_2 r_1 e^{-i\omega/\Delta\nu_{\text{fsr}}}} \tag{3.100}$$

Expression (3.100) is calculated and plotted in Figure 3.2. What we see is that $F(\omega)$ has a near constant amplitude of 1, except at $\omega = n\Delta\nu_{\text{fsr}}$, for $n \in \mathbb{Z}$. At these values, F dips to minima in amplitude, and the phase rolls sharply from positive to negative (and the phase wraps back from $-\pi$ to $+\pi$ for $\omega = (n+1/2)\Delta\nu_{\text{fsr}}$). This reflects our intuitive understanding of a Fabry-Pérot cavity, that when light shines into the cavity, all of the light gets reflected back, unless the frequency of the light is resonant with one of the cavity modes $n\Delta\nu_{\text{fsr}}$, for some $n \in \mathbb{Z}$.

3.4 Optomechanical Coupling

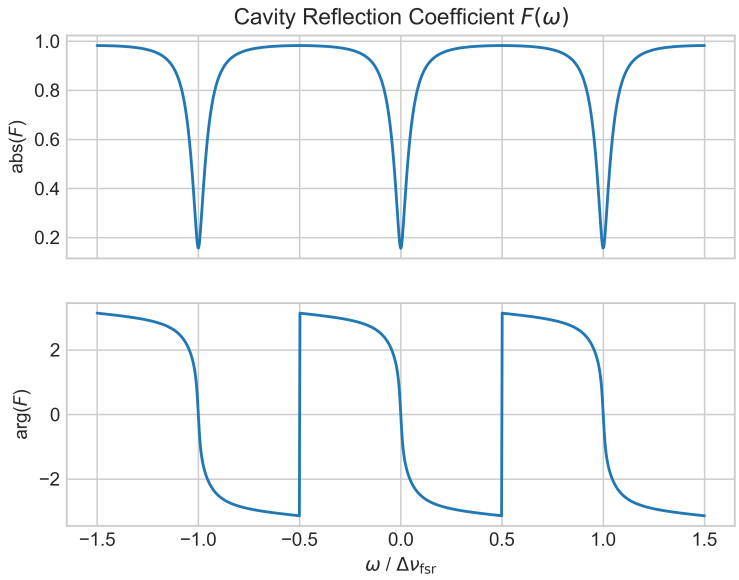

Figure 3.2: The cavity reflection coefficient, equation (3.100), as a function of the laser frequency, in units of the free spectral range $\Delta\nu_{\mathrm{fsr}}$. For this simulation, $r_1 = 0.8$, and $r_2 = 0.85$.

3.4.1 Effect of the Mechanics on the Optics

In Section 3.2 and Section 3.3, we discussed both the mechanical resonator and the Fabry-Pérot cavity as harmonic oscillators. A central concept of this thesis is the discussion of *coupled harmonic oscillators*. In this section, we describe the optomechanical interaction, which couples the mechanical and the electromagnetic (i.e., optical) oscillators.

We begin with the two equations of motion for the mechanical and optical oscillators (Equations (3.19) and (3.83), respectively), and we also consider the interaction of the mechanical motion with the optical field. In essence, we consider the assumed Hamiltonian of Equation (3.79), and obtain the interaction potential V. This discussion largely adapts Aspelmeyer's review [52] and Mason's thesis [33, Ch.1] on the optomechanical interaction.

Recall from Section 3.3.1 and Equation (3.43) that the frequency of the optical field, $\omega_c^{(n)}$, is

$$\omega_c^{(n)} = \frac{\pi c n}{L}, \quad n \in \mathbb{Z}^+ \tag{3.101}$$

where L is the separation between the cavity mirrors. Now, we assume that the cavity mirrors are movable. Without loss of generality to this theoretical discussion, suppose that only one mirror moves by a displacement x. This sets the cavity length to $L + x$, so the allowed frequencies take the form

$$\omega_c^{(n)}(x) = \frac{\pi c n}{L + x} = \omega_c^{(n)}(0) \frac{1}{1 + x/L} \tag{3.102}$$

Furthermore, if $x \ll L$, we can Taylor expand $\omega_c^{(n)}(x)$ as

$$\omega_c^{(n)}(x) \approx \omega_c^{(n)}(0) - Gx \tag{3.103}$$

where

$$G = \omega_c^{(n)}(0)/L \tag{3.104}$$

is the optical frequency shift per displacement x.

We can write the equation of motion for the cavity field amplitude a (Equation (3.83)) in terms of the shifted optical frequency (Equation (3.103)) as[8]

$$\dot{a} = -\left(\frac{\kappa}{2} + i(\omega_c - Gx)\right) a + \sqrt{\kappa_{\text{in}}}\, a_{\text{in}} \tag{3.105}$$

(having rewritten $\omega_c^{(n)}(0) \triangleq \omega_c$ for brevity of notation). Furthermore, we can take the expression for x in terms of the dimensionless mechanical amplitude c (Equation (3.14)) and plug it into Equation (3.105):

$$\begin{aligned} \dot{a} &= -\left(\frac{\kappa}{2} + i\left(\omega_c - Gx_{\text{ZPF}}(c + c^\dagger)\right)\right) a + \sqrt{\kappa_{\text{in}}}\, a_{\text{in}} \\ &= -\left(\frac{\kappa}{2} + i\left(\omega_c - g_0(c + c^\dagger)\right)\right) a + \sqrt{\kappa_{\text{in}}}\, a_{\text{in}} \end{aligned} \tag{3.106}$$

where we have defined the optomechanical coupling strength per single photon

$$g_0 = Gx_{\text{ZPF}} \tag{3.107}$$

g_0 is often simply referred to as the optomechanical coupling constant.

3.4.2 Effect of the Optics on the Mechanics

In this section, we describe the mechanical force that the light exerts on a mirror of the optical cavity, to cause a displacement x of the mirror. This force is known as the radiation pressure force. We then write down an equation of motion for the mechanical amplitude c with this force.

Recall from quantum mechanics that a photon that possesses frequency ω_c has energy $E = \hbar\omega_c$ and momentum $p = E/c = \hbar k_c$, where $k_c = \omega_c/c$ is the wavenumber. If the photon collides with the mirror and bounces in the opposite direction in a perfectly elastic collision, the momentum is now $-\hbar k_c$. The momentum imparted to the photon is $-2\hbar k_c$. By conservation of

[8] Replacing ω_c by $\omega_c(x)$ in Equation (3.105) amounts to a Born-Oppenheimer approximation [71] [72, p.369, Ch.10]. In quantum chemistry, this assumes that because atomic nuclei are much heavier than electrons, atomic nuclei can be treated as stationary relative to electrons, so their wavefunctions can be treated separately. Analogously, in this system, the cavity wavelength $\omega_c(x)$ is much larger than the mechanical mode wavelengths ω_n, so the mirror position $x(t)$ changes much more slowly than $a(t)$.

momentum, the momentum imparted to the mirror is

$$\Delta P_{\text{mirror, single-photon}} = +2\hbar k_c \tag{3.108}$$

Recall also that the change in momentum per change in time is the force:

$$F = \frac{\Delta P}{\Delta t} \tag{3.109}$$

The round-trip time for a single photon in the cavity is

$$\Delta t = 2L/c \tag{3.110}$$

where c in Thus, the force imparted on the mirror by one photon is

$$\begin{aligned} F_{\text{radiation, single-photon}} &= \hbar c k_c / L \\ &= \hbar c(\omega_c/c)/L \\ &= \hbar\omega_c/L \\ &= \hbar G \end{aligned} \tag{3.111}$$

where we used Equation (3.104) in the last line of Equation (3.111).

The cavity we consider in this experiment contains many orders of magnitude more than one photon, so to obtain the total radiation pressure force, we simply multiply Equation (3.111) by the average number of photons $n_c = \langle a^\dagger a \rangle$. Since these equations of motion are being treated in the classical regime, it suffices to take $n_c = |a|^2$, so the total radiation pressure force on the cavity mirror is

$$F_{\text{rad}} = \hbar G \, |a|^2 \tag{3.112}$$

For the mechanical equation of motion, we plug Equation (3.112) into Equation (3.18):

$$c_{\text{in}} = +ig_0 \, |a|^2 + \tilde{c}_{\text{in}} \tag{3.113}$$

where $\tilde{c}_{\text{in}}$ is any additional force on the mirror. We simply use $\tilde{c}_{\text{in}} = c_{\text{in}}$ to denote this additional force:

$$\dot{c} = -\left(i\omega_m + \frac{\gamma}{2}\right) c + ig_0 \, |a|^2 + c_{\text{in}} \tag{3.114}$$

3.4.3 Optomechanical Equations of Motion: An Alternate Derivation from Input-Output Theory

In Sections 3.4.1 and 3.4.2, we obtained Equations (3.106) and (3.114) for the mechanical and optical fields c and a. We record them here:

$$\dot{a} = -\left(\frac{\kappa}{2} + i\omega_c\right) a + ig_0(c + c^\dagger)a + \sqrt{\kappa_{\text{in}}}\, a_{\text{in}} \tag{3.115a}$$

$$\dot{c} = -\left(\frac{\gamma}{2} + i\omega_m\right) c + ig_0 \left|a\right|^2 + c_{\text{in}} \tag{3.115b}$$

An alternative, quicker derivation of Equations (3.115) can be found by using the discussion of the radiation pressure force in Section 3.4.2 and applying it directly to input-output theory (Section 3.3.2). Indeed, we can take the optical Hamiltonian (Equation (3.82)) and expand ω_c in terms of the membrane mirror shift x via Equation (3.103):

$$\begin{aligned} H_{\text{optical}}(x) &= \hbar\omega_c(x)(a^\dagger a + 1/2) \\ &\approx \hbar(\omega_c(x=0) - Gx)(a^\dagger a + 1/2) \\ &= H_{\text{optical}}(x=0) - \hbar G x(a^\dagger a + 1/2) \end{aligned} \tag{3.116}$$

The second term in Equation (3.116) is the potential associated with the radiation pressure force

$$\begin{aligned} V_{\text{rad}} &= -\hbar G x(\left|a\right|^2 + 1/2) \\ &= -\hbar g_0(c + c^\dagger)(\left|a\right|^2 + 1/2) \end{aligned} \tag{3.117}$$

Indeed,

$$F_{\text{rad}} = -\frac{dV_{\text{rad}}}{dx} = \hbar G \left|a\right|^2, \tag{3.118}$$

in agreement with Equation (3.112) Now, plug Equation (3.117) into Equation (3.79), and turn the crank of input-output theory for c:

$$\begin{aligned} \dot{c} &= \frac{1}{i\hbar}[c, \mathcal{H}_{\text{mechanical}} + V_{\text{rad}}] - \frac{\gamma}{2}c + c_{\text{in}} \\ &= -i\omega_m c + ig_0 \left|a\right|^2 - \frac{\gamma}{2}c + c_{\text{in}}, \end{aligned} \tag{3.119}$$

which agrees with Equation (3.115b). Similarly, for a,

$$\begin{aligned} \dot{a} &= \frac{1}{i\hbar}[a, \mathcal{H}_{\text{optical}} + V_{\text{rad}}] - \frac{\kappa}{2}a + \sqrt{\kappa_{\text{in}}}\, a_{\text{in}} \\ &= -i\omega_c a + ig_0(c + c^\dagger)a - \frac{\kappa}{2}a + \sqrt{\kappa_{\text{in}}}\, a_{\text{in}}, \end{aligned} \tag{3.120}$$

in agreement with Equation (3.115a).

Qualitatively, another way to understand the physical light-matter coupling is to consider laser beatnotes. The laser at frequency ω_{L} sends light into the cavity. Then the motion of the mechanical mode at frequency ω_m produces motional sidebands at frequencies near $\omega_L \pm \omega_m$. These sidebands then beat with the laser tone, and this produces an intensity beatnote near ω_m. The magnitude of this beatnote is influenced by the cavity susceptibility at the motional sideband frequency. This is a spring, with some (complex) spring constant, in that the beatnote produces oscillatory motion at frequency ω_m, which produces an oscillatory force at frequency ω_m.

3.4.4 Linearizing the Optomechanical E.O.M.'s

Frequently, we linearize the equations of motion such that they do not contain products of a or c. This makes the equations of motion easy to solve with Fourier analysis. We begin with a driving laser of frequency ω_{L}:

$$a_{\mathrm{in}}(t) = \bar{a}_{\mathrm{in}} e^{-i\omega_{\mathrm{L}} t} \tag{3.121}$$

Without taking the optomechanical interaction into account, the cavity field is $a(t) = \bar{a}e^{-i\omega_L t}$, where $\bar{a}$ is given by Equation (3.90). Now, we suppose that the optomechanical interaction places small fluctiuations onto $\bar{a}$:

$$\bar{a} \to \bar{a} + d(t) \tag{3.122}$$

Thus,

$$a(t) = (\bar{a} + d(t))e^{-i\omega_{\mathrm{L}} t} \tag{3.123}$$

We assume that the fluctuations $d(t)$ are of the same order as the mechanical mode amplitude c. Thus, we can use perturbation theory to analyze the motion in orders of $d(t)$. Without loss of generality, set the origin of the x-axis such that $c(t)$ has a mean fluctuation of $\bar{c} = 0$.

We now plug Equation (3.123) into Equation (3.115a):

$$\dot{a} = -\left(\frac{\kappa}{2} + i\omega_c\right) a + ig_0(c + c^\dagger)a + \sqrt{\kappa_{\mathrm{in}}}\, a_{\mathrm{in}} \tag{3.124}$$

which becomes

$$-i\omega_{\mathrm{L}}(\bar{a} + d(t)) + \dot{d}(t) = -\left(\frac{\kappa}{2} + i\omega_c\right)(\bar{a} + d(t)) + ig_0(c + c^\dagger)(\bar{a} + d(t)) + \sqrt{\kappa_{\mathrm{in}}}\, a_{\mathrm{in}} \tag{3.125}$$

Since c and $d(t)$ are assumed to be of the same order, we see a 0th-order and a 1st-order equation

in $d(t)$ and c from Equation (3.125):

$$(0): \qquad -i\omega_{\mathrm{L}}\bar{a} = -\left(\frac{\kappa}{2} + i\omega_c\right)\bar{a} + \sqrt{\kappa_{\mathrm{in}}}\, a_{\mathrm{in}} \tag{3.126}$$

$$(1): \qquad -i\omega_{\mathrm{L}} d(t) + \dot{d}(t) = -\left(\frac{\kappa}{2} + i\omega_c\right) d(t) + ig_0\bar{a}(c + c^\dagger) \tag{3.127}$$

Equation (3.126) is just Equation (3.83), with the same solution (Equation (3.90)). Write

$$\Delta = \omega_L - \omega_c \tag{3.128}$$

$$\alpha = \bar{a}g_0 \tag{3.129}$$

Then Equation (3.127) becomes

$$\dot{d}(t) = -\left(\frac{\kappa}{2} - i\Delta\right) d(t) + i\alpha(c + c^\dagger) \tag{3.130}$$

We remark that since $\bar{a} = \sqrt{n_c}$, the optomechanical coupling strength α can be arbitrarily enhanced by driving the cavity with higher laser power (i.e., more photons). Often, α is written as g [52, p.1394].

We may also plug Equation (3.123) into the equation of motion for $c(t)$ (Equation (3.115b)):

$$\begin{aligned} \dot{c} &= -\left(\frac{\gamma}{2} + i\omega_m\right) c + ig_0\Big(|\bar{a}|^2 + \bar{a}d^\dagger(t) + \bar{a}^\dagger d(t) + |d(t)|^2\Big) + c_{\mathrm{in}} \\ &\approx -\left(\frac{\gamma}{2} + i\omega_m\right) c + ig_0\Big(\bar{a}d^\dagger(t) + \bar{a}^\dagger d(t)\Big) + c_{\mathrm{in}} \end{aligned} \tag{3.131}$$

where we drop the $ig_0 |\bar{a}|^2$ term, since it just adds a constant frequency offset to $c(t)$, and we also drop the $ig_0 |d(t)|^2$ term, since we are only considering terms that are 0th or 1st order in $d(t)$.

Thus, we have a set of equations of motion that are linear in $d(t)$:

$$\dot{d}(t) = -\left(\frac{\kappa}{2} - i\Delta\right) d(t) + i\alpha(c + c^\dagger) \tag{3.132a}$$

$$\dot{c}(t) = -\left(\frac{\gamma}{2} + i\omega_m\right) c(t) + i\alpha d^\dagger(t) + i\alpha^* d(t) + c_{\mathrm{in}} \tag{3.132b}$$

3.4.5 Optomechanical Spring: Solution to the Linearized E.O.M.'s

Equations (3.132) are now very simple to solve with the Fourier transform . The Fourier transforms of Equations (3.132), per the definition in Equation (3.4), are

$$-i\omega d[\omega] = -\left(\frac{\kappa}{2} - i\Delta\right) d[\omega] + i\alpha(c[\omega] + c^\dagger[\omega]) \tag{3.133a}$$

$$-i\omega c[\omega] = -\left(\frac{\gamma}{2} + i\omega_m\right) c[\omega] + i\alpha d^\dagger[\omega] + i\alpha^* d[\omega] + c_{\text{in}}[\omega] \tag{3.133b}$$

With simple algebra, these can be rewritten as

$$\left[\frac{\kappa}{2} - i(\omega + \Delta)\right] d[\omega] = i\alpha(c[\omega] + c^\dagger[\omega]) \tag{3.134a}$$

$$\left[\frac{\gamma}{2} - i(\omega - \omega_m)\right] c[\omega] = i\alpha d^\dagger[\omega] + i\alpha^* d[\omega] + c_{\text{in}}[\omega] \tag{3.134b}$$

We define the optical and mechanical susceptibilities

$$\chi_c[\omega] = \frac{1}{\kappa/2 - i(\omega + \Delta)} \tag{3.135a}$$

$$\chi_m[\omega] = \frac{1}{\gamma/2 - i(\omega - \omega_m)} \tag{3.135b}$$

In fact, $\chi_m[\omega]$ (Equation (3.135b)) and $\chi_x[\omega]$ (Equation (3.10)) are related by

$$\chi_m[\omega] = -2im\omega_m\chi_x[\omega] \tag{3.136}$$

The susceptibilities (Equations (3.135)) recast Equations (3.134) as

$$d[\omega] = i\alpha\chi_c[\omega](c[\omega] + c^\dagger[\omega]) \tag{3.137a}$$

$$\chi_m[\omega]^{-1}c[\omega] = i\alpha d^\dagger[\omega] + i\alpha^* d[\omega] + c_{\text{in}}[\omega] \tag{3.137b}$$

We remark that Equation (3.137a) is a direct consequence of the initial assumption that the mechanical fluctuations $c(t)$ and the optical fluctuations $d(t)$ are on the same order. Per Equation (3.14),

$$d[\omega] = +i\sqrt{n_c}\, G\chi_c[\omega]\, x[\omega] \tag{3.138}$$

so $d[\omega]$ is indeed proportional to $x[\omega]$.

In Equations 3.137, because we are measuring mechanical motion of the mechanical resonator, we want to solve for $c[\omega]$ without involving $d[\omega]$ or $d^\dagger[\omega]$. Equation (3.137a) already gives $d[\omega]$ in terms of $c[\omega]$ and $c^\dagger[\omega]$. However, as noted by Equations A.3 and A.2 in Appendix A, we solve

for $d^\dagger[\omega]$ by first taking the complex conjugate of Equation (3.132a):

$$\dot{d}^\dagger(t) = -\left(\frac{\kappa}{2} + i\Delta\right) d(t) - i\alpha^*(c + c^\dagger) \tag{3.139}$$

Now we Fourier transform Equation (3.139):

$$-i\omega d^\dagger[\omega] = -\left(\frac{\kappa}{2} + i\Delta\right) d^\dagger[\omega] - i\alpha^*(c[\omega] + c^\dagger[\omega]), \tag{3.140}$$

whence

$$\begin{aligned} d^\dagger[\omega] &= -i\alpha^* \left(\frac{\kappa}{2} + i(-\omega + \Delta)\right)^{-1} (c[\omega] + c^\dagger[\omega]) \\ &= -i\alpha^* \chi_c^*[-\omega](c[\omega] + c^\dagger[\omega]) \end{aligned} \tag{3.141}$$

Substitute Equations (3.137a) and (3.141) into Equation (3.137b):

$$\chi_m[\omega]^{-1} c[\omega] = i\alpha\Big(- i\alpha^* \chi_c^*[-\omega](c[\omega] + c^\dagger[\omega])\Big) + i\alpha^*\Big(+ i\alpha\chi_c[\omega](c[\omega] + c^\dagger[\omega])\Big) + c_{\text{in}}[\omega] \tag{3.142}$$

In Appendix A, we argued that we can drop the counter-rotating $c^\dagger[\omega]$ terms, since we are in the high-Q limit. Thus, we drop them in Equation (3.142):

$$\chi_m[\omega]^{-1} c[\omega] = |\alpha|^2 \Big(\chi_c^*[-\omega] - \chi_c[\omega]\Big) c[\omega] + c_{\text{in}}[\omega] \tag{3.143}$$

Define the optomechanical self-energy as

$$\Sigma[\omega] = -i\,|\alpha|^2 \Big(\chi_c[\omega] - \chi_c^*[-\omega]\Big) \tag{3.144}$$

and write Equation (3.143) as

$$\Big(\chi_m[\omega]^{-1} + i\Sigma[\omega]\Big) c[\omega] = c_{\text{in}}[\omega] \tag{3.145}$$

In analogy with Equation (3.22), we can define a modified mechanical susceptibility as

$$\begin{aligned} \tilde{\chi}_m[\omega] &= \frac{1}{\gamma/2 - i(\omega - \omega_m) + i\Sigma[\omega]} \\ &= \frac{1}{(\gamma - 2\,\text{Im}\{\Sigma[\omega]\})/2 - i(\omega - \omega_m - \text{Re}\{\Sigma[\omega]\})} \end{aligned} \tag{3.146}$$

Thus, we finally arrive at the core phenomena of optomechanical coupling: the optical spring

and damping:

$$\delta\omega_m = +\mathrm{Re}\big\{\Sigma[\omega]\big\} \tag{3.147a}$$

$$\delta\gamma_m = -2\,\mathrm{Im}\big\{\Sigma[\omega]\big\} \tag{3.147b}$$

That is, the optomechanical interaction modifies the mechanical mode frequency and damping, via the complex spring formed by the light-matter coupling.

We move back to the time domain by noting that the mechanical linewidth γ_m is much smaller than the cavity linewidth κ. $\Sigma[\omega]$ is written in terms of the cavity susceptibility, so it can only vary significantly for a range of ω that is of order κ. Thus, $\Sigma[\omega] \approx \Sigma[\omega_m]$, and so

$$\delta\omega_m = +\mathrm{Re}\big\{\Sigma[\omega_m]\big\} \tag{3.148a}$$

$$\delta\gamma_m = -2\,\mathrm{Im}\big\{\Sigma[\omega_m]\big\} \tag{3.148b}$$

We summarize this section, and leave the results in a convenient closed form, in terms of the applied laser power P and detuning from the cavity mode Δ.[9] Recall from Equation (3.129) that

$$\alpha = \bar{a} g_0$$

Recall also Equation (3.90):

$$\bar{a} = \sqrt{\kappa_{\mathrm{in}}}\,\frac{1}{\kappa/2 - i\Delta}\bar{a}_{\mathrm{in}},$$

which we use here, just as with the nonmechanically coupled cavity (Section 3.3), since it is the solution of Equation (3.126), which is 0th order in $d(t)$. Then recall Equation (3.84):

$$|a_{\mathrm{in}}| = \sqrt{\frac{P}{\hbar\omega_c}}$$

Plug these into Equations (3.148) and (3.144) to get

$$\delta\omega_m(P,\Delta) = g_0^2\kappa_{\mathrm{in}}\,\frac{1}{(\kappa/2)^2+\Delta^2}\,\frac{P}{\hbar\omega_L}\left\{\frac{\Delta+\omega_m}{(\kappa/2)^2+(\Delta+\omega_m)^2} + \frac{\Delta-\omega_m}{(\kappa/2)^2+(\Delta-\omega_m)^2}\right\} \tag{3.149a}$$

$$\delta\gamma_m(P,\Delta) = g_0^2\kappa_{\mathrm{in}}\,\frac{1}{(\kappa/2)^2+\Delta^2}\,\frac{P}{\hbar\omega_L}\left\{\frac{\kappa}{(\kappa/2)^2+(\Delta+\omega_m)^2} - \frac{\kappa}{(\kappa/2)^2+(\Delta-\omega_m)^2}\right\} \tag{3.149b}$$

Equations 3.149 is plotted in Figure 3.3, for various values of ω_m/κ. We see two regimes:

[9] The reader may find this form useful if they wish to fit measured optical spectra to obtain optomechanical coupling parameters.

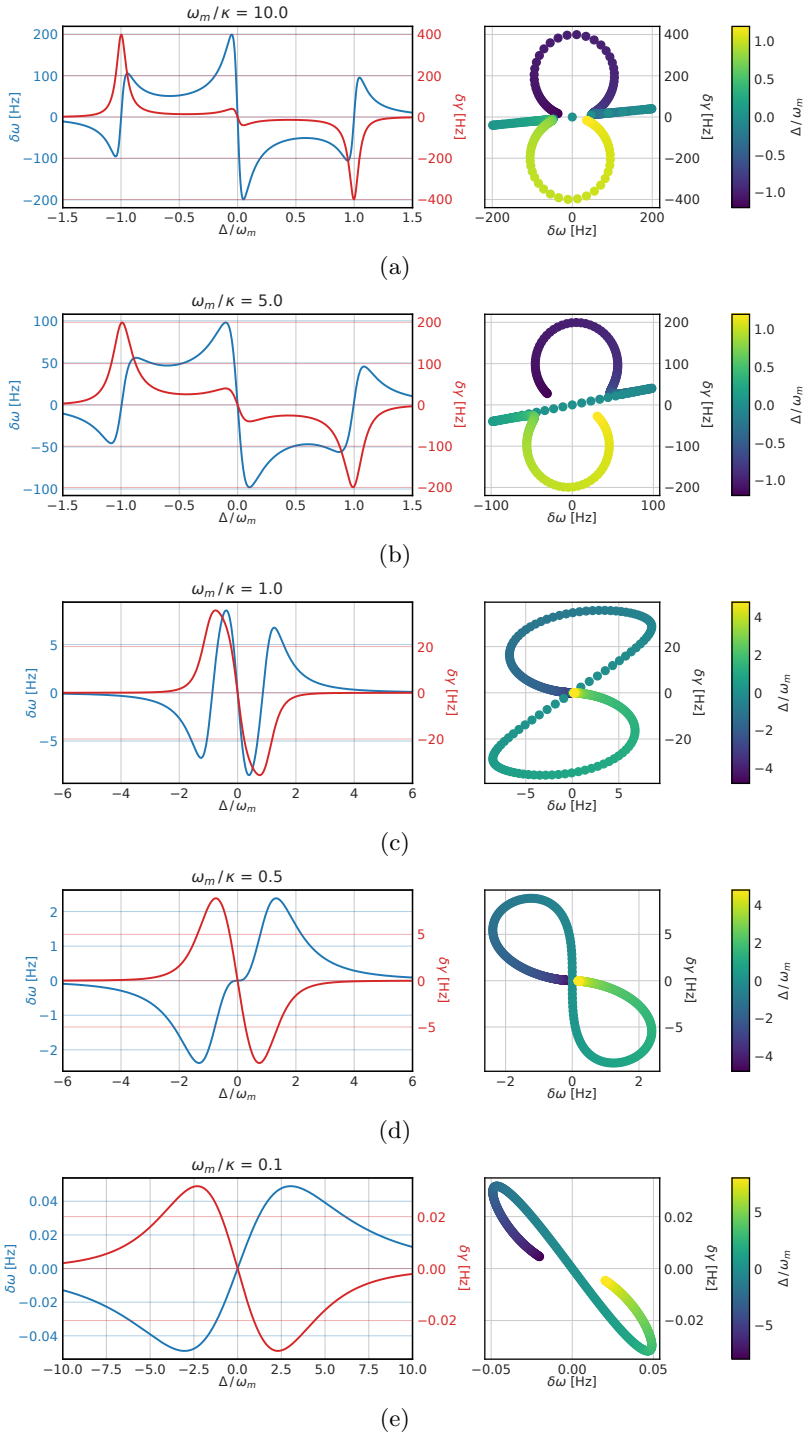

Figure 3.3: The optomechanical interaction plotted in the resolved sideband and the unresolved sideband regimes. The left-hand sides show the optomechanical frequency and damping shifts versus the swept laser detuning Δ, and the right-hand sides show these shifts in the complex plane, defined by the frequency and damping shifts. In each plot, $\omega_m = 1\,\mathrm{kHz}$, $\sqrt{\kappa_{\mathrm{in}}}\,|a_{\mathrm{in}}| = 100\,\mathrm{kHz}$, $g_0 = 1\,\mathrm{Hz}$.

the resolved sideband regime, for which $\omega_m \gg \kappa$; and the unresolved sideband regime, for which $\omega_m \ll \kappa$ [52, p.1413]. Figure 3.3 progresses through these regimes, from resolved to unresolved.[10]

In the resolved sideband regime, the mechanical linewidth changes by the maximum amount at $\Delta = \pm\omega_m$; it is maximally damped at $\Delta = -\omega_m$, and maximally antidamped at $\Delta = +\omega_m$. The mechanical frequency changes by the most near $\Delta = 0$, or near $\Delta \approx \pm\Delta$. However, at $\Delta = \pm\omega_m$, the frequency change $\delta\omega$ crosses zero.

In the unresolved sideband regime, the optomechanical shift is simpler; in the vicinity of $\Delta \approx \pm\frac{\kappa}{/2\sqrt{3}}$, the mechanical frequency shifts by a maximal amount, and the damping shift is less than the frequency shift by a factor of ω_m/κ. This can be understood as follows: in the resolved sideband regime, there are three "wings" for the optomechanical frequency shift, and one peak and one antipeak in the damping. As ω_m/κ decreases, the damping peak and antipeak move closer to $\Delta = 0$, and destructively interfere when they approach $\Delta = 0$. The "wings" of the optomechanical frequency shift destructively interfere as ω_m/κ decreases, so that they become only one "wing."

We should remark on the complex plane $\mathbb{C}$ spanned by the real and imaginary parts of the optomechanical shift in both the resolved ($\omega_m \gg \kappa$) and unresolved ($\omega_m \ll \kappa$) regimes. In the resolved sideband regime, sweeping Δ in a range that includes $\Delta = \pm\omega_m$ will sweep all four quadrants of the complex plane, as seen in Figure 3.3. Since P simply scales $\delta\omega$ and $\delta\gamma$ linearly, tuning Δ and P will span essentially all of $\mathbb{C}$. However, in the unresolved sideband regime, sweeping Δ will only include the upper left and lower right quadrants of the complex plane, so in the unresolved sideband regime, the optomechanical shift does not span the whole complex plane. In the asymptotic limit of $\omega/\kappa \to 0$, the optomechanical shift is only on the real line.

3.5 Two-Mode Optomechanics

3.5.1 Nearly Degenerate Two-Mode Optomechanical Coupling

In this section, we use the optomechanical interaction introduced in Section 3.4 to couple two mechanical modes. This mechanical-mode-coupling is a key phenomenon for this thesis, as we find exceptional points in this system by tuning the mechanical mode frequencies and dampings to an exceptional point degeneracy.

We develop the theory of two-mechanical-mode coupling (herein simply called "two-mode coupling") from the same physics as discussed in Section 3.4. Similar to Equation (3.79), the

[10] In practice, for this thesis, an optomechanical system can be considered in the resolved sideband regime if ω_m is merely greater than κ by a factor of 2 or so. This is sufficient to realize an optomechanical span similar to Figure 3.3a. Similarly, it is considered to be in the unresolved sideband regime if $\omega_m < \kappa$.

total Hamiltonian with two mechanical modes, with annihilation operators c_1 and c_2, is

$$\mathcal{H} = \hbar\omega_c \left(a^\dagger a + \frac{1}{2}\right) + \sum_{j=1}^{2} \hbar\omega_j \left(c_j^\dagger c_j + \frac{1}{2}\right) + V_{\mathrm{rad}} \tag{3.150}$$

Each mechanical mode c_1 and c_2 is coupled to the same optical mode a. Thus, the radiation-pressure potential V_{rad} is given by linear superposition of the two radiation-pressure potentials for c_1 and c_2 (c.f. Equation (3.117)):

$$V_{\mathrm{rad}} = -\sum_{j=1}^{2} \hbar g_j \left(a^\dagger a + \frac{1}{2}\right)\left(c_j + c_j^\dagger\right) \tag{3.151}$$

When we follow input-output theory, as in Section 3.4.3, we obtain the equations of motion:

$$\dot{a} = -\left(\frac{\kappa}{2} + i\omega_c\right) a + \sum_{j=1}^{2} i g_j (c_j + c_j^\dagger) a + \sqrt{\kappa_{\mathrm{in}}}\, a_{\mathrm{in}} \tag{3.152a}$$

$$\dot{c}_1 = -\left(\frac{\gamma_1}{2} + i\omega_1\right) c_1 + i g_1 \left|a\right|^2 + c_{\mathrm{in},1} \tag{3.152b}$$

$$\dot{c}_2 = -\left(\frac{\gamma_2}{2} + i\omega_2\right) c_2 + i g_2 \left|a\right|^2 + c_{\mathrm{in},2} \tag{3.152c}$$

By again invoking an argument of linear superposition, we can linearize Equations (3.152), following the prescription in Section 3.4.4 to write the linearized equations of motion:

$$\dot{d}(t) = -\left(\frac{\kappa}{2} - i\Delta\right) d(t) + \sum_{j=1}^{2} i\alpha_j (c_j + c_j^\dagger) \tag{3.153a}$$

$$\dot{c}_1(t) = -\left(\frac{\gamma_1}{2} + i\omega_1\right) c_1(t) + i\alpha_1 d^\dagger(t) + i\alpha_1^* d(t) + c_{\mathrm{in},1} \tag{3.153b}$$

$$\dot{c}_2(t) = -\left(\frac{\gamma_2}{2} + i\omega_2\right) c_2(t) + i\alpha_2 d^\dagger(t) + i\alpha_2^* d(t) + c_{\mathrm{in},2} \tag{3.153c}$$

where

$$a_{\mathrm{in}}(t) = \bar{a}_{\mathrm{in}} e^{-i\omega_{\mathrm{L}} t} \tag{3.154}$$

$$a(t) = (\bar{a} + d(t)) e^{-i\omega_{\mathrm{L}} t} \tag{3.155}$$

$$\alpha_j = \bar{a} g_j, \quad j = 1, 2 \tag{3.156}$$

In the absence of any optical field in Equations (3.153) (i.e., $d(t) = 0$), then Equations (3.153) become a compact matrix equation:

$$\dot{C}(t) = \begin{pmatrix} -(\gamma_1/2 + i\omega_1) & 0 \\ 0 & -(\gamma_2/2 + i\omega_2) \end{pmatrix} C(t) + C_{\mathrm{in}}(t) \tag{3.157}$$

where

$$C(t) = (c_1(t), c_2(t))^T \tag{3.158a}$$

$$C_{\text{in}}(t) = (c_{\text{in},1}(t), c_{\text{in},2}(t))^T \tag{3.158b}$$

The solution to Equation (3.157), in the frequency domain, is

$$C[\omega] = \begin{pmatrix} \chi_1[\omega] & 0 \\ 0 & \chi_2[\omega] \end{pmatrix} C_{\text{in}}(t) \tag{3.159}$$

where the mechanical susceptibility of mode j is

$$\chi_j[\omega] = \frac{1}{\gamma_j/2 - i(\omega - \omega_j)} \tag{3.160}$$

This solution contains no hybridization between modes 1 and 2; an excitation of mode 1 (2) remains in mode 1 (2) for all values of t. For the rest of this discussion, we look at the effect of the (linearized) optical mode $d(t)$, and see that it hybridizes modes 1 and 2.

With nonzero $d(t)$, we follow the prescription of Section 3.4.5, by taking the Fourier transform (Equation (3.4)) of Equations (3.153), solve out the $d[\omega]$ and $d^\dagger[\omega]$, and drop the counter-rotating $c_j^\dagger[\omega]$ terms in the high-Q limit. We obtain

$$\left(\frac{\gamma_1}{2} - i(\omega - \omega_1)\right) c_1[\omega] = (\chi_c^*[-\omega] - \chi_c[\omega])(|\alpha_1|^2 c_1[\omega] + \alpha_1^* \alpha_2 c_2[\omega]) + c_{\text{in},1}[\omega] \tag{3.161a}$$

$$\left(\frac{\gamma_2}{2} - i(\omega - \omega_2)\right) c_2[\omega] = (\chi_c^*[-\omega] - \chi_c[\omega])(|\alpha_2|^2 c_2[\omega] + \alpha_1^* \alpha_2 c_2[\omega]) + c_{\text{in},2}[\omega] \tag{3.161b}$$

Note that we have used the fact that

$$\alpha_j = \bar{a} g_j, \quad j = 1, 2, \tag{3.162}$$

so

$$\alpha_1^* \alpha_2 = \alpha_1 \alpha_2^* = |\alpha_1 \alpha_2| \,. \tag{3.163}$$

In analogy with the definition of the self-energy term (Equation (3.144)) of Section 3.4, we define the *self-energy matrix*

$$\Sigma[\omega] = \begin{pmatrix} -i|\alpha_1|^2 & -i|\alpha_1 \alpha_2| \\ -i|\alpha_1 \alpha_2| & -i|\alpha_2|^2 \end{pmatrix} \left(\chi_c[\omega] - \chi_c^*[-\omega]\right) \tag{3.164}$$

Take Equation (3.164), Equations (3.161), and use the definition in (3.158) to write a matrix

equation of motion in the Fourier domain:

$$-i\omega C[\omega] = -i\begin{pmatrix}\omega_1 - i\gamma_1/2 & 0\\ 0 & \omega_2 - i\gamma_2/2\end{pmatrix} C[\omega] - i\Sigma[\omega]C[\omega] + C_{\text{in}}[\omega] \tag{3.165}$$

Since $\chi_c[\omega]$ only changes appreciably over a range of ω comparable to κ, $\Sigma[\omega]$ is approximately constant near the values of ω that drive the two mechanical modes. Thus, we easily move back to the time-domain:

$$\dot{C}(t) = -i\mathcal{H}_{\text{eff}}[P,\Delta]\, C(t) + C_{\text{in}}(t) \tag{3.166}$$

where the "effective Hamiltonian" is given by

$$\mathcal{H}_{\text{eff}}[P,\Delta] = \begin{pmatrix}\omega_1 - i\gamma_1/2 & 0\\ 0 & \omega_2 - i\gamma_2/2\end{pmatrix} + \Sigma[P,\Delta] \tag{3.167}$$

$\Sigma[P,\Delta]$ is the coupling term:

$$\Sigma[P,\Delta] = \begin{pmatrix}-ig_1^2 & -ig_1g_2\\ -ig_1g_2 & -ig_2^2\end{pmatrix}\sigma[P,\Delta] \tag{3.168a}$$

$$\sigma[P,\Delta] = \frac{P}{\hbar\omega_{\text{L}}}\frac{\kappa_{\text{in}}}{(\kappa/2)^2+\Delta^2}\left[\frac{1}{\kappa/2 - i(\omega_0+\Delta)} - \frac{1}{\kappa/2 + i(-\omega_0+\Delta)}\right] \tag{3.168b}$$

and where $\omega_0 = (\omega_a + \omega_b)/2$.

If we take the bare eigenvalues of the system to be

$$\lambda_j = \omega_j - i\gamma_j/2 \tag{3.169}$$

then the eigenvalues of $\mathcal{H}_{\text{eff}}$ (Equation (3.167)) are

$$\begin{aligned}\mu_\pm =& \frac{1}{2}(\lambda_1 + \lambda_2 - ig_1^2\sigma - ig_2^2\sigma)\\ &\pm \frac{i}{2}\sqrt{(i\lambda_1 + i\lambda_2 + (g_1^2+g_2^2)\sigma)^2 - 4i(i\lambda_1\lambda_2 + g_2^2\lambda_1\sigma + g_1^2\lambda_2\sigma)},\end{aligned} \tag{3.170}$$

and the corresponding eigenvectors are

$$v_\pm = \left(\frac{i\lambda_1 - i\lambda_2 + g_1^2\sigma - g_2^2\sigma \pm \sqrt{(i\lambda_1+i\lambda_2+(g_1^2+g_2^2)\sigma)^2 - 4i(i\lambda_1\lambda_2 + g_2^2\lambda_1\sigma + g_1^2\lambda_2\sigma)}}{2g_1g_2\sigma},\quad 1\right)^T \tag{3.171}$$

It can be shown algebraically that the eigenvalues and eigenvectors become equal if σ (Equation

(3.168b)) satisfies

$$\sigma \to (\omega_1 - i\gamma_1/2 - \omega_2 + i\gamma_2/2)\left(-i(g_1^2 - g_2^2) \pm 2g_1 g_2\right)/(g_1^2 + g_2^2) \tag{3.172}$$

Setting σ to this value sets the discriminant in Equations (3.170) and (3.171) to zero, which sets the square root terms to zero.

The condition in Equation (3.172) can be satisfied in the resolved sideband regime ($\kappa < \omega_{1,2}$). In this regime, P and Δ control the springs and dampings in a linearly independent manner. However, in the unresolved sideband regime ($\kappa > \omega_{1,2}$), P and Δ appear in σ (Equation (3.168b)) as the product $P \times \Delta$. One needs two linearly independent real parameters to make a (traceless) set of complex values equal, so the experiment in this thesis must operate in the resolved sideband regime.

When the condition on σ (Equation (3.172)) is realized, the single eigenvalue of the system has only one eigenvector. This brings $\mathcal{H}_{\text{eff}}$ to an exceptional point (as described in Section 2.4.2) in the (P, Δ) parameter space.

We should note that, fundamentally, there is no restriction on which mechanical modes can be coupled with this interaction. However, the interaction described in this section can only be used with mechanical modes that are already "nearly degenerate." Precisely, this means that their bare detuning $|\omega_2 - \omega_1|$ is less than the largest feasible optomechanical spring. For the experiment in [6], which uses the physics described in this system, this amounts to a bare splitting of 400 Hz, for a cavity of $\kappa = 170$ kHz, and the experiment input laser powers of several hundred microwatts. If we wish to use this scheme to couple two modes that are much farther away, we would need to use much more laser power, which may not be practical.[11] Thus, in Section 3.5.2, we describe a method with Floquet modes to couple mechanical modes that have an essentially arbitrary bare splitting.

3.5.2 Nondegenerate Two-Mode Coupling via Floquet Theory: Writing the Hamiltonian

The discussion of two-mode coupling with an optical mode in Section 3.5.1 is central to this thesis work. In particular, in this thesis, we couple three mechanical modes together. However, the three nearly degenerate mechanical modes of our membrane – the (5,5), (7,1), and the (1,7) modes (see Section 4.1 for details on the mechanical membrane) – are difficult to address with the optical alignment of our cavity with our membrane. [12] Thus, it is most practical to use the

[11] One practical problem with applying too much laser power is that it can destabilize the control laser lock (Section 5.2).

[12] The experiment best addresses the (2,2), (1,2), (2,1) and (1,1) modes for the ground-state cooling experiment [64]

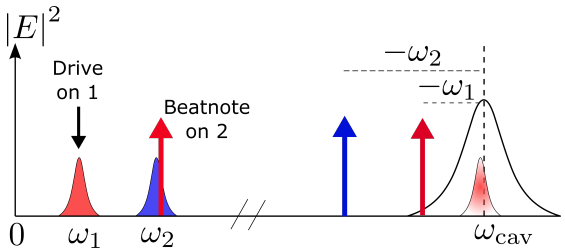

Figure 3.4: Two highly nondegenerate mechanical modes, coupled by two laser tones. A mechanical drive is applied at frequency $\omega = \omega_1$ (red Lorentzian). The motion at ω_1 creates a motional sideband (red-white Lorentzian) with the red laser tone (rightmost red arrow), which is detuned from the cavity resonance ω_c by $-\omega_1$. The motional sideband beats with the blue laser tone (blue arrow), which is detuned by $-\omega_2$ from the same cavity resonance. This beatnote is at $\omega = \omega_2$ (leftmost red arrow), and drives the membrane at $\omega = \omega_2$.

existing experimental setup to couple the mechanical modes that the setup is best at driving and reading out – even if those modes are highly nondegenerate.

Highly nondegenerate mechanical modes can be coupled with a time-dependent Hamiltonian $H(t)$, which oscillates at a frequency near the frequency difference between modes. For instance, we realize this $H(t)$ to couple two modes with two laser tones: laser tone j has a detuning $\Delta_j \approx -\omega_j$ from the cavity mode, which is nearly resonant with the mode of frequency ω_j. This $H(t)$ also effects light-matter coupling on the modes (Section 3.5.1), which tunes the modes to an exceptional point in the (rotating) Floquet frame. In the following, we use $\tilde{\omega}_j$ to denote mechanical mode j, $j \in \mathbb{Z}^+$, in the (nonrotating) lab frame, and $\tilde{\mathcal{H}}$ to denote the Hamiltonian in the (nonrotating) lab frame. We use ω_j to denote mechanical mode j, $j \in \mathbb{Z}^+$, in the (rotating) Floquet frame, and $\mathcal{H}$ to denote the Hamiltonian in the (rotating) Floquet frame.

Suppose that we have two mechanical modes, given by frequencies ω_1 and ω_2, with mechanical dampings γ_1 and γ_2, and optomechanical coupling constants g_1 and g_2. Then apply two optical laser tones of laser powers P_1 and P_2, detuned from the cavity mode Ω_c by Δ_1 and Δ_2, respectively (i.e., the laser frequency is $\omega_{j,\mathrm{L}} = \Omega_c + \Delta_j$). These laser detunings will be set to roughly

$$\Delta_j = -\omega_j + \delta + \eta_j, \quad j = 1, 2. \tag{3.173}$$

Thus, tone 1 (2) will optomechanically control mode 1 (2). δ is a common frequency shift between the tones, which we are free to tune. η_j is a fixed frequency shift, for each $j = 1, 2$, which is on the order of the optomechanically shifted γ_j. η_j is set in order to tune the bare mechanical mode splitting in the rotating frame.

Throughout this analysis, we will need to assume that the laser tone splitting is closed to the bare mechanical mode splitting. That is, we must assume that

$$|\Delta_1 - \Delta_2| - |\omega_2 - \omega_1| = \mathcal{O}(\gamma_{j,\,\mathrm{O.M.}})_{j=1,2} \tag{3.174}$$

which is to say that the laser splitting is within a few (optomechanically dampened) mechanical linewidths of the bare frequency splitting.

The physical coupling that the two laser tones create is described as follows: when mode 1 (2) is mechanically driven, mode 1 (2) will produce a motional sideband with laser tone 1 (2). This motional sideband of mode 1 (2) has frequency

$$\begin{aligned} \omega_{\text{side }1(2)} &= \Omega_c + \Delta_{1(2)} + \omega_{1(2)} \\ &= \Omega_c + \delta + \eta_{1(2)}, \end{aligned} \tag{3.175}$$

and is resonant with the cavity mode. This sideband then beats with tone 1 (2), producing an oscillating intensity beatnote (and hence a force) at frequency

$$\begin{aligned} \omega_{\text{beat }1(2)} &= \omega_{\text{side }1(2)} - (\Omega_c + \Delta_{1(2)}) \\ &= \omega_{1(2)}, \end{aligned} \tag{3.176}$$

which is approximately resonant with mode 1 (2). This beatnote optomechanically controls mechanical mode 1 (2), with the same optomechanical interaction described in Section 3.4. [13]

In addition to the beatnote at frequency $\omega_{\text{beat }1(2)}$ that gets produced from the beat of the tone at $\Omega_c + \Delta_{1(2)}$ and the sideband at $\omega_{\text{side }1(2)}$, the same sideband at $\omega_{\text{side }1(2)}$ beats with the other laser tone at $\Omega_c + \Delta_{2(1)}$, and produces a second beatnote at frequency

$$\begin{aligned} \omega'_{\text{beat }2(1)} &= \omega_{\text{side }1(2)} - (\Omega_c + \Delta_{2(1)}) \\ &= \omega_{2(1)} + \eta_{1(2)} - \eta_{2(1)} \end{aligned} \tag{3.177}$$

This beatnote at $\omega'_{\text{beat }2(1)}$ is nearly resonant with mode 2(1), so this beatnote drives the membrane at mechanical mode 2(1), in addition to the initial drive at mode 1(2). This beating couples mode 1(2) to mode 2(1). This additional beatnote drive is depicted in Figure 3.4.

We can write down the essential elements of the interaction Hamiltonian

$$H_{\text{int}} = \begin{pmatrix} H_{11} & H_{12} \\ H_{21} & H_{22} \end{pmatrix} \tag{3.178}$$

from this physical intuition. Let the cavity susceptibility be given by

$$\chi[\omega] = \frac{1}{\kappa/2 - i\omega} \tag{3.179}$$

[13] Of course, mode 1(2) can also produce a motional sideband with tone 2(1), and then this sideband can beat with tone 2(1) to produce an additional intensity beatnote at the frequency of mode 1(2). This is why, in the on-diagonal terms of Equation (3.178), there is a summation over the two laser tones.

(note that $\chi[\omega]^* = \chi[-\omega]$). We first consider the off-diagonal term H_{12}. Mode 1 produces a motional sideband of tone 1 at frequency $\Delta_1 + \omega_1$, relative to the cavity mode. This sideband picks up a factor of $-i\chi[\Delta_1+\omega_1]$ (with the $-i$ factor coming in, in analogy with the self-energy of the 1-tone optomechanical interaction of Section 3.4, Equation (3.144)). It oscillates at frequency $\Delta_{12} \triangleq \Delta_1 - \Delta_2$. We also multiply by the optomechanical single-photon coupling strengths for the two modes, g_1 and g_2, as well as by amplitudes of the annihilation and creation operators for modes 1 and 2, respectively:

$$a_1 = a_{1,\mathrm{in}}\,\chi[\Delta_1] = \sqrt{\frac{P_1}{\hbar\omega_{1,\mathrm{L}}}}\sqrt{\kappa_{\mathrm{in}}}\,\chi[\Delta_1] = \sqrt{\frac{P_1}{\hbar\omega_{1,\mathrm{L}}}}\,\frac{\sqrt{\kappa_{\mathrm{in}}}}{\kappa/2 - i\Delta_1} \tag{3.180a}$$

$$a_2^\dagger = a_{2,\mathrm{in}}^\dagger\,\chi[\Delta_2]^* = \sqrt{\frac{P_2}{\hbar\omega_{2,\mathrm{L}}}}\sqrt{\kappa_{\mathrm{in}}}\,\chi[-\Delta_2] = \sqrt{\frac{P_2}{\hbar\omega_{2,\mathrm{L}}}}\,\frac{\sqrt{\kappa_{\mathrm{in}}}}{\kappa/2 + i\Delta_2} \tag{3.180b}$$

The amplitudes of the creation and annihilator operators given in Equations (3.180) follow from the steady-state cavity field amplitudes found in Equation (3.90), in Section 3.3.3 (to 0th order in the mechanical mode amplitudes, as described in Section 3.4). Altogether, this product sets

$$\begin{aligned} H_{12}(t) &\approx -ig_1 a_1 g_2 a_2^\dagger\,\chi[\Delta_1 + \omega_1]e^{+i\Delta_{12}t} \\ &= -ig_1 g_2 \kappa_{\mathrm{in}}\frac{\sqrt{P_1 P_2}}{\hbar\omega_{\mathrm{L}}}\chi[\Delta_1]\chi[-\Delta_2]\chi[\Delta_1+\omega_1]e^{+i\Delta_{12}t} \end{aligned} \tag{3.181}$$

We drop the numerical subscript from $\omega_{j,\mathrm{L}}$, $j = 1, 2$, since the laser wavelength is 1064 nm, which has frequency 281 THz, and is much larger than any detunings used in this thesis. $H_{21}(t)$ can be written down with the same argument, with the roles of modes 1 and 2 reversed. This yields

$$\begin{aligned} H_{21}(t) &\approx -ig_1 a_1^\dagger g_2 a_2\,\chi[\Delta_2 + \omega_2]e^{-i\Delta_{12}t} \\ &= -ig_1 g_2 \kappa_{\mathrm{in}}\frac{\sqrt{P_1 P_2}}{\hbar\omega_{\mathrm{L}}}\chi[\Delta_2]\chi[-\Delta_1]\chi[\Delta_2+\omega_2]e^{-i\Delta_{12}t} \end{aligned} \tag{3.182}$$

The on-diagonal terms can be written with the same argument as for the off-diagonal terms. However, since each laser tone induces its own 1-tone optomechanical interaction on mode j, we sum the contributions to obtain the self-couplings. Thus,

$$H_{nn} = -ig_n^2\sum_{j=1}^{2}\frac{P_j}{\hbar\omega_{\mathrm{L}}}\kappa_{\mathrm{in}}\left|\chi[\Delta_j]\right|^2\chi[\Delta_j + \omega_n] \tag{3.183}$$

Equation (3.178), with entries given by Equations (3.181), (3.182), and (3.183), is essentially the interaction Hamiltonian between two highly nondegenerate mechanical modes, which are coupled via the beatnote (though it misses one motional sideband term, as described in the following section; we will derive a self-energy matrix that goes into these matrix terms, in place of the cavity susceptibility factor $-i\chi[\Delta_j + \omega_j]$). In the following section, we justify the

Hamiltonian in Equation (3.178) more rigorously, from the optomechanical equations of motion.

3.5.3 Nondegenerate Two-Mode Coupling: Equations of Motion

In this subsection, we will derive Equation (3.178) via the optomechanical equations of motion. This derivation adapts Mason's derivation [33, Ch.5.2], though we expand it slightly.

If we drive the cavity with two laser tones, with frequencies

$$\omega_{j,\mathrm{L}} = \omega_c + \Delta_j, \quad j = 1, 2 \tag{3.184}$$

where ω_c is a single cavity mode frequency that both lasers are near, and powers P_1 and P_2, then the input field is

$$\begin{aligned} a_{\mathrm{in}}(t) &= \bar{a}_{1,\mathrm{in}}\, e^{-i\omega_{1,\mathrm{L}}t} + \bar{a}_{2,\mathrm{in}}\, e^{-i\omega_{2,\mathrm{L}}t} \\ &= e^{-i\omega_c t}\left(\bar{a}_{1,\mathrm{in}}\, e^{-i\Delta_1 t} + \bar{a}_{2,\mathrm{in}}\, e^{-i\Delta_2 t}\right) \end{aligned} \tag{3.185}$$

The differential equations of motion for the cavity field and the two mechanical modes remain unchanged from Section 3.5.1; they are given by Equations (3.152). The Hamiltonian is given by Equation (3.150), with the radiation-pressure force potential given by Equation (3.151).

If there were only one laser tone, the solution would be given by Equation (3.90). By linear superposition, the solution for $a(t)$ is a superposition of the two fields given in Equation (3.90):

$$a(t) = e^{-i\omega_c t}\bar{a}(t) \tag{3.186}$$

where $\bar{a}(t)$, rather than being a steady-state amplitude, is a time-fluctuating mean amplitude:

$$\bar{a}(t) = \bar{a}_1 e^{-i\Delta_1 t} + \bar{a}_2 e^{-i\Delta_2 t} \tag{3.187a}$$

$$\bar{a}_j = \frac{\sqrt{\kappa_{\mathrm{in}}}}{\kappa/2 - i\Delta_j}\,\bar{a}_{j,\mathrm{in}}, \quad j = 1, 2 \tag{3.187b}$$

Now that we know, to 0th order in the mechanical fluctuations $c(t)$, that the cavity optical field is given by the mean field in Equation (3.186), we can linearize the equations of motion by following the prescription of Section 3.4.4. Thus, we write

$$a(t) = e^{-i\omega_c t}(\bar{a}(t) + d(t)) \tag{3.188}$$

where $d(t)$ are small fluctuations of motions about the mean fluctuating field $\bar{a}(t)$. $d(t)$ is again assumed to be of the same order as the mechanical field fluctuations $c(t)$. However, since $\bar{a}(t)$ is itself a time-varying field, the solution of the equations of motion in Equation (3.152) is more complicated than in Section 3.5.1. Nonetheless, the solution with the previous process is still

straightforward and tractable.

First, we plug Equation (3.188) into the cavity field equation of motion (Equation (3.152a)):

$$\begin{aligned}\frac{d}{dt}\left(e^{-i\omega_c t}(\bar{a}(t)+d(t))\right) = &-\left(\frac{\kappa}{2}+i\omega_c\right)e^{-i\omega_c t}(\bar{a}(t)+d(t)) \\ &+ i\sum_{j=1,2} g_j(c_j+c_j^\dagger)e^{-i\omega_c t}(\bar{a}(t)+d(t)) + \sqrt{\kappa_{\text{in}}}\,a_{\text{in}}(t)\end{aligned} \tag{3.189}$$

We apply perturbation theory in orders of $c(t)$ and $d(t)$ to separate Equation (3.189) into 0th and 1st order equations:

$$e^{-i\omega_c t}\left(-i\omega_c\bar{a}(t)+\frac{d\bar{a}}{dt}(t)\right) = e^{-i\omega_c t}\left(-\left(\frac{\kappa}{2}+i\omega_c\right)\bar{a}(t)+\sqrt{\kappa_{\text{in}}}\,a_{\text{in}}(t)\right) \tag{3.190a}$$

$$e^{-i\omega_c t}\left(-i\omega_c d(t)+\dot{d}(t)\right) = e^{-i\omega_c t}\left(-\left(\frac{\kappa}{2}+i\omega_c\right)d(t)+i\sum_{j=1,2} g_j(c_j+c_j^\dagger)\,\bar{a}(t)\right) \tag{3.190b}$$

Equation (3.190b) has the solution given by Equation (3.186). Equation (3.190b) simplifies to

$$\dot{d}(t) = -\frac{\kappa}{2}\,d(t) + i\sum_{j=1,2} g_j(c_j+c_j^\dagger)\,\bar{a}(t) \tag{3.191}$$

We also plug the linearized optical field (Equation (3.188)) into Equation (3.152b) and Equation (3.152c):

$$\begin{aligned}\dot{c}_j(t) &= -\left(\frac{\gamma_j}{2}+i\omega_j\right)c_j(t) + ig_j\,|\bar{a}(t)+d(t)|^2 \\ &= -\left(\frac{\gamma_j}{2}+i\omega_j\right)c_j(t) + ig_j\big(\,|\bar{a}(t)|^2 + \bar{a}(t)d(t)^\dagger + \bar{a}(t)d(t)^\dagger + |d(t)|^2\,\big)\end{aligned} \tag{3.192}$$

We ignore $|d(t)|^2$ in Equation (3.192), since it is of order $\mathcal{O}(d(t)^2)$. As for the $|\bar{a}(t)|^2$, since it is not constant in time, we cannot immediately drop it. We expand $|\bar{a}(t)|^2$:

$$|\bar{a}(t)|^2 = |\bar{a}_{1,\text{in}}|^2 + |\bar{a}_{1,\text{in}}|^2 + 2\,\text{Re}\Big(\bar{a}_{1,\text{in}}(\bar{a}_{2,\text{in}})^\dagger e^{-i(\Delta_1-\Delta_2)t}\Big) \tag{3.193}$$

The oscillating term in Equation (3.193) can be dropped if

$$|\Delta_1-\Delta_2| - \omega_j \gg \gamma_j, \quad j=1,2 \tag{3.194}$$

This ensures that the term is off-resonant with any mechanical mode frequency. If this holds, we may drop $|\bar{a}(t)|^2$ in Equation (3.192), and have

$$\dot{c}_j(t) = -\left(\frac{\gamma_j}{2}+i\omega_j\right)c_j(t) + ig_j\big(\,+\bar{a}(t)d(t)^\dagger + \bar{a}(t)d(t)^\dagger\big) \tag{3.195}$$

We now write Equations (3.191) and (3.195) as a summation over the laser indices:

$$\dot{d}(t) = -\frac{\kappa}{2}\, d(t) + i \sum_{j=1}^{2} g_j (c_j + c_j^\dagger) \sum_{k=1}^{2} \bar{a}_k e^{-i\Delta_k t} \tag{3.196a}$$

$$\dot{c}_j(t) = -\left(\frac{\gamma_j}{2} + i\omega_j\right) c_j + i g_j \sum_{k=1}^{2} \left(\bar{a}_k d(t)^\dagger e^{-i\Delta_k t} + \bar{a}_k^* d(t) e^{+i\Delta_k t}\right) \tag{3.196b}$$

3.5.4 Nondegenerate Two-Mode Coupling: Solving the Equations of Motion

To solve the equations of motion (Equations (3.196)), we take the Fourier transform (defined in Equation (3.4)). Per our definition of the Fourier transform, for any function $f(t)$ and a phase shift Δ, we have

$$\mathcal{F}[e^{-i\Delta t} f(t)](\omega) = \mathcal{F}[f(t)](\omega - \Delta) \tag{3.197}$$

With this, we can write

$$d[\omega] = +i\chi[\omega] \sum_{l=1}^{2} \sum_{m=1}^{2} g_l \bar{a}_m (c_l[\omega - \Delta_m] + c_l^\dagger[\omega - \Delta_m]) \tag{3.198a}$$

$$d^\dagger[\omega] = -i\chi[\omega] \sum_{l=1}^{2} \sum_{m=1}^{2} g_l \bar{a}_m^* (c_l[\omega + \Delta_m] + c_l^\dagger[\omega + \Delta_m]) \tag{3.198b}$$

$$\chi_j[\omega]^{-1}\, c_j[\omega] = +i g_j \sum_{k=1}^{2} (\bar{a}_k d^\dagger[\omega - \Delta_k] + \bar{a}_k^* d[\omega + \Delta_k]) \tag{3.198c}$$

where the cavity susceptibility $\chi[\omega]$ is given by Equation (3.179), and the mechanical susceptibility $\chi_j[\omega] = (\gamma_j/2 - i(\omega - \omega_j))^{-1}$ is given in Equation (3.135b).

As in previous systems discussed in this chapter, we algebraically solve out the $d[\omega]$ and $d^\dagger[\omega]$ terms in Equations (3.198) to get an equation for $c_j[\omega]$. To make the equation more compact, we define relative laser detunings

$$\Delta_{km} = \Delta_k - \Delta_m, \quad k, m = 1, 2. \tag{3.199}$$

Then

$$_j[\omega]^{-1}\, c_j[\omega] = +i g_j \sum_{k=1}^{2} \Big((-i)\bar{a}_k \chi[\omega - \Delta_k] \sum_{l=1}^{2} \sum_{m=1}^{2} g_l \bar{a}_m^* (c_l[\omega - \Delta_{km}] + c_l^\dagger[\omega - \Delta_{km}]) \tag{3.200}$$

$$+ i\bar{a}_k^* \chi[\omega + \Delta_k] \sum_{l=1}^{2} \sum_{m=1}^{2} g_l \bar{a}_m (c_l[\omega + \Delta_{km}] + c_l^\dagger[\omega + \Delta_{km}]) \Big)$$

which becomes

$$ {}_j[\omega]^{-1}\, c_j[\omega = g_j \sum_{k=1}^{2}\sum_{l=1}^{2}\sum_{m=1}^{2} \Big(+ \bar{a}_k g_l \bar{a}_m^* \chi[\omega - \Delta_k]\big(c_l[\omega - \Delta_{km}] + c_l^\dagger[\omega - \Delta_{km}]\big) \\ - \bar{a}_k^* g_l \bar{a}_m \chi[\omega + \Delta_k]\big(c_l[\omega + \Delta_{km}] + c_l^\dagger[\omega + \Delta_{km}]\big)\Big) \tag{3.201} $$

In the last line of Equation (3.201), note that we can swap the k and m indices, note that $\Delta_{km} = -\Delta_{mk}$, and get

$$ \chi_j[\omega]^{-1}\, c_j[\omega] = g_j \sum_{k=1}^{2}\sum_{l=1}^{2}\sum_{m=1}^{2} g_l \bar{a}_k^* \bar{a}_m \big(\chi[\omega - \Delta_m] - \chi[\omega + \Delta_k]\big) \\ \big(c_l[\omega + \Delta_{km}] + c_l^\dagger[\omega + \Delta_{km}]\big) \tag{3.202} $$

We can define a self-energy matrix (in analogy with the optomechanical self energy matrix of Equation (3.144)):

$$ \boxed{\Sigma_{km}[\omega] = -i\bar{a}_k^* \bar{a}_m \Big(\chi[\omega + \Delta_k] - \chi[\omega - \Delta_m]\Big)} \tag{3.203} $$

so that Equation (3.201) becomes

$$ \chi_j[\omega]^{-1}\, c_j[\omega] = -ig_j \sum_{k=1}^{2}\sum_{l=1}^{2}\sum_{m=1}^{2} g_l \Sigma_{km}[\omega]\Big(c_l[\omega + \Delta_{km}] + c_l^\dagger[\omega + \Delta_{km}]\Big) \tag{3.204} $$

We can simplify Equation (3.204) by breaking the summation into diagonal and off-diagonal parts D_j and O_j, and using the fact that $\Delta_{jj} = 0$ and $\Delta_{jk} = -\Delta_{kj}$:

$$ \chi_j[\omega]^{-1}\, c_j[\omega] = -ig_j(D_j[\omega] + O_j[\omega]) \tag{3.205} $$

where

$$ D_j[\omega] = \sum_{l=1}^{2} g_l \Big(\Sigma_{11}[\omega] + \Sigma_{22}[\omega]\Big)\Big(c_l[\omega] + c_l^\dagger[\omega]\Big) \tag{3.206a} $$

$$ O_j[\omega] = \sum_{l=1}^{2} g_l \Big\{\Sigma_{12}[\omega]\Big(c_l[\omega + \Delta_{12}] + c_l^\dagger[\omega + \Delta_{12}]\Big) + \Sigma_{21}[\omega]\Big(c_l[\omega - \Delta_{12}] + c_l^\dagger[\omega - \Delta_{12}]\Big)\Big\} \tag{3.206b} $$

We treat the on-diagonal term D_j (Equation (3.206a)) first by noting that, since the mechanical resonator has $Q \gg 1$, we can drop the $c_l^\dagger[\omega]$ terms, per the discussion in Appendix A. Second, since ω_1 and ω_2 are well-separated by multiple mechanical linewidths, $c_{l,l\neq j}[\omega]$ will be

small at $\omega \approx \omega_j$. Thus, we get

$$D_j[\omega] = g_j\Big(\Sigma_{11}[\omega] + \Sigma_{22}[\omega]\Big)c_j[\omega] \tag{3.207}$$

We treat the off-diagonal term O_j (Equation (3.206b)) with the assumption that the laser tone splitting is within a few mechanical linewidths of the bare mechanical mode splitting (see Equation (3.174)). With this assumption, we again drop the counter-rotating $c_l^\dagger[\omega \pm \Delta_{12}]$ terms, since they resonate at $-\omega_l$ and $-2\omega_l + \omega_{m,m\neq l}$, respectively, which are both negative and can be dropped under the high-Q approximation.

Next, we break the summation in Equation (3.206b) by considering the summation index l when $l = j$ and $l \neq j$. For $l = j$, and $j = 1$, then since $c_1[\omega]$ and $c_1[\omega + \Delta_{12}]$ peak at ω_1 and ω_2, respectively, $c_1[\omega + \Delta_{12}]$ can be dropped. Similarly, $c_1[\omega - \Delta_{12}]$ peaks at $2\omega_1 - \omega_2$, so it can be dropped as well. Then, for $l = j$ and $j = 2$, it can be similarly argued that $c_2[\omega \pm \Delta_{12}]$ are negligible. Thus, we next consider $l \neq j$.

For $l \neq j$ in the summation in Equation (3.206b), we note that if $j = 1$, then $l = 2$, and $c_2[\omega + \Delta_{12}]$ peaks at $\omega = \omega_1$, since $c_2[\omega]$ peaks at $\omega = \omega_2$. Thus, this term is not negligible. Similarly, for $j = 2$, and $l = 1$, $c_1[\omega - \Delta_{12}]$ peaks at $\omega = \omega_2$. Thus, we find

$$O_j[\omega] = \Big\{g_l\Sigma_{12}[\omega]c_l[\omega + \Delta_{12}] + \Sigma_{21}[\omega]c_l[\omega - \Delta_{12}]\Big\}_{l,l\neq j} \tag{3.208}$$

Finally, we'll note that only one term in the above peaks at the same frequency as $c_j[\omega]$. Thus, the off-diagonal terms are simply

$$O_1[\omega] = g_2\Sigma_{12}[\omega]c_2[\omega + \Delta_{12}] \tag{3.209a}$$

$$O_2[\omega] = g_1\Sigma_{21}[\omega]c_1[\omega - \Delta_{12}] \tag{3.209b}$$

The equations of motion (Equation (3.205)) can now be written as

$$\chi_1[\omega]^{-1}c_1[\omega] = -ig_1^2\Big(\Sigma_{11}[\omega] + \Sigma_{22}[\omega]\Big)c_1[\omega] - ig_1g_2\Sigma_{12}[\omega]c_2[\omega + \Delta_{12}] \tag{3.210a}$$

$$\chi_2[\omega]^{-1}c_2[\omega] = -ig_1g_2\Sigma_{21}[\omega]c_1[\omega - \Delta_{12}] - ig_2^2\Big(\Sigma_{11}[\omega] + \Sigma_{22}[\omega]\Big)c_2[\omega] \tag{3.210b}$$

Under the high-Q approximation for the mechanical resonator, and since the mechanical linewidths γ_j are much smaller than κ,and since $\Sigma_{jk}[\omega]$ only varies appreciably on the order of κ, we can

treat $\Sigma_{jk}[\omega]$ as constant:

$$\left(\frac{\gamma_1}{2} - i(\omega - \omega_1)\right) c_1[\omega] = -ig_1^2\Big(\Sigma_{11}[\omega_1] + \Sigma_{22}[\omega_1]\Big)c_1[\omega] - ig_1g_2\Sigma_{12}[\omega_1]c_2[\omega + \Delta_{12}] \tag{3.211a}$$

$$\left(\frac{\gamma_2}{2} - i(\omega - \omega_2)\right) c_2[\omega] = -ig_1g_2\Sigma_{21}[\omega_2]c_1[\omega - \Delta_{12}] - ig_2^2\Big(\Sigma_{11}[\omega_2] + \Sigma_{22}[\omega_2]\Big)c_2[\omega] \tag{3.211b}$$

where we have replaced $\chi_j[\omega]^{-1}$ with its definition. Now, we easily take the inverse Fourier transform of Equations (3.211):

$$\dot{c}_1(t) = -i\Big\{ (\omega_1 - i\gamma_1/2)\, c_1 + g_1^2 \sum_{k=1}^{2} \Sigma_{kk}[\omega_1]c_1[\omega] + g_1g_2\Sigma_{12}[\omega_1]e^{+i\Delta_{12}t}c_2 \Big\} \tag{3.212a}$$

$$\dot{c}_2(t) = -i\Big\{ (\omega_1 - i\gamma_2/2)\, c_2 + g_2^2 \sum_{k=1}^{2} \Sigma_{kk}[\omega_2]c_2[\omega] + g_1g_2\Sigma_{21}[\omega_2]e^{-i\Delta_{12}t}c_1 \Big\} \tag{3.212b}$$

Let $C(t) = (c_1(t), c_2(t))^T$ be a vector quantity. Equation (3.212) can be written with a Hamiltonian.

$$\dot{C}(t) = -i\mathcal{H}(t)C(t) \tag{3.213}$$

where

$$\mathcal{H}(t) = H_0 + H_{\text{int}}(t) \tag{3.214a}$$

$$H_0 = \begin{pmatrix} \omega_1 - i\gamma_1/2 & 0 \\ 0 & \omega_2 - i\gamma_2/2 \end{pmatrix} \tag{3.214b}$$

$$H_{\text{int}}(t) = \begin{pmatrix} \sigma_{11} & \sigma_{12}e^{+i\Delta_{12}t} \\ \sigma_{21}e^{-i\Delta_{12}t} & \sigma_{22} \end{pmatrix} \tag{3.214c}$$

and the σ_{jk} terms are given by

$$\sigma_{jj} = g_j^2 \sum_{k=1}^{2} (\Sigma_{kk}[\omega_j]) \tag{3.215a}$$

$$\sigma_{jk} = g_j g_k \Sigma_{jk}[\omega_j] \tag{3.215b}$$

and where $\Sigma_{jk}[\omega]$ is given by Equation (3.203).

3.5.5 Nondegenerate Two-Mode Coupling: Time-Independent Floquet Frame

Understanding the dynamics of Equation (3.214) is greatly simplified if we choose a basis in which it is time-independent. We refer to this as *entering the rotating frame*.

By way of illustration, we consider a 2×2 unitary transformation

$$U(t) = \begin{pmatrix} e^{i(\theta+T/2)t} & 0 \\ 0 & e^{i(-\theta+T/2)t} \end{pmatrix} \tag{3.216}$$

where θ and T are free parameters, for the time being. Clearly $U(t)$ is unitary, since $UU^\dagger = U^\dagger U = \mathcal{I}$. Furthermore,

$$0 = \frac{d}{dt}(\mathcal{I}) = \dot{U}U^\dagger + U\dot{U}^\dagger \tag{3.217}$$

Define a change-of-basis

$$C'(t) = U(t)C(t) \tag{3.218}$$

Then, from Equation (3.213),

$$\frac{d}{dt}(U^\dagger C') = \mathcal{H}(t)(U^\dagger C') \tag{3.219}$$

Multiply both sides on the left by $U(t)$. Then the left-hand side is

$$U\dot{U}^\dagger C' + UU^\dagger C' = -\dot{U}U^\dagger C' + \dot{C}' \tag{3.220}$$

Then

$$\begin{aligned} \dot{C}' &= -Ui\mathcal{H}U^\dagger C' + \dot{U}U^\dagger C' \\ &= -i\mathcal{H}_{\rm rot}C' \end{aligned} \tag{3.221}$$

where the rotating-frame Hamiltonian is given by

$$\mathcal{H}_{\rm rot} = U\mathcal{H}U^\dagger + i\dot{U}U^\dagger \tag{3.222}$$

This simplifies to

$$\begin{aligned} \mathcal{H}_{\rm rot}(t) = &\begin{pmatrix} \omega_1 - i\gamma_1/2 & 0 \\ 0 & \omega_2 - i\gamma_2/2 \end{pmatrix} \\ &\begin{pmatrix} \sigma_{11} & \sigma_{12}e^{+i(\Delta_{12}+2\theta)t} \\ \sigma_{21}e^{-i(\Delta_{12}+2\theta)t} & \sigma_{22} \end{pmatrix} - \begin{pmatrix} \theta + T/2 & 0 \\ 0 & -\theta + T/2 \end{pmatrix} \end{aligned} \tag{3.223}$$

We make $\mathcal{H}_{\rm rot}(t)$ time-independent by setting $\theta = -\Delta_{12}/2$. T is an overall trace, which has no effect on the dynamics. Let us presciently set $T = \omega_1 + \omega_2$, and get

$$\mathcal{H}_{\rm rot} = \begin{pmatrix} \omega_1 + \Delta_{12}/2 - T/2 - i\gamma_1/2 & 0 \\ 0 & \omega_2 - \Delta_{12}/2 - T/2 - i\gamma_2/2 \end{pmatrix} + \begin{pmatrix} \sigma_{11} & \sigma_{12} \\ \sigma_{21} & \sigma_{22} \end{pmatrix} \tag{3.224}$$

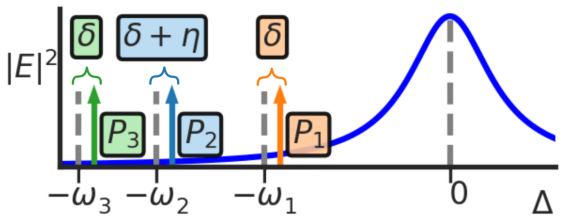

Figure 3.5: The three lasers used to optomechanically control three mechanical modes, plotted as intensity versus laser frequency. The laser frequency axis is set to zero at the cavity resonance for the control laser. The blue Lorentzian represents the cavity linewidth.

Lastly, we note that $\Delta_{12} \approx -\omega_1+\omega_2$. In fact, in Equation (3.173), we can set $\eta_1 = 0$ and $\eta_2 = -\eta$, for some η on the order of the mechanical linewidths. Then the rotating frame Hamiltonian is

$$\mathcal{H}_{\text{rot}} = \begin{pmatrix} +\eta/2 - i\gamma_1/2 & 0 \\ 0 & -\eta/2 - i\gamma_2/2 \end{pmatrix} + \begin{pmatrix} \sigma_{11} & \sigma_{12} \\ \sigma_{21} & \sigma_{22} \end{pmatrix} \tag{3.225}$$

Thus, we see that the bare frequency splitting has reduced considerably from $\omega_2 - \omega_1$ to $+\eta$. This Hamiltonian was used in [31], where $\omega_1 = 557.4\,\text{kHz}$, $\omega_2 = 705\,\text{kHz}$, and $\eta = 100\,\text{Hz}$, and the mode splitting in the Floquet frame was reduced by 3 orders of magnitude, from 148 kHz to 100 Hz. The laser powers used in that experiment were sufficient that the optomechanical interaction, captured in the σ_{jk} parameters, was sufficient to bring the system to a degeneracy in the Floquet frame.

3.6 Three-Mode Hamiltonian

In this section, we describe the Hamiltonian of the system used in this thesis experiment. This Hamiltonian uses the optomechanical interaction and Floquet theory to couple three mechanical modes.

We consider three mechanical modes: ω_1, ω_2, and ω_3. We optomechanically control their frequencies and dampings with three laser tones (the experimental implementation of these laser tones is described in Sections 5.1.1 and 5.3). With respect to a cavity mode Ω_c, these laser tones have powers P_1, P_2, and P_3, and frequencies

$$\omega_{j,\text{L}} = \Omega_c + \Delta_j \tag{3.226}$$

where Δ_j is a detuning from the cavity mode. Figure 3.5 In analogy with Section 3.5.2, we will define these detunings Δ_j by

$$\Delta_j = -\omega_j + \delta + \eta_j \tag{3.227}$$

where δ is a parameter that we tune. η_j is a fixed frequency shift, which is on the order of the optomechanically damped mechanical dampings, that sets the position of the degeneracy in the Floquet frame. We choose $\eta_1/2\pi = 0$, $\eta_2/2\pi = -100\,\text{Hz}$, and $\eta_3/2\pi = 0$ (and simply set $\eta \triangleq \eta_2 = 2\pi \times -100\,\text{Hz}$).

In this experiment, we choose modes with frequencies

$$\omega_1/2\pi = 352.243\,\text{kHz} \tag{3.228a}$$

$$\omega_2/2\pi = 557.217\,\text{kHz} \tag{3.228b}$$

$$\omega_3/2\pi = 704.837\,\text{kHz}, \tag{3.228c}$$

dampings

$$\gamma_1/2\pi = 4.4\,\text{Hz} \tag{3.229a}$$

$$\gamma_2/2\pi = 3.8\,\text{Hz} \tag{3.229b}$$

$$\gamma_3/2\pi = 3.6\,\text{Hz}, \tag{3.229c}$$

The measured values of κ and κ_{in} are

$$\kappa/2\pi = 190\,\text{kHz} \tag{3.230a}$$

$$\kappa_{\text{in}} = 0.267\kappa \tag{3.230b}$$

The optomechanical coupling rates are

$$g_1/2\pi = 0.198\,\text{Hz} \tag{3.231a}$$

$$g_2/2\pi = 0.304\,\text{Hz} \tag{3.231b}$$

$$g_3/2\pi = 0.300\,\text{Hz}, \tag{3.231c}$$

These values were measured via 1-tone optomechanical shift measurements, as described in Appendix C.

With the laser tone setup described above, and in Figure 3.5, the mechanical modes will couple with one another pairwise, with the same physical processes as described in Section 3.5.2: lasers 1 and 2 will couple modes 1 and 2, but not mode 3; lasers 1 and 3 will couple modes 1 and 3, but not mode 2; and lasers 2 and 3 will couple modes 2 and 3, but not mode 1. Take $\Delta_{jk} = \Delta_j - \Delta_k$. From Section 3.5.2, we know that the system Hamiltonian will take the periodic

form

$$\mathcal{H} = \begin{pmatrix} \omega_1 - i\gamma_1/2 & 0 & 0 \\ 0 & \omega_2 - i\gamma_2/2 & 0 \\ 0 & 0 & \omega_3 - i\gamma_3/2 \end{pmatrix} + \begin{pmatrix} \sigma_{11} & \sigma_{12}e^{+i\Delta_{12}t} & \sigma_{13}e^{+i\Delta_{13}t} \\ \sigma_{21}e^{-i\Delta_{12}t} & \sigma_{22} & \sigma_{23}e^{+i\Delta_{23}t} \\ \sigma_{31}e^{-i\Delta_{13}t} & \sigma_{32}e^{-i\Delta_{23}t} & \sigma_{33} \end{pmatrix} \tag{3.232}$$

The σ_{jk} terms are precisely the same as those given in Equations (3.215).

Let us now choose a change of basis that puts $\mathcal{H}$ into a time-independent rotating frame. Define the change of basis matrix

$$U(t) = \begin{pmatrix} e^{i(T-\theta)t} & 0 & 0 \\ 0 & e^{iTt} & 0 \\ 0 & 0 & e^{i(T-\rho)t} \end{pmatrix} \tag{3.233}$$

Per the discussion in Section 3.5.5, we obtain the rotating frame Hamiltonian

$$\begin{aligned} \mathcal{H}_{\text{rot}}(t) = &\begin{pmatrix} \omega_1 - i\gamma_1/2 - T + \theta & 0 & 0 \\ 0 & \omega_2 - i\gamma_2/2 - T & 0 \\ 0 & 0 & \omega_3 - i\gamma_3/2 - T + \rho \end{pmatrix} + \\ &\begin{pmatrix} \sigma_{11} & \sigma_{12}e^{+i(\Delta_{12}-\theta)t} & \sigma_{13}e^{+i(\Delta_{13}-\theta+\rho)t} \\ \sigma_{21}e^{-i(\Delta_{12}-\theta)t} & \sigma_{22} & \sigma_{23}e^{+i(\Delta_{23}+\rho)t} \\ \sigma_{31}e^{-i(\Delta_{13}-\theta+\rho)t} & \sigma_{32}e^{-i(\Delta_{23}+\rho)t} & \sigma_{33} \end{pmatrix} \end{aligned} \tag{3.234}$$

To make the above equation time-independent, we set

$$\theta = \Delta_{12} \tag{3.235a}$$

$$\rho = -\Delta_{23} \tag{3.235b}$$

Then, since $\Delta_{13} = \Delta_{12} + \Delta_{23} = \theta - \rho$, this rotating frame Hamiltonian is indeed time-independent. T is a free parameter that does not affect the dynamics. We can choose to set T to

$$T = \omega_2 \tag{3.236}$$

Then the time-varying change-of-basis matrix is

$$U(t) = \begin{pmatrix} e^{i(\omega_1+\eta)t} & 0 & 0 \\ 0 & e^{i\omega_2 t} & 0 \\ 0 & 0 & e^{i(\omega_3+\eta)t} \end{pmatrix} \tag{3.237}$$

The system Hamiltonian in the Floquet frame is given by

$$\mathcal{H}_{\text{rot}}\big(\delta, P_1, P_2, P_3\big) = \begin{pmatrix} -\eta - i\gamma_1/2 & 0 & 0 \\ 0 & -i\gamma_2/2 & 0 \\ 0 & 0 & -\eta - i\gamma_3/2 \end{pmatrix} + \begin{pmatrix} \sigma_{11} & \sigma_{12} & \sigma_{13} \\ \sigma_{21} & \sigma_{22} & \sigma_{23} \\ \sigma_{31} & \sigma_{32} & \sigma_{33} \end{pmatrix} \tag{3.238}$$

where the σ_{jk} terms are given in Equations (3.215).

Chapter 4

Membrane-in-the-Middle Platform

4.1 Membrane

4.1.1 Membrane Mechanical Modes

In this section, we describe the mechanical mode frequencies for the 2D membrane that we employ in this experiment.

The vibrational frequencies of the mechanical modes for a 2D rectangular membrane with side lengths L_x and L_y are given by

$$\nu_{m,n} = \nu_{1,1}\sqrt{\frac{(m/L_x)^2 + (n/L_y)^2}{(1/L_x)^2 + (1/L_y)^2}}\,, \quad m, n \in \mathbb{Z}^+ \tag{4.1}$$

where $\nu_{1,1}$ is the fundamental vibrational mode.[1] See Appendix B for a derivation of Equation 4.1.

A special case of Equation 4.1 is when the membrane is a square, in which case, $L_x = L_y = L$. Then Equation 4.1 becomes

$$\nu_{m,n} = \nu_{1,1}\sqrt{\frac{m^2 + n^2}{2}}\,, \quad m, n \in \mathbb{Z}^+ \tag{4.2}$$

Another special case is when the membrane is nearly square. Then we can write the side lengths as $L_x = L(1 + \delta x/2)$ and $L_y = L(1 - \delta x/2)$, for some small asymmetry term $\delta x \ll 1$. Then we can use a Taylor expansion to write the membrane vibrational frequencies (4.1), to first order in

[1] If one prefers, one can write these frequencies in terms of $\omega_{m,n} = 2\pi\nu_{m,n}$, where $\omega_{m,n}$ is the angular frequency, and $\nu_{m,n}$ is the ordinary frequency.

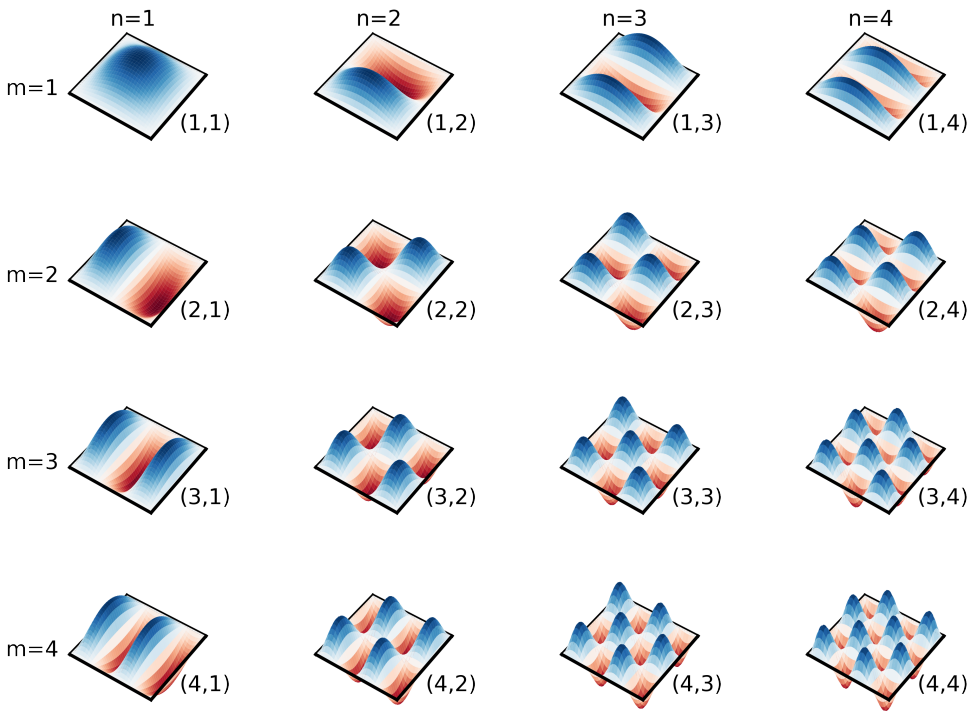

Figure 4.1: The vibrational modes of the square membrane (Equation 4.4). The blue color is the high value, the red color is the low value, and the white color is the zero.

δx, as

$$\begin{aligned} \nu_{m,n} &\approx \nu_{1,1}\sqrt{\frac{m^2(1+\delta x)+n^2(1-\delta x)}{2}} \\ &\approx \nu_{1,1}\sqrt{\frac{m^2+n^2}{2}}\left(1+\frac{m^2-n^2}{2(m^2+n^2)}\delta x\right) \end{aligned} \tag{4.3}$$

Thus, the side-length asymmetry introduced by the δx term lifts the degeneracy between the (m,n)-th and the (n,m)-th modes.

Figure 4.1 depicts the vibrational modes of the square membrane (c.f. Equation 4.2). The (m,n)-th mode has displacement

$$f(x,y) = \sin\left(\frac{m\pi x}{L}\right)\sin\left(\frac{n\pi y}{L}\right) \tag{4.4}$$

(see Appendix B for a derivation of Equation 4.4). In Figure 4.1, we see that (4.4) is a standing wave, and the (m,n)-th mode has m antinodes and $m+1$ nodes along the x-axis, as well as n antinodes and $n+1$ nodes along the y-axis.

4.1.2 Experimental Membrane and Mount

This subsection describes the experimental membrane used in this experiment. Because the membrane was situated inside of a cryogenic cavity before I joined the experiment, I largely summarize past theses [64, 33, 70] in this subsection.

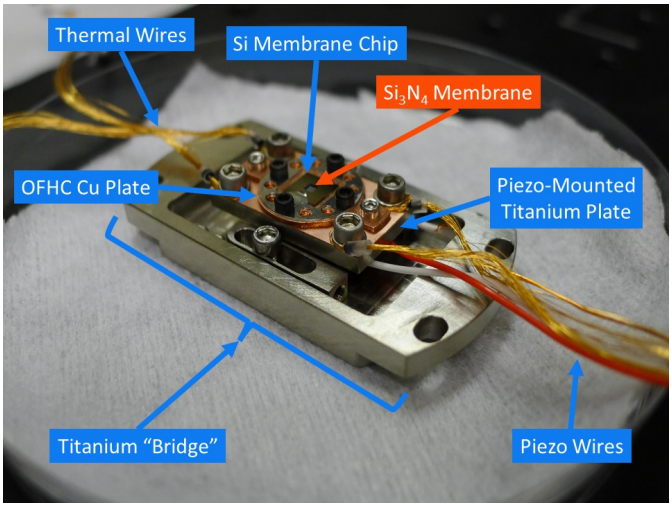

Figure 4.2: The membrane, mounted on its membrane mount.

In this experiment, we use a nearly square, nearly 2D, high-stress $1\,\text{mm} \times 1\,\text{mm} \times 50\,\text{nm}$ Si_3N_4 membrane, manufactured by Norcada, and with model number NX5100AS. [64, p.77] [33, p.35] [70, p.51]. This membrane has a fundamental mode frequency $\nu_{1,1} = 352.3\,\text{kHz}$.

The membrane is not perfectly square due to small manufacturing imprecisions, so the mechanical mode frequencies are given by Equation 4.3. The splitting between the $(2,1)$ and the $(1,2)$ modes is approximately $400\,\text{Hz}$, so the value of the δx parameter for our membrane in Equation 4.3 is approximately $\delta x \approx 0.001$.

Before mounting this membrane inside a cavity, the membrane and the other membranes in the same batch were cleaned with acetone, methanol, isopropyl alcohol, and O^2-plasma [33, p.35]. Then, the membrane used in this work was selected from the batch based on its quality factor at room temperature. These quality factors were measured via mechanical ringdowns (Section 4.1.3). At the time of the selection, the quality factors were on the order of 10^6 [33, p.35] [64, p.134]. Quality factors decreased to the order of 10^5 over the lifetime of this setup (see Section 4.1.3).

The SI_3N_4 membrane chip is secured to a mount, depicted in Figure 4.2. The chip is attached to a circular oxygen-free high-conductivity copper plate. [33, p.35] This plate is used to create a good thermal link to the heat sinking wires. The copper plate is attached to a rectangular titanium block. This titanium block sits on top a ring-shaped piezo actuator. Finally, both the piezo and the titanium block that contains the membrane chip as well as the copper plate are mounted on a titanium "bridge" [64, p.94].[2] Figure 4.2 shows the membrane secured with a leaf spring. However, in subsequent experiments [64, p.94] [33, p.35], the membrane is secured with Stycast 2850 epoxy at three of its corners, since it was found that the desired mechanical

[2]This titanium "bridge" sits on top of a PiezoKnob-based mirror mount, for in situ adjustment of the membrane position [64, p.94]. This feature was not used in the experiments discussed in this thesis.

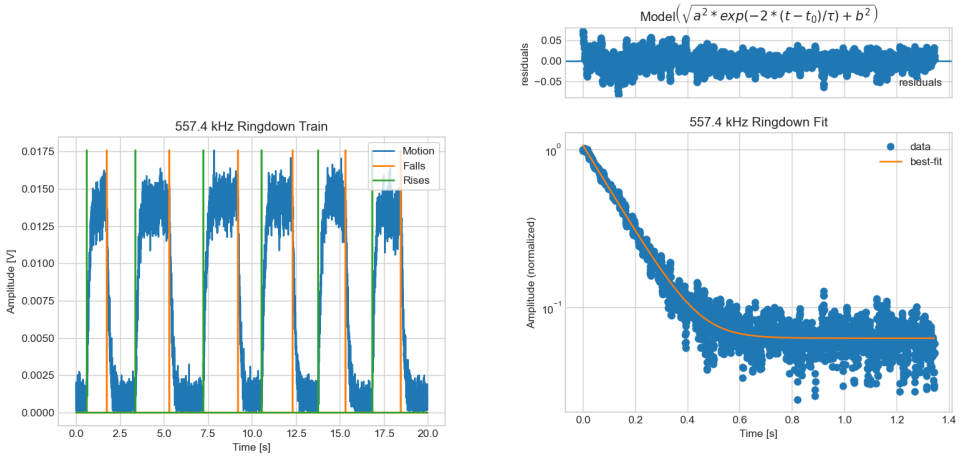

Figure 4.3: Left: a ringdown train of the 557.4 kHz mode. The sampling rate is 1800 samples per second, and the bandwidth on the lock-in amplifier is 100 Hz. The blue lines are the membrane mode motion. The orange vertical lines are where the drive was turned off. The green vertical lines are where the drive was turned on. These aid in the analysis. Right: a fit of the averaged motion over all of these ringdowns to the fit function (4.6). A value of $\gamma = 2\pi \times 2.0\,\text{Hz}$ is extracted from this fit.

properties of square membranes were achieved by securing them with epoxy instead of a leaf spring [64, p.94].

The ring piezo is used in this experiment to adjust the position of the membrane. At cryogenic temperatures, the ring piezo offers approximately 200 nm of translation range. We tune its position with an applied voltage in order to tune the cavity-membrane-mode coupling. Because we want to optimize this coupling for the experiment in this thesis (see Section 5.2.3 for a discussion on the choice of applied voltage), we send a DC signal to this piezo.[3] This signal is sent via batteries and strong low-pass filtering.[4] All ∼200 nm of the ring piezo's range could be realized with a voltage range of ∼0 V to ∼200 V, so we either use roughly twenty 9V batteries, or an SRS928 programmable DC voltage supply to set and fix the ring piezo position.

4.1.3 Membrane Mechanical Ringdowns

To characterize the linewidths of the membrane's mechanical modes, we perform ringdown measurements, by exciting the mode of interest, then turning off the excitation, and subsequently measuring the decay time τ. The linewidth γ is given by

$$\gamma = 2/\tau \tag{4.5}$$

[3] One can also use this ring piezo to excite a membrane mode. However, we instead drive the membrane using an AOM, as described in Section 5.1.1, since the noise stability of the AOM method is superior to the direct piezo-driving method.

[4] The low-pass filtering is achieved by putting a 1 MΩ resistor in series with the batteries, since the membrane piezo can be considered a 50 nF capacitor to ground [33, p.36].

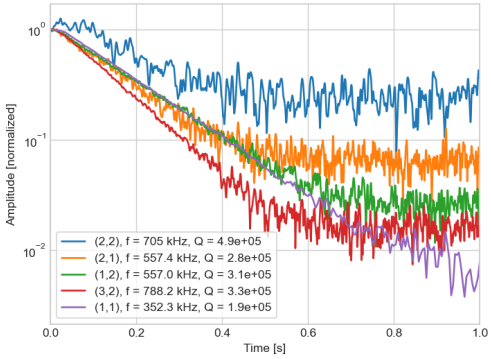

Figure 4.4: Ringdown trains for four mechanical modes.

Figure 7.1 depicts a ringdown train for the (2,1) mode, which has a frequency of 557.4 kHz (heterodyne lock-in detection of signals such as this is discussed in detail in Section 5.3.1). A drive to the membrane is applied at 557.4 kHz via an AOM (as described in Sections 5.1.1 and 5.3.1), which brings the amplitude to a high value. Then the drive is turned off, and the motion is allowed to relax. The green lines depict where the drive is turned on, and the orange lines depict where the drive is turned off. To aid in analysis, the green and orange lines are algorithmically selected: first, the data is smoothed via a rolling average; second, the rises and fall indices in the data are selected based on when the rolling average crosses threshold values. The green and orange lines delineate individual ringdowns, which are then averaged and fit to

$$f(t) = \sqrt{a^2 \exp(-2(t - t_0)/\tau) + b^2}, \tag{4.6}$$

as discussed in more detail in [64, p.133-4]. The most important characteristic of this function is τ, which determines the mechanical linewidth via (4.5).

The decay time τ is used to compute the quality factor

$$Q = \frac{\omega}{\gamma} = \frac{\omega\tau}{2} = \pi f \tau, \tag{4.7}$$

where we have written $\omega = 2\pi f$, for the mode frequency f in ordinary units.[5] The averaged ringdown motion of several mechanical modes is depicted in Figure 4.4; the ringdowns are annotated with their mode numbers, frequencies, and quality factors. These quality factors are an order of magnitude lower than the quality factors found in [33, p.36, Fig.2.3]. This decrease happened over the eight years that the same membrane was continuously installed in the cryostat.

[5] It is very easy to mistakenly forget to multiply by 2π, if one inadvertently uses the ordinary frequency f as the angular frequency ω...

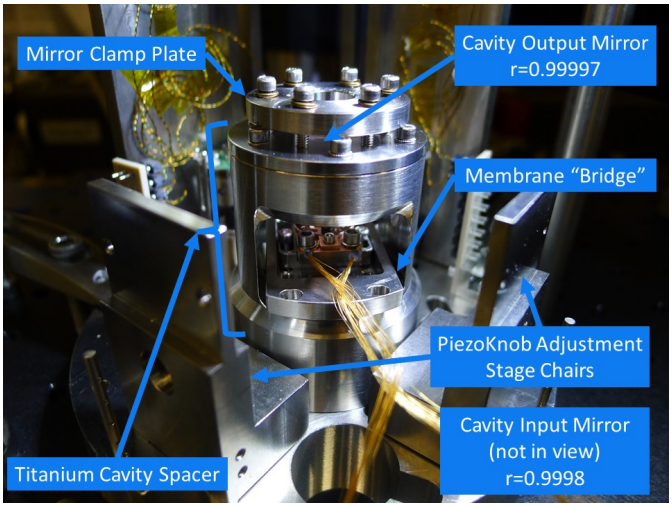

Figure 4.5: The optical cavity, with the membrane "bridge" (Figure 4.2) mounted inside.

4.2 Optical Cavity

The optical cavity used in this experiment, as well as in [70, p.53] [33, p.34-5] [64, p.95-6], is described in this section.

4.2.1 Description of the Optical Cavity

Figure 4.5 shows the membrane titanium "bridge" assembly (Section 4.1.2 and Figure 4.2). The optical cavity consists of two high-reflectivity mirrors, mounted on a titanium spacer. These mirrors were manufactured from a stack of alternating dielectric coatings, and deposited on a glass substrate. These mirrors are clamped between two plates, which are held together by screws and spring washers. These spring washers ensure that the screws provide even clamping force during a cooldown, despite the fact that the screws may have different thermal contractions from the mirror substrate [64, p.95]. One piece of Kapton® tape separates the mirrors from the spacer, as a buffer between the mirror glass and the spacer metal [33, p.34]. In Figure 4.5, one can see a hole on the bottom side of the titanium stage, which allows wires for the PiezoKnob actuators to pass through; these PiezoKnob actuators were used to tune the membrane's tip, tilt, and translation *in situ* [64, p.95], though this feature was not used in the experimental work of this thesis.

The two mirrors have reflectivities $r_{\text{output}} = 0.99997$ and $r_{\text{input}} = 0.9998$ [70, p.53] [64, p.90, p.96, Figure 26]. Figure 4.6 shows a batch of the mirrors used in this optical cavity. The output mirror is visible in Figure 4.5. The input mirror is under the cavity and is not visible in Figure 4.5. Because r_{output} is much greater than r_{input}, this is nearly a "single-sided" cavity. Since cavity measurements in this experiment are done in reflection, the transmission out of the output cavity mirror is not used. The titanium spacer separates the two mirrors by 3.7 cm; this

Figure 4.6: A batch of the mirrors used in the optical cavity of this experiment. Purchased from ATFilms.

corresponds to a free spectral range of ∼4 GHz [70, p.53] [33, p.35]. The cavity decay rate for the cavity in this experiment is $\kappa = 177\,\text{kHz}$, and the cavity input coupling rate is $\kappa_{\text{in}} = 0.267\kappa$. κ and κ_{in} can be found by measuring the cavity linewidth via its reflection spectrum (see Section 3.3.3, 3.3.4, and 4.2.2). κ may alternatively be measured from the optomechanical spring and damping (see Appendix C for descriptions of these measurements).

4.2.2 Characterizing the Cavity with a Cavity Scan

In this section, we characterize the cavity by sweeping one of the two lasers which couple to our cavity via our optical table setup (Section 5.1.1), and measuring the amplitude of the reflected light. We seek dips in the reflection, which correspond to cavity resonances. In addition, we sweep the ring piezo position (Section 4.1.2), which varies the cavity resonances. We tune these parameters together to find a laser-frequency-membrane-position configuration which best optimizes the laser-cavity coupling, in order to best facilitate heterodyne signal measurements (Section 5.3.1).

We begin by measuring the frequency tunability of the Prometheus Nd-YAG laser. We do this by using a wavelength meter which could measure wavelengths l near 1064 nm, then converting to frequency with the relation $f = c/l$. Then we change the laser temperature to change the laser frequency. The stated range of laser frequency control with this method is ∼60 GHz. In Figure 4.7, we see the measured laser frequency versus the laser temperature. The relationship is negatively sloped, aside from some "mode hop" discontinuities. In choosing laser frequencies, we would like the laser frequency fluctuations to remain small (in particular, these should be small relative to any feedback applied to lock the lasers; see Section 5.2). The initial laser frequency is therefore chosen carefully to avoid these mode hop points.

Next, we measure the reflection of the input light, as a function of the laser frequency and

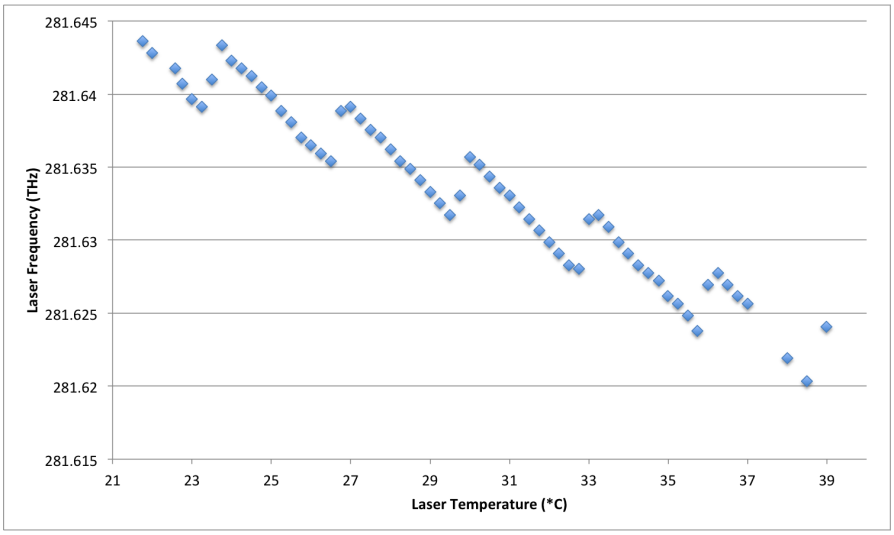

Figure 4.7: The control laser frequency versus the control laser temperature.

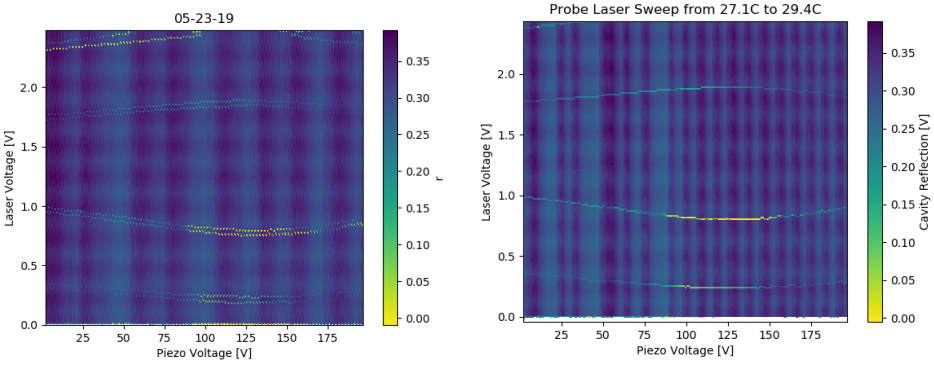

(a) (b)

Figure 4.8: A cavity scan measurement. a) the reflection is measured both while the temperature is ramped up and down. b) the reflection is measured only while the temperature is ramped up.

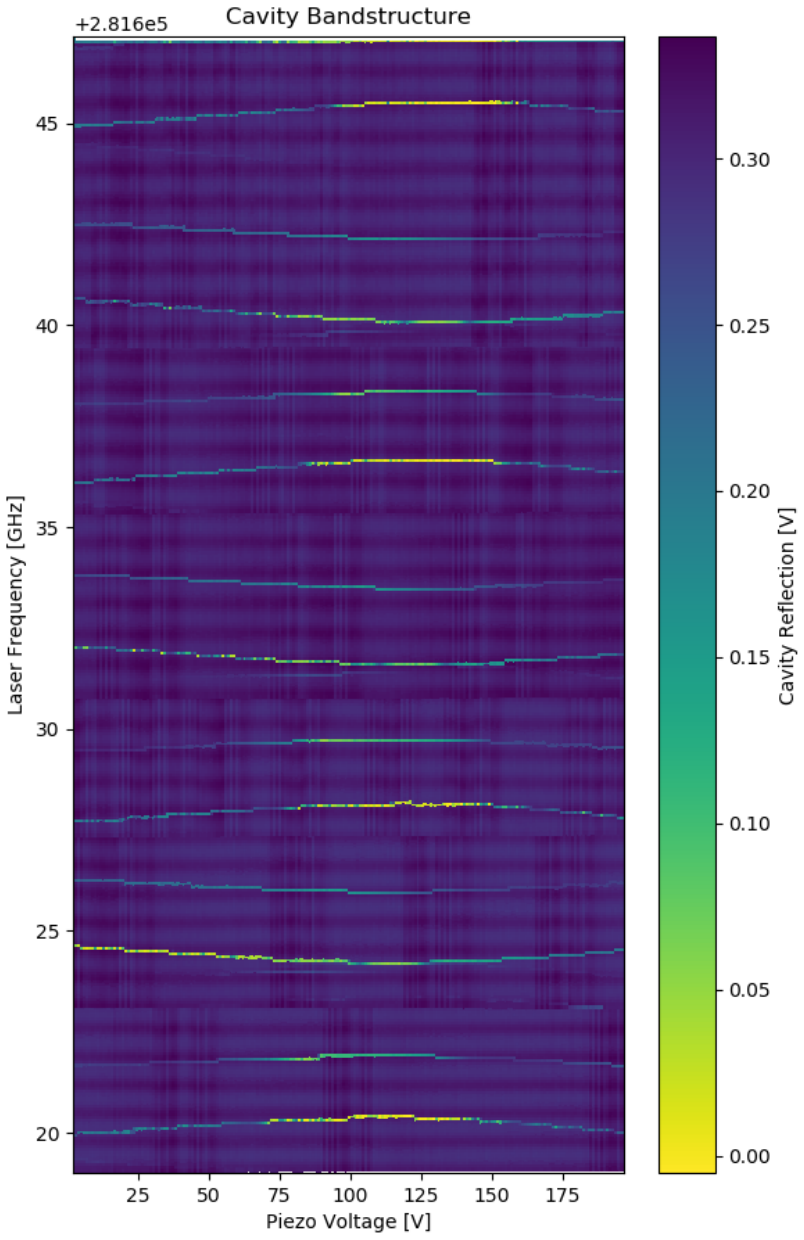

Figure 4.9: The scan of our cavity modes. The color axis shows the cavity reflection. The piezo voltage sweeps the membrane ring piezo voltage, which sweeps the membrane piezo position on a 1D axis. The laser frequency is swept by sweeping the laser temperature via an applied DC voltage.

the membrane ring piezo position (Section 4.1.2). We refer to this as a *cavity scan*. To step the ring piezo position, we use a Stanford Research Systems programmable DC voltage supply (SRS SIM928). The output range of the SIM928 is $-20\,\mathrm{V}$ to $20\,\mathrm{V}$. The membrane ring piezo admits 0 to $200\,\mathrm{V}$, so we use an operational amplifier (opamp) with a gain of -18.71 to achieve the desired $200\,\mathrm{V}$ range.

To step the laser frequency, we use a Rigol function generator, which outputs to the laser temperature control box. We apply a ramp from $0\,\mathrm{V}$ to $2.4\,\mathrm{V}$ to step the laser temperature by $2.1\,\mathrm{K}$, as the tuning coefficient is approximately $1\,\mathrm{K/V}$. The ramp-up time is set to $32.5\,\mathrm{s}$, to ensure that the laser frequency settling time is sufficient (though no systematic effort was made to determine a minimum effective temperature ramp time that would ensure sufficient laser frequency settling).

As the laser frequency is swept, the cavity reflection is measured, and the minimum value of the reflection is tracked. This is done with a National Instruments DAQ, which samples the reflection at $10\,\mathrm{kS/s}$. This is a very large sampling rate, relative to the set ramping time of $32.5\,\mathrm{s}$, so we bin the temperature axis, and plot the minimum value of the reflection in that bin.

The reflection minima can be plotted for either or both of the ramp rise and fall. Figure 4.8 show two configurations: on the left, the reflection minima are plotted for both the rise and fall of the ramp; on the right, only the minima corresponding to the rise are plotted. In order to avoid seeing two apparent "higher-order" cavity modes, in this measurement, we only record reflection minima on the rising portion of the temperature ramp.

Given that the Rigol function generator only has a DC output range of $5\,\mathrm{V}$, and also that we wish to avoid blindly sweeping through mode-hop frequencies (Figure 4.7), we perform a large cavity scan measurement by manually setting the laser temperature, then performing programmatic cavity scan measurements. We then convert the Rigol voltage axis to laser temperature (via Figure 4.7), and then concatenate the cavity scan measurements together in the laser frequency axis. Figure 4.9 shows the result of this concatenation.

The sinusoidal curves in the cavity reflection minima of Figure 4.9 show the cavity modes. These could be fundamental $\mathrm{TEM}_{0,0}$ modes, as well as higher-order modes. We assume that the fundamental modes are those that have the deepest reflection minima, since the initial alignment of the cavity and the optical fiber (Section 4.3) was such that the fiber was well-coupled with the fundamental modes. Based on this assumption, we assume that at piezo voltages of $0\,\mathrm{V}$, the $\mathrm{TEM}_{0,0}$ mode frequencies in Figure 4.9 are approximately $20\,\mathrm{V}$, $24\,\mathrm{V}$, $27.5\,\mathrm{V}$, $32.5\,\mathrm{V}$, $36\,\mathrm{V}$, $41\,\mathrm{V}$, $45\,\mathrm{V}$.

When choosing a membrane piezo voltage and a laser frequency, we would like the probe laser (Section 5.1.1) to couple easily to a cavity mode, so that it is easy to PDH-lock the probe

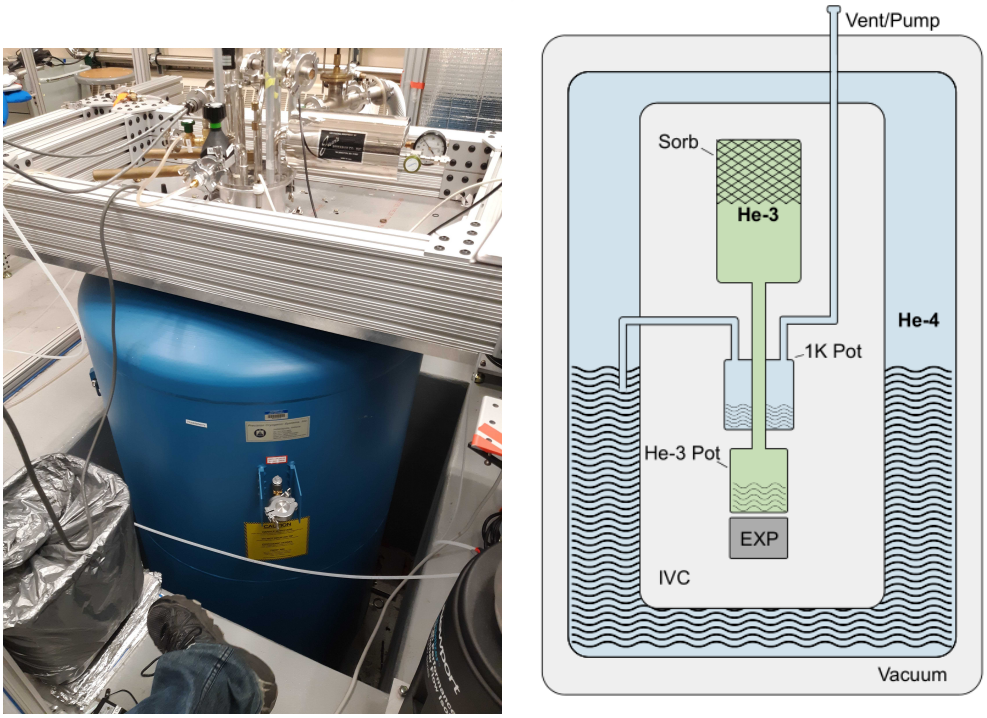

(a) (b)

Figure 4.10: a) an image of our cryostat. b) a schematic of the ^{3}He cryostatic environment. Figure b from [33, p.33, Figure 2.1] and [70, p.54, Figure 3.5].

laser (Section 5.2). Thus, we choose to set the probe laser at 25 GHz in Figure 4.9, and the membrane piezo position at 0 V. The control laser is locked by a frequency offset from the probe laser frequency, so it does not need to couple as strongly to its cavity mode, since we can simply increase the applied control tone power as needed (Section 5.3.2). The control laser frequency needs to be two FSR's away from the probe laser, to ensure that it addresses its cavity mode as the probe laser frequency tracks its mode (Section 5.2.2). Thus, we choose to set the control laser frequency at 32.5 GHz.

4.3 Cryostat

4.3.1 Description of the Cryostat

The optical cavity and the membrane in the optical cavity are placed in a "wet" ^{3}He fridge. This Janis fridge is shown in Figure 4.10a. A schematic of this fridge is shown in Figure 4.10b. The fridge has an interval vacuum chamber (IVC), which is submerged in a ^{4}He bath. This ^{4}He is at 4.2 K. It is replenished approximately every 9 or 10 days from an external source. This is distinct from "dry" fridges, which continually boil and recondense the ^{4}He in a closed cycle; this requires continuous use of compressors, which causes vibrations that add unwanted noise to the

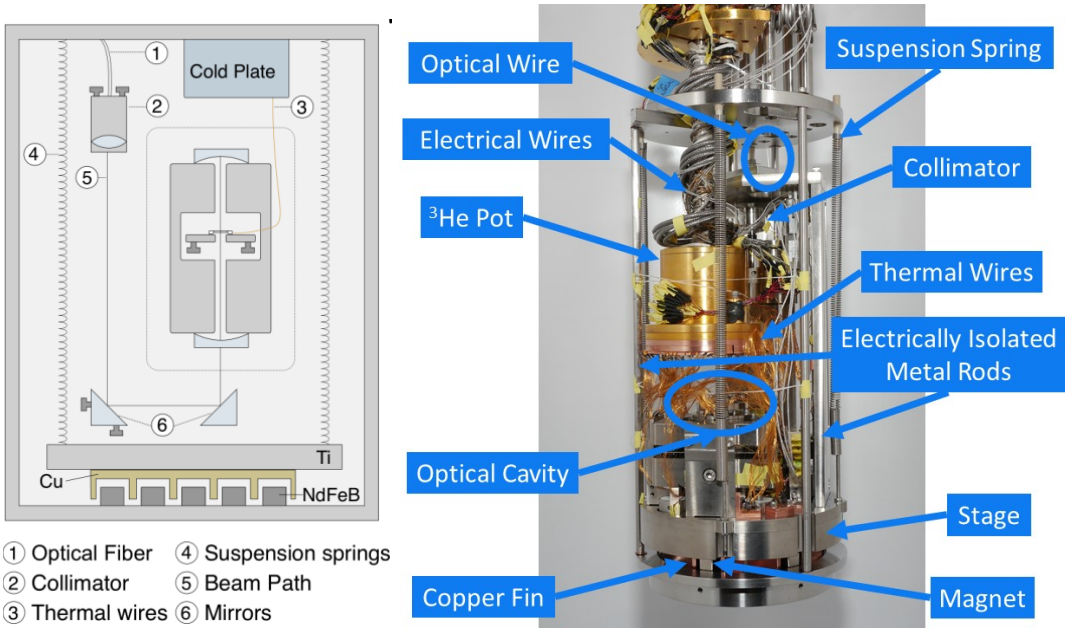

(a) (b)

Figure 4.11: The cryogenic platform used for this experiment. a. Schematic of the platform. b. Photo of the platform. Figure adapted from [33, p.34, Figure 2.2] and [70, p.56, Figure 3.6].

experiment.[6]

The IVC is connected to a chamber called the 1K pot (Figure 4.10b). The 1K pot has a vent that is either be vented or pumped. Pumping the 1K pot can be used to bring the ^{3}He pot to a base temperature of 300 mK (see [70, pp.54-5], [33, pp.33-4], [64, p.88] for a description of how this was done in past experiments). For the experimental work in this thesis, the 1K pot was never pumped, since the non-Hermitian dynamics do not fundamentally depend on the bath temperature. Thus, the only regular maintenance the fridge undergoes is the transfer of ^{4}He into the bath space, to replace the boiled-off ^{4}He.

A single mode fiber from the optical table (Section 5.1.1) is directed into the fridge (Figure 4.11). This fiber enters a collimator, which is a long, narrow tube that focuses the fiber light in free space in the direction of the cavity. Specifically, the collimator sends the light from the fiber in free space to a 45 degree adjustable steering mirror. This light then goes to a separate nonadjustable 45 degree mirror, which then directs the light into the input mirror of the cavity (Section 4.2.1).

The collimator and the adjustable steering mirror are mounted on 3-axis piezo-electrically controlled mounts, manufactured by JPE. The mounts have been highly stable with respect to long-term position drift; from 2018 to 2021, we never had to tune the motors for the collimator and mirror mounts.

[6] In particular, the noise from compressors for a dry fridge was undesired for the ground-state cooling experiment.[64]

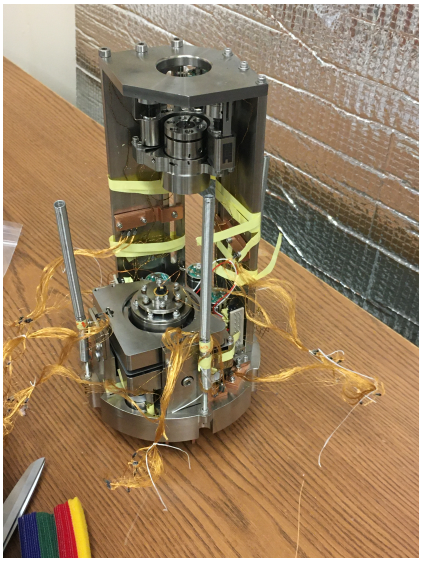

Figure 4.12: The springs, the collimator, and the optical cavity, removed from the helium insert. These were removed when the setup was disassembled and moved from SPL to YSB.

A strong thermal link needs to be maintained between the ^{3}He plate and the experimental optical cavity. Thus, roughly 1000 very thin, gold-coated copper wires connect these two, as shown in Figure 4.11. The connections are somewhat loose, so that the plate and the cryogenic platform are vibrationally isolated.

The Janis fridge is placed on pneumatic nitrogen gas supports (Newport S-2000A-128 [70, p.56]). This provides seismic isolation for the contents of the fridge. In addition, the cavity is built on a $\sim$1 kg Ti plate in the IVC. Titanium has low thermal contraction and high thermal conductivity in a cryogenic setting. This plate is suspended on critically damped springs, to further isolate the optical cavity from vibrations inside and outside the cryostat. The critical damping is achieved with eddy currents that come from the copper fins on the platform and permanent magnets fixed underneath the platform. Figure 4.12 shows the magnet, the springs, the collimator, and the optical cavity removed from the helium insert.

4.3.2 ^{4}He Recovery in the "Wet" Fridge

Because the fridge used in this experiment is a "wet" ^{3}He fridge, we do not continuously boil off and recondense the ^{4}He via adjacent compressors. Instead, we must bring an external dewar of ^{4}He to the fridge, and transfer the ^{4}He into the ^{4}He bath. This could be achieved by placing orders for 100 L dewars of liquid ^{4}He every week. However, this is cumbersome[7] and very expensive.[8] Thus, we opt instead to take the ^{4}He boil off from the fridge bath, and reliquefy the boil off in-house.

[7] To obtain these dewars for a given week, we would have to place dewar orders with Airgas by Thursday the week before.

[8] One 100 L dewar cost 1676.48 USD, on 2021 May 17.

The ^{4}He boil-off is collected via a recovery system. This recovery system is connected to a vent on the dewar bath. The recovery system takes the gaseous ^{4}He from the bath vent to a separate "recovery room." The recovery system has both a "small" and a "large" recovery line; the large line allows $\sim$16 oz/in^2, and a typical pressure in the small line is $\sim$3 oz/in^2. For normal, day-to-day operation of the fridge, the small recovery line is open, and the large line is shut. For ^{4}He transfers, the small line is shut, and the large line is open.

In the recovery room, the recovery line collects the gaseous ^{4}He into a series of tanks. These tanks can hold up to 8 bar of gas; any excess of this is released into the environment.

The helium tanks are connected to a Quantum Design ATP80 (Advanced Technology Purifier, 80 L).[9] This gas can contain water vapor, nitrogen vapor, and other impurities. Thus, the ATP cools the gas down to about 13 K, which is enough to condense any liquid or nitrogen vapor, but still above the liquefaction point of ^{4}He at 4.2 K. The impurities are collected in the ATP purifier cartridge. If this cartridge is saturated, the ATP will block the flow of gas. A compressor and coldhead provide the cooling (detailed in [73, Section 1.3.2]). The ATP outputs ^{4}He with a purity of better than 99.999%.

The output of the ATP goes to an ATL160 (Advanced Technology Liquefier, 160 L). The ATL has a 1.5 W coldhead, which actively cools the ^{4}He gas to below 5 K [74, p.1-2]. Any gas which is not liquefied is redirected back to our tanks, which then goes back to the ATP in a closed cycle. The ATL maintains the dewar at 1 psig, which allows the dewar to be ready for a helium transfer at will.

Over the course of the experiment, the ATL generally holds 80 L to 110 L (its capacity is 160 L). When the Janis fridge is low on liquid ^{4}He (as measured by a level-meter that measures the liquid ^{4}He level in the bath), the ATL liquefaction is stopped, and the ATL is carted over to the fridge. A transfer line is stuck into the ATL dewar and the fridge,[10] then the ATL transfer function is turned on. When 100 L is transferred from the ATL to the fridge, the next transfer is in 9-10 days. If done correctly, the transfer efficiency is such that gas ^{4}He cylinders need only be purchased every three months.

4.4 History of the MIM Experiment

The membrane-in-the-middle (MIM) setup used for this experiment was designed in 2012 for two major experiments: quadratic optomechanics and ground-state cooling [64] [33]. In the

[9] As necessary, we can supplementally order 10 L cylinders of ^{4}He gas, and supply these to the ATP. This puts 10 L into the recovery circulation system. Each of these cylinders cost 96.26 USD on 2020 December 4.

[10] More specifically, a transfer line is put into the ATL. The line is slowly inserted until the cold ^{4}He gas being expelled on the other side of the transfer line shows a "white flame;" this is a signature that the line has hit the liquid ^{4}He, and that air has been flushed out of the line. The other end of the line is then put into the fridge ^{4}He bath vent.

quadratic optomechanics experiment [75], two cavity modes were coupled to the motion of a single mechanical oscillator at avoided crossings in the cavity spectrum (c.f., Section 4.2.2). In the ground-state cooling experiment [76], a vibrational mode (at $\omega_m = 705\,\mathrm{kHz}$, with effective mass 43 ng) was cryogenically and optomechanically cooled close to its quantum ground state (to a phonon occupancy of 0.84 ± 0.22). The ground-state cooling experiment presented a major technical challenge with the laser noise, which set a fundamental limit on optomechanical cooling, which was overcome with two carefully locked filter cavities.

The MIM setup had been carefully engineered to achieve quantum ground-state cooling; ironically, the experiments performed after the ground-state cooling experiment were entirely classical. In 2016, the experiment was used to demonstrate energy transfer between two nearly-degenerate mechanical modes, with an optically-mediated coupling produced by one laser tone, by quasiadiabatically encircling a degeneracy known as an exceptional point [6]. Later in 2017 and 2018, the setup was extended to couple any two modes [31] with two laser tones, as well as to produce nonreciprocal, tunable, and continuous coupling between two modes via four laser tones [32]. All of these experiments only required coupled harmonic oscillators with an exceptional point degeneracy, and were essentially possible with any system of coupled harmonic oscillators besides the optomechanical MIM setup.

When I joined the MIM experiment in 2018, the main focus of the experiment was to explore higher-order exceptional points in coupled-oscillator systems. Specifically, the goal of the experiment was to experimentally demonstrate a third-order exceptional point (EP_3), and explore the extended EP_2 space near the EP_3 point. Restricted to a manifold surrounding EP_3, the extended EP_2 space is known, from algebraic geometry [14] [9], to form a trefoil knot. The experimental goal was to measure this EP_2 trefoil knot, and to measure eigenvalue braids around closed loops enclosing the knot.

Chapter 5

Data Acquisition

5.1 Optical Table

5.1.1 Optical Paths

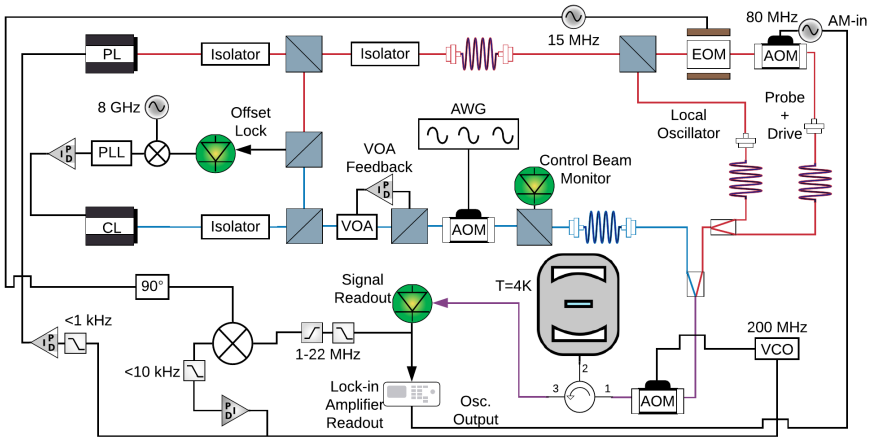

Figure 5.1: Detailed optical diagram. The red path is the probe laser path. The blue path is the control laser path. The purple path is the probe and control laser paths combined. Black lines denote electronics.

In this section, we provide an overview of the optical setup used in this experiment. This optical setup is responsible both for optomechanically controlling the membrane, which lives in a Fabry-Pérot cavity inside a 4K cryostat, as well as for driving and reading out the response of the membrane.

The full optical setup is shown in Figure 5.1. There are are two Nd:YAG lasers on the optical table: one laser is used to drive and read out the response of the mechanical membrane, and the other is used to optomechanically control the frequencies and dampings of the membrane's vibrational modes.

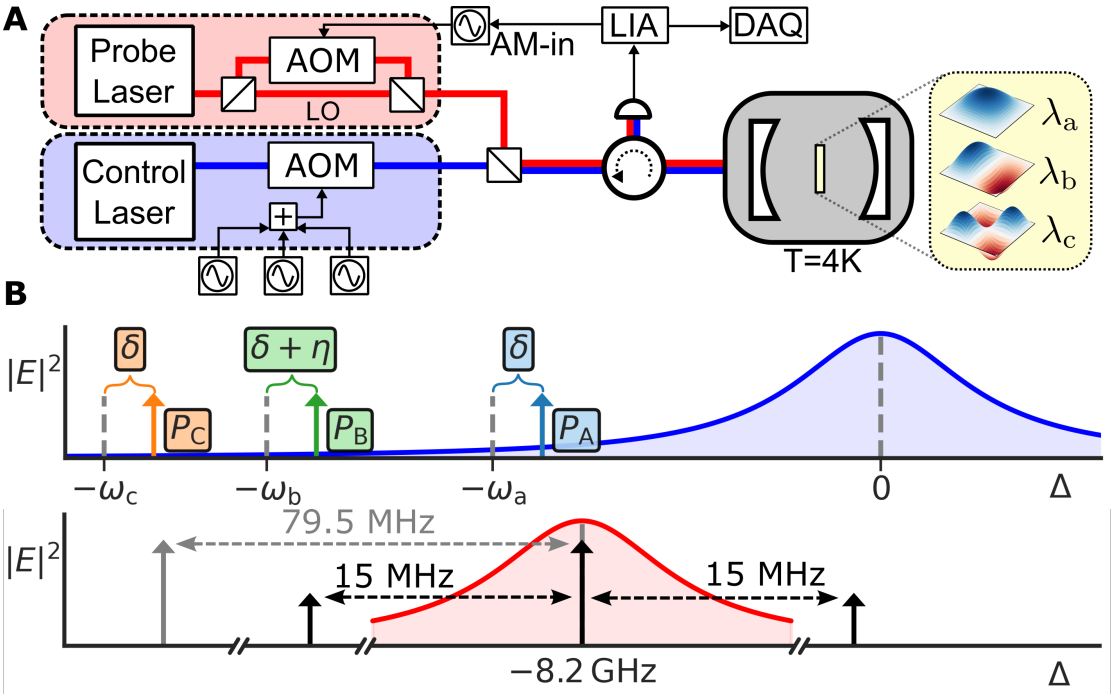

Figure 5.2: A: A simplified diagram of the experimental setup. B (upper): The control laser tones used in this experiment. The horizontal axis gives the detuning with respect to the cavity mode addressed by the control laser. The AOM produces three optical tones which optomechanically control the membrane mechanical modes. B (lower): The probe laser tones. The probe laser is approximately two FSR's red-shifted from the control laser frequency. The LO (grey) is −79.5 MHz away from the mechanical drive. The mechanical drive is produced by an AOM. The 15 MHz sidebands are produced by an EOM, and are used for PDH locking.

Probe Laser Path

The probe laser (Figure 5.1, red path) is used to mechanically drive the membrane, as well as read out its motion. The probe laser first goes through an isolator (which helps with frequency stability), then goes through a free-space polarizing beam splitter that splits into two paths: one responsible for the driving and probing, and another that is used for frequency-locking the control laser frequency to the probe laser frequency (with an RF frequency offset, as described in Section 5.2.2).

From the first beam splitter, the probe path is further split by a second free-space polarizing beam splitter (before this beam splitter, another isolator is used). This polarizing beam splitter creates the heterodyne measurement, by splitting the laser into a local oscillator (LO) path, and a modulated path that contains the mechanical drive.[1] The mechanical drive is produced as the output of a free-space acosto-optic modulator (AOM), which takes as its inputs the probe beam, and an RF tone created from a lock-in amplifier (Zurich HF2LI) and an electronic circuit (Section 5.3). This RF tone contains the mechanical drive, and has a frequency of approximately

[1]Before this polarizing beam splitter, the beam passes through a half-wave plate that rotates the polarization direction of the probe beam. We rotate this half-wave plate to tune the power in the LO, since the LO is created from the polarizing beam splitter.

79.5 MHz. Before the AOM, the probe beam is modulated by an electro-optic modulator (EOM), which adds phase modulation sidebands at ±15 MHz. These sidebands are used to lock the probe laser frequency to the cavity mode, as described in Section 5.2.2. These tones are shown in Figure 5.2 (red).

The free-space local oscillator and the AOM-driven paths are then put into fibers, which then get recombined via a fiber coupler. This path is recombined with the control-laser path (Figure 5.1, blue path) via another fiber coupler, and this three-path combination is sent to the cavity (Figure 5.1, purple path).

Control Laser Path

The control laser is produced from a second Nd:YAG laser. This control laser is also split by a polarizing beam splitter into two paths: one responsible for the control, and another that beats the control laser with the probe laser. The beatnote of these two lasers is used in a PI-loop to frequency-lock the control beam at the probe laser frequency, plus a frequency offset (Section 5.2.2). For the remainder of this section, we will talk about the second control-beam path, which is used for optomechanical control.

The control-beam intensity is regulated by a variable optical attenuator (VOA)-based feedback loop (Section 5.2.4). The purpose of this loop is to keep the control laser intensity fixed, before any control tones are created from RF inputs (discussed in Section 5.3.2).

With the intensity and the frequency of the control laser having been regulated by two PI feedback loops, we send this control beam as the input of another AOM. This AOM is driven by three RF tones, which produce the three optical tones responsible for optomechanically controlling the membrane mechanical modes considered in this experiment (Section 5.3). These three optical tones are shown in Figure 5.2 (blue), where they are determined by four experimental parameters: three laser powers P_k, $k = 1, 2, 3$, as well as a common detuning parameter δ (η is a fixed parameter that specifies the rotating frame $\mathcal{R}$, which is described in Section 3.6.

This AOM-modulated control beam is sent to a fiber, which is split by a 90:10 fiber-based nonpolarizing beam splitter. The 10% path is sent to a photodiode, which is used to measure the control tone powers, and ensure that the control tone powers are what is desired for the experiment (Section 5.3.3). The 90% path is then combined with the heterodyne signal from the probe beam path via a fiber coupler (Figure 5.1, red path), and this combined signal is sent to the cavity (Figure 5.1, purple path).

Probe and Control Paths Combined

The combination of the probe and control beam paths (Figure 5.1, purple path) is sent to the cavity in order to drive and read out the motion in a heterodyne measurement. Before this, the beam is sent to a fiber AOM, which is used as part of the frequency lock for both the probe and the control lasers (Section 5.2).

The output of the fiber AOM is sent into a circulator (Figure 5.1, port 1 of the circulator).[2] The input of port 1 of the circulator is output at port 2, which sends the beams to the cavity via a fiber. This fiber goes from the room-temperature optical table to the 4K cryostat, in which the cavity lives. The measurement is done in reflection, and the reflection is input to port 2, which is then output at port 3. The signal is then read out by a fiber photodiode, and the electronic signal is sent to a lock-in amplifier (Section 5.3). This same lock-in amplifier is the RF source used to drive the membrane (Section 5.3.1). The electronic signal is also used to generate a Pound-Drever-Hall (PDH) error signal, by mixing with the 15 MHz tones mentioned above. This signal is used to lock the probe laser to a cavity mode.

5.2 Laser Locking Methods

In this section, we describe the techniques that we employ to lock the lasers' frequencies and the control laser's intensity. We frequency-lock the probe laser frequency to a cavity resonance because temperature and mechanical fluctuations can cause the cavity resonance frequency to vary with time. This stabilizes the relative frequency between the probe laser and the cavity resonance, and minimizes the effect of these fluctuations on the frequencies of the driving and readout tones applied in this experiment. Additionally, we frequency-lock the control laser to the probe laser frequency, shifted by two free-spectral ranges (FSR's) of the cavity, so that the control laser addresses a separate cavity mode, and can be used for optomechanical control of the membrane mechanical modes. In addition to frequency-locking, we stabilize the intensity of the control laser beam, to minimize unwanted power fluctuations in the RF control tones.

5.2.1 PDH Locking the Probe Laser

To frequency-lock the probe laser to a cavity mode frequency, we employ a common locking technique called PDH laser frequency stabilization [77].

In principle, to lock the probe laser to a Fabry-Pérot cavity mode of interest, we can raster the laser frequency around, and look for a frequency where the reflection dips to zero. This

[2] Before this circulator input, the output of the fiber AOM is sent to a 99:1 fiber-based nonpolarizing beam splitter. The 1% path is sent to a photodiode for a power measurement. This measurement was historically used to measure the control beam and probe beam powers [6, 31, 32]. In this experiment, it was only used to measure the probe beam power, but it does not play a critical role in this experiment.

happens only if the laser frequency is resonant with the cavity mode, and for symmetric, lossless cavities. For a non-symmetric cavity with loss, the reflection has a minimum. When one identifies where the reflection is at a minimum, then one can track fluctuations in the reflection versus the laser frequency, and if the reflection rises, then the laser frequency can be adjusted to bring the reflection back to zero, and maintain the lock. The problem with this first approach is that there is an ambiguity in the sign of the fluctuation in frequency: since the reflection coefficient is symmetric about the resonance (Figure 3.2), we cannot tell whether the frequency increased or decreased from the resonance just from an increase in the reflection.

The PDH technique is essentially this technique just described, yet it measures the signal phase by beating the signal with the $+15\,\mathrm{MHz}$ and $-15\,\mathrm{MHz}$ tones. The phase is linear in the detuning Δ from the resonance. This technique has the advantage that, though the reflection coefficient is symmetric about a cavity resonance (Figure 3.2), the phase is antisymmetric near resonance, so keeping track of the phase tells which way the laser frequency drifts from the cavity resonance.[3]

In the experiment, we achieve PDH modulation by sending a sine wave of frequency $14.848\,\mathrm{MHz}$ from a function generator as an RF input to an electro-optic modulator (EOM), which also takes the probe laser as an input (Figure 5.1). The EOM phase modulates the laser tone, as described in Appendix D, and produces $14.848\,\mathrm{MHz}$ sidebands on the pure laser tone. Then the AOM subsequently frequency shifts this superposition by approximately $79.5\,\mathrm{MHz}$.

To produce the PDH error signal, we demodulate the signal from the cavity readout with another $14.848\,\mathrm{MHz}$ sinusoidal waveform. In principle, this demodulation sine wave could be 0 degrees phase-shifted from the modulation waveform (see Appendix D or [78, pp.83]). In practice, the phase shift that produces a PDH signal that looks like Figure D.1 might not be 0 degrees, due to the lengths of the cables that connect the function generators to the EOM and to the mixer, respectively.[4] Fortunately, this phase shift is stable for multiple months, so long as the cables remain unchanged. To find the correct phase shift, one can modulate the EOM with a sine wave, then seek a phase offset that makes the PDH signal "maximally bad," in the sense that it is zero at the cavity resonance. This means that the real part of Equation D.9 is zero at the resonance, so the correct phase shift is 90 degrees from this maximally incorrect one (see Appendix D).

We should also note that this PDH signal is actually used for two probe laser locks: one fast lock, and one slow lock. First, the fast lock: the PDH error signal itself is sent to a proportional-integral-differential (PID) controller. This PID device is a Mokulabs Liquid Instruments Moku:Lab device. The PID settings we use are $P = -48.0\,\mathrm{dBm}$, $I = 3.000\,\mathrm{kHz}$,

[3] For a detailed description and mathematical derivation, see Appendix D and reference [78].
[4] As of this writing, the phase shift is 110 degrees.

$D = 25.00\,\text{kHz}$, $I^+ = 1.000\,\text{kHz}$. The output of this PID controller is low-pass filtered to <10 kHz, and is sent to a voltage-controlled-oscillator (VCO), the RF output of which is sent as the RF input to a 200 MHz AOM that all the laser beams go through (Figure 5.1, purple path). This AOM is used to stabilize all laser beams together, with respect to the cavity mode. Second, the slow lock: the output of the first PID controller is also used as an input to a second PI controller, which happens to be the second input on the same Mokulabs device. The second PI controller has settings $P = 0.0\,\text{dBm}$, $I = 1.000\,\text{Hz}$. The output of this controller is low-pass filtered to <1 kHz, then sent to the probe laser piezo. This second lock accounts for slow drifts in the laser frequency and the cavity resonance.

5.2.2 Shifted Locking ("Slocking") the Control Laser

In addition to a probe laser, there is a separate control laser that addresses a separate cavity mode. We do this so that we can independently drive and read out the membrane motion with one laser, and optomechanically control the membrane mechanical modes with other laser tones, without having to worry about intracavity beatnotes. Instead of locking the control laser directly to a cavity mode, we instead lock it at a frequency offset away from the probe laser frequency. The main reason we do this is because, for control tones, we do not want any beams near resonance. However, PDH locking works best when locking close to a cavity resonance, so we do not use PDH locking for the control beam. Additionally, this simplifies the locking circuit, in that we avoid needing a second PDH lock for the second laser. In this section, we describe the frequency-offset locking, and in the subsequent section, we describe how we ensure that the control laser indeed addresses an additional cavity mode.

As depicted in Figure 5.1, we take the probe laser through a polarizing beam splitter (red path), and the control laser through another polarizing beam splitter (blue path). One of those paths is used to drive the membrane, and the other is used to control the membrane modes. The other two paths of those beam splitters are combined together through another beam splitter. The polarizations of these beams are tuned with half-wave plates such that most of the beams' power is used for the probe and control, and only a small portion is used in the probe-control combination. The beat between the probe and control lasers at the output of the beam splitter is detected on a high-frequency photodiode. The control laser frequency is *a priori* set at nearly 2 free spectral ranges of the cavity, or about 8.2 GHz, upshifted from the probe laser frequency. The 8.2 GHz beatnote is then downconverted with a mixer and a Rohde-Schwartz SMB100A function generator. We use this downconverted signal for a "frequency-Shifted Lock," affectionately known in the Jack Harris Lab as the "Slock."

In previous years of this experiment, an older Slock circuit was used. However, it did not

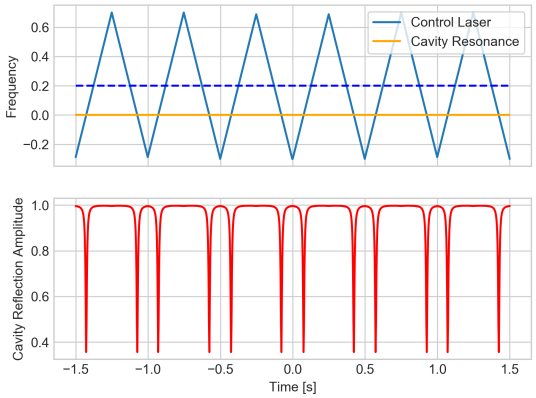

Figure 5.3: A simulation of sweeping the control laser frequency to find the cavity resonance. Top: the blue ramp is the frequency of the control laser (dashed blue line is the mean of the ramp), and orange is the cavity resonance. Bottom: cavity reflection in red. The reflection dips to minima whenever the ramped control laser frequency matches the cavity resonance (simulation done with cavity mirror reflections $r_1 = .9$, $r_2 = .95$).

provide enough stability in control laser detunings for this experiment, so we switched it out for several new ones. For discussions on the old Slock circuit, see [70] and [33, pp.45-46].

This new locking scheme takes the downconverted beatnote and sends it to a phase-locked-loop (PLL). This PLL is set to a center frequency of about 3 MHz. The output of this PLL is used as the error signal input to a PI control loop, on an additional Mokulabs unit, and the output of this control loop is fed to the control laser piezo. This locks the control laser frequency to the probe laser laser frequency, plus whatever frequency is chosen on the Rhode-Schwartz function generator (the exact value is discussed in the Sweetspot Measurement below; it is roughly 8.2 GHz).

5.2.3 Sweetspot Measurement

The slock that locks the control laser frequency to an offset of the probe laser frequency is not, *a priori*, necessarily resonant with any cavity mode. To ensure that it is resonant with the cavity mode, we must set the Rohde-Schwartz (RS) SMB100A RF frequency so that the control laser frequency is indeed two cavity FSR's away from the probe laser frequency.

After the correct RS frequency is found, the next step is to set the membrane piezo position. This is important because the optical modes change differently as a function of the membrane position, so the correct RS detuning changes as a function of the membrane position. Additionally, if this is not accounted for, then the control laser detunings are uncalibrated and unreliable due to their dependence on the membrane position. Thus, we need to minimize the dependence of the correct RS detuning on the membrane position. We call this the "sweetspot search."

First, to find the resonant RS frequency, we lock the probe laser to a cavity mode with the

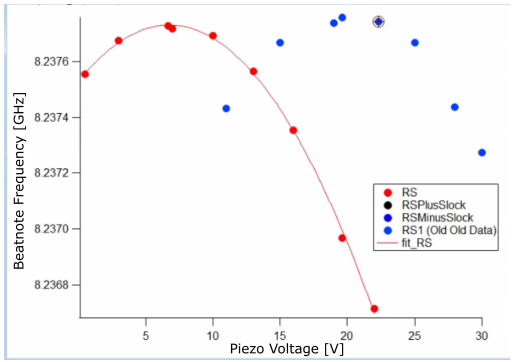

Figure 5.4: Sweetspot search after a helium transfer. The applied piezo voltage is swept, and the resonant Rohde-Schwartz (RS) frequency is plotted on the y-axis. The red points are the data taken after the transfer of 2021/11/07, and the blue points are the data taken from the previous transfer. The red points are fit to a parabola (red line), and the applied voltage and matching RS frequency are chosen.

PDH technique. We next lock the control laser to the probe laser.[5] Then, we turn on a control tone by sending an RF tone at 79.5 MHz as an input to the control AOM (the choice of 79.5 MHz is discussed in Section 5.3.2, which details the RF frequencies that optomechanically control the mechanical modes). We next turn on frequency modulation on the Rohde-Schwartz SMB100A. This effectively sweeps the control laser frequency around a center frequency. A simulation of this is depicted in Figure 5.3. If the cavity resonance is within the RS frequency sweep range, then the reflection will have dips. If the dips occur at the center of the RS frequency sweep, then the center frequency corresponds to the control laser frequency being on resonance with the cavity. A proxy for this is that if these dips are equispaced in frequency (and time), then the control laser frequency matches the cavity resonance.

We do this for a range of membrane positions, and find the position for which the difference between the two mode frequencies is least sensitive to the fluctuations in the membrane position. The membrane position is directly proportional to a DC voltage applied to the piezo, and the frequency difference vs the DC voltage is a parabola.[6] A sample sweetspot search is shown in Figure 5.4. Thus, we can seek the maximum (or minimum) of the parabola, and set the position to be at this extremal point. This minimizes the first derivative of the difference between the two modes' frequencies versus membrane position, and minimizes the sensitivity of the frequency difference to fluctuations in the membrane position. We repeat this procedure after every helium transfer.

[5] For this lock, we do not use the PLL-based feedback loop, but we use a "slock" integrated circuit, which works in the same way as the "slock" circuit discussed in [70] and [33, pp.45-46], but offers better lock frequency tunability. The tuning range of this integrated circuit is ~ 400 MHz before it unlocks. We use this integrated circuit for the sweetspot measurement because the PLL-based feedback loop has PID parameters that are optimized for stability and not dynamic range – it unlocks when the RS center frequency is swept, which we need to do in order to do the sweetspot measurement.

[6] The curve is actually sinusoidal (c.f., Figure 4.9), but we do these measurements over a region where the curve is approximately a parabola.

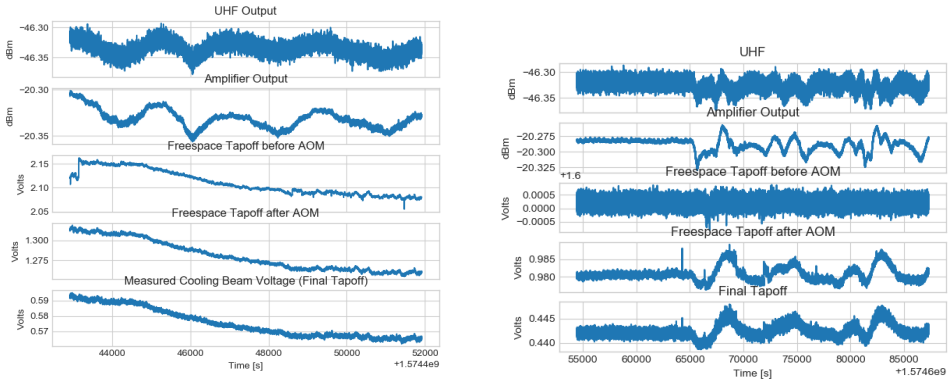

Figure 5.5: The effect of the control laser power stabilization. Left: the voltage vs time without the VOA power stabilization, taken over 2.5 hours. The value of (max-min)/min at the final tapoff before the cavity is 3.5%. Right: the voltage vs time with the VOA power stabilization, taken over 8 hours. The value of (max-min)/min is 1.8%.

5.2.4 Control Laser Power Stabilization

A big challenge in this experiment was ensuring that the control tone powers were very stable over the course of a measurement. In the experiment, we would do sets of multiple driven response measurements that could last for a whole day, or even two days, so we needed the control laser power itself to be held at a constant during that period.

To fix the control laser power that enters the control AOM, which is responsible for making control tones, we indirectly fix the control laser power with a variable optical attenuator (VOA). The VOA takes a fiber-optical input and an DC input, and has a fiber-optical output. The DC input determines the VOA attenuation factor.

The VOA is placed after the polarizing beam splitter that leads to the slock, but before the control AOM. After the VOA, we use a 90:10 nonpolarizing beam splitter to divert laser power to a PDA36A photodiode.[7] The output of the PDA36A photodiode is sent directly to a proportional-integral (PI) box (New Focus LB1005). All we do is turn that PI box on and send the output as the DC input to the VOA.

To test how well this feedback loop holds the control laser power constant, we apply an RF tone on the control AOM, and we measure the control laser power at three tapoff photodiodes: one that comes before the control AOM, one that comes after the control AOM, and one that comes after the fiber coupler that combines the control and probe beams, but just before the cavity that contains the membrane. We show this in Figure 5.5. In the left-hand side, we do not have any control laser power stabilization circuit, and on the right-hand side, we use the VOA-based power stabilization circuit described above. On the left side, we see that the unaddressed

[7] It is important that this beam splitter be nonpolarizing, because if we split the beam based on its polarization, we would conflate polarization fluctuations as intensity fluctuations, and the feedback to the laser intensity would be erroneous.

control power fluctuations before the AOM dominate the control tone power fluctuations that the cavity sees. On the right side, when these fluctuations are fed back to the control laser intensity and used to stabilize it, any fluctuations that occur at the final tapoff no longer occur before the AOM. Furthermore, the size of the fluctuations at the final tapoff, as quantified by $(V_{\max} - V_{\min})/V_{\min}$, has decreased between the two measurements.

This simple feedback loop is enough to hold the control laser power constant, to within 2% over a period of multiple days. In tandem with the Slock that directly locks the control laser frequency to the probe laser frequency, plus an offset, we can reliably specify control laser powers and detunings, and have them be fixed for the duration of our day-long experiments. We later further specify the precise control beam power that the cavity sees by calibrating the RF voltages that are sent to the control AOM, as described in Section 5.3.3.

5.3 Electronic Setup

5.3.1 Heterodyne Measurement Electronics

In this section, we describe how we drive the membrane, and how we read out the membrane motion.

To drive the membrane, we use an acousto-optic modulator (AOM) that has a response near 79.5 MHz. The RF signal required to actuate the AOM is produced with a Hewlett-Packard function generator (HP8642B). We also use the amplitude modulation input on the HP, and this amplitude modulation takes the mechanical drive at frequency ω_{AM} that we want to send. The frequency of this drive is hundreds of kilohertz. For this experiment, the primary drive frequencies ω_{AM} are 352 kHz, 557.4 kHz, and 705 kHz.

This mechanical drive signal ω_{AM}, which is carried by the HP8642B tone at 79.5 MHz, is sent from the HP8642B to the AOM (Figure 5.1, red path). This induces AM sidebands on the AOM carrier, at frequencies $79.5\,\mathrm{MHz} \pm \omega_{\mathrm{AM}}$. This signal then gets carried through the laser beam path described in Section 5.1.1. When the drive reaches the cavity and is reflected back, the membrane induces sidebands on the probe tone.

The signal from the cavity is then read from the circulator, and a photodiode reads the optical signal and produces an electronic response. This response is split by a bias tee into low- and high-frequency components (Figure 5.6). The low-frequency component is read directly on an oscilloscope. This DC signal is proportional to the total reflected laser beam power, and it is used to monitor the amplitude of the cavity reflection; when it is at a minimum, the probe laser is locked to its cavity mode. The other path contains higher frequency components, including the beatnote between the local oscillator beam and the probe beam at 79.5 MHz. The probe

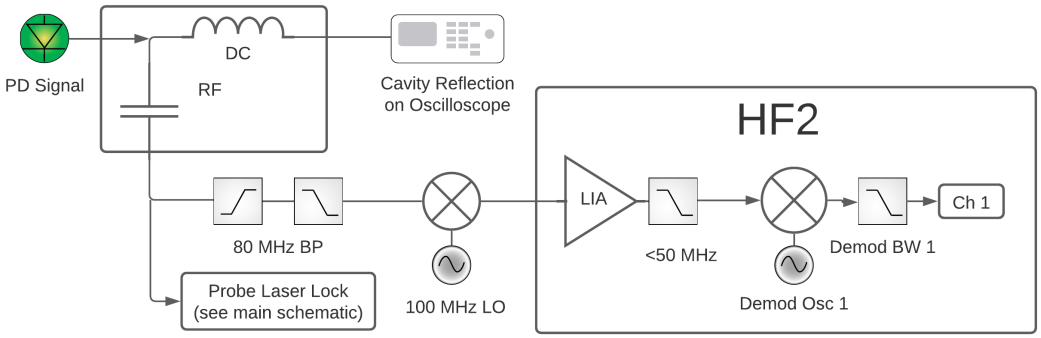

Figure 5.6: The measurement electronics that digitize the cavity signal. The cavity reflection is monitored on the oscilloscope in the top path. The membrane motion is measured with a Zurich HF2 LIA in the middle path. The probe laser is locked to a cavity mode in the bottom path (see Figure 5.1 and Section 5.2.1). Adapted from [33, Figure 2.8] and [70, Figure 3.9].

beam contains sidebands from the membrane motion, so the beatnote between the probe and the LO contains these sidebands as well. This signal is split into two paths: one to lock the probe laser to its cavity mode (Section 5.2.1), and another to read out the membrane motion with heterodyne measurement.

The heterodyne measurement path is sent through an 80 MHz bandpass filter, to isolate the 79.5 MHz beatnote between the local oscillator and the probe, then mixed with a 100 MHz source, since our HF2 lock-in amplifier can only read signals of up to 50 MHz. The HF2 then reads the downconverted 20.5 MHz beatnote with a lock-in amplifier. The lock-in amplifier demodulates the beatnote by the LO, which is locked by the PLL (Figure 5.6, where Osc 1 is the PLL-locked LO frequency). Finally, the lock-in amplifier reads this demodulated signal at a frequency ω_{read}. The signal $V[\omega_{\mathrm{read}}]$ is a complex signal, which is read in two quadratures (as described in Section 6.1.2). For the EP_2 and EP_3 measurements in this experiment (as described in Section 5.4 and Chapters 2 and 6), we set $\omega_{\mathrm{read}} = \omega_{\mathrm{AM}}$.[8]

5.3.2 Optomechanical Control Electronics

In this section, we describe how we produce optomechanical control tones. These tones are used to shift the frequencies and dampings of our mechanical modes. This lets us bring our system to exceptional points, and lets us explore the full space of eigenvalues near our triply degenerate exceptional point.

Optical tones are produced by sending the control laser of frequency ω_{L} through an acousto-optic modulator (AOM), then sending an RF input of frequency ω_{RF} to the AOM. The AOM diffracts the laser input into multiple spatially separated outputs, and each output has a Doppler-

[8] We are free to set ω_{read} to any frequency at which we want to read the membrane motion. For dynamics measurements, in which we drive one membrane mode ω_1 and transfer energy to a different mode ω_2, we set the HF2 drive frequency $\omega_{\mathrm{AM}} = \omega_1$ and read the membrane motion at $\omega_{\mathrm{read}} = \omega_2$, as in [6] and Chapter 7.

shifted frequency, equal to $\omega_{\mathrm{L}} + n\omega_{\mathrm{RF}}$, for all $n \in \mathbb{Z}$. For our experiment, we focus on the AOM output of frequency $\omega_{\mathrm{L}} + \omega_{\mathrm{RF}}$. The RF input gets sent to the control laser path (Figure 5.1, blue path). Then the control laser tone is shifted in frequency by the control RF signal, and gets carried through the laser path, as described in Section 5.1.1.

In the experiment, AOMs from Gooch and Housego were used to produce the optical control tones. These AOMs are designed to respond at RF center frequencies of around 79.5 MHz. We recall from Section 5.2.2 that the control laser frequency ω_{L} is locked to the probe laser frequency ω_{P} (of order 300 THz), plus a frequency offset Δ_{RS}, given by the Rohde-Schwartz frequency (having already PDH-locked ω_{P} to a cavity mode). We also recall that this Δ_{RS} is chosen during the sweetspot search (Section 5.2.3) such that a control tone from the AOM, applied at 79.5 MHz on the function generator, is two FSR's above ω_{P}, which sets $\Delta_{\mathrm{RS}} \approx 8.2\,\mathrm{GHz}$. We subsequently decrement the Rohde-Schwartz frequency Δ_{RS} to a frequency $\Delta'_{\mathrm{RS}} = \Delta_{\mathrm{RS}} - 705\,\mathrm{kHz}$, such that the RF input at 79.5 MHz drives at the red cavity sideband at 705 kHz, which optimally cools the $(2, 2)$ mechanical mode at 705 kHz. To drive at the red sideband at a different frequency ω_m, and thus optomechanically cool the membrane motion at frequency ω_m, the RF frequency is

$$\omega_{\mathrm{RF}} = 79.5\,\mathrm{MHz} + (705\,\mathrm{kHz} - \omega_m) \tag{5.1}$$

There are a number of ways we could produce these tones. The way this was done in [6] was to use a second Hewlett-Packard that could accept both amplitude and frequency modulation inputs. This was useful in producing control loops in both laser tone power and detuning. Another method that was used in the early phase of this project was to use a second Zurich HF2 to send three control tones. This had the limitation that the HF2 could only send tones of up to 50 MHz, and the AOM needs tones near 79.5 MHz, so we used an additional 100 MHz local oscillator and mixer, but this introduced power fluctuations from the mixer, which adds fluctuations to our intended control tone powers.

In the experiment, a control RF tone is produced from a Rigol function generator (Rigol DG4162) that can output sine waves of frequencies up to 100 MHz. We use two of these function generators: two ports on one, and one port on the second. The RF powers and detunings from the function generators themselves are very stable, up to the order of 1 mHz, and the voltages are stable up to 100 µV. Since we send frequencies of approximately 79.5 MHz and voltages of order 10 mV, this stability is very good for the experiment. We combine these into a 3-port signal combiner, and send this output through an amplifier that goes directly to the control AOM.

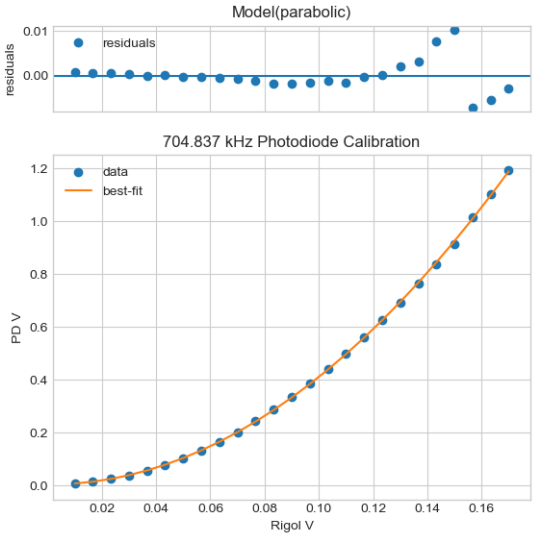

Figure 5.7: Calibration of the power of the control tone that addresses the 705 kHz mechanical mode, as a function of the RF input voltage. The RF frequency is set to 79.5 MHz. Blue points are data taken at each RF voltage from a Rigol function generator. The orange is a fit to a parabola of the form $aV^2 + bV + c$. Units are volts on both axes.

5.3.3 Calibration of Laser Powers

This section describes how, in the experiment, we ensure that the control laser powers are close to the desired control laser powers. This is important because, in order to realize exceptional points in the experimental (δ, P_1, P_2, P_3) parameter space (Figure 5.2), it is not enough to simply dial nominal control tone powers into the experiment and hope that the actual powers match the desired powers; we need to be able measure and control the control-tone powers *in situ*. To do this, we put the three optical tones through a 90:10 non-polarizing beam splitter one at a time, and then measure the optical powers in the 10% path as a function of the input function generator voltage. These curves then are fit to parabolas, and are used to choose function generator voltages that produce the desired control tone powers.

To measure the AOM output power, we send the AOM output to a 90:10 non-polarizing beam splitter, and measure the 10% path on a free-space photodiode. The amplitude of the AOM response is frequency-dependent, so we must take three RF inputs to address each of three of the mechanical mode frequencies in the experiment: $\omega_1 = 352.3\,\text{kHz}$, $\omega_2 = 557.2\,\text{kHz}$, and $\omega_3 = 705\,\text{kHz}$. We send each of those frequencies into the AOM, and measure the three responses there.[9] To account for the possibility of different cable lengths affecting the RF output to the AOM, we do these measurements on each of the three physical RF input lines. The photodiode gain is set such that the saturation point is above what we expect the needed control tone powers

[9]The RF output frequency has a precision of 1 mHz, so the frequency stability is very good, compared to the hundreds of kHz of the mechanical modes.

to be. For each of these RF frequencies, the photodiode voltage is quadratic in the RF input voltage, as shown in Figure 5.7. Then, the voltage that the photodiode reads is proportional to the laser power. From the photodiode spec sheet [79], the power P_{in} incident on the photodiode as a function of measured voltage V_{in} is $P_{\text{in}} = V_{\text{in}}/(2.38 \times 10^3\,\text{V/A})/(0.72\,\text{A/W})$. These two transformations together get a curve of the form $P(V_{\text{in}}) = aV_{\text{fg}}^2 + bV_{\text{fg}} + c$. A least-squares fit determines the coefficients a, b, c, and tells what voltage must be set on the function generator to get a desired control beam power.

5.4 Measurement of Exceptional Points

In this section, we discuss the data acquisition process that measures eigenvalue spectra in the MIM experiment.

The measurement procedure, from start to finish, is outlined here:

1. Lock the probe laser to a cavity mode via the PDH technique (Section 5.2.1)

2. Lock the control laser at a frequency offset from the probe laser. The RF offset is set by a function generator, and is approximately 8.2 GHz, which is approximately two FSR's of the cavity (Section 5.2.2).

3. Perform a sweetspot measurement to tune the frequency lock RF offset (so that the control laser addresses a separate cavity mode), and set the membrane piezo position (so that the optical mode addressed by the control laser moves in tandem with the optical mode addressed by the probe laser (Section 5.2.3)).

4. Perform rudimentary estimates of the optomechanical coupling constants for each of the membrane mechanical modes considered in this experiment. These measurements are also used to estimate the cavity linewidth.

5. Use these estimated coupling constants and the estimated cavity linewidth to estimate the location of exceptional points in our system.

6. Acquire datasets that contain the exceptional points in the (δ, P_1, P_2, P_3) experimental parameter space. These datasets can be one-, two-, or four-dimensional in the parameter space. For each value of these parameters in these datasets, set the control lasers to these parameters, then perform spectroscopy on the driven responses of the three mechanical modes. Do this for every point in the dataset (Section 5.4.1).

7. Analyze these datasets (Chapter 6). This involves fitting the spectra to extract the complex eigenvalues, then calculating the EP_2 and EP_3 metrics to determine the presence of

exceptional points in the parameter space.

5.4.1 Dataset Acquisition

Here, we discuss step 6 in the above list. When we begin measuring the data in this dataset, the three control tones are set to zero power. We then run a Python script, which takes the desired (δ, P_1, P_2, P_3) values in the dataset, to automatically execute the procedure below:

1. Perform a g_0 measurement, in order to set the control laser locking point such that a 79.5 MHz control tone on the Rigol function generator is set to address the 705 kHz mechanical mode. This g_0 measurement reveals the offset in the frequency axis. We correct the PLL center frequency by this offset.

2. Calibrate the three RF powers, as discussed in Section 5.3.3. This converts our desired experimental parameters from units of power to voltages on the function generators.

3. At a point in parameter space, do the following:

   (a) Set the Rigol function generators to the correct frequencies, and set all three outputs to zero power.

   (b) Measure the power in the probe beam path, with the local oscillator path blocked by a USB-controlled shutter. Then, for each control tone, set the control tone to the voltage that gets the intended power, then measure the probe power plus the control tone power, for each of the three control tones.

   (c) Set all three control tones voltages to the voltages that were obtained in the power calibration step, then open the local oscillator shutter.

   (d) For each of the 352.3 kHz, 557.4 kHz, 705 kHz modes, perform a driven response measurement. This entails sweeping the frequencies near each of these three mechanical modes, plus or minus about 400 Hz for each of them. A sample set of spectra is shown in Figure 5.8.

4. Do this for every point in the dataset. In the event that either the probe or the control lasers unlock in the measurement loop, the program halts and asks the user to relock the laser, then resume the measurement loop.

5. When the measurement finishes, set the function generator voltages to zero, turn the outputs off, then shut the local oscillator shutter.[10]

[10] A good way to ensure that resources are closed in Python is to use a `try:... finally:...` block. This way, if anything unexpected happens in the measurement loop that halts execution, the resources will be turned off in all cases[80, Section 8.4].

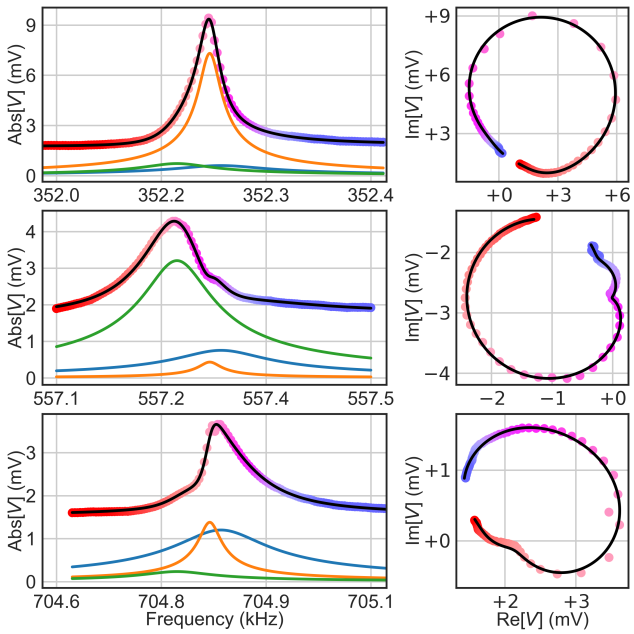

Figure 5.8: Driven response spectra for each of the three mechanical modes. The amplitudes of the spectra are plotted in the left-hand plots, and the same three spectra are plotted in the complex plane on the right-hand side. The red-to-blue coloring represents the drive frequency. This coloring serves to identify frequency values between the left- and right-hand plots. The black curves are fits to sums of nine Lorentzians (the fit is detailed in Chapter 6), and the blue, orange, and green curves are the individual Lorentzians extracted from these fits.

5.4.2 Zurich HF2 LIA and Drive Settings

For these measurements, the settings on the Zurich HF2LI were set such that the 3 dB bandwidth of the lock-in is set to 13.1 Hz, the filter is third order (18 dB/oct).

For spectroscopy, we scan a range of about 400 Hz around the mechanical modes. We use a settling time of 15 time constants at each point in the spectroscopy. The time constant sets the integration time of the demodulator inputs, which averages more measurement noise out [81, pp.64]. The time constant corresponding to a 13.1 Hz bandwidth is 12.1 ms. In the spectroscopy, we sample 120 frequency points in the sampling range, so the time it takes to do one spectrum is about $12.1\,\text{ms} \times 15 \times 120 \approx 21.8\,\text{s}$.

The amplitude of the signal sent from the Zurich is 400 mV. This signal goes to the AM port on the Hewlett-Packard (HP 8642B). The modulation depth is set to 10% in most measurements, and the carrier amplitude is 13 dBm. This RF drive goes to the probe AOM (Figure 5.1, red path), which then optically drives the membrane.

Importantly, the amplitude response of the membrane motion is roughly linear in the drive power, at these drive settings. This is important because when we do a driven response measurement, we do not want the response of the membrane motion to saturate and artificially broaden (thus increasing our extracted linewidths). We see that this saturation does not occur at these settings in Figure 5.9.

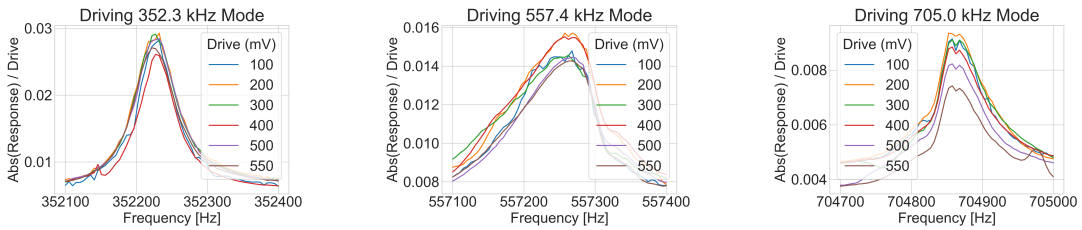

(a) $\omega_m = 352\,\text{kHz}$ (b) $\omega_m = 557.4\,\text{kHz}$ (c) $\omega_m = 705\,\text{kHz}$

Figure 5.9: Driven response for several driving amplitudes, at a modulation depth of 10% and a drive of 15.0 dBm RF power. The drive we do in most of the exceptional point measurements is 400 mV, which is well within the linear regime when three control tones are applied.

5.4.3 Dataset Shape

In this experiment, we had a four-dimensional parameter space. Because, in our current experimental setup, we need 30 seconds to measure one mechanical mode in the parameter space, we were not able to densely raster all four parameters to find the exceptional point structures we were interested in. Indeed, even for a modest 21^4 data points, at 30 seconds times three modes, would require more than 200 days! Thus, we needed to be somewhat strategic in our choice of datasets.

The first shape was a 4-dimensional dataset, but with $7 \times 5 \times 5 \times 5$ data points. This could be done in about one day, but it was not dense enough to resolve exceptional points by itself, with the problem being that either an exceptional point would slip in between the mesh, or the mesh would not contain an exceptional point at all. However, these 4-dimensional datasets were usable to create a *Hopf invariant* metric, which can determine if the EP_3 point is inside the volume that the 4-dimensional set defines.

Another approach was a 1-dimensional dataset. Then a 31-point scan could be done in about an hour. This has enough density and range in the parameter space to resolve an EP_2 or EP_3 point. In particular, when each of the four parameters are scanned individually, and the other three are held fixed at a possible EP_3 point, we can do multiple such 1D measurements to iteratively seek EP_3 points. We refer to this as a *whirlpool* measurement.

The most effective approach was to use 2-dimensional datasets to *slice through* the 4-dimensional parameter space. For a dense 31×31 dataset, the measurement could be performed in about a day (or we can be more strategic, and use a smaller or higher density). We used these slices to find EP_3 by performing multiple intersecting slice measurements. Then, even if EP_3 is not exactly on one slice, the three slices together are quite effective in locating EP_3. We also used the 2D slices to find EP_2, by placing the slices such that they would intersect our estimated EP_2 knot. Then the EP_2 points are on the 2D slices. We identify these EP_2 points algorithmically, as described in Section 6.4.2.

Chapter 6

Data Analysis

In this chapter, we describe how we take the mechanical spectra discussed in Chapter 5 and extract information about the eigenvalues and eigenmodes. We describe how this information is used to identify double and triple exceptional points (EP_2 and EP_3, respectively). Next, we describe two representations of these EP_2 points that demonstrate that these points form a trefoil knot. Finally, we use this data to demonstrate eigenvalue braiding around this knot.

6.1 Spectroscopy of Exceptional Points from Driven Response Measurements

6.1.1 Mechanical Displacement in Driven Measurements

In order to demonstrate exceptional point physics, we must measure the eigenvalues of the system at a given point in parameter space. We do this by applying a mechanical drive, whose frequency is near one of the mode frequencies. This is repeated for many frequencies. The response that we measure will have the form of a superposition of complex Lorentzians, with the frequency and linewidth of each corresponding to the real and imaginary parts of the eigenvalues, respectively. Additionally, the complex amplitudes of these Lorentzians are related to the eigenmode components.

First, we consider the driven equation of motion for a time-dependent harmonic oscillator,

$$i\dot{C}(t) = H(t)C(t) + F(t), \tag{6.1}$$

where $C(t)$ is the complex amplitude of motion, and $F(t) = F_0 e^{-i\omega_{\mathrm{AM}}t}$ is a sinusoidal driving term with frequency ω_{AM} (c.f., Equation (3.19)). F_0 is proportional to the vector $\mathbf{g} = (g_1, g_2, g_3)$, where g_k, $k = 1, 2, 3$, is the optomechanical coupling rate to mode k. $F(t)$ has units of Hz, since

it relates to a force $F_x(t)$, with units of Newtons, on the displacement $x(t)$, via Equation (3.18). The system Hamiltonian $H(t)$ was derived in Chapter 3, and is given by Equation (3.232) in the lab frame. **Notation:** we write the bare mode frequencies as $\omega_k^{(0)}$, $k = 1, 2, 3$, to distinguish them from the optomechanically cooled mode frequencies ω_k, $k = 1, 2, 3$. Because $H(t)$ is time-dependent, the solution $C(t)$ may be complicated. However, since $H(t)$ is periodic, we can apply Floquet theory to simplify the equation of motion. We can find a change of basis which puts the system into a Floquet frame[1] in which the Floquet-frame Hamiltonian H' is time-independent. A change-of-basis

$$C'(t) = U(t)C(t), \tag{6.2}$$

for a unitary transformation $U(t)$, which achieves a time-independent H' is discussed in Section 3.6. The corresponding $U(t)$ is given by Equation (3.237). We rewrite it here with the notation of this section for the bare mode frequencies:

$$U(t) = \begin{pmatrix} e^{i(\omega_1^{(0)}+\eta)t} & 0 & 0 \\ 0 & e^{i(\omega_2^{(0)})t} & 0 \\ 0 & 0 & e^{i(\omega_3^{(0)}+\eta)t} \end{pmatrix} \tag{6.3}$$

We thus write the Floquet-frame equation of motion as

$$i\dot{C}'(t) = H'C'(t) + F'(t) \tag{6.4}$$

We now consider Equation (6.4) in the Fourier domain:

$$\omega C'[\omega] = H'C'[\omega] + F'[\omega] \tag{6.5}$$

This is easily solved for $C'[\omega]$:

$$C'[\omega] = \chi[\omega] \cdot F'[\omega] \tag{6.6}$$

where the susceptibility $\chi[\omega]$ is given by

$$\chi[\omega] = (\omega I - H')^{-1} \tag{6.7}$$

If H' is diagonalizable, then H' can be diagonalized via a similarity transformation T as $H' = TDT^{-1}$, where D is a diagonal matrix consisting of the eigenvalues $\omega'_k - i\gamma'_k/2$, for $k = 1, 2, 3$, of H', and the three eigenvectors of H' make up the columns of T. Since T is a

[1] The Floquet frame may also be referred to as the "rotating frame." We use these terms interchangeably.

similarity transformation, it satisfies the constraint $\mathbb{I} = TT^{-1}$, which yields

$$1 = \sum_j T_{ij}(T^{-1})_{ji}, \quad i = 1, 2, 3 \tag{6.8}$$

H' is not everywhere diagonalizable; at an exceptional point, H' is similar to a Jordan block. However, the set of points in parameter space in which H' is not diagonalizable is a set of measure zero, and it cannot be realized exactly in this experiment. Therefore, in the domain of the experiment, H' is diagonalizable.

The susceptibility $\chi[\omega]$ can be diagonalized by the same similarity transformation T that diagonalizes H':

$$\chi[\omega] = T(\omega I - H')^{-1}T^{-1} \tag{6.9}$$

Its eigenvalues are $1/(\omega - (\omega'_k - i\gamma'_k/2))$, for $k = 1, 2, 3$.

The driven measurements we perform are a measure of the susceptibility $\chi[\omega]$, but in the lab frame, rather than the Floquet frame. The transformation of $C'[\omega] = (c'_1[\omega], c'_2[\omega], c'_3[\omega])^T$ into the lab frame is found by taking the Fourier transform of the vector components of Equation (6.2). This is written out in terms of the rotating-frame solution (Equation (6.6)):

$$\begin{aligned} c_1[\omega] &= \chi[\omega - \omega_1^{(0)} - \eta] \cdot F'[\omega - \omega_1^{(0)} - \eta] \\ c_2[\omega] &= \chi[\omega - \omega_2^{(0)}] \cdot F'[\omega - \omega_2^{(0)}] \\ c_3[\omega] &= \chi[\omega - \omega_3^{(0)} - \eta] \cdot F'[\omega - \omega_3^{(0)} - \eta] \end{aligned} \tag{6.10}$$

We also tranform the force vector $F'[\omega] = (f'_1[\omega], f'_2[\omega], f'_3[\omega])^T$ into the lab frame with the same transformation. For the $c_1[\omega]$ component,

$$\begin{aligned} c_1[\omega] =& \chi_{11}[\omega - \omega_1^{(0)} - \eta]f_1[\omega] + \\ & \chi_{12}[\omega - \omega_1^{(0)} - \eta]f_2[\omega + \omega_2^{(0)} - \omega_1^{(0)} - \eta] + \\ & \chi_{13}[\omega - \omega_1^{(0)} - \eta]f_3[\omega + \omega_3^{(0)} - \omega_1^{(0)}] \end{aligned} \tag{6.11}$$

where $\chi[\omega]$ has been written in tensor notation as

$$\chi[\omega] = \begin{pmatrix} \chi_{11} & \chi_{12} & \chi_{13} \\ \chi_{21} & \chi_{22} & \chi_{23} \\ \chi_{31} & \chi_{32} & \chi_{33} \end{pmatrix} \tag{6.12}$$

In the three summands of Equation 6.11, at a given drive frequency $\omega = \omega_{\mathrm{AM}}$, the strongest contribution comes from the $f_1[\omega]$ term, since the lock-in amplifier is set to detect motion only

near ω_{AM}, which makes the other two terms negligible. Hence, we approximate Equation 6.11 as

$$c_1[\omega] \approx \chi_{11}[\omega - \omega_1^{(0)} - \eta] f_1[\omega] \tag{6.13}$$

Furthermore, we have already diagonalized $\chi[\omega]$ using the diagonalization of H', in Equation (6.9) so for a drive $\omega_{\mathrm{AM}} = \omega_1^{(0)} + \delta\omega + \eta$, the response is

$$c_1[\omega_1^{(0)}+\delta\omega+\eta] = \left(\frac{T_{11}(T^{-1})_{11}}{\delta\omega - (\omega_1' - i\gamma_1'/2)} + \frac{T_{12}(T^{-1})_{21}}{\delta\omega - (\omega_2' - i\gamma_2'/2)} + \frac{T_{13}(T^{-1})_{31}}{\delta\omega - (\omega_3' - i\gamma_3'/2)} \right) f_1[\omega_1^{(0)}+\delta\omega+\eta] \tag{6.14}$$

Thus, this response is a sum of three Lorentzians of three complex eigenfrequencies. Similarly, for driving and reading out at $\omega_{\mathrm{AM}} = \omega_2^{(0)} + \delta\omega$, we get

$$c_2[\omega_2^{(0)} + \delta\omega] = \left(\frac{T_{21}(T^{-1})_{12}}{\delta\omega - (\omega_1' - i\gamma_1'/2)} + \frac{T_{22}(T^{-1})_{22}}{\delta\omega - (\omega_2' - i\gamma_2'/2)} + \frac{T_{23}(T^{-1})_{32}}{\delta\omega - (\omega_3' - i\gamma_3'/2)} \right) f_2[\omega_2^{(0)} + \delta\omega] \tag{6.15}$$

and for driving and reading out at $\omega_{\mathrm{AM}} = \omega_3^{(0)} + \delta\omega + \eta$, we get

$$c_3[\omega_3^{(0)}+\delta\omega+\eta] = \left(\frac{T_{31}(T^{-1})_{13}}{\delta\omega - (\omega_1' - i\gamma_1'/2)} + \frac{T_{32}(T^{-1})_{23}}{\delta\omega - (\omega_2' - i\gamma_2'/2)} + \frac{T_{33}(T^{-1})_{33}}{\delta\omega - (\omega_3' - i\gamma_3'/2)} \right) f_3[\omega_2^{(0)}+\delta\omega+\eta] \tag{6.16}$$

In this section, we have thus far found the complex amplitude of the mechanical displacement $C(t)$ in terms of the susceptibility (Equation (6.7)). We can relate this to the mechanical displacements themselves via Equation (3.14). Then, per the high-Q approximation (as shown in Appendix A), we can write

$$x_k[\omega] = (x_{\mathrm{ZPF}})_k \, c_k[\omega] = \sqrt{\frac{\hbar}{2m_k\omega_k}} \, c_k[\omega], \quad k = 1, 2, 3 \tag{6.17}$$

where m_k is an "effective mass" for mode k. Then the displacements $x_k[\omega]$, $k = 1, 2, 3$, in terms of the susceptibility $\chi[\omega]$, near $\omega = \omega_k^{(0)} + \delta\omega + \eta_k$, are

$$x_1[\omega_1^{(0)} + \eta + \delta\omega] = \frac{i}{2m\omega_1} \chi_{11}[\delta\omega] \, F_{x,1}[\omega_1^{(0)} + \eta + \delta\omega] \tag{6.18a}$$

$$x_2[\omega_2^{(0)} + \delta\omega] = \frac{i}{2m\omega_2} \chi_{22}[\delta\omega] \, F_{x,2}[\omega_2^{(0)} + \delta\omega] \tag{6.18b}$$

$$x_3[\omega_3^{(0)} + \eta + \delta\omega] = \frac{i}{2m\omega_3} \chi_{33}[\delta\omega] \, F_{x,3}[\omega_3^{(0)} + \eta + \delta\omega] \tag{6.18c}$$

6.1.2 Quadrature Measurements

In this section, we discuss the quadrature measurements performed when we drive the membrane via an AOM (Section 5.3.1) with an optical tone of power P_p and at a frequency $\omega = \omega_k^{(0)} + \delta\omega$, $k = 1, 2, 3$, and $\delta\omega$ is in a small range. This is achieved with a laser tone that has amplitude modulation sidebands on it (see Section 5.3.1). Thus, the laser frequency ω_{L} is set to carrier frequency of one of the cavity modes, with an amplitude modulation frequency $\omega_{\mathrm{AM}} = \omega_k^{(0)} + \delta\omega$. We assume that only some fraction ξ of the nominal probe laser power P_p, for $0 < \xi < 1$, gets to the amplitude modulation sideband.

The probe laser tone acts as an input laser to the cavity, and so it induces an optomechanical interaction (c.f., Section 3.4). We can use perturbation theory to examine the cavity field $a_p(t)$ due to the probe laser, as in Section 3.4.4. Namely, we get (Equation (3.123))

$$a_p(t) = (\bar{a} + d(t))e^{-i\omega_{\mathrm{L}}t} \tag{6.19}$$

where ω_{L} is the laser frequency. $\bar{a}$ is given by (Equation (3.90))

$$\bar{a} = e^{i\theta_p}\frac{\sqrt{\kappa_{\mathrm{in}}}}{\kappa/2 - i\Delta}\sqrt{\frac{P_p}{\hbar\omega_{\mathrm{L}}}} \tag{6.20}$$

where θ_p is a phase-mismatch between the incoming and outgoing amplitude. Since the probe tone is made up of AM sidebands on the main probe laser frequency ω_{L}, which is set to a cavity mode, the main cavity field amplitude is set with $\Delta = 0$. The factor ξ is connected to the AM sideband, so it does not show up in the mean carrier cavity field. Thus,

$$\bar{a}_{\mathrm{carrier}} = e^{i\theta_p}\frac{\sqrt{\kappa_{\mathrm{in}}}}{\kappa/2}\sqrt{\frac{P_p}{\hbar\omega_{\mathrm{L}}}} \tag{6.21}$$

$d(t)$ has a Fourier-space equation of motion, in terms of the displacement $x[\omega]$ (Equation (3.134a)).

$$\begin{aligned} d[\omega] &= ig_0\bar{a}\left(\frac{\kappa}{2} - i(\omega + \Delta)\right)^{-1}(c[\omega] + c^\dagger[\omega]) \\ &= ig_0\bar{a}\left(\frac{\kappa}{2} - i(\omega + \Delta)\right)^{-1}x[\omega]/x_{\mathrm{ZPF}} \end{aligned} \tag{6.22}$$

For the kth mode, we drive near $\omega = \omega_k^{(0)} + \eta_k + \delta\omega$. This is done with the AM sideband at $\Delta = -\omega_k^{(0)} - \eta_k - \delta\omega$, and we get the corresponding component of $d[\omega]$:

$$d[\omega_k^{(0)} + \eta_k + \delta\omega] = g_k\frac{2i\bar{a}}{\kappa}\sqrt{\frac{2m_k\omega_k}{\hbar}}x_k[\omega_k^{(0)} + \eta_k + \delta\omega] \tag{6.23}$$

We plug in the equations of the displacements in terms of the susceptibilities (Equation

(6.18)). For mode 1,

$$\begin{aligned} d[\omega_1^{(0)}+\eta_1+\delta\omega] &= g_1\frac{2i\bar{a}}{\kappa}\sqrt{\frac{2m_1\omega_1}{\hbar}}\frac{i}{2m_1\omega_1}\,\chi_{11}[\delta\omega]F_{x,1}[\omega_1^{(0)}+\eta+\delta\omega] \\ &= -g_1\frac{\bar{a}}{\kappa}\sqrt{\frac{2}{\hbar m_1\omega_1}}\,\chi_{11}[\delta\omega]F_{x,1}[\omega_1^{(0)}+\eta+\delta\omega] \\ &\approx -\frac{g_1}{\kappa}\frac{e^{i\theta_p}\sqrt{\kappa_{\rm in}}}{\kappa/2}\sqrt{\frac{\xi P_p}{\hbar\omega_{\rm L}}}\sqrt{\frac{2}{\hbar m_1\omega_1}}\,\chi_{11}[\delta\omega]F_{x,1}[\omega_1^{(0)}+\eta+\delta\omega] \end{aligned} \tag{6.24}$$

We write the force $F_{x,1}$ as the radiation-pressure force from the AM sideband:

$$\begin{aligned} F_{x,1}[\omega_1^{(0)}+\eta+\delta\omega] &\approx \hbar\frac{g_1}{x_{\rm ZPF}}\,|\bar{a}_{\rm AM}|^2 \\ &\approx \frac{g_1\kappa_{\rm in}\sqrt{2m_1\hbar\omega_1}}{(\kappa/2)^2+(\omega_1^{(0)})^2}\frac{\xi P_p}{\hbar\omega_L} \end{aligned} \tag{6.25}$$

Then the amplitude $d[\omega_1^{(0)}+\delta\omega]$ is

$$\begin{aligned} d[\omega_1^{(0)}+\eta+\delta\omega] &\approx e^{i(\theta_p-\pi)}\left(\frac{2g_1}{\kappa}\right)^2\left(\frac{\kappa_{\rm in}P_p}{\hbar\omega_L}\right)^{3/2}\xi\,\frac{1}{(\kappa/2)^2+(\omega_1^{(0)})^2}\,\chi_{11}[\delta\omega] \\ &= e^{i(\theta_p-\pi)}\,A_0\,\frac{g_1^2}{(\kappa/2)^2+(\omega_1^{(0)})^2}\,\chi_{11}[\delta\omega] \end{aligned} \tag{6.26}$$

where we have a real amplitude

$$A_0 = \frac{4\xi}{\kappa^2}\left(\frac{\kappa_{\rm in}P_p}{\hbar\omega_L}\right)^{3/2} \tag{6.27}$$

A_0 is independent of the choice of $\omega_k^{(0)}$ to drive. A_0 has units of Hz.

Equation (6.26) gives the optical fluctuations in terms of the susceptibility (Equation (6.7)). The measured voltage quadratures $V_k[\omega]$ are proportional to $d[\omega]$. Since $d[\omega]$ is dimensionless, there is a factor τ, which has units of volts. Furthermore, there is a phase factor that gets added for each mode k, θ_k, which this model does not account for by itself. Let us absorb these factors into one factor β_k:

$$\beta_k = e^{i\theta_k}\frac{\tau A_0}{(\kappa/2)^2+(\omega_k^{(0)})^2} \tag{6.28}$$

The measured voltage quadratures at $\omega=\omega_1^{(0)}+\eta+\delta\omega$, $\omega=\omega_2^{(0)}+\delta\omega$, and $\omega=\omega_3^{(0)}+\eta+\delta\omega$,

are thus

$$V_1[\omega_1^{(0)} + \eta + \delta\omega] = \beta_1 g_1^2 \left(\frac{T_{11}(T^{-1})_{11}}{\delta\omega - (\omega_1' - i\gamma_1'/2)} + \frac{T_{12}(T^{-1})_{21}}{\delta\omega - (\omega_2' - i\gamma_2'/2)} + \frac{T_{13}(T^{-1})_{31}}{\delta\omega - (\omega_3' - i\gamma_3'/2)} \right) \tag{6.29a}$$

$$V_2[\omega_2^{(0)} + \delta\omega] = \beta_2 g_2^2 \left(\frac{T_{21}(T^{-1})_{12}}{\delta\omega - (\omega_1' - i\gamma_1'/2)} + \frac{T_{22}(T^{-1})_{22}}{\delta\omega - (\omega_2' - i\gamma_2'/2)} + \frac{T_{23}(T^{-1})_{32}}{\delta\omega - (\omega_3' - i\gamma_3'/2)} \right) \tag{6.29b}$$

$$V_3[\omega_3^{(0)} + \eta + \delta\omega] = \beta_3 g_3^2 \left(\frac{T_{31}(T^{-1})_{13}}{\delta\omega - (\omega_1' - i\gamma_1'/2)} + \frac{T_{32}(T^{-1})_{23}}{\delta\omega - (\omega_2' - i\gamma_2'/2)} + \frac{T_{33}(T^{-1})_{33}}{\delta\omega - (\omega_3' - i\gamma_3'/2)} \right) \tag{6.29c}$$

We see that the measured voltage quadratures are each superpositions of three complex Lorentzians, just like the mechanical displacements.

6.1.3 Extracting Eigenvalues from Spectra

In this experiment, we measure the mechanical response around three membrane modes: the (1,1) mode ($\omega_1^{(0)} = 352.3\,\text{kHz}$), the (2,1) mode ($\omega_2^{(0)} = 557.2\,\text{kHz}$), and the (2,2) mode ($\omega_3^{(0)} = 705.0\,\text{kHz}$). A sample measurement is shown in Figure 5.8. This section describes the fit function used to extract the system eigenvalues, as well as a measurement of the eigenmode degeneracy.

These three spectra are taken in the lab frame. However, the fit is done in a Floquet frame. Let the frequency coordinates of these three measurements be ω_1, ω_2, and ω_3. We take the lab frame measurements into a Floquet frame in post-processing, via the transformation

$$\begin{aligned} \omega_1 &\to \omega_1' = \omega_1 - \omega_1^{(0)} - \eta \\ \omega_2 &\to \omega_2' = \omega_2 - \omega_2^{(0)} \\ \omega_3 &\to \omega_3' = \omega_3 - \omega_3^{(0)} - \eta \end{aligned} \tag{6.30}$$

With this choice of transformation (described in detail in Section 3.6; c.f. Equation (6.3)), these Floquet-frame frequency coordinates $\omega_1', \omega_2', \omega_3'$ are near $\omega = 0$ (even though this is just a choice of offset, and it does not affect the analysis).

The response is a sum of three complex Lorentzians, because the motion in one frequency sweep range has three components: the response of the membrane at the drive frequency, and the other two are from the other two mechanical modes. These components arise from the intensity beatnotes between the motional sideband of the first mechanical mode and the control laser near its resonance, and the other two control lasers.

The spectrum for a single complex Lorentzian $z(x)$ is given by

$$z(x) = \frac{se^{i\phi}}{x - (\omega - i\gamma/2)} + b_R + ib_I \tag{6.31}$$

Since there are three spectra, there are three superpositions of three Lorentzians each. The Floquet frame frequencies will be the same between the three spectra. Thus, the response z_i, $i = 1, 2, 3$, has the form

$$z_i(x) = \sum_{j=1,2,3} \frac{s_{ij}e^{i\phi_{ij}}}{x - (\omega_j - i\gamma_j)} + b_{R,j} + ib_{I,j} \tag{6.32}$$

The three spectra, measured as Equation (6.29), are simultaneously fit to 9 complex amplitudes, 3 complex eigenvalues, and 3 complex backgrounds (Equation (6.32)), for a total of 30 real free parameters. At a first level of analysis, the quantities of interest are the 3 complex eigenvalues, as we reach exceptional points when they become degenerate. Then, in principle, we are done extracting information once we have these 3 complex numbers.

However, in addition to the 3 complex eigenfrequencies, we also have two uses for the complex heights $s_{ij}e^{i\phi_{ij}}$. The first is that they are not independent, but satisfy (c.f., Equation (6.8))

$$\begin{aligned} \sum_j s_{ij}e^{i\phi_{ij}} &= 1, \quad i = 1, 2, 3 \\ \sum_i s_{ij}e^{i\phi_{ij}} &= 1, \quad j = 1, 2, 3 \end{aligned} \tag{6.33}$$

This drops the number of fit parameters from 30 to 26. The second use is that the $s_{ij}e^{i\phi_{ij}}$ are useful in determining the degeneracy of eigenvectors: as the eigenmodes become parallel, the s_{ij} diverge. We can quantify this by deriving an *eigenvector indicator* (as described in Section 6.3.1) that goes to zero as the heights diverge.

6.2 Finding an EP$_3$ Point in a 4D Space

In this thesis, we seek to find EP$_2$ points on a hypersurface that encloses EP$_3$, and demonstrate that these EP$_2$ points form a trefoil knot. In this section, we find EP$_3$. If a given hypersurface encloses EP$_3$, we can be sure (per the discussion in Section 2.5) that the set of EP$_2$ points on this hypersurface forms a trefoil knot, as this thesis seeks to demonstrate.

In the analyses of the datasets below, we consider the metric d_3:

$$d_3(\delta, P_1, P_2, P_3) = |\lambda_1 - \lambda_2| + |\lambda_2 - \lambda_3| + |\lambda_3 - \lambda_1| \tag{6.34}$$

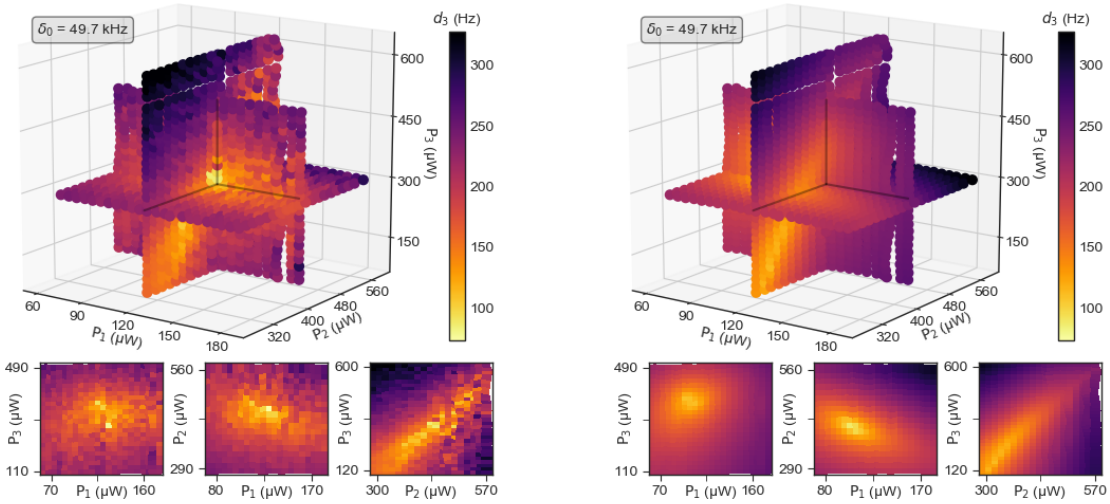

(a) Data (b) Theory

Figure 6.1: Three 2-parameter slices through the 4-dimensional control space. These slices sweep two out of three of P_i, $i = 1, 2, 3$, with δ fixed at $\delta = 2\pi \times 49.7\,\text{kHz}$. The 3D plot shows the slices intersecting. The bottom row shows the individual slices. The colorbar is the d_3 metric (Equation (6.34)). Plot (a) represents raw data. Plot (b) represents theoretical estimates of d_3, based on our optomechanical model.

Clearly, $d_3 = 0$ if and only if all three eigenvalues $(\lambda_1, \lambda_2, \lambda_3)$ are equal. Thus, d_3 can be used to quantify how close the experimental parameters are to realizing the system's EP$_3$.

6.2.1 Slices with 2D Sheets

The most successful measurements of the EP$_3$ were done by fixing two of the four parameters, and sweeping the other two parameters as "slices" through the 4D control space. If these sheets are taken such that they intersect near an estimated EP$_3$, then we expect to see minima in d_3 near this estimated EP$_3$.

There are six sheets that can be rastered when we choose 2 of the 4 parameters to be swept. In Figure 6.1, we see three of these 2D sheets plotted in a 3D plot. These sheets were chosen to intersect each other at the estimated EP$_3$ of

$$(\delta/2\pi, P_1, P_2, P_3)_{\text{Estimate}} = (49.7\,\text{kHz}, 115\,\mu\text{W}, 387\,\mu\text{W}, 285\,\mu\text{W}) \tag{6.35}$$

This initial estimate is based on the measured g_0, and solving for the parameters that make $x = \det(H)$ and $y = \text{Tr}(H)^2$ both be zero, and thus bring the system to its EP$_3$.

In Figure 6.1, we see that there are indeed minima in $d_3(\delta, P_1, P_2, P_3)$ near the intersection of three of the sheets. In the top row of Figure 6.2, we see all six of the 2D sheets, which were chosen to be near the estimated EP$_3$ values. The middle row shows these sheets after filtering the d_3 data by removing outliers and Gaussian filtering (described in more detail in Section 6.4.1). It should be noted that the filtering raises the minimum value of d_3, since the Gaussian

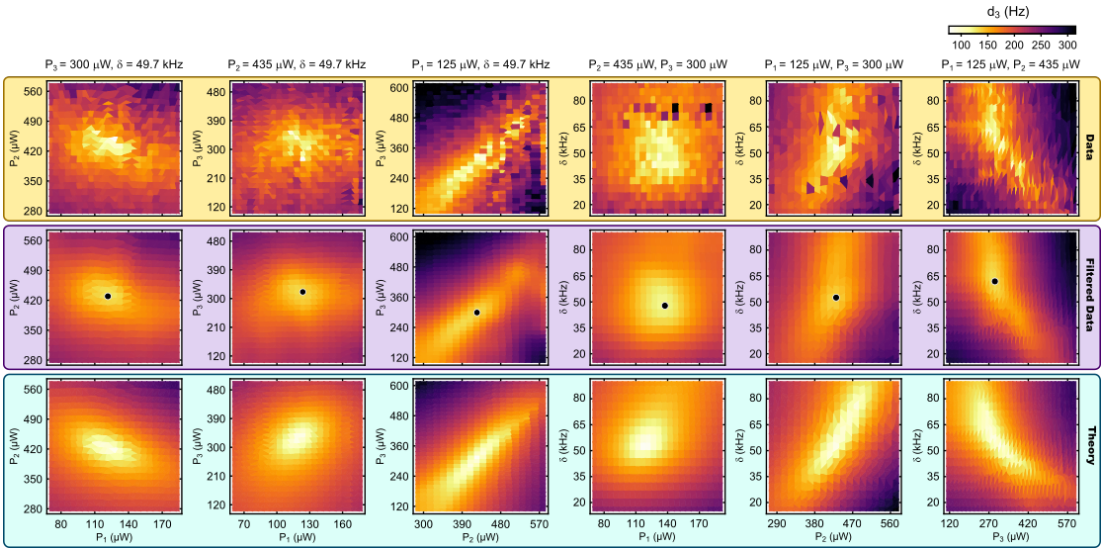

Figure 6.2: All $\binom{4}{2} = 6$ slices of the 4-dimensional space to find EP3, laid out in 6 columns. Data are plotted as colormaps, against the two free parameters. The colorbar is the metric d_3 (Equation (6.34)). The fixed parameters are captioned above each slice. The top row is raw data. The middle row is the filtered d_3 data (Section section:filtering). Note that the smoothed data have higher minima than the raw data, because the extrema are averaged by the filtering. The black dots are algorithmically chosen minima in the filtered d_3, which represent estimates of EP$_3$ points. The bottom row is theoretically calculated d_3 values, from our optomechanical model.

filter smooths the minimum. However, when we look for minima in d_3, the regions around the minima are smoother in the filtered data than in the raw data, so a minimum point is clearer in the filtered data. With this filtering, we can take the minimum values of d_3 and get their corresponding minimum points in all six of the filtered d_3 sheets. Based on these six minimum points, we place our best estimate of EP$_3$ to be at

$$(\delta/2\pi, P_1, P_2, P_3)_{\text{Measured; 2D Sheets}} = \Big(54(7)\,\text{kHz}, 128(8)\,\mu\text{W}, 428(3)\,\mu\text{W}, 304(15)\,\mu\text{W}\Big) \quad (6.36)$$

These values are merely the sample mean and sample standard deviation of the coordinates of the six sheet minima.

6.2.2 Slices with 1D "Whirlpool" Sweeps

Another method to raster through the 4-dimensional control space and find the system's EP$_3$ is to fix three of the parameters, and sweep the fourth one. An advantage of this is that the swept parameter can be stepped in increments much smaller than those used in the 2D sweeps.

We use these 1-dimensional sweeps iteratively, in the sense that we estimate parameters that will bring the system to EP$_3$, as mentioned in Subsection 6.2.1. Then we fix three of the parameters at these estimated values, and sweep the fourth. The value of the fourth parameter

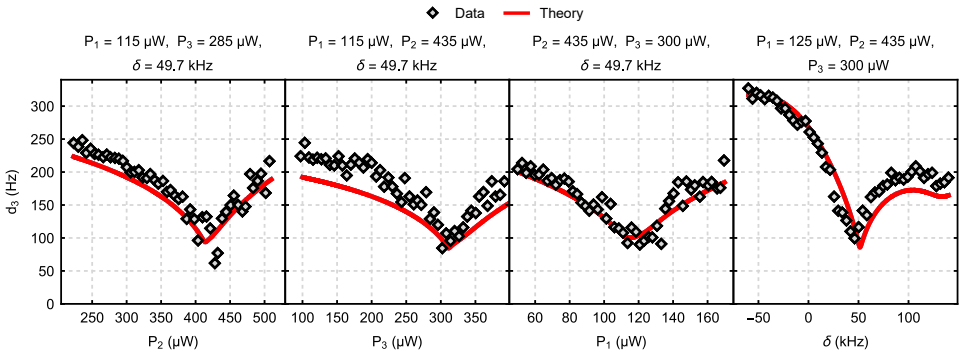

Figure 6.3: A series of 1-dimensional sweeps to minimize d_3 (Equation (6.34)). On the first one, initial parameters are set in P_1, P_3, and δ that are estimated to reach EP$_3$. P_2 is swept. The minimum value of P_2 found in this sweep is used as the fixed value of P_2 in the next measurement, and P_3 is swept for a minimum. This process is done iteratively to iteratively find a point in parameter space that best minimizes d_3.

at which d_3 is minimized is now our new candidate for the location of the minimum of d_3. We then do a second sweep, where this fourth parameter is fixed at the minimizing value, and we sweep the first parameter. We do this iteratively to find parameters that minimize d_3 and bring the system to EP$_3$. This sort of measurement was nicknamed the "whirlpool measurement" of EP$_3$.

Figure 6.3 shows a sample such "whirlpool measurement." In this measurement, EP$_3$ was initially estimated to be at $(\delta/2\pi, P_1, P_2, P_3) = (49.7\,\text{kHz}, 115\,\mu\text{W}, 387\,\mu\text{W}, 285\,\mu\text{W})$, as in Subsection 6.2.1. The first 1-dimensional sweep on the left fixes P$_k$, $k = 1, 3$, and δ at these values, and sweeps P_2. The minimizing value of P_2 is found at $P_2 = 435\,\mu\text{W}$. Then a second sweep is performed, where P_2 is fixed at $435\,\mu\text{W}$, and P_3 is swept. The minimizing value of $P_3 = 300\,\mu\text{W}$ is found. This process is iterated. At the end of these four measurements, the estimated EP$_3$ values are

$$(\delta/2\pi, P_1, P_2, P_3)_{\text{Measured; Whirlpool}} \approx \Big(50\,\text{kHz}, 125\,\mu\text{W}, 435\,\mu\text{W}, 300\,\mu\text{W}\Big) \tag{6.37}$$

The numbers in Equation (6.37) from the "whirlpool measurement" are in good agreement with those in Equation (6.36) from the sheet measurement.

An advantage of this method is that it takes less time than the sheet measurement; this method takes around 3 hours, whereas each sheet requires around 1 day. A disadvantage is that the minimum value of d_3 in each iteration does not reduce with each iteration. Indeed, typical minimum values in both these 1D sweeps and the 2D sheets are 70 to 100 Hz. In Figure 6.3, the minimum value is already below this range (due to luck), but due to both the fluctuations in our laser powers, and the cube root sensitivity of d_3 to these fluctuations near EP$_3$ itself, we find that the minimum d_3 value rarely go below this range.

6.2.3 Sparse 4D Sweeps: A Topological Quantification of Proximity to EP_3

In this section, we discuss another metric, in addition to d, to quantify the proximity to EP_3. This metric is called a *Hopf invariant*, which is a property possessed by a 3-sphere (or another suitably chosen hypersurface; in this case, a 4D hyperrectangle) that encloses the point $x = y = 0$ (where $x, y \in \mathbb{C}$; recall that $x = y = 0$ if and only if the system is at EP_3). The Hopf invariant is a scalar quantity χ which satisfies $\chi = -1$ when the hypersurface encloses $(x, y) = (0, 0)$ and $\chi = 0$ when it does not enclose $(x, y) = (0, 0)$.

The Hopf invariant on a 4D hypersurface $\mathbf{V}$ (n.b. $\mathbf{V}$ is three dimensional) is computed as

$$\chi = -\frac{1}{4\pi^2}\int_V \mathbf{A}\cdot\mathbf{F}d^3\mathbf{R} \tag{6.38}$$

where

$$\mathbf{u} = \frac{1}{\sqrt{|x|^2+|y|^2}}\begin{pmatrix} x \\ y \end{pmatrix} \tag{6.39}$$

and the vector quantities $\mathbf{A}$ and $\mathbf{F}$ are given by

$$\begin{aligned} \mathbf{A}_j &= \mathbf{u}^\dagger i\nabla_{\mathbf{R}_j}\mathbf{u} \\ \mathbf{F} &= \nabla_{\mathbf{R}}\times\mathbf{A} \end{aligned} \tag{6.40}$$

We can consider the integrand of (6.38), $\mathbf{A}\cdot\mathbf{F}$, as a charge density. Here, the charge density corresponds to a "point charge" at $(x, y) = (0, 0)$, so we can intuit Equation 6.38 similarly to Gauss' Law. In analogy to Gauss' Law, χ does not depend on the chosen surface V.

Given that the surface V is a 4D hyperrectangle, we can write (6.38) more explicitly as

$$\begin{aligned} \chi = -\frac{1}{4\pi^2}\Big(&+\int_{\delta=\mathrm{Min}}\mathbf{A}\cdot\mathbf{F}\,d^3\mathbf{R} - \int_{\delta=\mathrm{Max}}\mathbf{A}\cdot\mathbf{F}\,d^3\mathbf{R} \\ &-\int_{P_\mathrm{A}=\mathrm{Min}}\mathbf{A}\cdot\mathbf{F}\,d^3\mathbf{R} + \int_{P_\mathrm{A}=\mathrm{Max}}\mathbf{A}\cdot\mathbf{F}\,d^3\mathbf{R} \\ &+\int_{P_\mathrm{B}=\mathrm{Min}}\mathbf{A}\cdot\mathbf{F}\,d^3\mathbf{R} - \int_{P_\mathrm{B}=\mathrm{Max}}\mathbf{A}\cdot\mathbf{F}\,d^3\mathbf{R} \\ &-\int_{P_\mathrm{C}=\mathrm{Min}}\mathbf{A}\cdot\mathbf{F}\,d^3\mathbf{R} + \int_{P_\mathrm{C}=\mathrm{Max}}\mathbf{A}\cdot\mathbf{F}\,d^3\mathbf{R}\Big) \end{aligned} \tag{6.41}$$

The integral (6.41) does not depend on the volume of V, but only on whether the hyperrectangle that V encloses contains $x = y = 0$. Then, when evaluating (6.41) with finite differences, as we do in the experiment, it suffices to take data that is in a grid. For each 3D face F, suppose

that it is in an (m, n, p) grid. Then calculate

$$\begin{aligned} u &= \{u_{ijk};\ i = 0, \ldots, m-2; j = 0, \ldots, n-2; k = 0, \ldots, p-2\} \\ u_x &= \{u_{ijk};\ i = 1, \ldots, m-1; j = 0, \ldots, n-2; k = 0, \ldots, p-2\} \\ u_y &= \{u_{ijk};\ i = 0, \ldots, m-2; j = 1, \ldots, n-1; k = 0, \ldots, p-2\} \\ u_z &= \{u_{ijk};\ i = 0, \ldots, m-2; j = 0, \ldots, n-2; k = 1, \ldots, p-1\} \end{aligned} \tag{6.42}$$

We then get finite differences

$$\begin{aligned} dudx &= u_x - u \\ dudy &= u_y - u \\ dudz &= u_z - u \end{aligned} \tag{6.43}$$

Then we get finite-element terms $\mathbf{A}$ and $\mathbf{F}$:

$$\begin{aligned} A_x &= i * \sum u^* * dudx \\ A_y &= i * \sum u^* * dudy \\ A_z &= i * \sum u^* * dudz \\ F_x &= i * \sum (dudy)^* * dudz - (dudz)^* * dudy \\ F_y &= i * \sum (dudz)^* * dudx - (dudx)^* * dudz \\ F_z &= i * \sum (dudx)^* * dudy - (dudy)^* * dudx \end{aligned} \tag{6.44}$$

These summations are taken over the complex dimension in x and y. Note that the F_x, F_y, F_z are nonzero, since the $dudx, dudy, dudz$ terms are complex. Then we take all of the terms from (6.44), and calculate

$$\chi_{\text{finite}} = \frac{1}{(2\pi)^2} \sum_F A_x * F_x + A_y * F_y + A_z * F_z \tag{6.45}$$

Since we calculate the Hopf invariant over a finite-size mesh, we can check how well Equation 6.45 converges to Equation 6.38.[2] To check this, we design, in experimental coordinates (δ, P_1, P_2, P_3), a 4D hyperrectangle that encloses the simulated EP$_3$ from Equation 6.35. The span is chosen such that $\Delta P_1 = 100\,\mu\text{W}$, $\Delta P_2 = 200\,\mu\text{W}$, $\Delta P_3 = 200\,\mu\text{W}$, and $\Delta\delta = 100\,\text{kHz}$. As n increases, we expect the Hopf invariant to tend toward -1. Indeed, in Figure 6.4, we see the real part of the Hopf invariant be 0 for $n = 1$, and get to -0.9 at $n = 29$. The imaginary part is expected to tend toward zero; in this graph, it asymptotes to -0.2. Since, in our experiment, it took one day to raster a 4D mesh of size $(7, 5, 5, 5)$, we did not attempt to experimentally check

[2] In this simulation, since x and y must be dimensionless, but the Hamiltonian H from which $x = \det(H)$ and $y = 0.5\text{Tr}(H^2)$ has dimensions of $2\pi \times$ Hz, we scale H by a factor ξ_0, which we chose as $\xi_0 = 1/(2\pi \times 10\,\text{Hz})$ for this simulation.

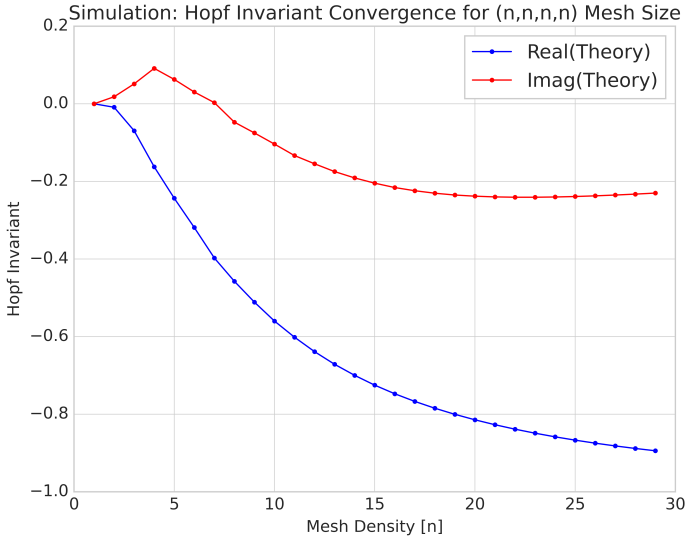

Figure 6.4: Simulation: the Hopf Invariant, as a function of the finite mesh size n for a mesh of size (n, n, n, n).

Figure 6.4.

We also investigate the dependence of the Hopf invariant on the displacement of the surface V from EP_3. To do this, we experimentally defined a $(7, 5, 5, 5)$ surface that enclosed EP_3, and then added offsets to a chosen axis. For this experiment, we added offsets to the P_2 axis. What we see in Figure 6.5 is a dependence on the displacement such that the real part of the Hopf invariant reaches a minimum of about -0.17 at $0\,\mu W$, and it is nearly 0 at a displacement of $\pm 300\,\mu W$, which is the largest displacement we measured at. The imaginary part is zero for large displacements, but it reaches a value of $+0.1$ at $0\,\mu W$, which is comparable to the dip in the real part. This might be an effect of the coarse mesh that we were limited to in this experiment, as discussed with Figure 6.4. It can also be an effect of error in estimating the location of EP_3 (see Section 6.2.4). We also plot alongside these points theoretically estimated curves for the Hopf invariant, for the same $(7, 5, 5, 5)$ meshes used in these measurements. Even the theory does not estimate that $\chi = -1$ at EP_3, because of the coarse mesh; this is consistent with Figure 6.4. Still, the data and theory agree well that there is a dip near our posited EP_3.

One could do the same experiment as done for Figure 6.5 for the other three experimental parameters δ, P_1, P_3. We did not check these dependences experimentally, because having done the measurements of Figure 6.5, as well as the main measurements of d_3 in Sections 6.2.1 and 6.2.2, we felt that we had adequately located EP_3 to move onto the main work of this thesis: finding EP_2 on a hypersurface that encloses EP_3. Nonetheless, the simulated dependences of χ on the other three parameters are plotted in Figure 6.6. Thus, this Hopf invariant provides a useful method for determining whether EP_3 lies inside a given hypersurface, which relies only on

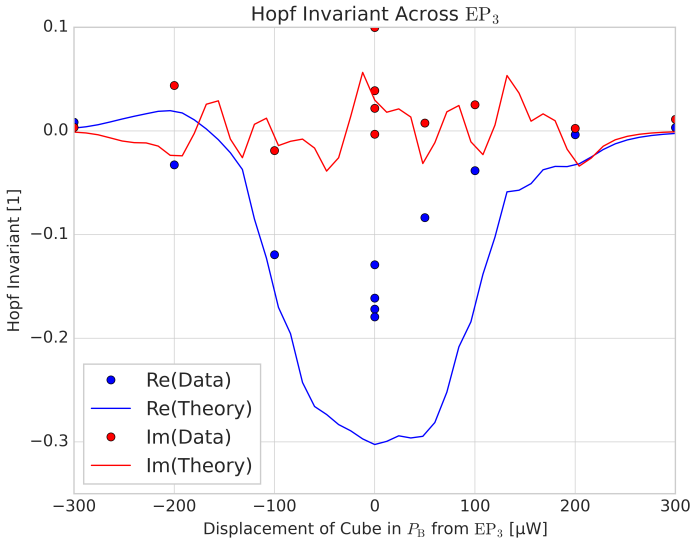

Figure 6.5: The Hopf Invariant swept across EP_3 in P_B.

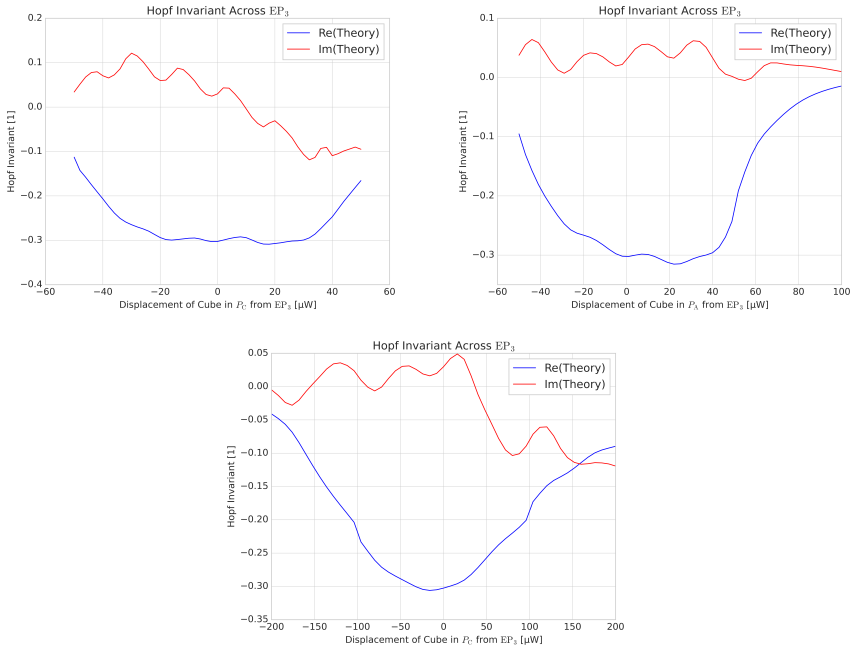

Figure 6.6: Simulated dependence of χ on the other experimental parameters.

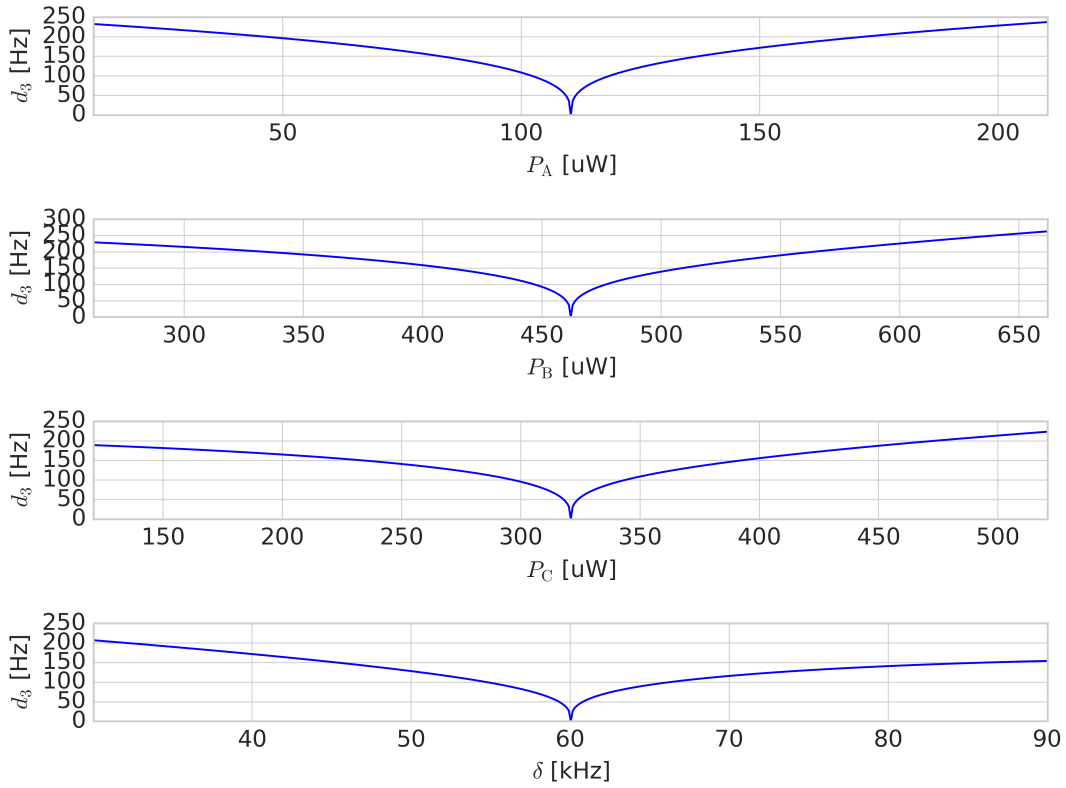

Figure 6.7: d_3 dependence on the (δ, P_1, P_2, P_3) parameters, for simulated lines that reach the numerically estimated EP$_3$.

the boundary behavior of the system eigenvalues on the hypersurface.

6.2.4 Noise Limits on d_3

Ideally, d_3 is precisely zero at EP$_3$, and has a sharp cube-root dependency on the (δ, P_1, P_2, P_3) parameters.[3] In this section, we numerically simulate and analyze typical values of d_3, while considering Gaussian fluctuations in the (δ, P_1, P_2, P_3) parameters.

We consider four 1D simulated datasets that sweep each of the four (δ, P_1, P_2, P_3) parameters, with each line centered around the numerically estimated EP$_3$ (Equation 6.35), and the other parameters fixed at their estimated EP$_3$ values. These lines have 501 points, each. Figure 6.7 depicts these sweeps. As we see from these curves, the d_3 minimum is very sharp as a function of the parameters. A typical value of d_3 away from EP$_3$ is from 100 Hz to 250 Hz. This makes sense, since at $(\delta, P_1, P_2, P_3) = (0, 0, 0, 0)$, $d_3 = 200$ Hz (Section 3.6). To rise from 0 Hz to 50 Hz, the parameters need to fluctuate around EP$_3$ by about

$$\big(\delta(\delta/2\pi), \delta P_1, \delta P_2, \delta P_3\big)_{50\,\mathrm{Hz\,BW}} \approx \big(1.56\,\mathrm{kHz}, 2\,\mu\mathrm{W}, 4\,\mu\mathrm{W}, 5.6\,\mu\mathrm{W}\big) \tag{6.46}$$

[3] See Appendix E for a detailed analytical derivation of this.

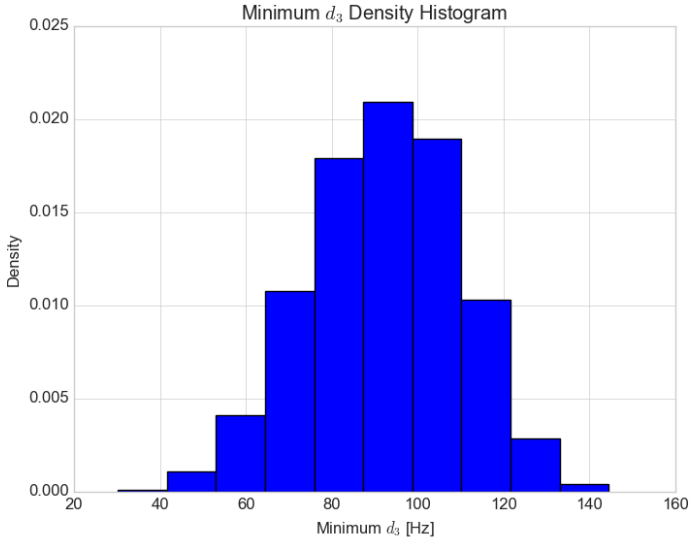

Figure 6.8: A Monte Carlo simulation of the minimum value of d_3 of a 4D hyperrectangle centered about EP$_3$. The simulation perturbs the parameters in the perfect hyperrectangle by Gaussian fluctuations parametrized by Equation 6.47.

In the experiment, typical fluctuations were

$$\big(\delta(\delta/2\pi), \delta P_1, \delta P_2, \delta P_3\big)_{\text{Expt.}} \approx \big(5\,\text{kHz}, 5\,\mu\text{W}, 10\,\mu\text{W}, 10\,\mu\text{W}\big) \tag{6.47}$$

Thus, we were limited in how close we could bring the measured d_3 to zero, and so limited in how close to EP$_3$ we could approach.

To consider a typical value of a minimum d_3 in a dataset, let us perform a Monte-Carlo simulation in which we consider a set of 4D simulated datacubes centered about the numerically estimated EP$_3$ (Equation 6.35). These 4D cubes are identical, save for Gaussian noise added to each parameter value in one cube. The eigenvalues and d_3 values are evaluated according to the optomechanical model (Section 3.6). For this Monte-Carlo simulation, we take there to be 5000 of these cubes. These Gaussian noise standard deviations are set to the typical fluctuations given in Equation 6.47.

The minimum values of d_3 for each of these 5000 simulated datacubes are shown in Figure 6.8. As we see, perturbations typical in our experiment perturb the minimum value of d_3 away from $d_3 = 0\,\text{Hz}$, but still well below the value of $d_3 = 200\,\text{Hz}$ found far from EP$_3$. In the histogram, the mean d_3 is 92 Hz, the standard deviation is 18 Hz, the maximum is 144 Hz, and the minimum is 30 Hz. Thus, seeking points for which $d_3 \approx 90\,\text{Hz}$ is an achievable target for our experiment. Indeed, in the result summarized in Figures 6.1 and 6.2, we see d_3 minima below 90 Hz. In addition, the measured EP$_3$ (Equation 6.36) and estimated EP$_3$ (Equation 6.35) agree to within a factor of several times the typical fluctuations given in Equation (6.47), thus showing

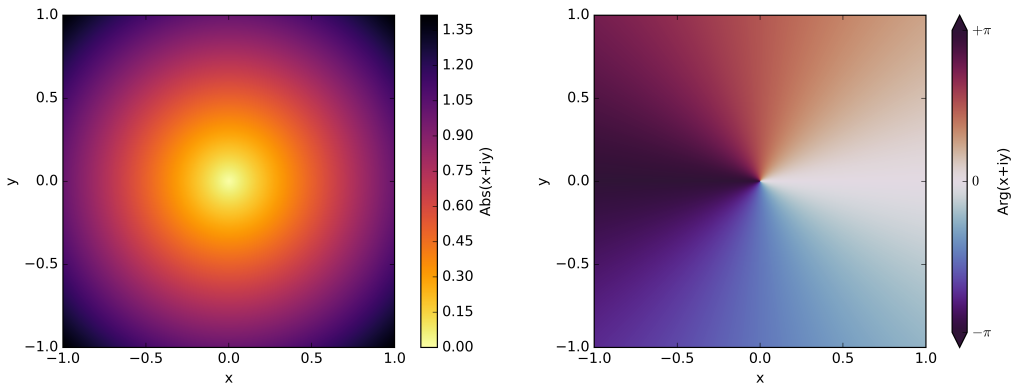

Figure 6.9: A plot of Abs(z) and Arg(z), against the real and imaginary parts of $z = x + iy$, in the left- and right-hand plots, respectively. There is a minimum at $x = 0$ and $y = 0$ (left), as well as a vortex at $x = 0$ and $y = 0$ (right).

that this experiment has done a good job of localizing EP$_3$.

6.3 Obtaining EP$_2$ Points

One of the major goals of this thesis is to demonstrate that the EP$_2$ subspace, when restricted to an appropriately chosen 3D hypersurface of the 4D control space, forms a trefoil knot. In this section, we discuss the metrics that are used in the experiment to determine the locations of EP$_2$. We also discuss the choice of a practical hypersurface in which to search for the trefoil knot of EP$_2$.

6.3.1 Quantifying Proximity to EP$_2$

Quantifying EP$_2$ Eigenvalue Degeneracy with the Discriminant

Given a set of eigenvalues $(\lambda_1, \lambda_2, \lambda_3)$ that are obtained at a point (δ, P_1, P_2, P_3) in experimental parameter space, a simple way to quantify how close the system is to EP$_2$ is to calculate the discriminant of the characteristic polynomial defined by $(\lambda_1, \lambda_2, \lambda_3)$:

$$D(\lambda_1, \lambda_2, \lambda_3) = \Big((\lambda_1 - \lambda_2)(\lambda_2 - \lambda_3)(\lambda_3 - \lambda_1)\Big)^2 \tag{6.48}$$

Note that D (6.48) is complex, unlike the d_3 metric of Equation (6.34). Thus, we seek minima in the absolute value of D, and also seek phase winding in D.

Near an EP$_2$ point, we expect the complex discriminant to vary linearly when the system is brought away from EP$_2$. See Appendix E.1 for a derivation of this. In Figure 6.9, linear behavior of the discriminant (which is linear near EP$_2$) is depicted: there is a minimum in $|D|$ at the origin, as well as a 2π phase winding around the vortex at the origin. We seek these

minima and vortices in Section 6.4.

Quantifying EP$_2$ Eigenmode Degeneracy with Lorentzian Heights

The metric d_3 is useful for indicating a triple eigenvalue degeneracy. Similarly, D indicates a double (or higher order) eigenvalue degeneracy. To investigate exceptional points, which are points at which both the eigenvalues and eigenvectors are degenerate, we must also indicate any *eigenvector degeneracy*. D and d_3 are not directly dependent on the eigenvectors, so they are insufficient to conclude the presence of an eigenvector degeneracy by themselves.

The most direct way to infer the eigenvector degeneracy would be to measure all three complex vector components of each of the three eigenmodes, or nine complex numbers altogether. Our experiment is not designed to measure these components. However, we can infer degeneracies in these eigenmodes from the nine complex amplitudes of the nine Lorentzians that we extract from the driven response measurements.

Let $s_{jk}e^{i\phi_{jk}}$, $j,k = 1,2,3$, be the complex amplitude of the kth Lorentzian from the jth driven response measurement. Define the "height indicator" matrix elements h_{kj} as

$$h_{kj} = \frac{s_{jk}e^{i(\phi_{jk}-\theta_k)}}{\tau A_0}\frac{\omega_k^2 + (\kappa/2)^2}{g_k^2}, \tag{6.49}$$

where τ and A_0 are constants that relate the mechanical displacements to the measured voltages, and θ_k are phase mismatches between the applied drive and the measured motion. See Section 6.1.2 for a discussion of these constants. Empirically, we determine from measurements that $1/\tau A_0 = 2.42 \times 10^{-6}\, 1/\sqrt{\mathrm{V} \times \mathrm{Hz}}$ and that $\theta_1 = 0.79\pi$, $\theta_2 = -0.23\pi$, and $\theta_3 = 0.52\pi$. The key property of the h_{jk} is that, if there is an eigenmode degeneracy, then at least one of the s_{jk} diverges, so at least one h_{jk} will as well.

The *height indicator* is defined as

$$E = \frac{1}{\det(h)^2}, \tag{6.50}$$

where h is the 3×3 matrix whose elements are defined in Equation (6.49). Since we are taking the reciprocal of the determinant of this matrix, if one of the components of h diverges, then $\det(h)$ diverges. But then E tends toward zero. Moreover, since E is a complex number that grows linearly near EP$_2$, like D, its argument winds around any zero in D by 2π (as depicted in Figure 6.9).

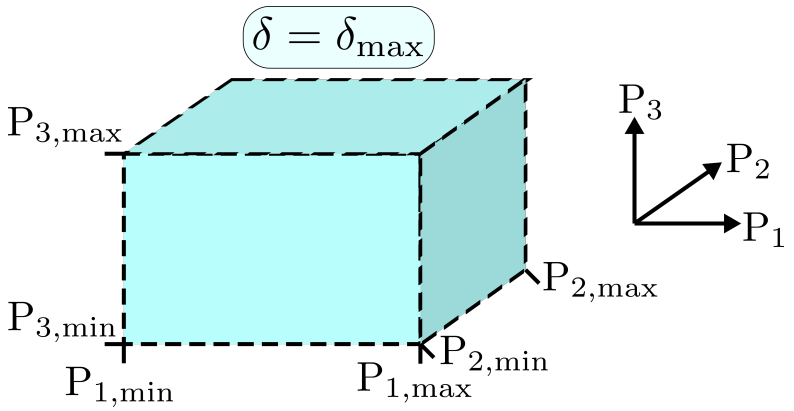

Figure 6.10: One of the eight faces of the 4D hyperrectangle over which data is taken. This particular face is the $\delta_{\max}$ face.

6.3.2 Choosing a Hypersurface: The 3D Hyperrectangular Surface

In Chapter 2, it was predicted that the subspace of EP_2 points in the 4D parameter space, when restricted to a suitably chosen 3D hypersurface that encloses EP_3, forms a trefoil knot. In this subsection, we describe the hypersurface chosen for this experiment. This hypersurface is the surface of a 4D hyperrectangle, in the four experimental coordinates (δ, P_1, P_2, P_3). Additionally, we describe how to visualize this hypersurface.

We chose to take data by rastering the surface of a 4D hyperrectangle in the four experimental coordinates (δ, P_1, P_2, P_3).[4] These values of (δ, P_1, P_2, P_3) are defined by four minimum and maximum values: $\delta_{\min}$ and $\delta_{\max}$; $P_{1,\min}$ and $P_{1,\max}$; and so on. This hypersurface is rastered by choosing one coordinate at a time to hold fixed at its minimum or maximum, then sweeping the other three values. The rastering of one such 3D cube is depicted in Figure 6.10.

We obtain eight hyperfaces of this 4D hyperrectangle by sweeping in this manner: the $\delta_{\min}$-

[4]Naively, the first type of surface tried in this experiment was a set of experimental coordinates that attempted to realize a 3-sphere in the Jordan-Arnol'd space (Chapter 2). Then the EP_2 points in these parameter coordinates would immediately realize the knot, when converted to Jordan-Arnol'd space. We attempted this, but the problem was that the g_0 values fluctuated between measurements; fluctuations δg_0 made the mapping between experimental coordinates and Jordan-Arnol'd coordinates (Chapter 3) fluctuate with fluctuations of order $(\delta g_0)^2$ and $(\delta g_0)^3$.

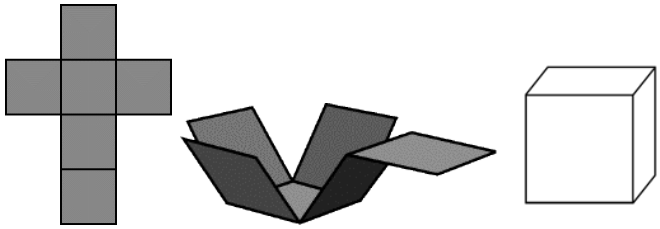

(a) (b) (c)

Figure 6.11: a: The surface of a 3D cube, unfolded into six 2D squares. b: Folding the six squares back up into the surface of a 3D cube. c: The folded squares, which now make up the surface of a 3D cube. Figures a and b are from [82].

face, the $\delta_{\max}$-face, and so on. The values of the minima and maxima are:

$$\begin{aligned} \delta_{\min} &= -10\,\text{kHz} \\ \delta_{\max} &= 105.6\,\text{kHz} \\ \text{P}_{1,\min} &= 22\,\mu\text{W} \\ \text{P}_{1,\max} &= 240\,\mu\text{W} \\ \text{P}_{2,\min} &= 289\,\mu\text{W} \\ \text{P}_{2,\max} &= 675\,\mu\text{W} \\ \text{P}_{3,\min} &= 78\,\mu\text{W} \\ \text{P}_{3,\max} &= 702\,\mu\text{W} \end{aligned} \tag{6.51}$$

These values were chosen such that they would satisfy three criteria: they enclose the EP_3 values (Equation 6.36); they are far enough away from EP_3 that any P_k or δ fluctuations would not affect the criterion that the hyperrectangle encloses the EP_3 point; and the features of the trefoil knot of EP_2 points would be well-resolved. We should remark that the eight hyperfaces of this 4D hyperrectangle are each 3D rectangles.

Of these eight 3D rectangles, some of them share common 1D edges and 2D faces. These edges can be identified by "gluing" the common edges together. To understand this, by analogy with one fewer dimension, we can consider a 3D cube. One technique to depict the surface of the 3D cube on a 2D sheet of paper is to draw each of its six 2D faces on the page (Figure 6.11a). Some of the faces are naturally joined together, if they share common 1D edges. Then, we can traverse the entire 2D surface, as long as we agree that if we end up off the edge of the 2D map, we "wrap around" to the other side, like many Atari video games. Furthermore, if we then fold up the faces (Figure 6.11b), we can get the entire surface of the 3D cube (Figure 6.11c).[5]

[5]A more formal mathematical treatment of this concept can be considered by defining a "quotient map" $p : X \to Y$, where X is the six-square $2D$ space, and Y is the surface of the 3D cube. For more details, see [43, Ch. 2, §22, p.134]. In particular, Figure 22.5 on [43, Ch. 2, §22, p.138] is a nice illustration of the quotient mapping.

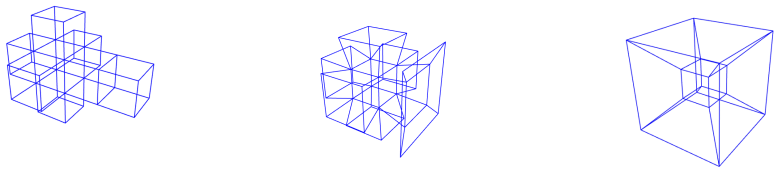

(a) (b) (c)

Figure 6.12: a: the eight 3D cubes which are the faces of the 4D hyperrectangle joined together by identifying the faces of the 3D cubes. b and c: folding the eight 3D cubes together to represent the data as a tesseract.

In analogy to the treatment of the surface of the 3D cube in the preceding paragraph and Figure 6.11, we can visualize the surface of the 4D hyperrectangle by instead visualizing the eight 3D rectangles that make up its surface. Some of the ones that share a common 2D face are glued together in Figure 6.12a.[6] This is, in principle, enough to represent all of the data points on the surface of this hyperrectangle, if we apply the discussion about wrapping around the 2D faces of a 3D cube to these 3D rectangular hyperfaces. But, we can make it more compact by "folding" the 3D faces together (Figure 6.12b), and then joining them together (Figure 6.12c). Figure 6.12c is designed to look like the tesseract [85].

Visual information is lost when we draw the surface of the 4D hyperrectangle as a tesseract, as we do in Figure 6.12c. The most glaring loss is that one of the eight 3D cubes was "blown up" and sent to the exterior; the other seven cubes are drawn inside the eighth exterior cube.[7] However, this disadvantage can be mitigated if we choose our hyperrectangular surface such that no EP_2 points will appear in one of the eight faces. Indeed, the boundary values we choose set it such that no EP_2 points are estimated to appear in the $P_{1,\min}$ or the $P_{1,\max}$ faces. Thus, only six of the eight 3D cubes are in Figure 6.12c, since the final one is superfluous. This gives us one way to represent a 4D hypersurface in a 3D plot!

6.3.3 Discretization and Scanning of 3D Rectangles

In order to obtain EP_2 points within these eight 3D rectangle faces, we vary the free parameters of the 3D rectangle. We perform spectroscopy to extract eigenvalues and the Lorentzian heights, and calculate the discriminant and the eigenvector indicator (Equations 6.48, 6.49, and 6.50).

This experiment employed two approaches to search for EP_2 points: we first tried rastering

[6] A diagram such as this is called a *net*. [83, 84]

[7] More formally, Figure 6.12c is a Schlegel diagram of the tesseract, which is a (perspective) projection of a polytope from $\mathbb{R}^d$ into $\mathbb{R}^{d-1}$. In this Schlegel diagram, the vertex from which the projection is made is chosen such that one face encloses the other seven faces [86].

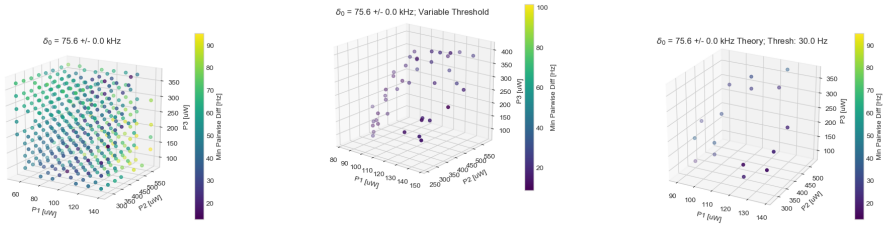

(a) All data. (b) Thresholded measured data. (c) Thresholded theory data.

Figure 6.13: Plots of several 3D rasters of the $\delta_{\max}$ face, with each dataset aggregated into one here. (a) is all data, colored by min-diff. (b) is those points with measured min diff below a gradient threshold of 20 Hz at $P_3 = 78\,\mu W$, and 25 Hz at $P_3 = 702\,\mu W$. (c) is theoretical calculations of those points, with min diff below 30 Hz.

all three free parameters in one face (namely, the δ-max face); and second, we tried fixing two parameters in a face, and rastering the other two. As discussed in Subsection 5.4.3, we had the most success with the latter approach.

In this section, we look at the approach where we scan all three free parameters.

Our first approach to raster a 3D face of the 4D hyperrectangle was to simply fix the one free parameter to the face, then raster the other three. For example, to raster the $\delta_{\max}$ face, we would raster the other three parameters. We did this several times, and then aggregated them into one 3D plot. Figure 6.13 is one such plot. The points are colored by a *minimum pairwise difference*, or *min-diff* defined as

$$\min \operatorname{diff}(\lambda_1, \lambda_2, \lambda_3) = \min\left(\{|\lambda_1 - \lambda_2|, |\lambda_2 - \lambda_3|, |\lambda_3 - \lambda_1|\}\right) \tag{6.52}$$

As an aside, as crude as Equation 6.52 is, it still highlights one essential characteristic of a point at EP_2: that if we sit at EP_2, then two eigenvalues become equal, so the min-diff becomes zero. Another obvious but useful fact is that the min-diff (Eq. 6.52) is zero if and only if the discriminant (Eq. 6.48) is zero.

Though the plot in Figure 6.13a shows which points are closer to EP_2 than other, the plot is quite unwieldy, since we aim to determine if the EP_2 points form a knot. Thus, we decided to threshold for those points with min-diff below some nominal values, to see if those points that remained were obviously knot strands. A major difficulty we had with this approach was how to pick the threshold value, since higher control laser powers introduced more eigenvalue fluctuations, which lead higher min-diff values. A somewhat useful choice was to use a graded threshold, where the threshold was lower for small laser powers and higher for high laser powers (Figure 6.13b). This can be compared with theoretically calculated data, based on the optomechanical model (Figure 6.13c).

The utility of Figures such as Figure 6.13 was limited, because despite our best efforts to

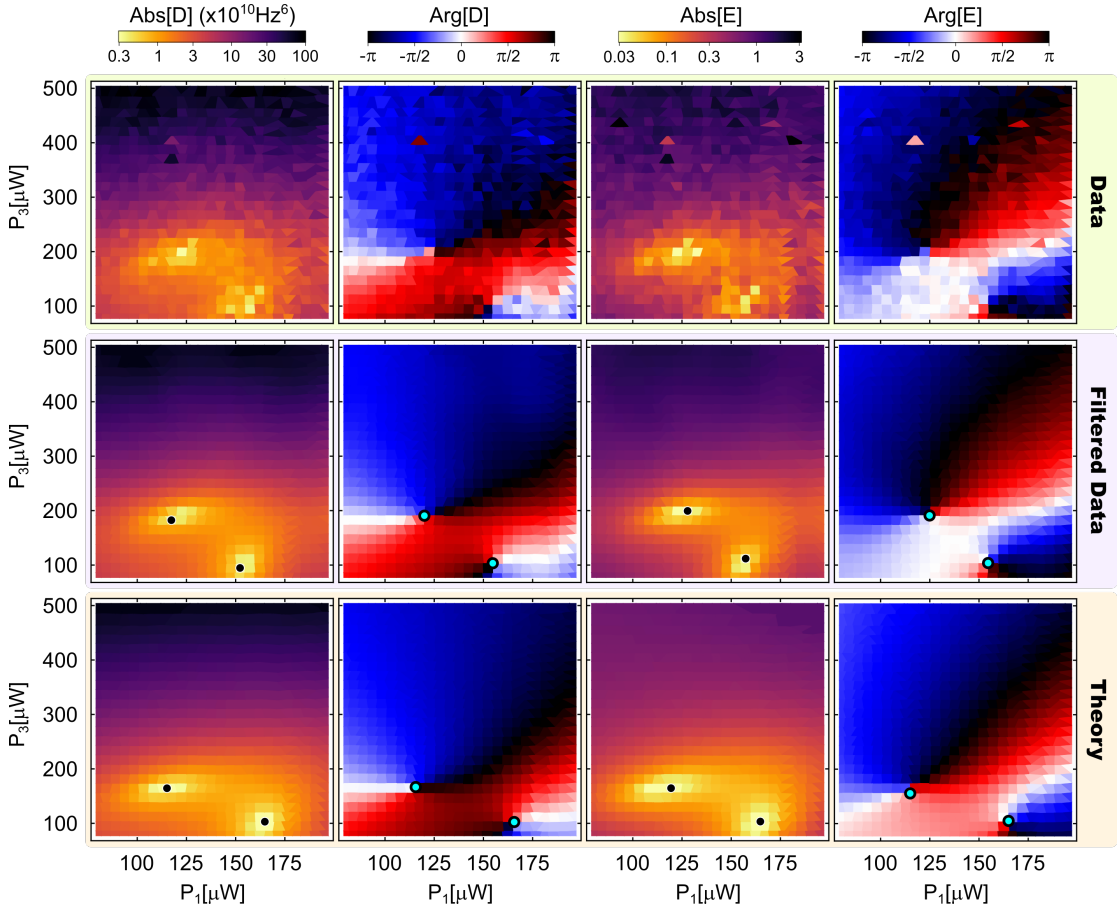

Figure 6.14: A slice taken to measure EP$_2$. The left two columns are the magnitude and phase of the discriminant D, respectively. The right two columns are the magnitude and phase of the eigenvector indicator E, respectively. The first row is raw data. The second row is filtered data (as described in Section 6.4.1). The black and cyan points in the magnitude and phase plots, respectively, are algorithmically chosen minima and vortices, which represent our estimates of EP$_2$ points (as described in Section 6.4.2). The third row is theoretically predicted data.

threshold points based on min-diff (or on the absolute value of the discriminant), we did not have enough density to distinguish minima in min-diff or discriminant with the 3D raster; as discussed in Subsection 5.4.3, a $9 \times 9 \times 9$ dataset required time on the order of one day. Thus, we switched to 2D rasters. Figure 6.14 is one such dataset, where the raster density is high enough that two different minima in the magnitude of the discriminant are very well-resolved.

In addition to a high resolution of the absolute value of the discriminant, the 2D rastering technique offers other analytical advantages, which we discuss in Section 6.4.

6.4 Analysis of EP$_2$ Slices

In this section, we discuss the techniques that we employ in order to quantitatively and algorithmically identify EP$_2$ points in a 2D dataset. Namely, having extracted the eigenvalues and Lorentzian complex heights for each pixel in a 2D dataset, and having calculated D (Eq. 6.48)

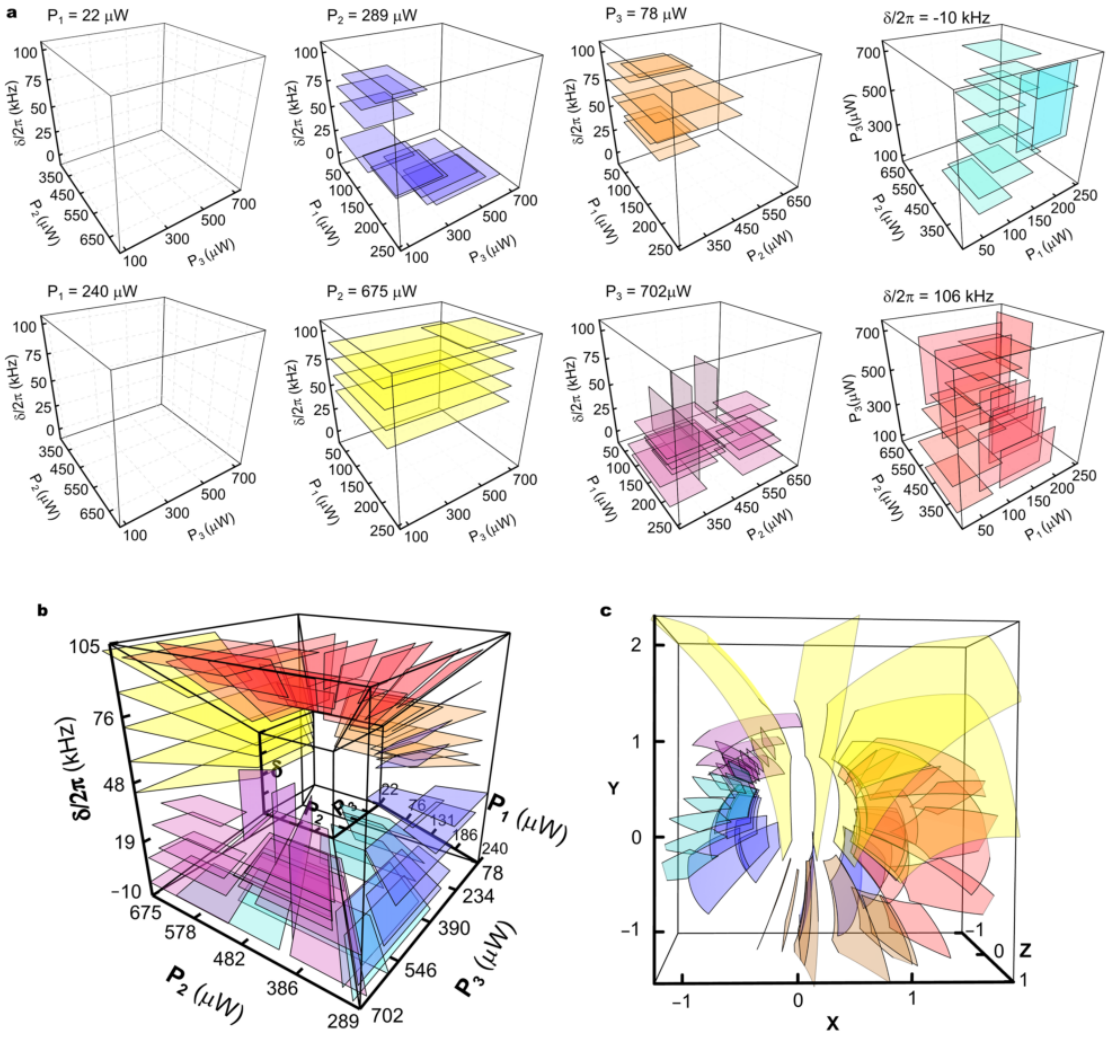

Figure 6.15: The sixty-one 2D slices performed over the hypersurface described in Section 6.3.2. a: the 61 slices on each of the eight faces of the hypersurface. b: the 61 slices, assembled in the "rectilinear stereographic" projection of the hypersurface (detailed in Section 6.5.1). c: the 61 slices, assembled in the 3D stereographic projection of the hypersurface (detailed in Section 6.5.2).

and E (Eq. 6.49-6.50) for each pixel, we smooth out the D and E values with two filters (Section 6.4.1). We then algorithmically identify minima in $|D|$ and $|E|$, as well as vortices in the arguments (Section 6.4.2). These algorithmically obtained values are deemed EP_2-candidates. Figure 6.14 shows the results of this analysis: the filtering of the data and the algorithmic selection of EP_2 candidate points, as well as the theoretically estimated data from the optomechanical model (this model is described in Section 3.6).

The analyses of this section are performed over sixty-one 2D slices (Figure 6.15) taken across the hypersurface (described in Section 6.3.2).

6.4.1 Filtering of EP_2 Slices

In order to algorithmically identify EP_2 points, we first smooth the raw complex D and E data with two filters. We employ this filtering because when we perform measurements across the EP_2 for D (Eq. 6.48) and E (Eq. 6.49-6.50) , we might find multiple spurious "local minima" or "vortices" in a cluster, even though we should only expect one minimum or vortex per cluster to be our EP_2 point.

The job of the filtering is thus to try to reduce the noise in our discriminant and eigenvector indicator measurement data before we algorithmically identify a candidate EP_2 point. We first use an "outlier remover" filter which removes any anomalously large or small values in the real and imaginary parts of the data. Second, we use a Gaussian filter, which convolves the data with a Gaussian kernel.

Outlier Removal Filter

Before we do any smoothing of our data, we first reject any outlier data pixels. We do this because the output of the Gaussian filter is essentially taking a moving average of the pixels in a neighborhood of a given pixel; an outlier of an extremely large (or small) magnitude will artificially make the amplitudes of the neighboring pixels disproportionately larger (or smaller) than they would be if the outliers were removed (see Figure 6.19a for an example of this).

The outline of the outlier-filtering algorithm on a 2-dimensional dataset D is as follows:

1. Given a data point p in the data set D, define a 5×5 grid G of points, with p as the center point (i.e. if the indices of G_{ij} are labeled from $i, j = 0$ to 4, then p is the $(2, 2)$ point).
   (a) If none of the i, j indices of G_{ij} go outside the borders of D, continue to next step
   (b) If the of the i, j indices of G_{ij} would go past the border of D, then only consider the points which lie in the overlap of G_{ij} and D (i.e. G may have less than $5 \times 5 = 25$ points).
2. For all points in G, compute Q_1 and Q_3, which are the first and third quartiles of the values in G (or the 25th and 75th percentiles, respectively). This gets the interquartile range, $IQR = Q_3 - Q_1$.
3. We define an outlier from the dataset G as any point q for which

$$q \notin (Q_1 - s * IQR, Q_3 + s * IQR) \tag{6.53}$$

where s is a nonnegative constant. This is a test by Tukey [87]. s is typically set to 1.5 to indicate an outlier, but could be set to 3 to indicate far-out data. In our data analysis, we

set

$$s = 6, \tag{6.54}$$

since our discriminant and eigenvector indicator data (Eqs (6.48) and (6.50)) are positive-skewed.

(a) If p is an outlier, per Eq. (6.53), then replace p with the median of G.

(b) If p is not an outlier, per Eq. (6.53), then leave p as-is.

A NumPy implementation of this outlier-filter algorithm is in Appendix F.

We perform the outlier filter separately on the real and imaginary parts of the discriminant (6.48) and the eigenvector indicator (6.50).

Gaussian Smoothing

The two-dimensional Gaussian filter $\mathcal{G}$ is a linear filter, which means it can be writen as a convolution of the data $f(x, y)$ with some kernel $g(x, y)$:

$$\mathcal{G}[f](x, y) = \int_{\alpha=-\infty}^{\infty} \int_{\beta=-\infty}^{\infty} f(\alpha, \beta) g(x - \alpha, y - \beta)\, d\alpha\, d\beta \tag{6.55}$$

In this case, the kernel $g(x, y)$ is

$$g(x, y) = \frac{1}{2\pi\sigma^2} e^{-\frac{x^2+y^2}{2\sigma^2}} \tag{6.56}$$

where σ is the standard deviation of the kernel. [88, pp.125-126] [89, pp.33] [90, pp.5] One can also express this kernel in terms of its full width at half maximum (FWHM) [91]:

$$\text{FWHM} = 2\sqrt{2 \ln 2}\, \sigma \approx 2.3548\, \sigma \tag{6.57}$$

One way to think of this filter is that each pixel is replaced by a moving weighted average of the neighboring pixels. The Gaussian kernel (6.56) sets the weights for the average, such that the pixels close to the center pixel are weighted more highly than those away from the center.

To make rigorous this concept of a moving average in relation to a convolution, we can consider a boxcar function, as in Figure 6.16a. If one wants to simply do a moving average of a pixel of data with its three nearest neighbors, one can convolve the data (Eq. (6.55)) with a two-dimensional boxcar function of width 3, which is zero outside of $x \in (-1.5, 1.5)$ and $y \in (-1.5, 1.5)$.

In a digital implementation, this convolution of an image with a boxcar filter of 3 pixels is

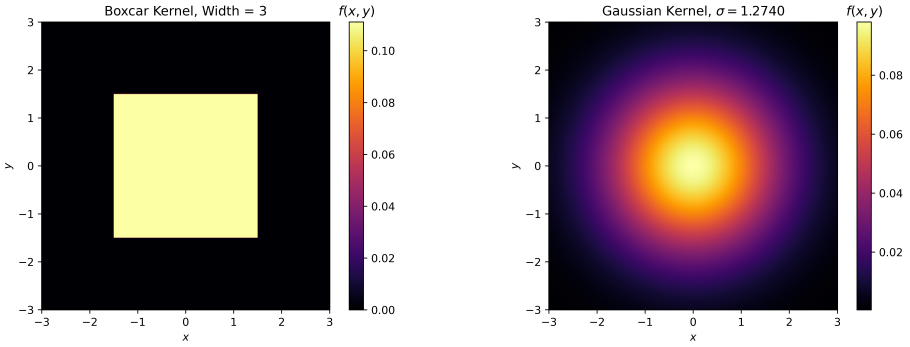

(a) Boxcar kernel.

(b) Gaussian kernel.

Figure 6.16: Kernels that can be convolved with a data to get a "moving average" of a pixel with its nearest neighbors, so as to reduce noise in data. Left is the boxcar kernel, with a width of 3 units, and right is a Gaussian kernel, with a FWHM of 3 units, chosen to match the width of the boxcar on the left ($\sigma = 1.2740$, from Eq. (6.57))

done by convolving the 2D data with a discretized version of the boxcar filter [89, pp.5]:

$$\text{boxcar filter} = \frac{1}{9}\begin{bmatrix} 1 & 1 & 1 \\ 1 & 1 & 1 \\ 1 & 1 & 1 \end{bmatrix} \tag{6.58}$$

The discretized convolved data is obtained by the summation

$$C_i = \sum_j I_{i+k-j} W_j \tag{6.59}$$

It should be understood that i, j, k are two-dimensional indices, with range from $(0, 0)$ to $(2, 2)$. Here, W_j is the weight filter kernel, I_{i+k-j} is the image input data, k is the coordinate of the center of the weights kernel (in this example, $k = (1, 1)$ is the center, where k goes from $(0, 0)$ to $(2, 2)$) [92, scipy.ndimage.convolve] [93].

Now, the boxcar filter (such as the 3-pixel one in (6.58)) does an *unweighted* average of the pixels in the 3-pixel neighborhood of the center pixel. We can instead weight with a Gaussian kernel (6.56), to give those pixels farther away from the center less weight in the filtering. A discretized version of the Gaussian kernel, for some σ, can be obtained by plugging in integers to (6.56). In theory, this requires (bi)infinitely many matrix coefficients. However, the filter can be truncated beyond a certain number of standard deviations σ [90, pp.6]. In particular, we can ignore 3 standard deviations, since 99.73% of data lies within 3 standard deviations. For example, to approximate a Gaussian kernel of $\sigma = 1$, one can use the integer valued 5×5 matrix

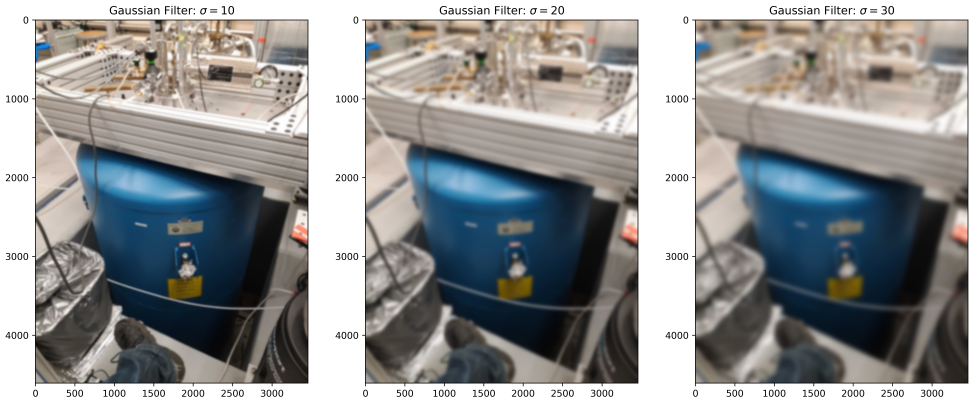

Figure 6.17: The results of Gaussian-filtering an image (showing the cryostat in which these experiments were performed). Higher values of σ correspond to a stronger pixel blurring, i.e. a stronger pixel smoothing.

[90, pp.7]:

$$G_{5\times5}^{\sigma=1} = \frac{1}{273}\begin{bmatrix} 1 & 4 & 7 & 4 & 1 \\ 4 & 16 & 26 & 16 & 4 \\ 7 & 26 & 41 & 26 & 7 \\ 4 & 16 & 26 & 16 & 4 \\ 1 & 4 & 7 & 4 & 1 \end{bmatrix} \tag{6.60}$$

This works, because $1/273 \approx 0.00366$, which is below 1% on the farthest boundary of the matrix.[8]

With the Gaussian filter (6.56), a higher σ corresponds to more smoothing, or blurring, of the image or data. For instance, we can apply this filtering to the image of our cryostat in Figure 4.10a. Figure 6.17 shows the result of applying a Gaussian smoothing filter, for several choices of σ. In this case, $\sigma = 10$ provides fairly minimal blurring, and $\sigma = 30$ provides more blurring.

This Gaussian filter is used on both the real and the imaginary parts of the discriminant and eigenvector indicator data individually. The middle and bottom two rows of Figure 6.18 show the smoothing process. One can see by eye that the real and imaginary parts of the discriminant data are smoother after the Gaussian filter. We also plot the magnitude and phase of these data and filtered data, respectively. What we obtain in this image is that the minimum in the magnitude is smoother than in the raw data, and the phase has an obvious vortex point in the filtered data, unlike in the raw data. We also note that we did not decrease the depth of the magnitude dip, since we did not directly use the filter on the magnitude, but on the real and imaginary components.

We can remark here why it was important to do the outlier filter before doing the Gaussian filter. The reason is that if the Gaussian filter encounters pixels with large outlying values from

[8]SciPy chooses to truncate 4 standard deviations by default; its truncate argument truncates to 4.0 standard deviations [94]. 99.9938% of the data lies within 4 standard deviations.

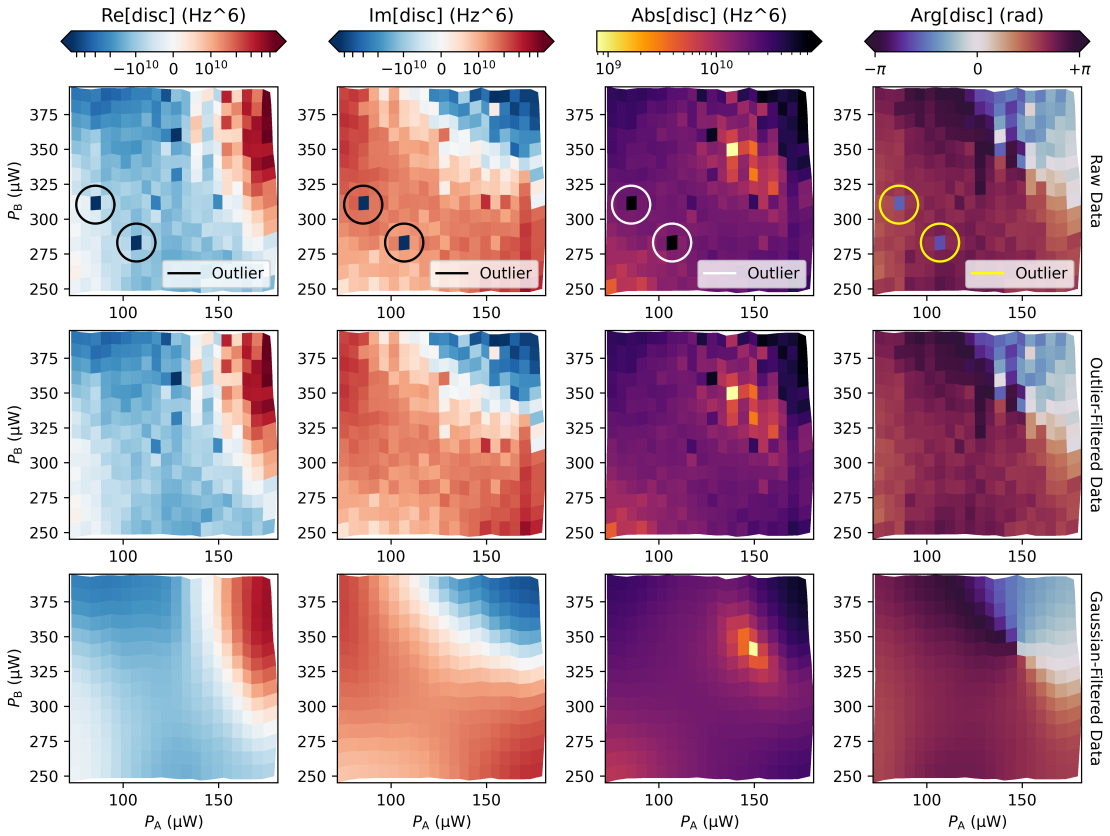

Figure 6.18: The results of filtering our discriminant data with our filtering procedure. First, we outlier-filter the raw data (top row), by replacing outlier pixels (in circles; top) with median-filtered pixels (middle row). Next, we Gaussian-filter the outlier-filtered data to smooth the data (bottom row), with Gaussian standard deviation $\sigma = 10/(2\pi)$. These filters are applied to the real and imaginary components of the discriminant (left two columns). The corresponding magnitude and phases are plotted alongside them (right two columns). The gaussian filter is implemented in [94] [92].

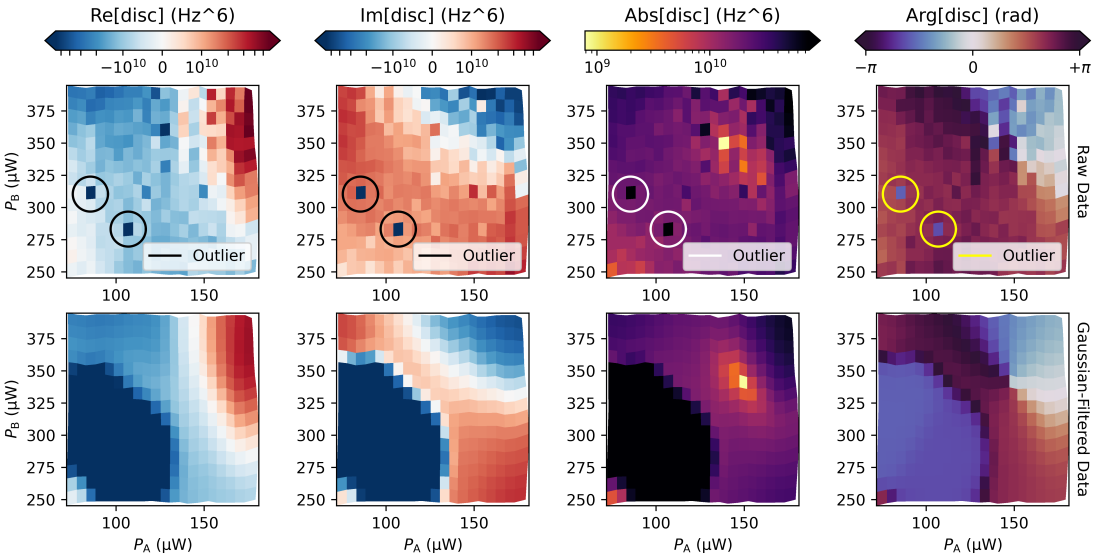

(a) $\sigma = 10/2\pi$

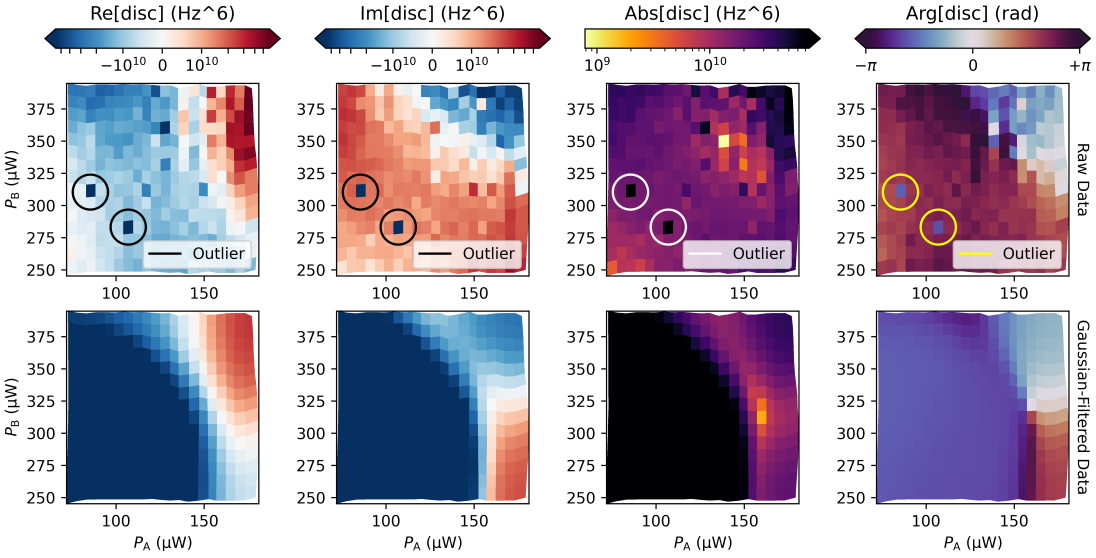

(b) $\sigma = 20/2\pi$

Figure 6.19: The results of Gaussian-filtering the real and imaginary components of the discriminant data without first outlier-filtering the data. Convolving the non-outlier pixels with the outlier salt and pepper pixels with the non-outlier pixels spreads the outlier values over the rest of the data.

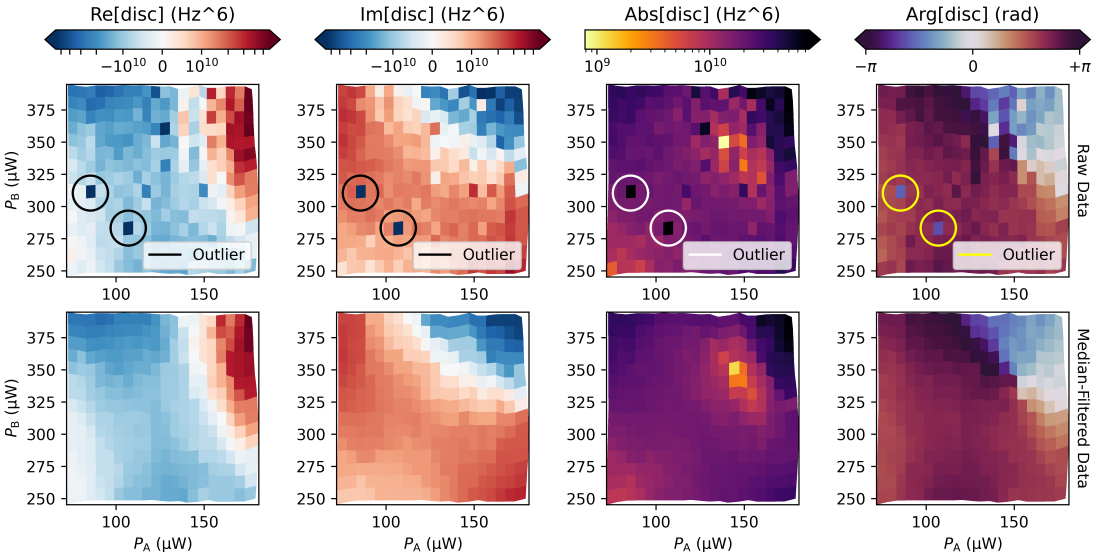

Figure 6.20: The result of applying a median filter of size $= (3, 3)$ to the real and imaginary discriminant data. It replaces outlier salt and pepper noise pixels with less noisy pixels, as well as smoothes out the data, by itself.

the rest of the data, these outliers will average with the much smaller pixels, and "smear" the outlier value over a broader area. Figure 6.19 shows an example of this: the large salt and pepper pixels in the raw data become large blobs in the Gaussian-filtered data. This can hamper any image analysis algorithms (Subsection 6.4.2) that seek minima in the magnitude or vortices in the phase. In particular, even though the blob misses the minima and vortices that we seek in Figure 6.19a with $\sigma = 10/2\pi$, the blob does obstruct them in Figure 6.19b with $\sigma = 20/2\pi$ (which is merely double the filter width used in our experimental analysis). Thus, to avoid defeating the Gaussian filter with salt and pepper noise, we remove the salt and pepper noise with the outlier filter first.

Alternative Approaches: Median Filter and General Considerations

In this section, we discuss an alternative method of smoothing the data: the median filter. The median filter operates on a pixel by taking subsections of the data around the pixel, defined by some window, and replacing the pixel with the median of the subsection. The median is an averaging function, like the convolution, but it handles outliers by simply dropping outliers from the median calculation, as opposed to summing the outlier term in the calculation of a convolution. Thus, a small median filter removes our outliers and smoothes the data in one fell swoop (Figure 6.20).

The median filter has a downside compared to the Gaussian filter, in that it is not as efficient at removing Gaussian noise [88, pp.132]. This is because, instead of taking a mean, or a convolution with a Gaussian, the median filter *selects* one pixel from the window to replace the

pixel. We can see the effect of the median filter (Figure 6.20) as well as the outlier-Gaussian filter combination (Figure 6.18): the output of the combination is smoother, since most of the measurement noise is Gaussian, and only a small portion of the noise is salt and pepper noise. Thus, we opted to handle the the salt and pepper noise with a customized outlier filter (see Appendix F for an implementation), and then remove the Gaussian noise itself with a Gaussian filter [94] [95].

Alternative approaches to handle salt and pepper noise are suggested in [88, pp.133]. One such approach is an α-trimmed mean, which averages together all pixels except for the fraction α that are the smallest and largest. Since our salt and pepper noise was limited, this might have thrown out more pixels than needed for the smoothing. Another choice is a weighted median, which computes the median in a window which duplicates pixels that are closer to the center of the window. This could remove salt and pepper noise, while keeping more non-salt-and-pepper noisy pixels fixed, in a way similar to our outlier filter.

Finally, as an aside, we remark that median filters, and nonlinear filters in general, are useful in edge preservation for computer vision [88, pp.133]. One can then use a convolution with the derivative of a Gaussian for edge detection [89]. As interesting as edge detection is to computer vision, we were interested in EP_2 points in this work, so we did not need edge preserving properties of the median filter.

6.4.2 Algorithmically Finding EP_2 Points

The final step in analyzing EP_2 datasets is the selection of points in the datasets that represent our best estimate of the location of EP_2 . One could do this by eye, based on the raw discriminant (6.48) or eigenvector indicator (6.50) data. However, we can make a much stronger, more quantitative statement about where EP_2 lies in our data if we algorithmically choose EP_2 candidate points from our data. In particular, we can do this after we apply the filtering techniques discussed in Section 6.4.1, so that we run these algorithms on datasets that have their noise reduced. We then employ the algorithms discussed below to quantitatively determine the location of EP_2 points. These two algorithms operate individually on the magnitude and phase, respectively, of the discriminant and eigenvector indicator. Thus, we end up with four methods to identify EP_2 points in the control space.

Minima Finder

This algorithm operates on $|D|$ (6.48) and $|E|$ (6.50), and seeks all local minima over a window $\mathcal{W}$ of some specified size. It then rejects spurious minima by checking the second derivatives of $|D|$ and $|E|$, and only accepting those points with a large enough second derivative. We operate

with the second derivative because if $|D|$ or $|E|$ show a true minimum, as opposed to a minimum due to a random fluctuation, we would expect the 2nd derivative to consistently have a positive curvature that reflects the presence of this minimum.

Step by step, the algorithm is as follows:

1. Let the $|D|$ or $|E|$ dataset points X_{ij} be indexed by (i, j), for $0 \leq i \leq N_i - 1$ and $0 \leq j \leq N_j - 1$. Let P_{ij} and Q_{ij} denote the values of the first and second experimental parameter which raster X_{ij}. For each point in the dataset strictly within the dataset, i.e. for which $1 \leq i \leq N_i - 2$ and $1 \leq j \leq N_j - 2$, take a window $\mathcal{W}_{ij}$ of 3 pixels by 3 pixels, i.e. with points (k, l), where $i - 1 \leq k \leq i + 1$ and $j - 1 \leq l \leq j + 1$. Check if $\text{Abs}(X_{ij})$ is less than *all* points within the window $\mathcal{W}_{ij}$. If no, then X_{ij} is not a local minimum. If yes, proceed to the next step.

2. Compute the 2nd partial derivative matrix of X_{ij} with a finite difference calculation. This can be done by the formulae

$$(X_{ij})_{xx} = \frac{X_{i+1,j} - 2X_{ij} + X_{i-1,j}}{h^2} \tag{6.61}$$

$$(X_{ij})_{yy} = \frac{X_{i,j+1} - 2X_{ij} + X_{i,j-1}}{k^2} \tag{6.62}$$

$$(X_{ij})_{xy} = \frac{X_{i+1,j+1} - X_{i-1,j+1} - X_{i+1,j-1} + X_{i-1,j-1}}{4hk} \tag{6.63}$$

   where $h = (P_{i+1,j} - P_{i-1,j})/2$ and $k = (Q_{i,j+1} - Q_{i,j-1})/2$ are finite differences in the parameter axes.

3. Compute the 2nd derivative determinant matrix:

$$(X_{ij})'' = (X_{ij})_{xx}(X_{ij})_{yy} - (X_{ij})_{xy}^2 \tag{6.64}$$

4. For all points in the window W from Step 1, compute $\mu[X''_{kl}]$ and $\sigma[X''_{kl}]$, for all (k, l) that index $\mathcal{W}_{ij}$.

5. Report X_{ij} as a true minimum only if

$$(X_{ij})'' > \mu[X''_{kl}]_{(k,l)\in\mathcal{W}_{ij}} + 2\sigma[X''_{kl}]_{(k,l)\in\mathcal{W}_{ij}} \tag{6.65}$$

   If X_{ij} is reported as a true minimum, we report the corresponding swept parameters P_{ij} and Q_{ij}, as well as the fixed parameters in this slice, as an EP_2 point in (δ, P_A, P_B, P_C) parameter space.

In Figure 6.14, we can see the result of applying this algorithm to a dataset: there are

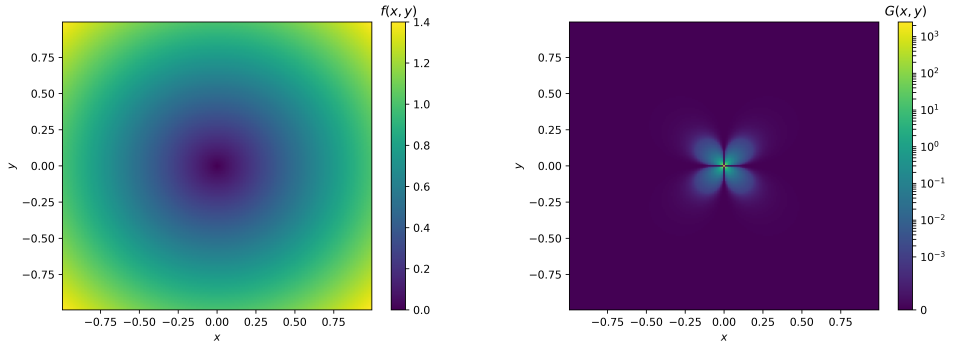

Figure 6.21: The computation of the second derivative test determinant (b) for the function $f(x, y) = \sqrt{x^2 + y^2}$ (a). The determinant has a singularity at $(x, y) = (0, 0)$. This singularity motivates our minimum finding algorithm for the discriminant (6.48) and the eigenvector indicator (6.50).

two "obvious" clusters of minima in this data. This data is filtered, and then two points are automatically chosen as minima of $|D|$ and $|E|$ from this algorithm (marked as black dots in the first and third columns of Figure 6.14).

For a rationale behind these 2nd derivative tests, we recall one- and two-dimensional calculus. For a one-dimensional curve, $f(x)$ for which both the first and second derivatives, $f'(x)$ and $f''(x)$ are defined, at a point x_0 for which $f(x)$ is a maximum or minimum, then $f'(x_0) = 0$. Furthermore, if $f''(x_0) > 0$, then f has a local maximum at x_0, and if $f''(x_0) < 0$, then f has a local minimum at x_0. [96] [97] Generalizing to a function $f(x, y)$ of two variables, for which all of its partial derivatives up to second order are defined, suppose that (x_0, y_0) is a critical point (a local minimum or a maximum). Then $f_x(x_0, y_0) = 0$ and $f_y(x_0, y_0) = 0$. Furthermore, when we compute the second derivative test determinant $G = f_{xx}f_{yy} - f_{xy}f_{yx}$ at (x_0, y_0), then if $G > 0$ and $f_{xx}(x_0, y_0) > 0$, the point is a local maximum. If $G > 0$ and $f_{xx}(x_0, y_0) < 0$, the point is a local minimum [96] [97] [98].

Applying the above discussion to our data, we compute partial derivatives from finite differences as above, then compute the second derivative test from the above discussion. The criterion in Step 5 is empirically motivated; we expect $|D|$ (6.48) and $|E|$ (6.50) to have functional dependence similar to $f(x, y) = \sqrt{x^2 + y^2}$. For this $f(x, y)$, G asymptotically blows up as $1/\varepsilon^2$, for perturbations of radius ε from a minimum $(0, 0)$. This singularity is demonstrated in Figure 6.21. We can then check for those points X_{ij} for which $(X_{ij})''$ satisfies the criterion in Equation (6.65), i.e. we select those points which exceed the mean value of X'' in the window $\mathcal{W}_{ij}$ by two standard deviations. Thus, even though we do not apply the classic second derivative test from multidimensional calculus, as discussed in [96], we can still identify local minima in our datasets.

Vortex Finder

The previous EP$_2$-finding algorithm operates on the magnitude of D (6.48) and E (6.50). This algorithm identifies EP$_2$ points based on vortices in the phase of D and E. Vortices in the phase are points around which the phase wraps around by $2\pi n$, for some nonzero integer n. In particular, for the function $f(z)$ which admits a Taylor zeries $f(z) \approx z_0 + az$, for some $z_0, a \in \mathbb{C}$, $f(z)$ has a vortex only at z_0; a counterclockwise loop that encloses z_0 wraps the phase around by 2π, but a counterclockwise loop that does not enclose z_0 wraps the phase by 0 (see Figure 6.9 for an example, with $z_0 = 0$).

The algorithm that detects vortices in the D and E data is as follows:

1. Let the D or E dataset points X_{ij} be indexed by (i, j), for $0 \leq i \leq N_i - 1$ and $0 \leq j \leq N_j - 1$. Let P_{ij} and Q_{ij} denote the values of the first and second experimental parameter which raster X_{ij}. For each point in the dataset strictly within the dataset, i.e. for which $1 \leq i \leq N_i - 2$ and $1 \leq j \leq N_j - 2$, take a window $\mathcal{W}_{ij}$ of 3 pixels by 3 pixels. $\mathcal{W}_{ij}$ is spanned by the indices (k, l) where $i - 1 \leq k \leq i + 1$ and $j - 1 \leq l \leq j + 1$.

2. Create an closed ordered list of the pixels on the perimeter of $\mathcal{W}_{ij}$, which ends at the same index that it begins. This makes a "closed loop" in software. Without loss of generality, we can take this list to be $\big[(i-1, j-1), (i, j-1), (i+1, j-1), (i+1, j), (i+1, j+1), (i, j+1), (i-1, j+1), (i-1, j), (i-1, j-1)\big]$.

3. Plot the arguments of D (6.48) or of E (6.50) against these indices. These phases will be values from $-\pi$ to $+\pi$.

4. Apply a standard phase unwrapping algorithm to this ordered list of phases. This will remove the 2π discontinuity in the phase, if there is one.[9]

5. The final unwrapped phase data will have a starting point and an ending point that differs by either 0 or by an integer multiple of 2π. If the start and final phases are equal, then X_{ij} is not a vortex point. If they differ by 2π, then X_{ij} is a vortex point, and we then report the corresponding swept parameters P_{ij} and Q_{ij}, as well as the fixed parameters in this slice, as an EP$_2$ point in $(\delta, P_\mathrm{A}, P_\mathrm{B}, P_\mathrm{C})$ parameter space.

6.5 Measuring the EP$_2$ Trefoil Knot

One of the major goals of this experiment was to demonstrate that the EP$_2$ points on a hypersurface of the 4-dimensional eigenvalue control space enclosing EP$_3$ possesses a trefoil knot

[9] One such standard algorithm is the `numpy.unwrap` function in NumPy [99]. Another is the `PhaseUnwrap` function in Mathematica [100].

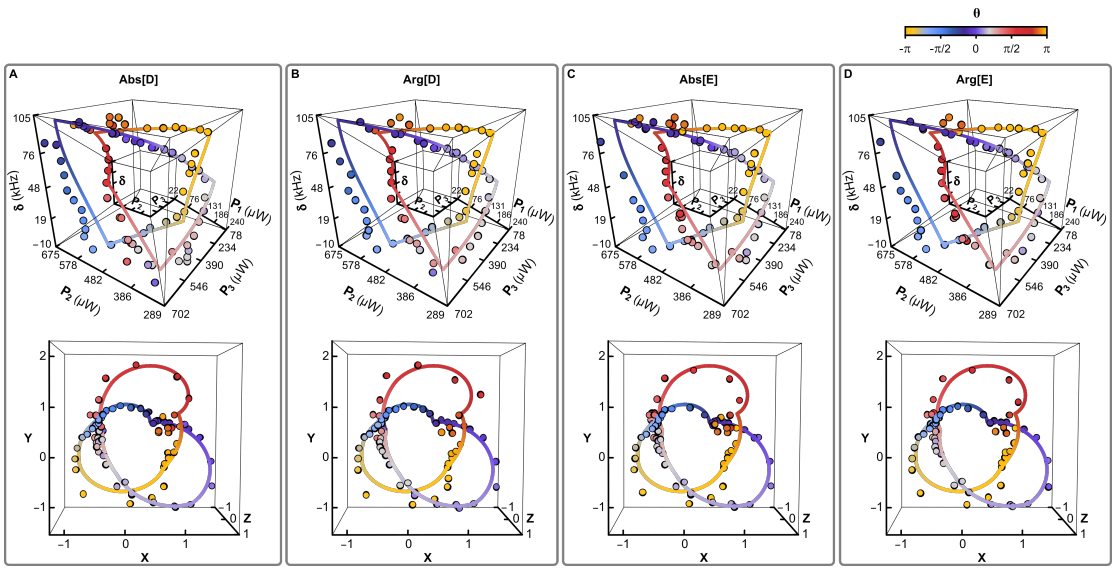

Figure 6.22: All of the EP$_2$ points that were algorithmically found from all of the 61 datasets in this experiment, via all four methods in Section 6.4.2. The columns represent each of the four methods. The top row is the tesseract representation of the 3D hypersurface. The bottom row is the stereographic projection of the 4D data. The circles represent the algorithmically obtained EP$_2$ points, and the line represents a theoretically estimated EP$_2$ curve. The points are colored by θ (Equation 2.115; upper right corner).

structure. In this section, we describe the visualization of these measured EP$_2$ points, and determine that they do form a trefoil knot.

We performed spectroscopy (Section 6.1) to extract eigenvalues and complex Lorentzian amplitudes on datasets of a surface described in Section 6.3 that encloses an EP$_3$ point (Section 6.2). From these, we calculate the discriminant D (Equation (6.48)) and eigenvector indicator E (Equation (6.50)), and then perform post-processing analysis (Section 6.4) to algorithmically ascertain any EP$_2$ points in these datasets. In this section, we aggregate these EP$_2$ points, and assemble them in two visualizations of the 3D hypersurface.

6.5.1 Rectilinear Stereographic Projection

This representation aims to represent data which lives in the 4D control space as a 3D image. It takes the eight faces of the 3D hyperrectangle described in Section 6.3.2, and depicted in Figure 6.10, and identifies their common edges together. This transformation leaves the the "outer" face distended to an "infinity." There is a map from the other seven faces to the seven regions in the "tesseract," such that their common faces are visually joined.

For this visualization, the "inner" face is chosen to be the $P_{1,\min}$ face, and the "outer" face is the $P_{1,\max}$ face. This choice is made because the 4D hypersurface is chosen so that no EP$_2$ points were expected to appear on these two faces.

The linear transformation for this visualization is as follows:

1. Find scaling terms that scale the experimental coordinates (δ, P_1, P_2, P_3) to dimensionless line segments that span from -0.4 to $+0.4$. For each experimental coordinate Z, we can consider this a linear map of $z = m_Z Z + b_Z$, where $z \in (-0.4, +0.4)$. Since Z has corresponding minimum and maximum values $Z_{\min}$ and $Z_{\max}$, m_Z and b_Z can easily be solved for with point-slope form:

$$\begin{aligned} m_Z &= \frac{+0.4 - (-0.4)}{Z_{\max} - Z_{\min}} \\ b_Z &= 0.4 - m_Z\, Z_{\max} \end{aligned} \tag{6.66}$$

2. For each of the six faces of the hypersurface that are shown in this representation, this step makes the (δ, P_1, P_2, P_3) points on this face live in a dimensionless cube of shape $0.8 \times 0.8 \times 0.8$, centered about $(0, 0, 0)$, using the values in Equation 6.66 found in Step 1. Take the experimental coordinates (δ, P_1, P_2, P_3), which is a tuple of four elements, and then apply the linear transformations of Step 1 to return a tuple $X = (x_1, x_2, x_3)$ of three elements (the fourth is redundant, since these X's lie on one of the eight faces of the 4D hyperrectangle). For the six regions on the exterior of the "tesseract," this transformation is as follows:

   - δ: $\big(m_{P_1} P_1 + b_1, m_{P_2} P_2 + b_2, m_{P_3} P_3 + b_3\big)$
   - P_2: $\big(m_{P_1} P_1 + b_1, m_{P_3} P_3 + b_3, m_\delta \delta + b_\delta\big)$
   - P_3: $\big(m_{P_1} P_1 + b_1, m_{P_2} P_2 + b_2, m_\delta \delta + b_\delta\big)$

3. This step puts the six dimensionless cubes of step 2 into their respective regions on the "tesseract" image. Rotate and reflect, as necessary, the points of a given hyperface on the 4D hyperrectangle, then shift them to the left or the right in 3D space. This maps each point to one of the seven regions on the exterior of the "tesseract." The $P_{1,\min}$ face is left fixed in the interior, so it is left unchanged; the $P_{1,\max}$ face is distended to "infinity." Neither of these faces are depicted, since the 4D hypersurface is chosen so that no EP$_2$ points lie on these two faces. As for the other six faces, given a scaled point X from step 2, let $R_q(\theta)$ be a rotation about the q-axis (where $q \in \{x, y, z\}$) by θ, and let M_x be a reflection about the x-axis. Then the points X are transformed as:

   - $\delta_{\min}$: $A = \big(M_x \circ R_z(+\pi/2) \circ R_y(+\pi/2)\big) \cdot X + (0, 0, -0.8)$
   - $\delta_{\max}$: $A = \big(\mathbb{I} \circ R_z(-\pi/2) \circ R_y(-\pi/2)\big) \cdot X + (0, 0, +0.8)$
   - $P_{2,\min}$: $A = \big(M_x \circ \mathbb{I}\big) \cdot X + (-0.8, 0, 0)$
   - $P_{2,\max}$: $A = \big(\mathbb{I} \circ \mathbb{I}\big) \cdot X + (+0.8, 0, 0)$

- $P_{3,\min}$: $A = \big(\mathbb{I} \circ R_z(-\pi/2)\big) \cdot X + (0, -0.8, 0)$
- $P_{3,\max}$: $A = \big(M_x \circ R_z(+\pi/2)\big) \cdot X + (0, +0.8, 0)$

4. This step takes the six cubes, which have been put in their correct places, and stretches their ends so that they form 3D trapezoidal prisms. Let $A = (A_1, A_2, A_3)$ be the data points from step 3. Then, depending which face A lies on, transform A as follows:

   - $\delta_{\min}$: $A \mapsto \{A_1 \times (-c(A_3 + 0.4) + 1), A_2 \times (-c(A_3 + 0.4) + 1), A_3\}$
   - $\delta_{\max}$: $A \mapsto \{A_1 \times (+c(A_3 - 0.4) + 1), A_2 \times (+c(A_3 - 0.4) + 1), A_3\}$
   - $P_{2,\min}$: $A \mapsto \{A_1, A_2 \times (-c(A_1 + 0.4) + 1), A_3 \times (-c(A_1 + 0.4) + 1)\}$
   - $P_{2,\max}$: $A \mapsto \{A_1, A_2 \times (+c(A_1 - 0.4) + 1), A_3 \times (+c(A_1 - 0.4) + 1)\}$
   - $P_{3,\min}$: $A \mapsto \{A_1 \times (+c(A_2 - 0.4) + 1)), A_2, A_3 \times (+c(A_2 - 0.4) + 1)\}$
   - $P_{3,\max}$: $A \mapsto \{A_1 \times (-c(A_2 + 0.4) + 1)), A_2, A_3 \times (-c(A_2 + 0.4) + 1))\}$

   The value c can be used to smoothly transform the cube into the final trapezoidal prism; $c = 0$ corresponds to the identity, and $c = 2.5$ corresponds to the final trapezoidal prism. This was useful in generating the videos of the tesseract transformation shown in [1, Supplement].

We use this projection to show all of the EP$_2$ points collected from the four algorithmic methods described in Section 6.4.2. These results are depicted in the top row of Figure 6.22. The circles are the algorithmically found EP$_2$ points. The curve is a theoretically estimated curve of the EP$_2$ points on the 3D hypersurface (as described in Section 3.6). The coloring is done by the quantity θ (Equation 2.115). θ is expected to wrap by 2π around the 1D curve once. This lets us impose an ordering on the algorithmically obtained points.

From Figure 6.22 (top row), we see that the data and their supporting theoretical curves do form a trefoil knot; the curve is not simply a circle (or a "unknot"), since it cannot be smoothly deformed into a circle. This tesseract visualization maintains any knot topology from the full 4D space, because even though the 4D surface is being represented in three dimensions, the edges that are adjacent in 4D remain adjacent in this 3D projection [86]. Thus, this tesseract representation of the EP$_2$ points demonstrates that the EP$_2$ curve is a trefoil knot.

6.5.2 Stereographic Projection

In addition to the tesseract representation (Section 6.5.1), we can also represent the EP$_2$ points on the 3D hypersurface in 4 dimensions via a stereographic projection into $\mathbb{R}^3$. We then inspect the curve in this 3-dimensional representation, and see that it is a knot in this projection as well (though this is already mathematically guaranteed, since the projections are isomorphic).

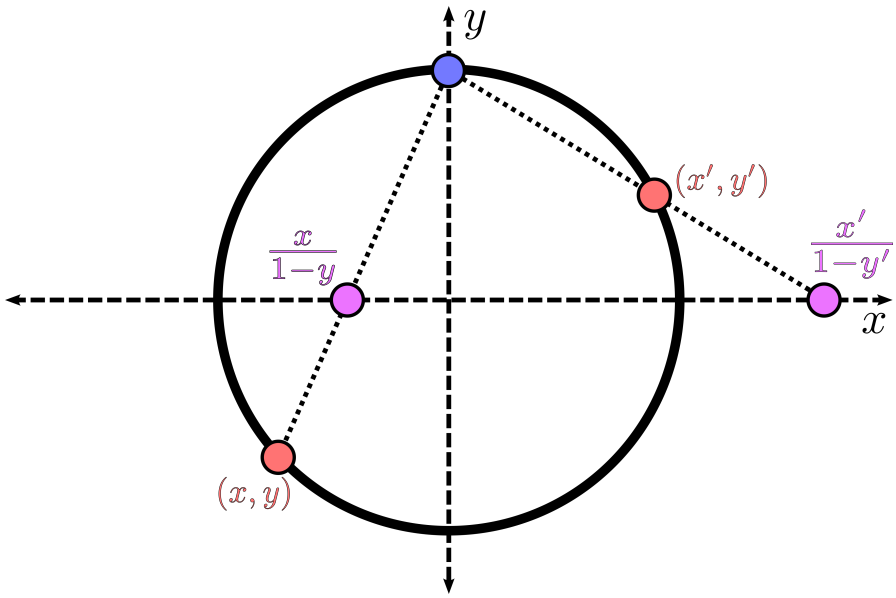

Figure 6.23: A stereographic projection of the unit circle ($|x|^2 + |y|^2 = 1$) onto the real line (x-axis). The north pole is chosen as $(0, 1)$ (blue). The points (x, y) and (x', y') on the circle (red) are mapped onto the points $x/(1-y)$ and $x'/(1-y')$ on the real line (purple).

To understand this map, we briefly review the stereographic projection of the unit circle onto the 1D line. This map takes a point (x, y) on the circle (where (x, y) satisfy the constraint $|x|^2 + |y|^2 = 1$) and plots it on the real line by the mapping

$$(x, y) \mapsto \mathcal{X} = \frac{x}{1-y}. \tag{6.67}$$

The mapping is depicted in Figure 6.23. Geometrically, this mapping can be interpreted as taking a point on the unit circle, and drawing a line segment through the point (red in Figure 6.23) and the point $(x, y) = (0, 1)$ (blue in Figure 6.23). The point at which the line segment intersects the real line is at $x/(1-y)$ (purple in Figure 6.23). [101] [102]

The stereographic projection map is easily seen to be invertible, from the above discussion. For completeness, we write the inverse here:

$$\mathcal{X} \mapsto \left(x = \frac{2\mathcal{X}}{\mathcal{X}^2 + 1}, y = \frac{\mathcal{X}^2 - 1}{\mathcal{X}^2 + 1} \right) \tag{6.68}$$

Since it is invertible, we see that there is a one-to-one correspondence between the points on the real line and the unit circle, with the "north pole" at $(0, 1)$ removed. This projection is a conformal map [102], so the angles (and shape) of the EP$_2$ structure are preserved by the map (though not necessarily its length).

The choice of pole in the stereographic projection need not be $(0, 1)$. Indeed, we can consider a stereographic projection with a different pole (p, q), which is also on the unit circle ($|p|^2 + |q|^2 =$

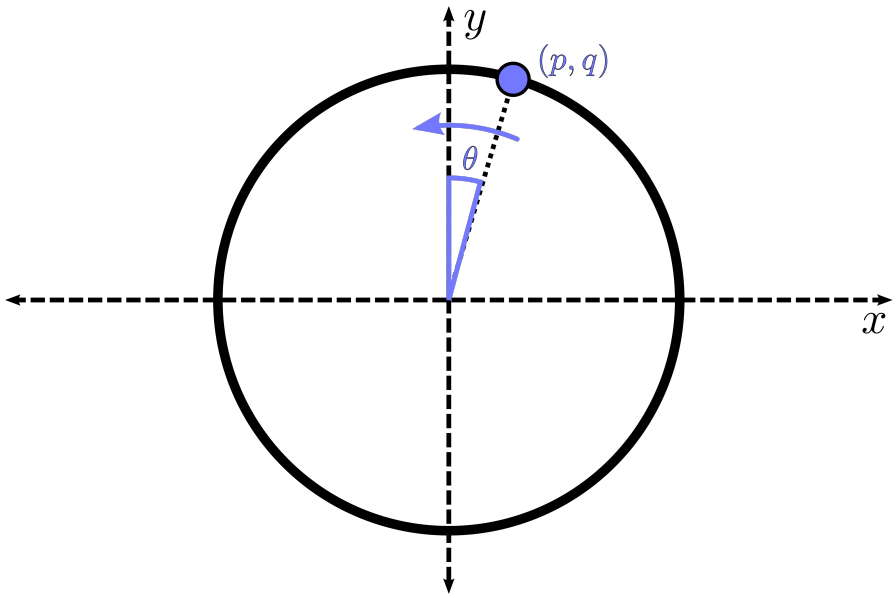

Figure 6.24: A stereographic projection of the unit circle ($|x|^2 + |y|^2 = 1$) onto the real line (x-axis). The north pole is chosen as (p, q) (blue), so we rotate the coordinate system to one in which (p, q) is at the origin.

1), as seen in Figure 6.24. Then we can rotate the coordinate system of the circle to one in which the point (p, q) is at the origin. This is accomplished via the rotation matrix

$$R_\theta = \begin{pmatrix} \cos\theta & -\sin\theta \\ \sin\theta & \cos\theta \end{pmatrix}, \tag{6.69}$$

where θ is given by $\tan\theta = p/q$. After this transformation is applied, we apply the stereographic projection (Eq. 6.67). This lets us bijectively map the unit circle, minus the pole, onto the real line via any choice of pole.

We can generalize this stereographic map to N dimensions, by mapping the $N-1$-sphere onto $\mathbb{R}^{N-1}$. Indeed, let $(x_1, x_2, \ldots, x_N)$ be a point on the unit sphere (so $|x_1|^2+|x_2|^2+\cdots+|x_N|^2 = 1$). We can take the north pole to be $(0, 0, \ldots, 1)$, and project the point on the sphere to a point on $\mathbb{R}^{N-1}$ via

$$(x_1, x_2, \ldots, x_N) \mapsto \left(\mathcal{X}_1 = \frac{x_1}{1-x_N}, \mathcal{X}_2 = \frac{x_2}{1-x_N}, \ldots, \mathcal{X}_{N-1} = \frac{x_{N-1}}{1-x_N}\right) \tag{6.70}$$

Define the quantity

$$s^2 = \sum_{i=1}^{N-1} \mathcal{X}_i^2 \tag{6.71}$$

The inverse of (6.70) is given by

$$(\mathcal{X}_1, \mathcal{X}_2, \ldots, \mathcal{X}_{N-1}) \mapsto \left(x_1 = \frac{2\mathcal{X}_1}{s^2+1}, x_2 = \frac{2\mathcal{X}_2}{s^2+1}, \ldots, x_N = \frac{s^2-1}{s^2+1}\right), \tag{6.72}$$

so this map is also invertible. Furthermore, it is also a conformal map, so it will preserve the structure of the EP$_2$ space. Finally, if we wish to stereographically project from a pole $(p_1, \ldots, p_N)$, we can rotate the coordinates $(x_1, \ldots, x_N)$ to a coordinate system in which $(p_1, \ldots, p_N)$ is at $(0, \ldots, 0, 1)$. One (nonunique) way to accomplish this is to apply rotation matrices

$$R_1 = \begin{pmatrix} \cos\theta_1 & 0 & 0 & 0 & \ldots & 0 & -\sin\theta_1 \\ 0 & 1 & 0 & 0 & \ldots & 0 & 0 \\ 0 & 0 & 1 & 0 & \ldots & 0 & 0 \\ 0 & 0 & 0 & 1 & \ldots & 0 & 0 \\ & & & & \ddots & & \\ 0 & 0 & 0 & 0 & \ldots & 1 & 0 \\ \sin\theta_1 & 0 & 0 & 0 & \ldots & 0 & \cos\theta_1 \end{pmatrix}$$

$$\vdots \tag{6.73}$$

$$R_{N-1} = \begin{pmatrix} 1 & 0 & 0 & 0 & \ldots & 0 & 0 \\ 0 & 1 & 0 & 0 & \ldots & 0 & 0 \\ 0 & 0 & 1 & 0 & \ldots & 0 & 0 \\ 0 & 0 & 0 & 1 & \ldots & 0 & 0 \\ & & & & \ddots & & \\ 0 & 0 & 0 & 0 & \ldots & \cos\theta_{N-1} & -\sin\theta_{N-1} \\ 0 & 0 & 0 & 0 & \ldots & \sin\theta_{N-1} & \cos\theta_{N-1}. \end{pmatrix}$$

where θ_k is given by

$$\tan\theta_k = \frac{p_k}{\sqrt{p_N^2 - p_k^2 + \sum_{j=1}^{k} p_j^2}}. \tag{6.74}$$

Then we first apply the rotation matrix $R_{N-1}R_{N-2}\ldots R_2R_1$ to the coordinates, and then apply the stereographic projection map from Equation 6.70. This provides an invertible map from $S^{N-1} - \{(p_1, p_2, \ldots, p_N)\}$ to $\mathbb{R}^{N-1}$.

To employ the stereographic projection (6.70), we take the experimentally measured EP$_2$ points, which have dimensions of $2\pi \times$ kHz and μW, and change the coordinate system to a dimensionless one centered around $(0, 0, 0, 0)$. We consider the experimental coordinates $(\delta, P_\mathrm{A}, P_\mathrm{B}, P_\mathrm{C})$ as having an origin at the empirically measured EP$_3$ point

$(\delta_{\mathrm{EP}_3}, P_{\mathrm{A,EP}_3}, P_{\mathrm{B,EP}_3}, P_{\mathrm{C,EP}_3})$, and define the dimensionless coordinates (x_r, y_r, z_r, w_r):

$$\begin{aligned}
x_r &= \frac{\frac{\delta}{\delta_{\mathrm{EP}_3}} - 1}{\sqrt{\left(\frac{P_1}{P_{1,\mathrm{EP}_3}} - 1\right)^2 + \left(\frac{P_2}{P_{2,\mathrm{EP}_3}} - 1\right)^2 + \left(\frac{P_3}{P_{3,\mathrm{EP}_3}} - 1\right)^2 + \left(\frac{\delta}{\delta_{\mathrm{EP}_3}} - 1\right)^2}} \\
y_r &= \frac{\frac{P_3}{P_{3,\mathrm{EP}_3}} - 1}{\sqrt{\left(\frac{P_1}{P_{1,\mathrm{EP}_3}} - 1\right)^2 + \left(\frac{P_2}{P_{2,\mathrm{EP}_3}} - 1\right)^2 + \left(\frac{P_3}{P_{3,\mathrm{EP}_3}} - 1\right)^2 + \left(\frac{\delta}{\delta_{\mathrm{EP}_3}} - 1\right)^2}} \\
z_r &= \frac{\frac{P_1}{P_{1,\mathrm{EP}_3}} - 1}{\sqrt{\left(\frac{P_1}{P_{1,\mathrm{EP}_3}} - 1\right)^2 + \left(\frac{P_2}{P_{2,\mathrm{EP}_3}} - 1\right)^2 + \left(\frac{P_3}{P_{3,\mathrm{EP}_3}} - 1\right)^2 + \left(\frac{\delta}{\delta_{\mathrm{EP}_3}} - 1\right)^2}} \\
w_r &= \frac{\frac{P_2}{P_{2,\mathrm{EP}_3}} - 1}{\sqrt{\left(\frac{P_1}{P_{1,\mathrm{EP}_3}} - 1\right)^2 + \left(\frac{P_2}{P_{2,\mathrm{EP}_3}} - 1\right)^2 + \left(\frac{P_3}{P_{3,\mathrm{EP}_3}} - 1\right)^2 + \left(\frac{\delta}{\delta_{\mathrm{EP}_3}} - 1\right)^2}}
\end{aligned} \tag{6.75}$$

With the 4D dimensionless coordinates in Equation 6.75, we can then stereographically project them onto $\mathbb{R}^3$, after we choose a suitable pole. The pole chosen for this projection is (in experimental coordinates)

$$\left(\delta_{\mathrm{pole}}/(2\pi), P_{1,\mathrm{pole}}, P_{2,\mathrm{pole}}, P_{3,\mathrm{pole}}\right) = \left(55\,\mathrm{kHz}, P_{1,\mathrm{min}}, 596\,\mu\mathrm{W}, P_{3,\mathrm{EP}_3}\right) \tag{6.76}$$

The mapping in Equation 6.75 maps this pole to $(0.1, 0, -0.83, 0.55)$. For comparison, a pole at $(\delta_{\mathrm{EP}_3}, P_{1,\mathrm{EP}_3}, P_{2,\mathrm{max}}, P_{3,\mathrm{EP}_3})$ would map to $(0, 0, 0, 1)$ in the dimensionless coordinates (6.75). We apply the rotation matrices described in Equation 6.73 (these rotate by $\theta_1 = 10.30^\circ, \theta_2 = 0^\circ, \theta_3 = -56.04^\circ$) to put the (x_r, y_r, z_r, w_r) coordinates into a rotated coordinate system (x_r', y_r', z_r', w_r'), and then we apply the stereographic projection:

$$X = \frac{x_r'}{1 - w_r'},\ Y = \frac{y_r'}{1 - w_r'},\ Z = \frac{z_r'}{1 - w_r'} \tag{6.77}$$

The analytically obtained EP$_2$ coordinates (Section 6.4), as given in Equation 6.77, are then plotted in the bottom row of Figure 6.22. The circles are the algorithmically found EP$_2$ points, via the four methods in Section 6.4.2, with each plot corresponding to one of the four methods. The curve is a theoretically estimated curve of the EP$_2$ points on the 3D hypersurface (as described in Section 3.6). The coloring is again done by θ (Equation 2.115).

In the stereographically projected plots of the bottom row of Figure 6.22, we see that the EP$_2$ points and the theoretically predicted curve form a trefoil knot (c.f. Section 6.5.1). Moreover, the stereographic projection (Equation 6.77) is a conformal map [102], so it locally preserves angles and the shape of the knot. More precisely, it generically preserves knot equivalence classes.[10] Thus, since the curve is a trefoil knot in the projected $\mathbb{R}^3$ space, it is a trefoil knot on

[10] "Generically," because if the projection point happens to lie on the knot, then the stereographic projection

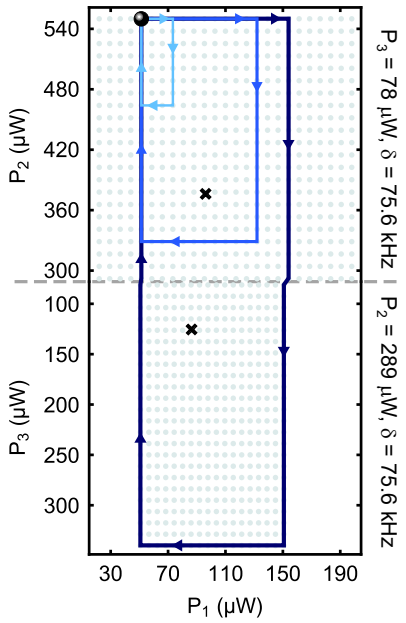

Figure 6.25: The datasets over which closed loops were realized in order to demonstrate eigenvalue braiding (Figure 6.26). The axes denote the swept parameters, and the legend to the right denotes the fixed parameters. Top (bottom) sheet: P_1 and P_2 (P_3) were the swept parameters in these sheets, while δ and P_3 (P_2) were the fixed parameters. The black circular dot denotes the common start and end point of these rectangular loops. Black crosses denote the measured EP_2 points. The cyan, light-blue and dark-blue loops correspond to the A, B, and C columns of Figure 6.26, respectivey.

the hypersurface.

6.6 Eigenvalue Braiding

In Section 6.5, we experimentally established that the EP_2 points on a 3-hypersurface that encloses EP_3 form a trefoil knot. This experiment also aims to execute loops in the complement of the EP_2 space in the 3-hypersurface and realize eigenvalue braiding. In this section, we experimentally demonstrate that the kind of braid (more precisely, the braid's isotopy equivalence class) that is realized depends on how the loop encloses the EP_2 curve. This shows that the complement of the EP_2 space on the 3-hypersurface has as its fundamental group the braid group B_3 (Section 2.5.4).

To experimentally realize eigenvalue braiding along closed loops in the parameter space, we execute closed loops in the vicinity of the EP_2 trefoil knot on our chosen experimental hypersurface (Equation 6.51), and plot their eigenvalues along the loop. An obvious way to do this would be to specify the four parameters $\big(\delta(t), P_1(t), P_2(t), P_3(t)\big)$ as a function of time $t \in [0, T]$, where $\delta(0) = \delta(T)$, $P_1(0) = P_1(T)$, etc. However, to demonstrate eigenvalue braiding, it suffices to use the data from the EP_2-finding spectroscopy (for example, Figure 6.14), and extract data

fails to preserve the knot. Yet the knot points lie on a set of measure zero in the 4D control space, so this poor choice of a projection point is very rare.

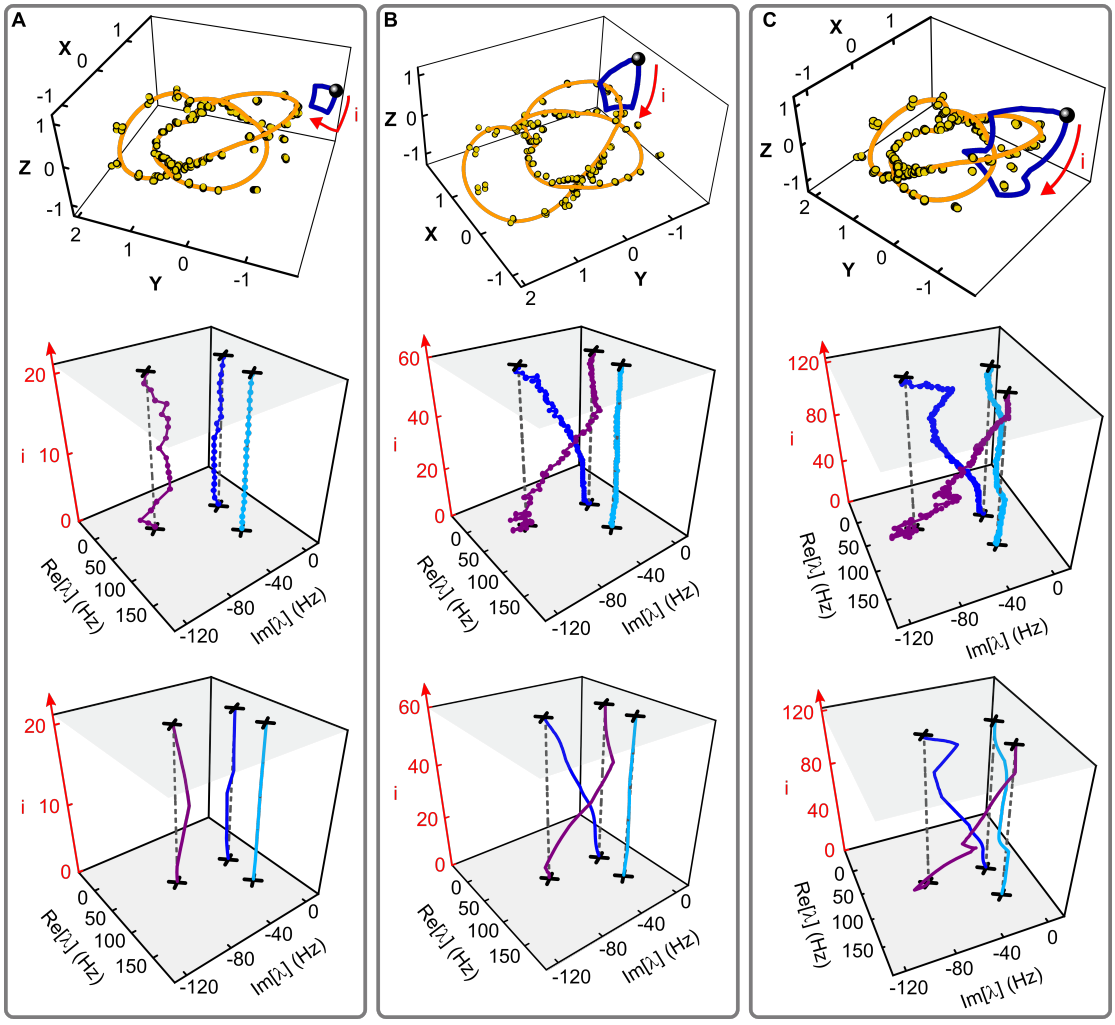

Figure 6.26: The eigenvalue trajectories of the loops in Figure 6.25. Columns A, B and C correspond to the cyan, light-blue and dark-blue loops of Figure 6.25, respectively. The top row is the rectangular loop (dark blue), with its start/end (black dot). The yellow points are the EP_2 points, as obtained in Section 6.4, and the yellow curve is the estimated EP_2 curve. Middle row is the extracted eigenvalue data along the loop. i traces out the loop from its beginning to end. Bottom row is theoretically estimated eigenvalues.

from these datasets in post-processing.

Figure 6.25 shows two 2D datasets, over which three rectangular loops are realized in post-processing. In these 2D datasets, each datapoint is addressed by a pair of indices (i, j), and the (i, j) indices are chosen to realize various rectangular loops.[11] With these points, we note the three complex eigenvalues λ_i as a function of n, where n is the nth (i, j) index in the chosen rectangular loop. Figure 6.25 shows these loops in experimental parameter space (δ, P_1, P_2, P_3).

Figure 6.26 shows the eigenvalue trajectories that these rectangular loops trace out, as well as the loops' positions in relation to the EP_2 trefoil knot. The second row shows the extracted eigenvalues along these loops, and the third row shows the theoretically estimated eigenvalues along these loops. The eigenvalue trajectories are interpolated among the eigenvalue data points

[11] Of course, there is nothing special about the choice that the loops be rectangular, but they are very simple to realize in 2D-indexed datasets.

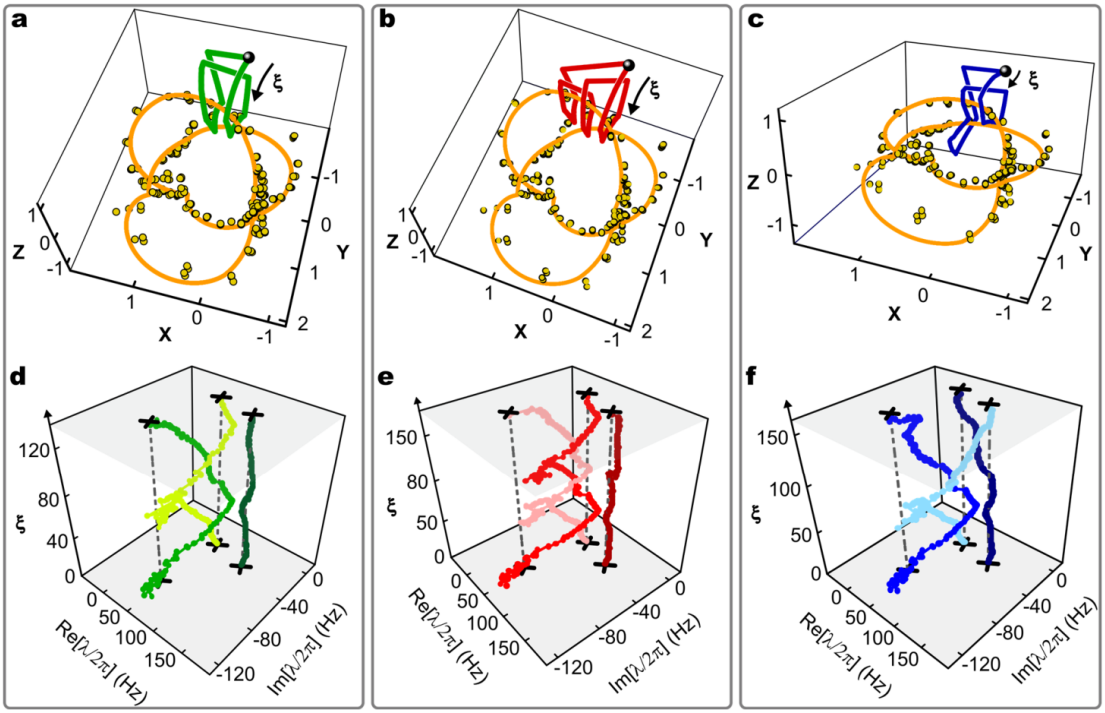

Figure 6.27: A collection of loops (a-c) and eigenvalue spectra trajectories (d-f). The three loops are each from a different loop homotopy class. The three loops realize the braids σ_1^2, σ_1^3, and $\sigma_1\sigma_2\sigma_1$, respectively.

by a coloring algorithm (detailed in Appendix G), which orders the eigenvalues at each index i such that the eigenvalue trajectories are continuous between index i and index $i+1$, for all i.

In Figure 6.26, we see that the three loops in Figure 6.25 realize three classes of eigenvalue trajectories: one in which no eigenvalues are exchanged, one in which two out of three eigenvalues are exchanged, and one in which all three eigenvalues are exchanged. The trajectory that the loop realizes depends on the way that the loop encloses the knot. For these particular loops, the loop that does not enclose the knot swaps zero eigenvalues (A); the loop that encloses one strand of the knot swaps two eigenvalues (B); and the loop that encloses two strands of the knot swaps three eigenvalues (C).[12]

More generally, the eigenvalue trajectories in Figure 6.26 are braids of N=3 strands, which evolves 3 distinct points in the complex plane. These three braids do not belong to the same isotopy class; they cannot be continuously deformed into one another while keeping their endpoints fixed and their strands from passing through one another during the deformation. As discussed in more detail in Section 2.5.4, the braid's isotopy class is determined by the homotopy class of the loop. These three braids can be regarded as generators of the braid group B_3 of the three eigenvalues of our system, as depicted in Figure 2.6. This experimentally demonstrates the discussion in Section 2.5.4, in which we say that the fundamental group of the nondegenerate

[12]The reader should not erroneously conclude from this statement about the specific loops in Figure 6.26 that *any* control loop which encloses zero strands swaps zero eigenvalues, etc. A counterexample may be found in Figure 6.28.

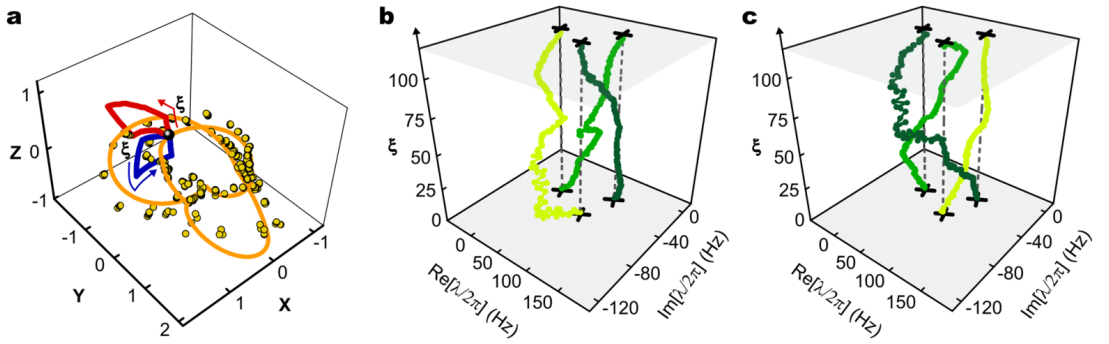

Figure 6.28: A demonstration of the noncommutativity of the eigenvalue braid group B_3 (b-c), via noncommutation of the control loops (a). Performing the red loop, then blue loop, produces (b); performing the blue loop, then red loop, produces (c).

parameter space is the braid group B_3. Figure 6.27 shows the use of the generators in Figure 6.26 to create more complicated control loops, and thus more complicated eigenvalue braids. This illustrates again that the loop homotopy class determines the braid isotopy class.

Figure 6.28 demonstrates the non-Abelian character of B_3. In Figure 6.28, two different loops, belonging to different homotopy classes (they encircle different parts of the EP_2 knot, so they cannot be continuously deformed into one another without intersecting through the knot), are shown. We concatenate the two loops, then look at the braids that are produced. Performing the red loop, then the blue loop, produces a braid in one braid isotopy class; performing the blue loop, then the red loop, produces a braid in a different braid isotopy class, since these two braids cannot be continuously deformed into one another without intersecting the braids or moving the start and end points of the eigenvalue trajectories. For these particular braids, (b) swaps two eigenvalues, and (c) swaps all three eigenvalues. Thus, the braid concatenation and loop concatenation operations are not commutative. This is expected, since the fundamental group of the control space, as well as B_3, are noncommutative.

Chapter 7

Future: Real-Time Control Loops

In this chapter, we describe preliminary measurements of the amplitude as well as the phase of excitations of the membrane during real-time control loops performed near the EP_2 trefoil knot. In [6], the energy transferred by driving one mode of a 2-mode system and executing a control loop was measured by examining only the amplitude of the modes' motion. That work also demonstrated nonreciprocity of the control loops: energy is either transferred or not depending on the direction of the loop. The nonreciprocal behavior depends critically on the relative gain and loss of the modes. The goal of this chapter is to discuss considerations in measuring the geometric (Berry) phase over control loops in a future experiment.

7.1 Non-Hermitian Berry Phase

7.1.1 The Adiabatic Theorem

The *adiabatic theorem* states that, given a system specified by a time-varying dynamical matrix $H(t)$, if the system state begins in an eigenstate $\psi_n(0)$ of $H(0)$, then if $H(t)$ is changed "slowly enough," the state remains in the eigenstate $\psi_n(t)$ of $\mathcal{H}(t)$ [72, p.368-369, Ch.10]. By a "slow enough variation," we mean that the time-scale T of the change satisfies

$$T \gg 2\pi\hbar/(E_b - E_a) \tag{7.1}$$

where $E_a(t)$ and $E_b(t)$ are any relevant energy eigenvalues of $\mathcal{H}(t)$ [5, p.355]. The key result is that the $\psi_n(t)$ can be identified with the $\psi_n(0)$ via their smooth evolution. The *adiabatic approximation* can be made when the adiabatic theorem holds.

The adiabatic theorem is only guaranteed to hold for a Hermitian dynamical matrix which varies slowly enough (Equation (7.1)), as is proven in Section 7.1.2. The theorem does not hold

in general for non-Hermitian dynamical matrices; however, the adiabatic theorem does hold for non-Hermitian systems in some cases, as discussed in Section 7.1.4.

Example: Simple Harmonic Oscillator

Some nice pedagogical classical examples of the adiabatic approximation are presented in [103].

For instance, if we consider a one-dimensional simple harmonic oscillator of mass m and frequency ω, [103, Sections III-IV], its total energy is given by $E = K + V$, where $K = m\dot{x}^2/2$ is the kinetic energy, $V = m\omega^2 x^2/2$ is the potential energy, and x is the position coordinate. If ω is constant, the solution to the harmonic oscillator equation of motion, $-\omega^2 x = \ddot{x}$, is

$$x(t) = Ae^{i\omega t} + Be^{-i\omega t} \tag{7.2}$$

Now, suppose that $\omega(t)$ is slowly varied, such that the change in ω in one cycle T, $\delta\omega$, satisfies $\delta\omega/\omega \ll 1$. We may try an adiabatic approximation of Equation (7.2),

$$x(t) = Ae^{i\omega(t)t} + Be^{-i\omega(t)t} \tag{7.3}$$

Then we take the time derivative of Equation (7.3):

$$\begin{aligned} \dot{x}(t) &= Ae^{i\omega(t)t}(i\omega(t) + i\dot{\omega}(t)t) + Be^{-i\omega(t)t}(-i\omega(t) - i\dot{\omega}(t)t) \\ &= \left(i\omega(t)Ae^{i\omega(t)t} - i\omega(t)Be^{-i\omega(t)t}\right)(1 + t\dot{\omega}(t)/\omega(t)) \end{aligned} \tag{7.4}$$

Over one period T, $T\dot{\omega}(t)/\omega(t) = \delta\omega/\omega \ll 1$, so

$$\begin{aligned} \dot{x}(t) &\approx i\omega(t)Ae^{i\omega(t)t} - i\omega(t)Be^{-i\omega(t)t} \\ \ddot{x}(t) &\approx -\omega(t)^2\left(Ae^{i\omega(t)t} + Be^{-i\omega(t)t}\right) \end{aligned} \tag{7.5}$$

Thus, the adiabatic approximation of Equation (7.3) satisfies $\ddot{x} = -\omega^2 x$.

We can also seek a quantity that remains constant when the simple harmonic oscillator is adiabatically varied [103][III-IV]. We consider a shift $\omega_0 \mapsto \omega_0 + \delta\omega$, for $\delta\omega/\omega \ll 1$. Then, with $E_0 = m\dot{x}^2/2 + m\omega^2 x^2/2$,

$$\begin{aligned} E_0 + \delta E &= m\dot{x}^2/2 + m\left(\omega + \delta\omega\right)^2 x^2/2 \\ &\approx m\dot{x}^2/2 + m\omega^2(1 + 2\delta\omega/\omega)x^2/2 \\ &= E_0 + m\omega^2 x^2 \delta\omega \end{aligned} \tag{7.6}$$

Thus, the variation δE is

$$\delta E = m\omega x^2 \delta\omega \tag{7.7}$$

We can take the time-average $f_\tau = \frac{1}{\tau}\int_0^\tau f(t)d\tau$ of the above, over one period $\tau = T$. ω is assumed to change very little over one period T, so $\omega_T = \omega$. This yields

$$\delta E = m\omega x_T^2 \delta\omega \tag{7.8}$$

By the relation in Equation (7.8), E also changes very little over T, so $E_T = E$. Then the time-averaged potential relates to the time-averaged position by

$$V_T = m\omega^2 x_T^2 \omega^2/2 \tag{7.9}$$

By the Virial theorem for a simple harmonic oscillator [3, pp.86], $V_T = K_T = E/2$, so

$$E = m\omega^2 x_T^2 \tag{7.10}$$

Plugging Equation (7.10) into (7.8), we get

$$\delta E/E = \delta\omega/\omega \tag{7.11}$$

Hence, E/ω is a constant when ω is adiabatically varied. Equivalently, since $T = 2\pi/\omega$, the product ET is constant over an adiabatic variation of $\omega(t)$.

The quantity ET being constant over an adiabatic variation is an example of the general adiabatic invariance for the classical action $S = \oint p dx$ from classical mechanics, as proven by Ehrenfest [103, Section II] [104]. For the oscillator, $S = \oint mv dx = \oint mv^2 dt = \oint 2K dt = 2K_T T = ET$ [103, Sections III-IV].

7.1.2 Proof of the Adiabatic Theorem for Hermitian Systems

The adiabatic theorem always holds for a hermitian Hamiltonian $\mathcal{H}(t)$ which varies slowly enough (as in Equation (7.1)). $\mathcal{H}(t)$ governs the evolution of a state vector $|\Psi(t)\rangle$ via the Schrödinger equation

$$i\hbar\frac{\partial}{\partial t}|\Psi(t)\rangle = \mathcal{H}(t)|\Psi(t)\rangle \tag{7.12}$$

The adiabatic theorem states that, if a state $|\Psi(t)\rangle$ of $\mathcal{H}(t)$ starts in the eigenstate $|\psi_n(t)\rangle$ at $t = 0$, and if $\mathcal{H}(t)$ is varied slowly enough, per Equation (7.1), then the state at time t is

approximately

$$\boxed{|\Psi(t)\rangle \approx e^{i\theta_n(t)} e^{i\xi_n(t)} |\psi_n(t)\rangle} \tag{7.13}$$

where the *dynamical phase* is

$$\boxed{\theta_n(t) = -\frac{1}{\hbar}\int_0^t E(t')\,dt'} \tag{7.14}$$

and the *geometric phase* is

$$\boxed{\xi_n(t) = i\int_0^t \left\langle \psi_n(t') \middle| \frac{\partial}{\partial t'} \psi_n(t') \right\rangle dt'} \tag{7.15}$$

For pedagogy, as well as to motivate Berry phase later [105], we show a proof here [72, p.371-373]. This proof assumes Hermiticity of $\mathcal{H}(t)$ and nondegeneracy of the eigenenergies $E_n(t)$.

Proof. An eigenstate $|\psi_n(t)\rangle$ of Equation (7.12) satisfies

$$\mathcal{H}(t)\,|\psi_n(t)\rangle = E_n(t)\,|\psi_n(t)\rangle\,, \tag{7.16}$$

and the eigenstates are orthonormal:

$$\langle \psi_m(t) | \psi_n(t) \rangle = \delta_{mn} \tag{7.17}$$

A formal solution of Equation (7.12), in terms of the eigenstates, is

$$|\Psi(t)\rangle = \sum_n c_n(t) e^{i\theta_n(t)} |\psi_n(t)\rangle \tag{7.18}$$

where the dependence of the phase factors of $c_n(t)$ on $E_n(t)$ has been absorbed into $\theta_n(t)$, as given in Equation (7.14). Note that $c_n(t)$, as given in Equation (7.18) would be constant if $\mathcal{H}(t)$ were time-independent.

When we plug Equation (7.18) into the time-dependent Schrödinger equation (7.12), the equation is

$$i\hbar \sum_n \left[\dot{c}_n(t)\,|\psi_n(t)\rangle + c_n(t) \left|\dot{\psi}_n(t)\right\rangle + i c_n(t)\dot{\theta}_n(t)\,|\psi_n(t)\rangle \right] e^{i\theta_n(t)} = \sum_n c_n(t) \big(\mathcal{H}(t)\,|\psi_n(t)\rangle\big) e^{i\theta_n(t)} \tag{7.19}$$

Since

$$\dot{\theta}_n(t) = -E_n(t)/\hbar, \tag{7.20}$$

we get

$$\sum_n \left[\dot{c}_n(t)\,|\psi_n(t)\rangle + c_n(t) \left|\dot{\psi}_n(t)\right\rangle \right] e^{i\theta_n(t)} = 0 \tag{7.21}$$

We use orthonormality of the $\psi_n(t)$ (which is guaranteed by the Hermiticity of $\mathcal{H}(t)$) to find that

$$\begin{aligned}\dot{c}_m(t)e^{i\theta_m(t)} &= -\sum_n c_n(t)\left\langle \psi_m \middle| \dot{\psi}_n(t)\right\rangle e^{i\theta_n(t)} \\ &= -c_m(t)\left\langle \psi_m \middle| \dot{\psi}_m(t)\right\rangle e^{i\theta_m(t)} - \sum_{n\neq m} c_n(t)\left\langle \psi_m \middle| \dot{\psi}_n(t)\right\rangle e^{i\theta_n(t)}\end{aligned} \tag{7.22}$$

Shortly, we will use the adiabatic approximation to drop the second term in the above.

We take the time-derivative of the Schrödinger equation (7.12), and find

$$\dot{\mathcal{H}}(t)\left|\psi_n(t)\right\rangle + \mathcal{H}(t)\left|\dot{\psi}_n(t)\right\rangle = \dot{E}_n(t)\left|\psi_n(t)\right\rangle + E_n(t)\left|\dot{\psi}_n(t)\right\rangle \tag{7.23}$$

Now take the inner product with $\langle\psi_m(t)|$, for $m \neq n$, and again use the Hermiticity of $\mathcal{H}(t)$:

$$\left\langle\psi_m(t)\right| \dot{\mathcal{H}}(t)\left|\psi_n(t)\right\rangle = \big(E_n(t) - E_m(t)\big)\left\langle \psi_m(t) \middle| \dot{\psi}_n(t)\right\rangle \tag{7.24}$$

Plug Equation (7.24) into Equation (7.22) (using nondegeneracy of $E_n(t)$):

$$\dot{c}_m(t) = -c_m(t)\left\langle \psi_m(t) \middle| \dot{\psi}_m(t)\right\rangle - \sum_{n\neq m} c_n(t)\frac{\left\langle\psi_m\right| \dot{\mathcal{H}} \left|\psi_n\right\rangle}{E_n - E_m} e^{i(\theta_n - \theta_m)} \tag{7.25}$$

The adiabatic approximation is now made by dropping the second term. This is done by assuming that, over one period $T = 2\pi/\omega_1$ of the Hamiltonian ground-state energy ω_1, that $\delta\mathcal{H}(t) = T \times \dot{\mathcal{H}}(t)$ is much smaller than $\mathcal{H}(t)$.[1] This is justified if we assume the "slowness condition" of Equation (7.1). Then the solution to the above is approximately

$$c_m(t) \approx c_m(0)e^{i\xi_m(t)} \tag{7.26}$$

where $\xi_m(t)$ is the geometric phase, given in Equation (7.15).

Finally, we have the state $|\Psi(t)\rangle$:

$$\left|\Psi(t)\right\rangle \approx \sum_n c_n(0)e^{i\xi_n(t)}e^{i\theta_n(t)}\left|\psi_n(t)\right\rangle \tag{7.27}$$

In particular, if the state begins in an eigenstate $|\psi_n(0)\rangle$ of $\mathcal{H}(0)$, with $c_n(0) = 1$ and $c_k(0) = 0$, for all $k \neq n$, then, via Equation (7.27), the time-evolved state is approximately given by Equation (7.13), so the state remains in the nth eigenstate of $\mathcal{H}(t)$, as claimed. ■

[1] An analysis that explicitly checks this assumption for an exactly-soluble two-mode system is given in [106].

7.1.3 Berry Phase

The geometric phase (7.15) is physically observable in both classical and quantum systems. For example, in a classical system, the geometric phase can be observed in parallel transport of a Foucault pendulum [72, p.376-377]. In quantum mechanics, in which the geometric phase had been thought to be inconsequential before Berry's work [105], the geometric phase is physically observable via interferometry. In particular, if the Hamiltonian $\mathcal{H}(t)$ depends on N parameters $\mathbf{R}(t) = \big(R_1(t), \ldots, R_N(t)\big)$:

$$\mathcal{H}(t) \doteq \mathcal{H}\big(R_1(t), \ldots, R_N(t)\big), \tag{7.28}$$

then the time-derivative of the eigenstates $|\psi_n(t)\rangle$ follows

$$\partial_t |\psi_n(t)\rangle = \partial_t \mathbf{R}(t) \cdot (\nabla_R |\psi_n(R_1(t), \ldots, R_N(t))\rangle) \tag{7.29}$$

The geometric phase then becomes [107]

$$\xi_n(t) = i \int_{\mathbf{R}(0)}^{\mathbf{R}(t)} \langle \psi_n(\mathbf{R}) | \nabla_R \psi_n(\mathbf{R}) \rangle \cdot d\mathbf{R} \tag{7.30}$$

Berry's phase results when $\mathbf{R}(0) = \mathbf{R}(T)$, at the end of the loop duration T (i.e., $\mathbf{R}$ forms a closed control loop ∂S around a surface S):

$$\boxed{\xi_n = i \oint_{\partial S} \langle \psi_n(\mathbf{R}) | \nabla_R \psi_n(\mathbf{R}) \rangle \cdot d\mathbf{R}} \tag{7.31}$$

So long as the path taken by $\mathbf{R}(t)$ satisfies the adiabatic assumption, then Berry's phase does not depend on the dynamics, but only on the path taken by $\mathbf{R}(t)$ in the control space; the dynamic phase (Equation (7.14)) captures the dynamical dependence. The quantity

$$\mathbf{A}_n(\mathbf{R}) = i \langle \psi_n(\mathbf{R}) | \nabla_R \psi_n(\mathbf{R}) \rangle \tag{7.32}$$

is the *Berry connection*, or *Berry potential* [34] [107] [72, p.381]. By using the generalized Stokes' theorem [105],

$$\oint_{\partial S} \mathbf{A}_n(\mathbf{R}) \cdot d\mathbf{R} = \int_S [\nabla_{\mathbf{R}} \times \mathbf{A}_n(\mathbf{R})] \cdot d\mathbf{a} \tag{7.33}$$

we find the *Berry curvature* $\nabla_{\mathbf{R}} \times \mathbf{A}_n(\mathbf{R})$.

7.1.4 Considerations for Non-Hermiticity

For a Hermitian $\mathcal{H}(t)$ and a variation of $\mathcal{H}(t)$ which is sufficiently slow (i.e., it satisfies Equation (7.1)), the adiabatic theorem always holds. In contrast, for a non-Hermitian $\mathcal{H}(t)$, the adiabatic

theorem need not hold at all: if the system possesses a "dominant" mode, which has the highest gain relative to the other modes, then the adiabatic theorem can only hold for this mode [108] [33, Appendix A]. If a different mode becomes dominant (as can happen when the control loop encloses an exceptional point; c.f., Chapter 2), then energy can transfer to that new dominant mode [109] [110] [33, Appendix A].

With non-Hermitian systems, one considers different limits of the loop duration. A *quasiadiabatic* control loop is slow, but not asymptotically slow [34]. Theoretical [111] as well as experimental works show that quasiadiabatic control loops that enclose an exceptional point can place energy in a different mode than it began in. Experimental platforms that have demonstrated this include a microwave cavity [112], a waveguide [7], and the membrane-in-the-middle experiment [6].

Another loop-duration regime is the adiabatic limit, in which the loop duration is asymptotically slow. Theory work [34] shows that, for a non-Hermitian system with an exceptional point space, certain asymptotically slow control loops ($T \to \infty$) *entirely within* the EP subspace, and a particular initial state vector, the state returns to itself, and picks up a phase factor θ, which satisfies the Puisseux series [34]

$$\theta = \sum_{r=1}^{n} T^{1-r/n} \int_0^1 ds\, f_r(H(s)) \tag{7.34}$$

where $f_r(z)$ are complex functions. The $r = n$ term (i.e., the order T^0 term) is the Berry phase. The particular initial state vector for which this result holds is the dominant mode of $\mathcal{H}(t = 0)$ (or, rather, the dominant mode of $\mathcal{H}(t = 0)' = J_n + T^{-1}A(t = 0)$, where $A(s)$ is the Berry connection). The control loop must be chosen so that this initial state vector remains the dominant mode across the entire loop.

If the system is initialized in the dominant mode, and a control loop is executed such that it encloses an EP, but another mode becomes dominant, then a *diabatic* (or "sudden") transition can occur [108] [33, Appendix A]. One might ask whether it is generically possible to create a time-dependent Hamiltonian $\mathcal{H}(t)$ that can take energy from one initialized state, and transfer it to another. Counter-diabatic driving [113], which assumes that the effective Hamiltonian is

$$\mathcal{H}_{\text{eff}} = \mathcal{H}_0 - \dot{\lambda} A_\lambda \tag{7.35}$$

adds a counter-driving term

$$\mathcal{H}_{\text{CD}} = \dot{\lambda} A_\lambda \tag{7.36}$$

so that the system evolves via a desired $\mathcal{H}_0$. A closely related framework is transitionless quantum

driving [114], which suggests that, given a Hamiltonian $\mathcal{H}_0$, there is a nearby Hamiltonian $\mathcal{H}'$ for which the transition amplitudes are exactly zero, in the adiabatic limit. The review paper [115] expands on counter-diabatic driving: given a Hamiltonian $\mathcal{H}_0(t)$, with approximate eigenstates $\left|\psi_n^{(0)}(t)\right\rangle$ in the adiabatic limit, a Hamiltonian $H(t)$ is found that sets the approximate eigenstates $\left|\psi_n^{(0)}(t)\right\rangle$ of $\mathcal{H}_0(t)$ to be the *exact* eigenstates of $\mathcal{H}(t)$. This is achieved with the unitary operator

$$U(t) = \sum_n e^{i\xi_n(t)} e^{i\theta_n(t)} \left|\psi_n(t)\right\rangle \left\langle\psi_n(0)\right| \tag{7.37}$$

The time-evolution Hamiltonian $\mathcal{H}(t) = i\hbar\dot{U}(t)U^\dagger(t)$, which has the exact eigenstates $|\psi_n(t)\rangle$ is

$$\mathcal{H}(t) = \mathcal{H}_0(t) + \mathcal{H}_{\mathrm{CD}}(t) \tag{7.38}$$

where

$$\mathcal{H}_0(t) = \sum_n E_n(t) \left|\psi_n(t)\right\rangle \left\langle\psi_n(t)\right| \tag{7.39a}$$

$$\mathcal{H}_{\mathrm{CD}}(t) = i\hbar \sum_n \Big[\left|\partial_t\psi_n(t)\right\rangle \left\langle\psi_n(t)\right| - \left\langle\psi_n(t)|\partial_t\psi_n(t)\right\rangle \left|\psi_n(t)\right\rangle \left\langle\psi_n(t)\right| \Big] \tag{7.39b}$$

By using Equation (7.24), we can cast $\mathcal{H}_{\mathrm{CD}}(t)$ as the easier-to-compute

$$\mathcal{H}_{\mathrm{CD}}(t) = i\hbar \sum_n \sum_{m\neq n} \frac{\left|\psi_m(t)\right\rangle \left\langle\psi_m(t)\right| \partial_t\mathcal{H}_0(t) \left|\psi_n(t)\right\rangle \left\langle\psi_n(t)\right|}{E_n(t) - E_m(t)} \tag{7.40}$$

Transitionless quantum driving and counter-diabatic driving fall under the umbrella of "shortcuts to adiabaticity," and are further discussed in [115]. Another perturbative method based on the Magnus expansion is used to describe the evolution of systems that enclose an exceptional point; this method enables non-reciprocal, topological energy transfer which is faster than an adiabatic process [116].

7.2 Ringdown Train Electronics

In this section, we explore techniques to measure the geometric phase accumulated by a state after a given dynamical loop. We wish to perform dynamical loops with essentially the same experimental setup which obtains exceptional points (e.g., the setup described in Chapters 4 and 5, which obtains exceptional points in Chapter 6). We describe the electronics which apply the dynamical loops in Section 7.2.1, and we describe the waveforms which encode the dynamical loops into the control tones in Section 7.2.2.

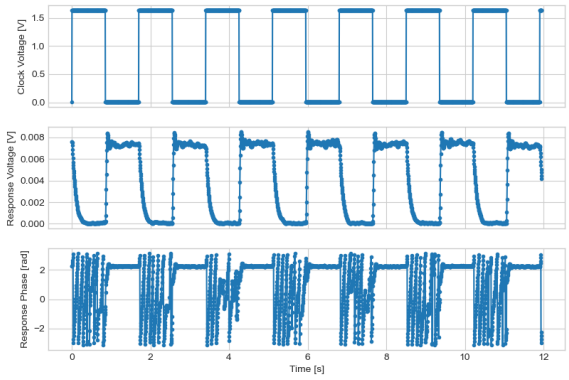

Figure 7.1: A ringdown train. The clock voltage is in the top row, the response voltage is in the middle, and the response phase is in the bottom row.

Figure 7.2: The HP8642B signal generator used to generate control tones in the 2016 experiment (used to generate the AM modulation in the probe in this experiment). AM and FM inputs are on the left-hand side, and the output is on the right-hand side.

7.2.1 Modifications for Dynamics

In Chapter 5, we detailed the optical table (Section 5.1.1) and the electronic setup (Section 5.3) used in the main experiment. In this section, we describe the modifications made to the electronic setup in order to enable dynamical loops. No changes were needed in the optical table.

We apply a ringdown train (Figure 7.1; c.f., Section 4.1.3) to the experiment by triggering the drive with a square clock voltage. The gate voltage is sent to a voltage switch, with two inputs V_1 and V_2. V_1 is set to the HF2 drive (as in Section 5.3.1), and V_2 is 50 Ω-terminated. When the clock is low, the drive at a frequency ω_{AM} is applied; when the clock is high, the gate cuts off the drive, and allows the membrane motion to relax in a ringdown. For this experiment, the clock will trigger a dynamical pulse in the function generators which supply the control tones. This will create a dynamical loop in parameter space. We record both amplitude and phase information for the response.

In the 2016 MIM experiment with dynamical loops [6] [33, Section 4.3], there was one control tone, supplied by an HP8642B function generator (shown in Figure 7.2), which has two separate AM and FM ports. The AM port modulates the control tone power, and the FM port modulates

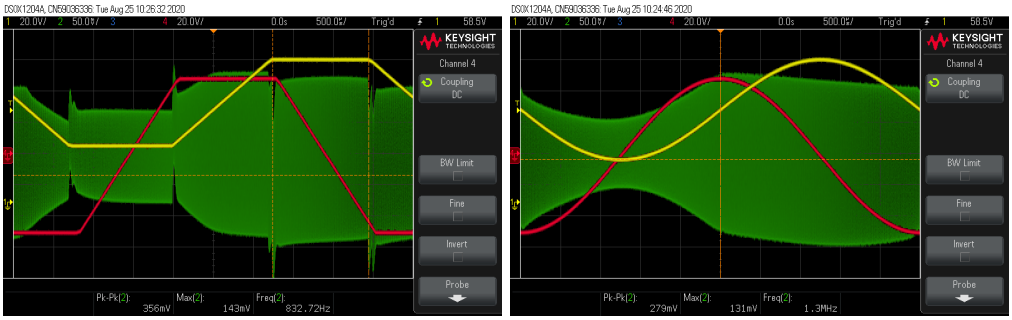

(a) (b)

Figure 7.3: The result of applying two trapezoids (a) and two sines (b) for AM and FM modulation, via an external modulation input port and a variable RF attenuator, respectively. The output waveform (green), is frequency-modulated from 200 kHz to 1.2 MHz. The amplitude is a complicated function of the attenuator transfer function. The red waveform creates FM modulation, and the yellow waveform creates AM modulation.

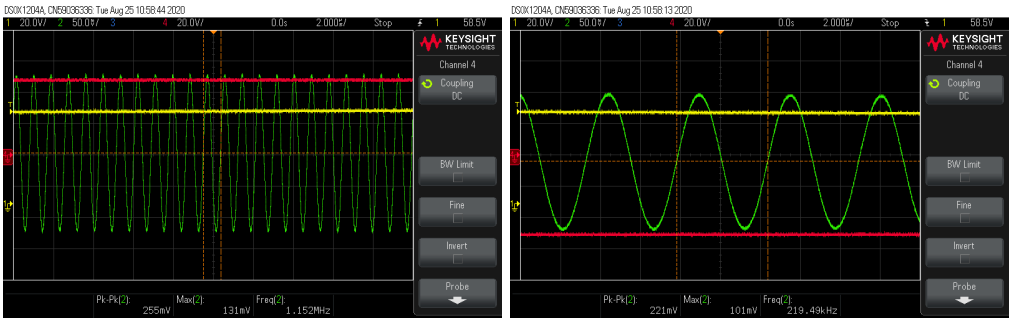

(a) (b)

Figure 7.4: The result (green) of applying a low voltage and a high voltage to the FM port (both red). The low voltage (a) sets the frequency to 200 kHz, and the high voltage (b) sets the frequency to 1.2 MHz. The yellow voltage is an AM input to the RF attenuator, and is held constant for these traces.

the control tone frequency.

In the experiment in this thesis, we use three RigolDG4162 function generators to produce three separate control tones. To perform dynamical loops, we could replace them with three HP8642B function generators, and then use a Rigol function generator with two outputs to send both an AM and an FM pulse. However, the HP8642B function generator is obsolete.[2] Thus, we instead work with the function generators that we have, and use other electronics techniques to get a similar effect.

The three function generators which supply the three control tones (Section 5.3.2) each have one external modulation input port, which accept input voltages from -5 V to 5 V. This port can be used for AM or FM. However, to fully emulate the experiment in [6], we would need to simultaneously amplitude- and frequency-modulate the control tones.

An approach that we tried out in order to achieve simultaneous AM and FM modulation

[2] A new model from Keysight that has two modulation external ports, the Keysight E8663D function generator, goes for 42,500 USD on eBay, refurbished.

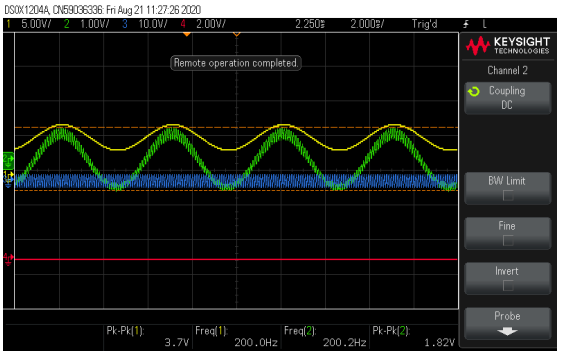

Figure 7.5: The output of the variable RF attenuator (green), with a 200 Hz AM input (yellow), and a 10 kHz RF tone (blue), when no DC block is applied to the output.

was to use a variable RF attenuator and a DC block (to remove a low-frequency component from the modulation input) to attenuate the output voltage, and the external modulation input to frequency-modulate. The variable RF attenuator and the FM port of a function generator each receive an input from a function generator. Figure 7.3 shows the results of applying input waveforms to the FM port and the variable RF attenuator.

Figure 7.3 shows that the amplitude of the output wave, when AM modulated with the variable RF attenuator plus DC block, is a complicated function of the attenuator transfer function. Additionally, Figure 7.3a shows burrs when the trapezoid switches from a flat voltage to a ramping/falling voltage. The burrs do not appear in Figure 7.3b, but the output amplitude still behaves surprisingly. More work would be needed to calibrate the shape of the output using this method. The DC block is used to counter the addition of a frequency component by the AM input, as shown in Figure 7.5; without the DC block, the output is a wave with an attenuated amplitude, but the frequency components of both the RF tone and the AM input are present.

The output with only FM is shown in Figure 7.4. As expected, for a linear increase in voltage, the frequency linearly increases from the low frequency to the high frequency, via the FM port. A similar result is obtained by using the modulation port for AM instead of FM.

The techniques of this section can be used to simultaneously modulate the powers of any two of the three tones in this experiment, using AM modulation on the inputs of two of the function generators. This is sufficient to vary two out of the four parameters (δ, P_1, P_2, P_3). An applied pulse could be one of the built-in functions, or an AWG or a burst pulse (produced as described in Section 7.2.2). Simultaneous FM modulation of the three tones is possible as well, but this does not produce control loops in this experiment, since the detuning δ is the only frequency parameter of the four experimental knobs (δ, P_1, P_2, P_3). Thus, with this implementation, in this experiment, there are only 3 feasible choices of two parameters to vary in a dynamical loop. For the potential future experiment (Section 8.2), which would use two control laser tones 1 and 2, with parameters $(\delta_1, P_1, \delta_2, P_2)$, then either both of δ_1, δ_2 are varied, or P_1, P_2 are varied; this is

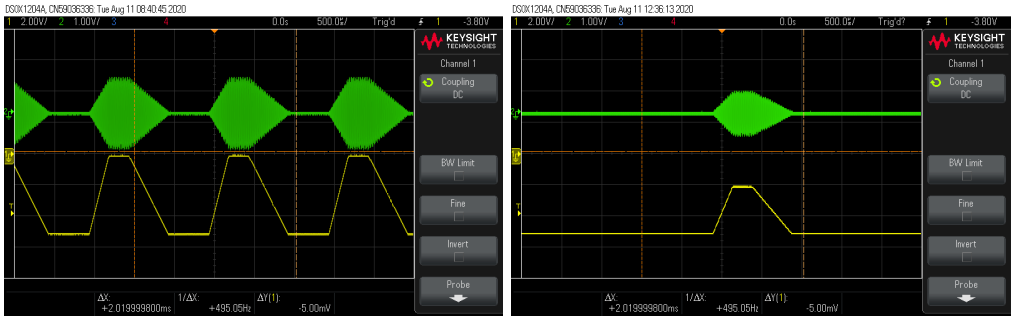

(a) (b)

Figure 7.6: Arbitrary waveforms generated on a function generator. Green is an AM modulated waveform, and yellow is the modulation input. a: a train of arbitrary waveforms. b: a pulsed waveform. In both of these, the rise time is 250 µs, the fall time is 500 µs, the high time is 500 µs, and the low time is 250 µs.

only 2 out of 6 possible choices of two parameters. To vary another combination of parameters, further work is needed to faithfully modulate both AM and FM with Rigol function generators alone.

7.2.2 AWG and Burst

In principle, to vary the powers and detunings of the control tones, it is enough to have AM and FM modulation. However, limiting our modulation tones to the built-in functions poses two limitations to the dynamical loop experiment. The first is that, in the dynamical phase experiment, we may desire more intricate dynamical loop geometries than the built-in functions provide. The second is that, in order to have a desired output control loop waveform, we may need to calibrate the modulation input so that the desired output is achieved (e.g., the nonlinear variable RF attenuator output, shown in Figure 7.3). Thus, we require arbitrary waveform generation (AWG) for our modulation tones.

In this section, we discuss how to write an arbitrary waveform with a Rigol function generator. This is achieved with the two programmer interface commands `VOLATILE` and `ARB`. `VOLATILE` sends a `float` array, with values from `-1.0` to `+1.0`, to the volatile memory of the function generator, and `ARB` specifies the sampling rate, amplitude, and offset of the waveform. An example in Python is given[3]:

```
inst = load_function_generator_with_pyvisa()
wave_arr = make_waveform_array()

# write the array of floats to the volatile memory
```

[3]The slicing syntax, `arr[i:-j]`, gets the entries in `arr` from `i` inclusive to `j` exclusive. We use the slice `str(list(wave_arr))[1:-1]` in this code because `str(list(wave_arr))` returns `[a_0,a_1,...,a_n]`, and we must remove the brackets from the `str`-representation, to get `a_0,a_1,...,a_n`, before sending it to the function generator programmer interface.

```
inst.write(f'SOUR{channel}:DATA VOLATILE, ' + str(list(wave_arr))[1:-1])
# write the sampling rate, amplitude, and offset of the volatile-memory waveform
inst.write(f'SOUR{channel}:APPL:ARB {sampling_rate},{amplitude},{offset}')
```

Listing 7.1: AWG Example

It is very important to note that the sampling rate is *not* the frequency of the waveform. Instead, if the period of the waveform is T, and the length of the array is L, then the *sampling time* is $s_t = T/L$, and the *sampling rate* is

$$s_r = 1/s_t = L/T \tag{7.41}$$

The amplitude and the offset have the usual units of volts. For the Rigol DG1022z function generator used in this test, the voltages range from $-5\,\mathrm{V}$ to $5\,\mathrm{V}$.

For example, to make a trapezoidal waveform with an arbitrary rising time `t_rise`, falling time `t_fall`, high time `t_high`, and low time `t_low`, as well as a desired time offset `t_offset`, number of array points[4] `num_points`, low voltage `low`, and high voltage `high`, one can write a method to make a `float` array, `trap_arr`, which specifies the trapezoid as a series of `float` values from `-1.0` to `+1.0`, send `trap_arr` to the `VOLATILE` command, and then send the amplitude, offset, and sampling rate via the `ARB` command:

```
import numpy as np
inst = load_function_generator_with_pyvisa()

def make_trapezoid(t,low,high,t_rise,t_fall,t_low,t_high):
  t1 = t_rise
  t2 = t1 + t_high
  t3 = t2 + t_fall
  t4 = t3 + t_low
  t = (t-t_offset) % t4
  if 0 <= t < t1:
    return +2.0/t1*t-1
  elif t1 <= t < t2:
    return +1.0
  elif t2 <= t < t3:
    return -2.0/(t3-t2)*(t-t2)+1
  elif t3 <= t <= t4:
    return -1.0
make_trapezoid_vec = np.vectorize(make_trapezoid) # this lets make_trapezoid iterate over the list of times ts
```

[4]The maximum number of points on the Rigol DG1022z is 4096.

Figure 7.7: Two burst-mode ellipsoids applied via a function generator, which is calibrated to create a sine wave in the control tone power. The clock is in purple, and the two function generator outputs are blue and yellow.

```
ts = np.linspace(0, period, num_points)
trap_arr = make_trapezoid_vec(ts,low,high,t_rise,t_fall,t_low,t_high)

amplitude = high-low
offset = (high+low)/2
period = float(t_rise+t_fall+t_low+t_high)
sampling_rate = num_points / period

inst.write(f'SOUR{channel}:DATA VOLATILE, ' + str(list(trap_arr))[1:-1])
inst.write(f'SOUR{channel}:APPL:ARB {sampling_rate},{amplitude},{offset}')
```

Listing 7.2: AWG Trapezoid Example

An example output of this code is shown in Figure 7.6a. One could use essentially the same code as above, replacing the `make_trapezoid` method with a more complicated waveform function.

The code in Listing 7.2 does not take into account the calibration setting of the nominal function generator voltage and the realized control tone power; this relationship is quadratic (Section 5.3.3). This calibration should be taken into account if one wishes to faithfully represent the desired waveform in the space of control tone powers. An example of an ellipsoid waveform, which takes the calibration into account to produce a sine wave in control power, is shown in Figure 7.7.

A useful feature for applying dynamical loops is to apply loops as pulses at preprogrammed times. This is easily accomplished with a gate voltage signal, such as a square wave (as mentioned in Section 7.2.1). The high voltage of the clock, which shuts off the mechanical drive, can also be used as an external trigger on the function generator. The external trigger input directs the function generator to output a single burst waveform (e.g., Figure 7.6b, Figure 7.7). Thus, we can use the clock to trigger two burst modulation waveforms from one function generator with two outputs (to keep the waveforms synced to one another), and realize dynamical loops with this, and have these two modulation waveforms create AM and FM modulation on the control tone function generators.

7.3 Complex Ringdown Trains

7.3.1 Complex Ringdown Response

In this section, we describe the response of the membrane to a ringdown measurement. Recall that the equation of motion for a driven harmonic oscillator of mass m, frequency ω_m, and damping γ_m, is (from Equation (3.3))

$$\ddot{x} + \omega_m^2 x + \gamma_m \dot{x} = F(t)/m \tag{7.42}$$

If the force $F(t)/m$ is a drive at a frequency ω_d, where $\omega_d \approx \omega_m$, then $F(t) = mf_0 e^{i\omega_d t}$, and the response is (c.f., Section 3.2):

$$\begin{aligned} x_{\text{driven}}(t) &\approx \frac{f_0}{\sqrt{4\omega_m^2(\omega_d - \omega_m)^2 + \gamma^2\omega_m^2}}\, e^{i\omega_d t + i\theta} \\ \theta &= \arctan\left(\frac{\gamma/2}{\omega_m - \omega_d}\right) \\ &\approx \frac{\pi}{2} \cdot \text{sgn}(\omega_m - \omega_d) - \frac{\omega_m - \omega_d}{\gamma/2} \end{aligned} \tag{7.43}$$

Thus, the motion oscillates at ω_d as well, and the amplitude peaks exactly at $\omega_d = \omega_m$. When the motion $x_{\text{driven}}(t)$ is read by a lock-in amplifier at frequency ω_{read} (see Section 5.3.1), $x_{\text{driven}}(t)$ is demodulated by the sinusoid $e^{-i\omega_{\text{read}}t}$, so the voltage $V_{\text{driven}}[\omega_{\text{read}}](t)$ is proportional to:

$$\begin{aligned} V_{\text{driven}}[\omega_{\text{read}}](t) &\propto x_{\text{driven}}(t) e^{-i\omega_{\text{read}}t} \\ &= \frac{f_0}{\sqrt{4\omega_m^2(\omega_d - \omega_m)^2 + \gamma^2\omega_m^2}} e^{i(\omega_d - \omega_{\text{read}})t + i\theta} \end{aligned} \tag{7.44}$$

When the drive is turned off at time $t = 0$, then the equation of motion becomes the undamped equation

$$\ddot{x} + \omega_m^2 x + \gamma_m \dot{x} = 0 \tag{7.45}$$

The solutions to this equation have the form

$$x_{\text{decay}}(t) = A[\omega_d] e^{i\omega_m t - \gamma t/2} + B[\omega_d] e^{-i\omega_m t - \gamma t/2} \tag{7.46}$$

where $A[\omega_d]$ and $B[\omega_d]$ are specified by the time conditions $x_{\text{decay}}(0) = x_{\text{driven}}(0)$ and $\dot{x}_{\text{decay}}(0) = \dot{x}_{\text{driven}}(0)$. For $\omega_d \approx \omega_m$, then

$$\begin{aligned} A[\omega_d] &\approx \frac{f_0}{\sqrt{4\omega_m^2(\omega_d - \omega_m)^2 + \gamma^2\omega_m^2}}\, e^{i\theta} \\ B[\omega_d] &\approx A[\omega_d](\omega_d - \omega_m)/2\omega_m \end{aligned} \tag{7.47}$$

Note that the undamped oscillator solution, Equation (7.46), with $|A[\omega_d]| \gg |B[\omega_d]|$ since $\omega_d \approx \omega_m$, oscillates at frequency ω_m, even though ω_d is not necessarily exactly equal to ω_m; the difference determines the amplitude of A and B in Equations (7.47).

We can read the motion of $x_{\text{decay}}(t)$ (Equation (7.46)) at a frequency ω_{read} by demodulating $x_{\text{decay}}(t)$ by the sinusoid $e^{-i\omega_{\text{read}}t}$ (as is done by the lock-in amplifier; see Section 5.3.1). This renders the measured voltage $V[\omega_{\text{read}}](t)$ as

$$\begin{aligned} V[\omega_{\text{read}}](t) &\propto x_{\text{decay}}(t)e^{-i\omega_{\text{read}}t} \\ &= A[\omega_d]e^{i(\omega_m-\omega_{\text{read}})t-\gamma t/2} \end{aligned} \tag{7.48}$$

Thus, when the drive is turned off, the amplitude of $V[\omega_{\text{read}}](t)$ is exponentially decaying, with rate $\gamma/2$, and the phase is changing at the rate $\omega_m - \omega_{\text{read}}$. This rate is dependent not on the drive frequency ω_d, but on the mode frequency ω_m and on the reading frequency ω_{read}; if the rate is zero, then $\omega_{\text{read}} = \omega_m$ exactly. Thus, driving the membrane near ω_m, sweeping ω_{read} in the vicinity of ω_m, and measuring the phase response of the ringdown measurements is one way to measure the mode frequency ω_m.

Figure 7.8 shows a series of ringdowns of a mechanical mode. The norm of the signal rises to a high value when the drive is turned on, and decays exponentially with rate $\gamma/2$ when the drive is cut off.[5] The phase changes linearly when the drive is cut off, with rate $\omega_m - \omega_{\text{read}}$. On the other hand, when the drive is still being applied, the phase rate of change is $\omega_d - \omega_{\text{read}}$ (as in Equation (7.44)); in the measurement in Figure 7.8, $\omega_{\text{read}} = \omega_d$, so the phase is constant on the ringups (though, as in the next paragraph, this need not be true).

In this section, we distinguish between ω_d and ω_{read} because, in dynamical loops, we wish to initialize one mode ω_1 by driving at $\omega_d \approx \omega_1$, and use dynamical loops to transfer the energy to ω_2. Thus, we read at frequency $\omega_{\text{read}} \approx \omega_2$. This is done after control tones have already been applied to bring the system modes to the desired initial values.

7.3.2 Complex-Averaged Ringdowns

A standard method of improving the signal-to-noise ratio is to take the average over many datasets (for these ringdowns, 100 datasets or more). For a ringdown measurement in which we are only interested in the decay rate γ, we can take the norms of the complex signals $V_k(t)$,

[5] The amplitude actually decays as $\sqrt{a^2e^{-\gamma t}+b^2}$ [64]. For a small background b, and at early times t, the amplitude decays approximately as $ae^{-\gamma t/2}+b$.

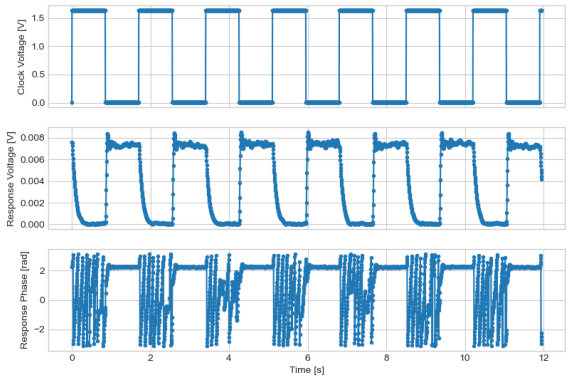

(a)

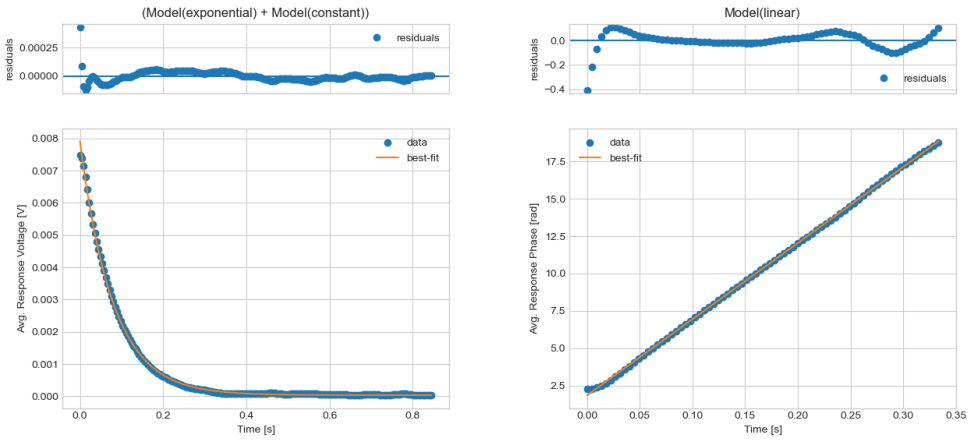

(b) (c)

Figure 7.8: A series of ringdown measurements of the $\omega_d/2\pi = 705\,\text{kHz}$ mode. The ringdowns are shown in (a), and they are averaged in (b) and (c). The top row of (a) shows the clock, the middle row shows the norm, and the bottom row shows the phase. (b) shows a fit of the average norm to an exponential decay, and (c) shows a linear fit of the average phase.

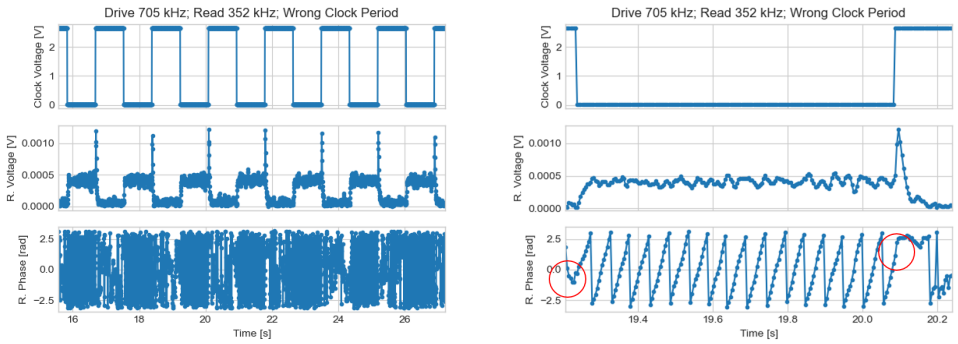

(a)

(b)

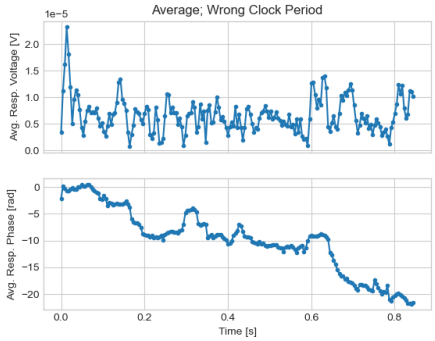

(c)

Figure 7.9: A ringdown train measurement of 100 ringdowns, in which the drive is at $\omega_d/2\pi = 705\,\text{kHz}$, and read-out frequency is $\omega_{\text{read}}/2\pi = 352\,\text{kHz}$. a: seven of the ringdowns are shown. The ringup period is $T = 1.7\,\text{s}$. Top row is the clock, middle row is the response amplitude, and bottom row is the response phase. b: one individual driving interval. Note that the response phase is shifted by the drive. c: the complex average (Equation (7.50)).

$k = 1, 2, \ldots, n$, and then take an average

$$a(t) = \frac{1}{n}\sum_{k=1}^{n} |V_k(t)| \tag{7.49}$$

This can be done with ringdown measurements done in Section 4.1.3.

In the 2016 nearly-degenerate-mode paper [6], the averaging in Equation (7.49) was used to determine that an eigenmode had been populated by a dynamical loop, after a different mode had been initialized. In the future MIM dynamics experiments, we also wish to investigate geometric phase. Thus, Equation (7.49) is insufficient. We instead use an average

$$c(t) = \frac{1}{n}\sum_{k=1}^{n} V_k(t) \tag{7.50}$$

However, if we naively apply Equation (7.50), then we can get an incorrect average. For instance, in Figure 7.9, we take a ringdown train of 100 ringdowns (seven are shown in 7.9a), and directly take the complex average of these ringdowns. Even when we are careful to separate the individual

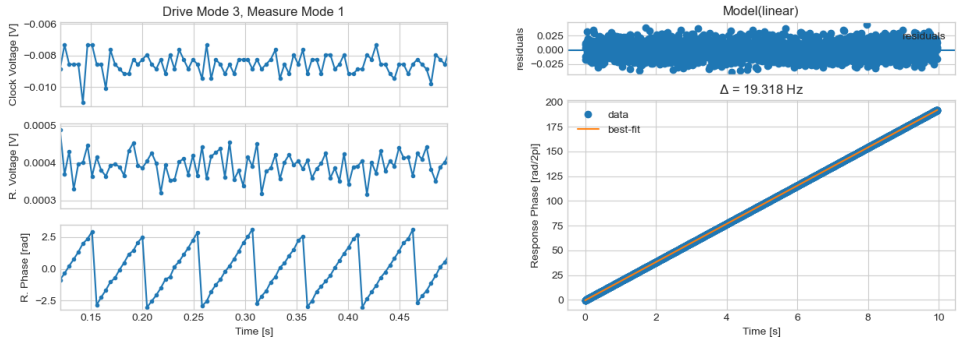

(a) (b)

Figure 7.10: Driven motion of mechanical mode 3 ($\omega_d/2\pi = 705\,\text{kHz}$), while reading mode 1 ($\omega_{\text{read}}/2\pi = 352\,\text{kHz}$), with control tones applied, so that motion at mode 3 drives mode 1 (as in Sections 3.6 and 5.3.2). a: the clock is high in the top row, the amplitude of the response is in the middle row, and the phase is shown in the bottom row. b: a linear fit of $\theta/(2\pi) = \Delta f \times t$. $\Delta f = 19.318\,\text{Hz}$ is extracted.

ringdown measurements such that they start at the same peak amplitude, the complex traces destructively interfere: despite that the individual ringdowns have initial amplitudes of 1 mV, their complex average has an initial amplitude of 0.01 mV (Figure 7.9c). This is caused by destructive interference from the individual traces: each trace starts at a phase value, because the ringup portion of the ringdown train adds a different phase offset θ_k, $k = 1, \ldots, n$, to each individual ringdown. This is shown in Figure 7.9b, where the red circles indicate that the ringup has shifted the phase. When the traces are averaged in the complex plane, the different θ_k phase-offset values cause destructive interference; this prevents us from smoothing out noise in the norm and phase. Hence, we must be careful how we handle the phase introduced by the ringup portions of the ringdown train when we take a complex average over n ringdowns.

An approach to handle the phase-offsets θ_k introduced by the ringup portions of the ringdown train is to ensure that θ_k is *the same* for each ringdown $k = 1, \ldots, n$. This can be done with a calibration of the ringup time T, by looking at the phase roll in the driven measurement (e.g., Figure 7.10). For a given driving frequency ω_d and lock-in readout frequency ω_{read}, the rate of change of the phase of the driven response is

$$\Delta f = (\omega_{\text{read}} - \omega_d)/2\pi. \tag{7.51}$$

Recall that $\Delta f = 19.318\,\text{Hz}$ in Figure 7.10 makes sense, despite that $\omega_d/2\pi = 705\,\text{kHz}$ and $\omega_{\text{read}}/2\pi = 352.3\,\text{kHz}$, since in the time-independent Floquet frame which the control tones introduce, the Floquet modes are split by an order of 100 Hz (Section 3.6). We can relate Δf to the phase change $\Delta\theta$ via

$$\Delta\theta/2\pi = \Delta f \times T \tag{7.52}$$

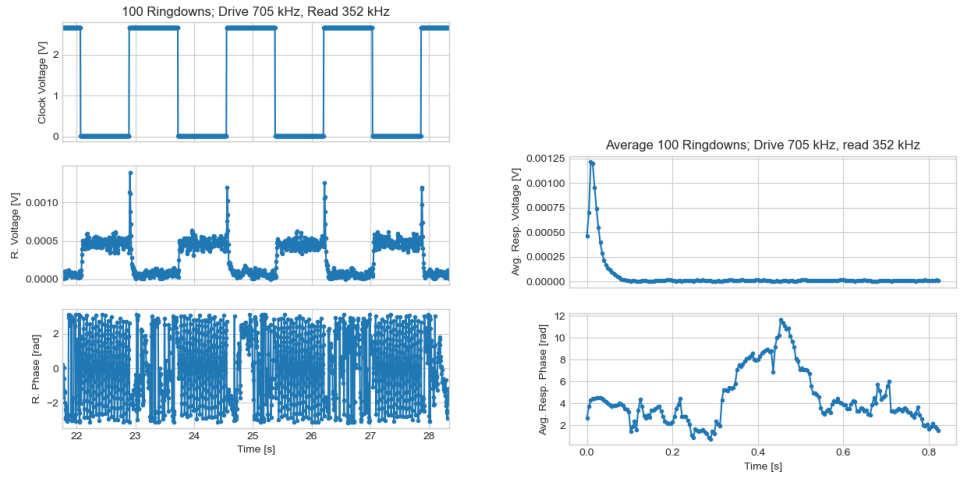

(a) (b)

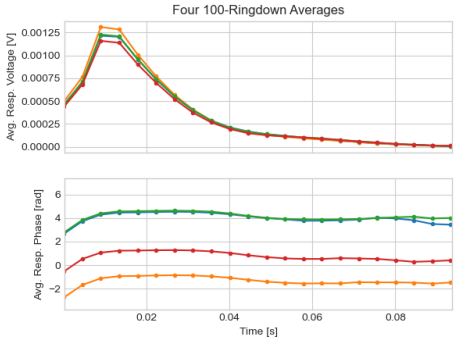

(c)

Figure 7.11: A ringdown train of 100 ringdowns, with the ringup time $T_m = 1.6565\,\mathrm{s}$ (satisfying Equation (7.53)), which drives at $\omega_d/2\pi = 705\,\mathrm{kHz}$ and reads at $\omega_{\mathrm{read}}/2\pi = 352.3\,\mathrm{kHz}$. a: four of the 100 ringdowns. b: the complex average (Equation (7.50)). c: zoom-in of four averages over four 100-ringdown measurements.

We desire the ringup to not add a phase offset to each ringdown measurement. This can be ensured by setting $\Delta\theta = 2\pi m$, $m \in \mathbb{Z}^+$, which yields a ringup duration T_m:

$$T_m = \frac{m}{\Delta f}, \quad m \in \mathbb{Z}^+ \tag{7.53}$$

Hence, we can pick a T_m which satisfies this condition, and is close to the duration we want. For instance, we can set the ringup period in the measurement of Figure 7.9 from $T = 1.7\,\mathrm{s}$ to $T_m = 1.6565\,\mathrm{s}$, for $m = 32$. We also set the ringdown time to equal the ringup time.

Having chosen a ringup time T_m which satisfies Equation (7.53), we can do ringdown trains of 100 ringdowns (Figure 7.11), and then take the complex average (Equation (7.50)). The individual ringdowns have initial amplitudes of $\sim 1.2\,\mathrm{V}$. The average has an initial amplitude of $1.25\,\mathrm{V}$, and is a much smoother curve than in Figure 7.9. Similarly, the phase is smooth (at least while the Brownian motion is still decaying). In Figure 7.11c, we do four 100-ringdown

trains, to show reproducibility. The result is four decays which have amplitudes comparable to the individual ringdowns in their corresponding datasets, and four smooth phase curves (with initial phase offsets determined by the overall start time of each ringdown train). The fact that the phase curves have been smoothed so well by this procedure provides an avenue to investigate the Berry phase associated with a dynamical loop.

7.4 Sample Dynamical Loop

To test out the electronic configuration for dynamics, we use a loop that we estimate will take an excitation from $\omega_3/2\pi = 705\,\text{kHz}$ to $\omega_1/2\pi = 352.3\,\text{kHz}$. We execute a loop that sweeps a rectangular loop in P_1 and P_2. $P_3 = 79.84\,\mu\text{W}$ and $\delta/2\pi = 105.6\,\text{kHz}$ are fixed. P_1 and P_2 are swept in a rectangular loop from

$$\begin{aligned} P_{1,\text{low}} &= 4.94\,\mu\text{W} \\ P_{1,\text{high}} &= 119.86\,\mu\text{W} \\ P_{2,\text{low}} &= 317.5\,\mu\text{W} \\ P_{2,\text{high}} &= 674.6\,\mu\text{W} \end{aligned} \tag{7.54}$$

The rectangular loop runs $T = 17\,\text{ms}$, and spends $T/4 = 4.25\,\text{ms}$ on each rectangular edge. The loop runs counterclockwise in (P_1, P_2) space, i.e.,

$$P_1(t) = \begin{cases} P_{1,\text{low}} + (P_{1,\text{high}} - P_{1,\text{low}})t/(T/4), & 0 \le t < T/4 \\ P_{1,\text{high}}, & T/4 \le t < T/2 \\ P_{1,\text{high}} + (P_{1,\text{low}} - P_{1,\text{high}})(t - T/2)/(T/4), & T/2 \le t < 3T/4 \\ P_{1,\text{low}}, & 3T/4 \le t < T \end{cases} \tag{7.55}$$

$$P_2(t) = \begin{cases} P_{2,\text{low}}, & 0 \le t < T/4 \\ P_{2,\text{low}} + (P_{2,\text{high}} - P_{2,\text{low}})(t - T/4)/(T/4), & T/4 \le t < T/2 \\ P_{2,\text{high}}, & T/2 \le t < 3T/4 \\ P_{2,\text{high}} + (P_{2,\text{low}} - P_{2,\text{high}})(t - 3T/4)/(T/4), & 3T/4 \le t < T \end{cases} \tag{7.56}$$

With this loop, we drive the $\omega_3/2\pi = 705\,\text{kHz}$, and read the membrane motion at the three modes. Figure 7.12 shows ringdowns of these modes, in which the mode is driven, then the loop is either executed or not executed when the drive is cut off, and the signal is allowed to ring down. For this loop, the main feature is the peak introduced by the loop at the 352.3 kHz mode. Figure 7.13 shows this peak, with the complex average taken over 100 ringdowns (Equation

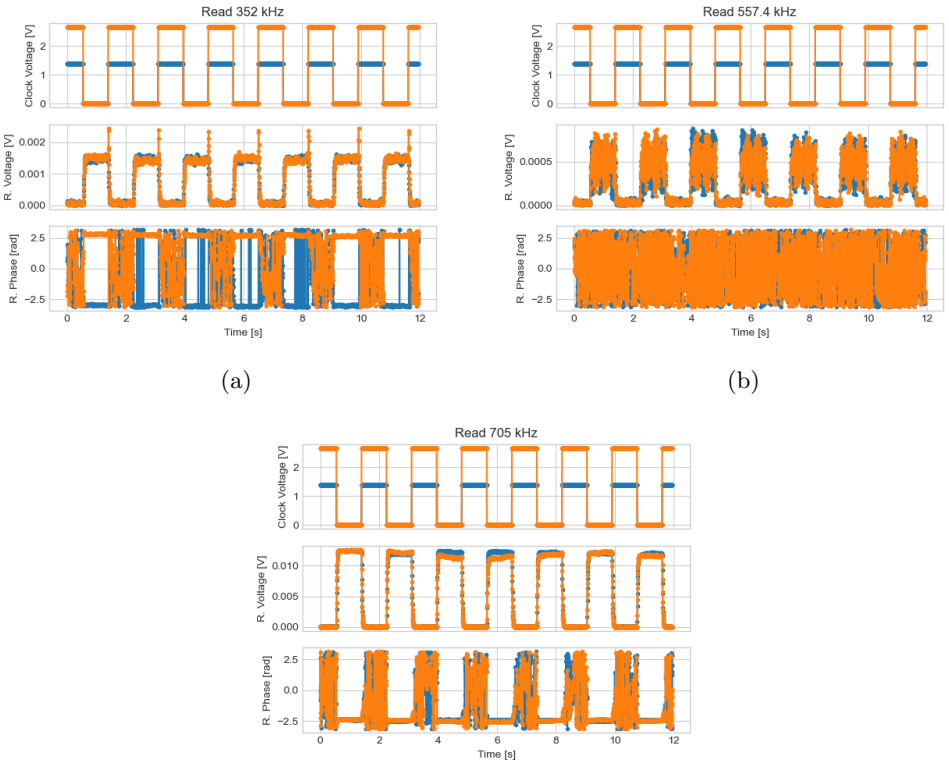

Figure 7.12: The response of a ringdown train in which the 705 kHz mode is driven, and the membrane amplitude of motion is read at each of the frequencies. Blue shows the ringdowns when the control loop is not applied, and orange shows the ringdowns when the control loop is applied.

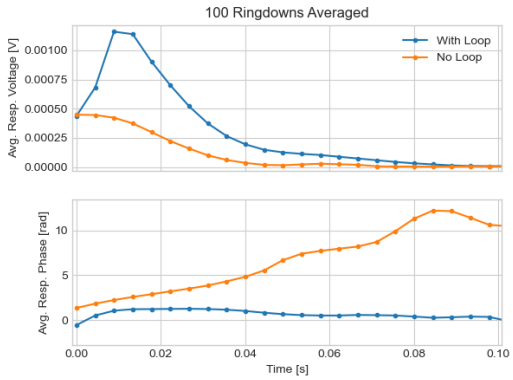

Figure 7.13: Complex averages of 100-ringdown ringdown trains, in which either the control loop is executed or not executed. The 705 kHz mode is driven, and the motion is read at 352.3 kHz. The plots show amplitude and phase.

(7.50)). The other striking feature is the phase change: the phase changes with a positive slope, for the ringdowns without the loop, and the phase is constant after the loop is completed (at $T = 17\,\text{ms}$ on the time-axis of Figure 7.13). The phase plot difference is consistent with placing energy in the 352.3 kHz mode, since the ringdown phase changes as $\omega_{\text{read}} - \omega_m$; the mode with the most energy dominates the phase, and the flat phase change indicates that energy is moved to the 352.3 kHz mode.

Chapter 8

Conclusion and Outlook

8.1 Summary

We designed a three-mode system of coupled damped harmonic oscillators in which we possess full control of the eigenvalue spectrum (Section 2.5). The particular system was an optomechanical setup which used three laser tones to address three mechanical modes of a Si_3N_4 membrane (Section 3.6). With four linearly parameters – the three laser powers and one common detuning (Chapter 5) – we reached any arbitrary point in the 3-mode eigenvalue control space. This was quantified by fitting nine Lorentzians and extracting eigenvalues from their center frequencies and linewidths (Section 6.1). We used an optomechanical model to predict the system's complex eigenvalues at any choice of three powers and one detuning (Section 3.6), and found excellent agreement between the measured and predicted eigenvalues.

In this three-mode system, we brought the system near its EP_3 point (Section 6.2). This was quantified both by measuring pairwise eigenvalue differences, as well as by measuring a topological invariant from a surface enclosing the EP_3 point. Then, in a neighborhood surrounding this EP_3 point, we measured EP_2 points (Sections 6.3 and 6.4), and found that they trace out a trefoil knot (Section 6.5), in agreement with established algebraic geometry [9].

Finally, we executed closed loops (Section 6.6) in the eigenvalue control space near, but excluding, the EP_2 degeneracies (Section 2.3), and found that this space realizes eigenvalue braids over the system's three eigenvalues (Section 2.5.4). We demonstrated that the isotopy class of these braids (demarcated by whether we can continuously morph one braid into another without moving the basepoints or shifting the strands through each other) is determined by the control loop homotopy class (demarcated by whether a loop can be continuously morphed into another without passing through the EP_2 trefoil knot (Section 2.5.2)). We then showed that we could form any element of the braid group B_3 by concatenating any of the generator loops

together (Section 2.5.4), and observed that the loop concatenation is noncommutative.

8.2 Outlook

Having observed striking features of n-mode non-Hermitian systems in our optomechanical system, we hope to expand our work on non-Hermitian optomechanical platforms. Since completing the work discussed in this dissertation and in [1], the MIM experiment has moved from Sloane Physics Laboratory to Yale Science Building. Thus, a new MIM setup is being developed, as of the writing of this thesis. Features of this new setup may include:

- **A Faster, Room-Temperature Apparatus:** The final data which was obtained for the EP_2 knot (Section 6.5) in this dissertation and in the paper [1] was obtained over several months.[1] For future experiments with a similar setup to the one described in Chapter 4 and Chapter 5, we can instead use a cavity with a shorter length, and hence a larger linewidth, to make much faster measurements (say, to measure an entire EP_2 trefoil knot in a day or so). There is no requirement for the work in this dissertation to use a cold-cavity, as that is a relic of the ground-state cooling experiment [76], so the new setup can instead be at room-temperature.

- **The Nearly Triply-Degenerate Modes:** In the setup discussed in this dissertation, the membrane was aligned in the cavity in such a way that it was difficult to measure the motion of the nearly-degenerate (7,1), (5,5), and (1,7) modes, in comparison to the (1,1), (2,1), and (2,2) modes which were used in this thesis. If the membrane (or the membrane mirror) is aligned such that the nearly triply-degenerate modes are most strongly coupled to the cavity (see [64] for more details on this), future experiments with a three-mode system can use these modes instead.

- **Simplified 3-Mode Coupling:** Another issue with using the nearly-degenerate (7,1), (5,5), and (1,7) modes in the previous MIM setup is that, if we attempt to separately control the three modes with three laser tones, the three laser tones do not address the modes in a linearly independent way, since they couple to the same cavity mode. Thus, we were required to use the Floquet coupling (Sections 3.5.2 and 3.6) to couple three modes. If we instead have three laser tones resonant with three separate cavity modes, then the power and detuning of each of the three laser will provide six control knobs that span the four-dimensional eigenvalue control space. The modes would then couple pairwise via the interaction described in Section 3.5.1.

[1] This set of data was the third complete EP_2 dataset.

This simplified setup provides an avenue toward

- **Control of the Entire Degenerate Subspace:** In the experiment described in this thesis, while we did possess arbitrary control of the eigenvalue control space, we did not possess arbitrary control over the *eigenmode* control space. With three lasers coupled to three separate cavity modes, we can use a number of tones to address the eigenmode components in a linearly independent manner.

- **Measurement of Berry Phase:** When one eigenmode is initialized with some energy, dynamical loops near exceptional points in the MIM experiment have been shown to transfer energy from one eigenmode to another [6] [31]. The heterodyne measurement process, which is the same one described in Section 5.3.1, measures the real and imaginary quadratures with sufficient precision that the phase of the complex amplitude of the mode can also be measured. We hope to use this to measure the Berry phase associated with control loops in the nondegenerate control space in future experiments.

- **Topological Energy Transfer in 3-Mode System:** A natural question to ask is how the eigenvalue braids in the three-mode system relate to dynamical energy transfer around dynamic loops near the EP_2 knot. The new experiment, with its improved speed at measuring the EP_2 knot, can then initialize one eigenmode, and then perform dynamical loops around the knot (c.f., [34]).

- **Reciprocal Energy Transfer:** The adiabatic theorem does not hold for non-Hermitian systems [108]; it is not true, in general, that if an eigenmode is initialized and a dynamical loop is performed, energy will transfer into another eigenmode. This is because, in order for energy to transfer, the state must start in the high-gain mode, and it cannot spend too much of the loop in the high-loss mode before the end of the loop [33, Appendix A] [108]. By pumping the modes with an applied laser, we might bypass this restriction (which was encountered in the previous MIM experiment on topological energy transfer [6]), by forcing a mode of choice to be a high-gain mode for a sufficient duration of an adiabatic loop [117], before ending the loop in a different mode [118].

As the list above exposits, experimental exploration of non-Hermitian physics continues to be a very active field. Non-Hermitian systems may play a key role in sensing, energy transfer, and topological quantum computation. I hope that this dissertation has provided a helpful introduction to spectral flow in non-Hermitian systems, and has further motivated optomechanics as a productive platform to develop the theory of non-Hermitian physics into practical experiments.

Appendix A

Derivation: Dropping the Counter-Rotating Term in the High-Q Limit

In Section 3.2.2, in reaching Equation (3.17), we did not make any use of the high-Q assumption. In this appendix, we do use this assumption, in order to drop the $c^*[\omega]$ term and arrive at Equation (3.19)

This derivation is accomplished by taking Equation (3.17) into the Fourier domain:

$$-i\omega c[\omega] = -i\omega_m c - \frac{\gamma_m}{2}\big(c[\omega] - c^*[\omega]\big) + c_{\rm in}[\omega] \tag{A.1}$$

We note two properties of Equation (A.1) that will be important in this argument. First, that, per the definition of the Fourier transform in Equation (3.4), $c[\omega]$ is the component of $c(t)$ that rotates at frequency $+\omega$. Second, that $c^*[\omega]$ is the Fourier transform of $c^*(t)$. We write this explicitly:

$$c^*[\omega] = \int_{-\infty}^{\infty} c^*(t)e^{i\omega t} = \left(\int_{-\infty}^{\infty} c(t)e^{-i\omega t}dt\right)^* \tag{A.2}$$

We point out from Equation (A.2) that $c^*[\omega]$ is the component of $c(t)$ that rotates at $-\omega$ (or, rather, it is the complex conjugate of this component of $c(t)$). We also point out that $c^*[\omega]$ (Equation A.2) is *not* the same thing as the complex conjugate of $c[\omega]$, which is given by

$$\Big(c[\omega]\Big)^* = \left(\int_{-\infty}^{\infty} c(t)e^{i\omega t}dt\right)^* = \int_{-\infty}^{\infty} c^*(t)e^{-i\omega t}dt \tag{A.3}$$

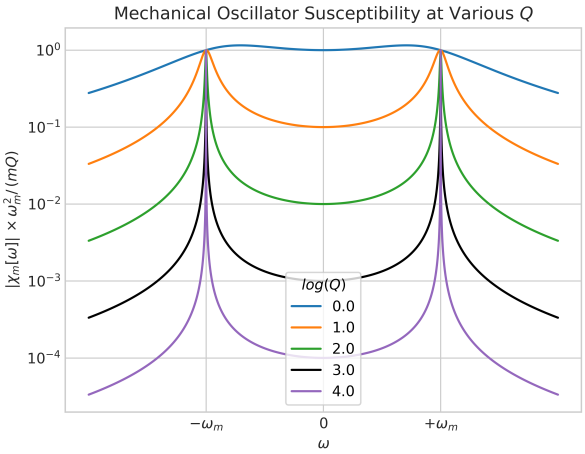

Figure A.1: The magnitude of the mechanical transfer function of a mechanical oscillator at various Q. The y-axis is made dimensionless by dividing by the approximate maximum values at resonance, $Q/(m\omega_m^2)$. This also puts the curves on the same scale to aid in the visual comparison across different Q values. We see that, even at modest Q, that the response peaks very sharply at ω near $\omega = \pm\omega_m$.

We can recast Equation (A.1) in terms of the mechanical transfer function (Equation (3.10)):

$$c[\omega] = -2im\omega_m\chi_x[\omega]\left(\frac{\gamma_m}{2}c^*[\omega] + c_{\text{in}}[\omega]\right) \tag{A.4}$$

Now, we consider the modulus of Equation (3.9). This modulus is

$$\left|\chi_x[\omega]\right| = \frac{1/m}{\sqrt{(\omega_m^2 - \omega^2)^2 + (\gamma_m\omega)^2}} \tag{A.5}$$

The critical points of $\left|\chi_x[\omega]\right|$ are at $\omega = 0$ and $\omega = \pm\sqrt{\omega_m^2 - \gamma_m^2/2} = \pm\omega_m\sqrt{1 - 1/2Q^2}$. The values of $\left|\chi_x[\omega]\right|$ are $1/(m\omega_m^2)$ and $Q/(m\omega_m^2)/\sqrt{1 - 1/(4Q^2)}$, respectively. If $Q > 1$, then $|\chi_x|$ has a local minimum at $\omega = 0$, and the other two critical points are maxima. If Q is very large, then the maximum values are very large, at $Q/(m\omega_m^2)$, to first order in Q. Furthermore, the maxima are located at $\omega \approx \pm\omega_m(1 - 1/(4Q^2)) \approx \pm\omega_m$. This behavior is shown in Figure A.1, where we have plotted the exact mechanical transfer function (Equation (3.9)) at various values of Q. As claimed, these susceptibilities peak close to $\pm\omega_m$, get asymptotically closer to $\pm\omega_m$ as Q asymptotes, and the peaks get narrower as Q increases, in agreement with these analytic results.

To find the bandwidth of this high-Q resonator, we seek the full width at half maximum (FWHM), so we need the ω at which $|\chi_x[\omega]|$ reaches $Q/(2m\omega_m^2)$. Doing this algebra, one finds

that this occurs at

$$\begin{aligned}\omega_{\mathrm{hm}} &= \pm\sqrt{-\frac{\gamma_m^2}{2}+\omega_m^2 \pm \frac{\sqrt{3}}{2}\sqrt{-\gamma_m^4+4\gamma_m^2\omega_m^2}} \\ &\approx \pm\frac{\gamma_m}{2} \pm \omega_m\left(1-\frac{1}{8Q^2}\right) \\ &\approx \pm\frac{\gamma_m}{2} \pm \omega_m = \pm\omega_m\left(1\pm\frac{Q}{2}\right)\end{aligned} \tag{A.6}$$

Thus, the FWHM is $\gamma_m = \omega_m/Q$, for very large Q.

The takeaway from this argument is that, for very large Q, the mechanical transfer function $\chi_x[\omega]$ peaks in its magnitude at $\omega = \pm\omega_m$, and the FWHM around these maxima is γ_m. But since $Q = \omega_m/\gamma_m$ is very large, then these peaks are very narrow over the spectral range of $\chi_x[\omega]$. Thus, for a drive $c_{\mathrm{in}}[\omega]$ at some frequency ω in Equation (A.4), $\chi_x[\omega]$ is appreciable only when $\omega_m - \gamma_m/2 < \omega < \omega_m + \gamma_m/2$ or when $-\omega_m - \gamma_m/2 < \omega < -\omega_m + \gamma_m/2$. Now, if the driving ω is nearly ω_m, then $c[\omega]$ will also peak sharply around $\omega_m - \gamma_m/2 < \omega < \omega_m + \gamma_m/2$. Then, $c[\omega]$ will not contain a component around $-\omega_m - \gamma_m/2 < \omega < -\omega_m + \gamma_m/2$, so, per the definition of $c^*[\omega]$ in Equation (A.2) and the discussion following it, $c^*[\omega]$ is negligible, and can thus be dropped from Equation A.4, and then immediately in Equation (A.1). We then inverse Fourier transform back to the time domain and end with Equation (3.19), as claimed.

Appendix B

Rectangular Membrane Frequency Derivation

In this appendix, we derive the expression for the (angular) mechanical mode frequencies of a rectangular membrane of length L_x and width L_y. These frequencies $\omega_{m,n}$ are indexed by integer indices $m, n \geq 1$:

$$\omega_{m,n} = \omega_{1,1}\sqrt{\frac{(m/L_x)^2 + (n/L_y)^2}{(1/L_x)^2 + (1/L_y)^2}} \tag{B.1}$$

where $\omega_{1,1}$ is the fundamental mode frequency.

To derive (B.1), we consider a boundary value problem (BVP) over the region in Figure B.1, governed by the wave equation

$$\partial_t^2 u(x,y,t) = c^2\left(\partial_x^2 u(x,y,t) + \partial_y^2 u(x,y,t)\right), \tag{B.2}$$

and subject to the boundary condition

$$u|_{\partial D} = 0, \tag{B.3}$$

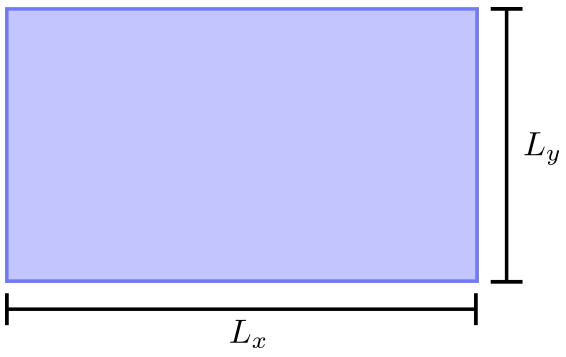

Figure B.1: A rectangular membrane with length L_x and width L_y.

or, equivalently,

$$u(0,y,t) = u(L_x,y,t) = 0;\ u(x,0,t) = u(x,L_y,t) = 0,\ \forall x \in [0,L_x], \forall y \in [0,L_y] \tag{B.4}$$

To solve this BVP, we can seek separable solutions $u(x,y,t)$ which can be written as

$$u(x,y,t) = f(x,y)\phi(t) \tag{B.5}$$

Now, plug Equation B.5 into Equation B.2:

$$\phi'' f = c^2 \phi \left(\partial_x^2 f + \partial_y^2 f\right) \tag{B.6}$$

We can then divide both sides of (B.6) by $c^2 u(x,y,t) = c^2 f(x,y)\phi(t)$:

$$\frac{1}{c^2}\frac{\phi''(t)}{\phi(t)} = \frac{\partial_x^2 f(x,y) + \partial_y^2 f(x,y)}{f(x,y)} \tag{B.7}$$

Now, the left-hand side of (B.7) is independent of x and y, while the right-hand side of (B.7) is independent of t. Thus, (B.7) must be a constant in all three of x, y, t, so it can be written as

$$\frac{1}{c^2}\frac{\phi''(t)}{\phi(t)} = \frac{\partial_x^2 f(x,y) + \partial_y^2 f(x,y)}{f(x,y)} = -k^2 \tag{B.8}$$

for some constant k. Thus, the left-hand side of (B.8) is the temporal part of the BVP, and the right-hand side is the spatial part. The right-hand side is also known as the Helmholtz equation $(\nabla^2 f)/f = -k^2$, where k is called the wavenumber. We handle the spatial part first, since the boundary conditions are specified in Equation B.4.

To solve the spatial part of the BVP, we can further separate $f(x,y)$ into a product:

$$f(x,y) = G(x)H(y) \tag{B.9}$$

Then the right-hand side of (B.8) can be written as

$$G''/G + H''/H = -k^2 \tag{B.10}$$

By subtracting H''/H from both sides of (B.10), we get

$$G''(x)/G(x) = -k^2 - H''(y)/H(y) \tag{B.11}$$

Once again, the left-hand and the right-hand sides of (B.11) are independent of each other, so

(B.11) must be equal to a constant, i.e.

$$G''(x)/G(x) = -k^2 - H''(y)/H(y) = -k_x^2 \tag{B.12}$$

Now that we have two ordinary differential equations in (B.12), we can write a solution for $G(x)$:

$$G(x) = Ae^{ik_x x} + Be^{-ik_x x} \tag{B.13}$$

From the boundary conditions in Equation B.4, we have $G(0) = 0$ and $G(L_x) = 0$. From $G(0) = 0$, we get

$$A + B = 0 \tag{B.14}$$

From $G(L_x) = 0$, we get

$$A\left(e^{ik_x L_x} - e^{-ik_x L_x}\right) = 2iA\sin(k_x L_x) = 0 \tag{B.15}$$

This holds if either $A = 0$, which is a trivial solution, or if

$$k_x = m\pi/L_x,\ m \in \mathbb{Z}^+ \tag{B.16}$$

Thus, we have solutions

$$G_m(x) = 2iA_m \sin(m\pi x/L_x),\ m \in \mathbb{Z}^+\,. \tag{B.17}$$

Similarly to the solution for $G(x)$, we can subtract G''/G from (B.10):

$$H''(y)/H(y) = -k^2 - G''(x)/G(x) = -k_y^2 \tag{B.18}$$

Applying the boundary conditions in Equation B.4, we then get

$$k_y = n\pi/L_y,\ n \in \mathbb{Z}^+ \tag{B.19}$$

and solutions

$$H_n(y) = 2iB_n \sin(n\pi y/L_y),\ n \in \mathbb{Z}^+\,. \tag{B.20}$$

Then, putting these into Equation B.9, and absorbing the constants into $A_{m,n} = (2iA_m)(2iB_n)$, we get solutions of the Helmholtz equation BVP:

$$f_{m,n}(x,y) = A_{m,n} \sin(m\pi x/L_x)\sin(n\pi y/L_y) \tag{B.21}$$

To get the time-dependent behavior, and the wave frequency, we plug Equation B.21 into Equation B.8:

$$\frac{1}{c^2}\frac{\phi''(t)}{\phi(t)} = -\pi^2\left((m/L_x)^2 + (n/L_y)^2\right) = -k^2 \tag{B.22}$$

This lets us index the values of k for which separable solutions to the wave equation exist by m, n:

$$k_{m,n} = \pi\sqrt{(m/L_x)^2 + (n/L_y)^2} \tag{B.23}$$

Furthermore, we can write the corresponding solutions $\phi_{m,n}(t)$:

$$\begin{aligned}\phi_{m,n}(t) &= C_{m,n}e^{+ick_{m,n}t} + D_{m,n}e^{-ick_{m,n}t} \\ &= C_{m,n}e^{+i\omega_{m,n}t} + D_{m,n}e^{-i\omega_{m,n}t}\end{aligned} \tag{B.24}$$

where the (m, n)-th (angular) mode frequency is given by

$$\omega_{m,n} = c\pi\sqrt{(m/L_x)^2 + (n/L_y)^2} \tag{B.25}$$

In particular, the fundamental mode frequency is

$$\omega_{1,1} = c\pi\sqrt{(1/L_x)^2 + (1/L_y)^2} \tag{B.26}$$

so we can recast the (m, n)-th mode frequency in terms of the fundamendal mode frequency to obtain Equation B.1.

We remark that a special case of Equation B.1 is the square membrane, where $L_x = L_y = L$. Then Equation B.1 becomes

$$\omega_{m,n} = \omega_{1,1}\sqrt{\frac{m^2+n^2}{2}}\,. \tag{B.27}$$

We also remark that, in order to obtain Equation B.1, no assumptions were made on the time-dependent behavior of this problem, aside from the wave-equation (B.2). The solutions of $\phi_{m,n}(t)$ could be found with additional assumptions on the problem (e.g. in the case of an initial-value problem, in which $u(x, y, 0) = v(x, y)$, for some spatial function $v(x, y)$). We have merely found the frequencies of the standing wave solutions of the BVP that the rectangular vibrating membrane determines.

Appendix C

Optomechanical Measurements

C.1 Extracting Optomechanical Coupling Constants

A central aspect of using the optomechanical interaction throughout this work is the measurement of optomechanical coupling constants (denoted in this thesis as g_0, or simply g).[1] In this section, we show measurements to extract these g values.

In Figure C.1, we drive the 705 kHz mode, apply a control laser tone of $\sim 100\,\mu W$, and sweep its detuning Δ from the cavity mode (see Section 5.3 for details on the electronic configuration). We then perform spectroscopy using the lock-in amplifier response (c.f., Section 6.1), and fit the data to a single Lorentzian (Figure C.2):

$$f(\Delta) = \frac{se^{i\phi}}{\Delta - (\omega_m - \frac{1}{2}i\gamma_m)} + b_R + ib_I \tag{C.1}$$

where the mode frequency and damping are ω_m and γ_m, the complex amplitude is $se^{i\phi}$, and the complex background is $b_R + ib_I$.

We perform Lorentzian fits (Figure C.2) for multiple values of Δ, and plot the extracted $\omega(\Delta)$ and $\gamma(\Delta)$ to get Figure C.1. We then fit this curve to the predicted form of the optomechanical spring and damping (Equations (3.149)) (as described in Section 3.4) to extract the values of g, $\omega_m^{(0)}$, $\gamma_m^{(0)}$ for this mode. We also extract κ from this fit, and allow for an offset Δ_0 in the frequency axis. The value of κ_{in} is not determined from this measurement, since g shows up in

[1] The convention in the Aspelmeyer review [52] is to use g_0 as the single-photon optomechanical coupling strength, and g as the light-enhanced optomechanical coupling strength: $g = \sqrt{n_{cav}}\, g_0$. In this work, g_0 and g are inferred from laser powers via measurements at photodiodes which are separated from the cavity by multiple fibers. This introduces losses which change the effective g_0 values: g_0 can be measured at ~ 3 Hz before the probe and control lasers are combined, where the value at the cavity is ~ 0.3 Hz. This distinction is irrelevant to this experiment, so we use the g_0 values at the photodiode before the lasers are combined. Hence, it is unimportant whether we denote the optomechanical constants as g_0 or g in this work.

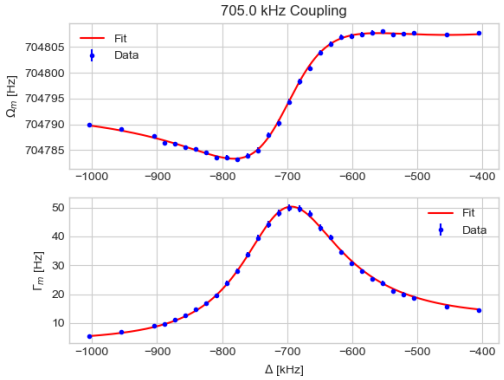

Figure C.1: A fit of the mechanical frequency and damping versus the control laser detuning, to determine the optomechanical coupling constant. The extracted g is $g = 0.320(1)\,\mathrm{Hz}$, the extracted $\omega_m^{(0)}/2\pi = 704\,793.78(5)\,\mathrm{Hz}$, the extracted $\gamma_m^{(0)}$ is $\gamma_m^{(0)}/2\pi = 0.85(4)\,\mathrm{Hz}$, the extracted Δ_0 is $\Delta_0/2\pi = -1700(400)\,\mathrm{Hz}$, the extracted κ is $\kappa/2\pi = 189\,700(1400)\,\mathrm{Hz}$. The value of κ_{in} is fixed at $\kappa_{\mathrm{in}}/2\pi = 48\,\mathrm{kHz}$.

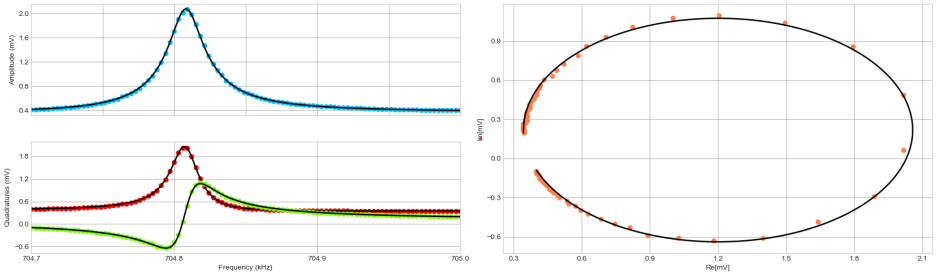

Figure C.2: A fit of the driven response to a single Lorentzian. The upper-left is the absolute value of the response, the lower-left is the quadratures of the response, and the right is the response in the complex plane. Dots are data, and lines are fits.

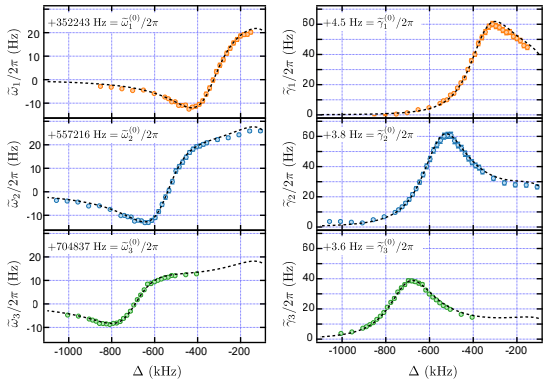

Figure C.3: A three-tone g measurement, with common κ and Δ_0 values, for the three modes in this experiment.

Equation (3.149) as $g^2\kappa_{\text{in}}$, so we must fix κ_{in} (or the ratio $\kappa_{\text{in}}/\kappa$). We fix $\kappa/\kappa_{\text{in}} = 0.267$. This lets us measure g, $\omega_m^{(0)}$, and κ.[2]

The measurement of Δ_0 is important, because this offset should be minimized before performing the main measurements in this thesis (described in Section 5.4). This is done by adding Δ_0 to the control laser frequency offset from the probe laser (Section 5.2.2).

We can measure the values of g for each of the three modes ($\omega_1^{(0)}/2\pi \approx 352.3\,\text{kHz}$, $\omega_2^{(0)}/2\pi \approx 557.2\,\text{kHz}$, and $\omega_3^{(0)}/2\pi \approx 705\,\text{kHz}$) with three separate measurements (each similar to the ones shown in Figures C.1 and C.2). We can also perform a three-tone fit of the three mode frequencies and dampings (Figure C.3), with a common κ and a common frequency-axis offset Δ_0. This vector-valued fit function yields the bare $\lambda^{(0)} = (\lambda_1^{(0)}, \lambda_2^{(0)}, \lambda_3^{(0)})$ and $\mathbf{g} = (g_1, g_2, g_3)$ values used in this experiment:

$$\lambda^{(0)} = \left((352\,243.3 - 2.2\text{i})\,\text{Hz}^{\pm 0.1\,\text{Hz}}, (557\,216.8 - 1.9\text{i})\,\text{Hz}^{\pm 0.1\,\text{Hz}}, (704\,836.7 - 1.8\text{i})\,\text{Hz}^{\pm 0.1\,\text{Hz}}\right) \tag{C.2a}$$

$$\mathbf{g} = \left(0.198\,\text{Hz}^{\pm 0.1\,\text{Hz}}, 0.304\,\text{Hz}^{\pm 0.1\,\text{Hz}}, 0.300\,\text{Hz}^{\pm 0.1\,\text{Hz}}\right) \tag{C.2b}$$

$\Delta_0/2\pi$ is $\lesssim 5\,\text{kHz}$, since it is calibrated out with the 1-tone g measurement (κ is also extracted, but it is measured with a "global" fit over the measured EP_2 points instead, as described in the next paragraph).

A "global" fit for the g and κ values can be done over the measured EP_2 points (Chapter 6). Let the measured EP_2 point parameters be $\Psi_{\text{EP2}}^{k,\text{expt}}$, and indexed by k. Let the theoretically obtained values of the parameters at a given $\mathbf{g}$ and κ be $\Psi_{\text{EP2}}^{k,\text{theory}}(\mathbf{g}, \kappa)$, via the model given

[2] $\gamma_m^{(0)}$ is also a fit parameter. However, since the optomechanically shifted damping is much larger than the bare damping, this measurement does not resolve $\gamma_m^{(0)}$ well. $\gamma_m^{(0)}$ can be determined from ringdown measurements, as in Section 4.1.3. For this experiment, γ_m is only $\sim 1\,\text{Hz}$, so it acts as a small perturbation to the values at which the system reaches exceptional points. We thus do not bother to measure $\gamma_m^{(0)}$ precisely.

in Section 3.6. Let us make these Ψ dimensionless, by dividing the (δ, P_1, P_2, P_3) of Ψ by the measured values at EP_3 (Equation (6.36)). We minimize the cost function

$$\begin{aligned} C &= \sum_k \left| \Psi_{\mathrm{EP2}}^{k,\mathrm{expt}} - \Psi_{\mathrm{EP2}}^{k,\mathrm{theory}}(\mathbf{g},\kappa) \right|^2 \\ &= \sum_k \left[\left(\frac{\delta_{\mathrm{EP2}}^{k,\mathrm{expt}} - \delta_{\mathrm{EP2}}^{k,\mathrm{theory}}(\mathbf{g},\kappa)}{\delta_{\mathrm{EP3}}} \right)^2 + \sum_l \left(\frac{(P_l)_{\mathrm{EP2}}^{k,\mathrm{expt}} - (P_l)_{\mathrm{EP2}}^{k,\mathrm{theory}}(\mathbf{g},\kappa)}{(P_l)_{\mathrm{EP3}}} \right)^2 \right] \end{aligned} \tag{C.3}$$

The theoretical values of $\Psi_{\mathrm{EP2}}^{k,\mathrm{theory}}(\mathbf{g},\kappa)$ at the kth slice are found within the 2D sheet defined by the slice (e.g., if the kth slice is a $P_1 \times P_3$ sheet, then the optomechanical model of Section 3.6 is applied at the fixed values of δ and P_2, and then a root $\left((P_1)_{\mathrm{EP2}}^{k,\mathrm{theory}}(\mathbf{g},\kappa), (P_3)_{\mathrm{EP2}}^{k,\mathrm{theory}}(\mathbf{g},\kappa)\right)$ of the discriminant polynomial D is found in the range

$$\left((P_1)_{\mathrm{EP2}}^{k,\mathrm{theory}}, (P_3)_{\mathrm{EP2}}^{k,\mathrm{theory}}\right) \in \left(0.65(P_1)_{\mathrm{EP2}}^{k,\mathrm{expt}}, 1.35(P_1)_{\mathrm{EP2}}^{k,\mathrm{expt}})\right) \times \left(0.65(P_3)_{\mathrm{EP2}}^{k,\mathrm{expt}}, 1.35(P_3)_{\mathrm{EP2}}^{k,\mathrm{expt}})\right) \tag{C.4}$$

The values which minimize the cost function (C.3) are

$$\mathbf{g}/2\pi = (0.1979, 0.3442, 0.3092)\,\mathrm{Hz} \tag{C.5a}$$

$$\kappa/2\pi = 173.84\,\mathrm{kHz} \tag{C.5b}$$

These values produce the theoretical curves, as well as the theoretical knot, in Chapter 6.

C.2 Cavity Measurements

There are two methods of ascertaining the value of κ in this experiment. One is with an optomechanical fit, which is the primary method used in this work. The other is directly, via fitting cavity resonances to Lorentzian signals. Since we measure the reflection, the fit function, in principle, would be [70, p.115]

$$f(\Delta) = G \left| \beta - \frac{\kappa_{\mathrm{in}}}{\kappa/2 - i(\Delta - \Delta_0)} \right|^2 + b \tag{C.6}$$

where b is a "dark background," G is a gain factor, Δ_0 is a frequency-axis offset, and β is an efficiency factor of our fiber coupling, which is empirically measured to be $\beta = \sqrt{0.77}$ [64, p.127]. In practice, G can vary with Δ, so we can measure $G(\Delta)$ by turning off the control laser tone, and measuring the signal

$$d(\Delta) = |G(\Delta)|^2 + b \tag{C.7}$$

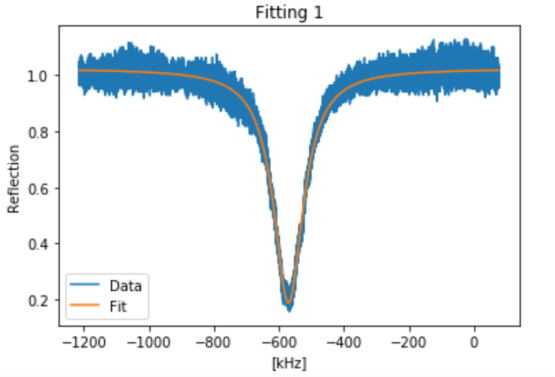

Figure C.4: A fit of the cavity linewidth.

We then fit the resonances to

$$f'(\Delta) = \frac{f(\Delta) - b}{d(\Delta) - b} = a \left| \beta - \frac{\kappa_{\text{in}}}{\kappa/2 - i(\Delta - \Delta_0)} \right|^2 \tag{C.8}$$

where a is a gain factor.

We performed measurements such as those in Figure C.4, and found values of κ and κ_{in} over these measurements. On one dataset,

$$\kappa/2\pi = 143(38)\,\text{kHz} \tag{C.9a}$$

$$\kappa_{\text{in}}/2\pi = 37(11)\,\text{kHz} \tag{C.9b}$$

The measurement of κ via the optomechanical fit is much less noisy than this method, so we prefer that for this experiment. Nonetheless, from these, we see the ratio

$$\kappa/\kappa_{\text{in}} \approx 0.26 \tag{C.10}$$

so we use this ratio to determine κ_{in}.

We remark that Equation (C.8) is symmetric around $\kappa_{\text{in}} = \kappa/2$, so either κ_{in} or $\kappa - \kappa_{\text{in}}$ can produce the same reflection curve. This confounding factor could be removed by measuring in both reflection and transmission. A future experiment will measure both the cavity reflection and transmission simultaneously, so κ_{in} can be determined from measurements of the cavity reflection in the complex plane (c.f., Figure 3.1b). Nonetheless, κ_{in} only enters our calculations in $g^2\kappa_{\text{in}}$ in the optomechanical shift (Equation (3.149)), so if we have made an error in measuring κ_{in} in this experiment, the error gets absorbed into our g definitions.

Appendix D

Pound-Drever-Hall (PDH) Frequency Locking

In the following discussion, we follow a pedogical introduction on PDH locking by Eric Black of LIGO [78].

When light is shown into a Fabry-Pérot cavity, light *is not transmitted* out of the cavity, unless the length of the cavity L_{cav} and the wavelength of the light λ_L satisfy

$$2L_{\text{cav}} = n\lambda_L, \quad n \in \mathbb{N} \tag{D.1}$$

If the reflection is instead measured, then light *is reflected* unless Equation (D.1) is satisfied. This can also be written in terms of the cavity's free spectral range $\Delta\nu_{\text{fsr}} = c/2L$, which implies that the frequency $f_L = c/\lambda_L$ satisfies[1]

$$f_L = n\Delta\nu_{\text{fsr}}, \quad n \in \mathbb{N} \tag{D.2}$$

With the condition in Equation (D.2), the intensity of the light reflected has resonances, (Section 3.3) with resonance peaks at $n\Delta\nu_{\text{fsr}},\ n \in \mathbb{N}$.

Now, suppose we have a frequency-tunable laser, and we wish to have our laser of frequency f_L be resonant with a cavity mode, which must be integer multiple of f_{fsr}. Without loss of generality, we consider a measurement of cavity reflection in this discussion. We could achieve this by looking at the reflection dips, and holding the reflection at a zero using a feedback loop. However, this does not work by itself, since the intensity is symmetric about the resonance frequency. If the intensity fluctuates upward, one cannot tell whether the laser frequency fluctuated in the positive

[1] or, in terms of the angular frequency $\omega_L = 2\pi f_L$, the condition is $\omega_L = n2\pi\nu_{\text{fsr}},\ n \in \mathbb{N}$.

or negative direction from the cavity resonance. However, the derivative with respect to laser frequency is antisymmetric near the resonance frequency, so if we can vary the laser frequency f_L and measure the derivative, then we can use the derivative to produce an error signal which is antisymmetric as a function of f_L. Then this error signal can be held at zero, and we can lock the laser to the cavity mode.

To produce this measurement, we can use phase interferometry, by modulating and demodulating the phase of the laser light with a sine wave $\beta \sin \Omega t$. Then, when we shine laser light with an oscillating electric field $E_0 e^{i\omega_L t}$ into the phase modulator, we get light incident on the cavity as

$$E_{\text{inc}} = E_0 e^{i(\omega_L t + \beta \sin \Omega t)} \tag{D.3}$$

This can be written in terms of $J_n(z)$, Bessel functions of the first kind, with the Jacobi-Anger identity $e^{iz\sin\theta} = \sum_{n=-\infty}^{\infty} J_n(z) e^{in\theta}$: [2]

$$\begin{aligned} E_{\text{inc}} &\approx E_0 \left(J_0(\beta) + 2iJ_1(\beta)\sin\Omega t\right) e^{i\omega_L t} && \text{(D.4)} \\ &= E_0 \left(J_0(\beta) e^{i\omega_L t} + J_1(\beta) e^{i(\omega_L+\Omega)t} - J_1(\beta) e^{i(\omega_L-\Omega)t}\right) && \text{(D.5)} \end{aligned}$$

This form makes it clear that the phase modulation has produce three tones: the main carrier tone in ω_L, and two sidebands at $\omega_L \pm \Omega$. We note that if the power in the main beam is $P_0 = |E_0|^2$, then the power in the carrier is $P_c = J_0(\beta)^2 P_0$ and the power in each sideband is $P_s = J_1(\beta)^2 P_0$ (or $P_c \approx P_0$ and $P_s \approx P_0\beta^2/4$, when $\beta \ll 1$).

Now we look at the reflected field from this phase-modulated incident field. With the reflection coefficient $F(\omega)$ calculated in Section 3.3, we see that the reflected field is

$$E_{\text{ref}} \approx E_0 \left(J_0(\beta)F(\omega_L)e^{i\omega_L t} + J_1(\beta)F(\omega_L+\Omega)e^{i(\omega_L+\Omega)t} - J_1(\beta)F(\omega_L-\Omega)e^{i(\omega_L-\Omega)t}\right) \tag{D.6}$$

And the power $P_{\text{ref}} = |E_{\text{ref}}|^2$ is

$$\begin{aligned} P_{\text{ref}} \approx & P_0|F(\omega_L)|^2 + P_s|F(\omega_L+\Omega)|^2 + P_s|(\omega_L-\Omega)|^2 + && \text{(D.7)} \\ & 2\sqrt{P_c P_s}\left(\text{Re}\left[G(\omega_L,\Omega)\right]\cos(\Omega t) + \text{Im}\left[G(\omega_L,\Omega)\right]\sin(\Omega t)\right) + \mathcal{O}(\Omega^2) && \text{(D.8)} \end{aligned}$$

where we have a function $G(\omega_L, \Omega)$ in terms of the reflection coefficients $F(\omega)$:

$$G(\omega_L,\Omega) = F(\omega_L)F^*(\omega_L+\Omega) - F^*(\omega_L)F(\omega_L-\Omega) \tag{D.9}$$

[2] If the amplitude β is very small ($\beta \ll 1$), it suffices to write $E_{\text{inc}} \approx E_0 e^{i\omega t}(1 + i\beta \sin \Omega t)$, and not use Bessel functions in this discussion.

The signal can be used to pick out the real or imaginary part of $G(\omega_L, \Omega)$, depending on whether Ω is slow or fast. If Ω is slow compared to ω_L, then it can be shown that $G(\omega)$ is purely real [78, pp.83]. However, if Ω is fast enough that $\omega \pm \Omega$ is not resonant with the cavity mode, but ω is, then $F(\omega_L \pm \Omega) \approx -1$, so $G(\omega) \approx -2i\,\mathrm{Im}[F(\omega_L)]$, and

$$P_{\mathrm{ref}} \approx \text{D.C. Terms} - 4\sqrt{P_s P_c}\,\mathrm{Im}[F(\omega_L)]\sin(\Omega t) + \mathcal{O}(\Omega^2) \tag{D.10}$$

If we mix this signal down with $\sin(\Omega t)$, then the surviving power term is $-4\sqrt{P_s P_c}\,\mathrm{Im}F(\omega_L)$.

Now, if the laser frequency is near a cavity resonance, then we can write

$$\frac{\omega_L}{\Delta\nu_{\mathrm{fsr}}} = 2\pi N + \frac{\delta\omega_L}{\Delta\nu_{\mathrm{fsr}}} \tag{D.11}$$

so the reflection coefficient (Equation (3.100)), to first order in $\delta\omega_L$, is

$$\begin{aligned} F(\omega_L) &= \frac{r(e^{i\omega_L/\Delta\nu_{\mathrm{fsr}}} - 1)}{1 - r^2 e^{i\omega_L/\Delta\nu_{\mathrm{fsr}}}} \\ &\approx \frac{ri\delta\omega_L/\Delta\nu_{\mathrm{fsr}}}{1 - r^2 - r^2 i\delta\omega_L/\Delta\nu_{\mathrm{fsr}}} \\ &\approx \frac{ri\delta\omega_L/\Delta\nu_{\mathrm{fsr}}}{(1-r^2)}(1 + \frac{r^2}{1-r^2} i\delta\omega_L/\Delta\nu_{\mathrm{fsr}}) \\ &\approx \frac{i\delta\omega_L/\Delta\nu_{\mathrm{fsr}}}{\pi/\mathcal{F}} = \frac{i}{\pi}\frac{\delta\omega_L}{\delta\nu} \end{aligned}$$

where $\delta\nu = \Delta\nu_{\mathrm{fsr}}/\mathcal{F}$, and where we employ the approximations that $\mathcal{F} \approx \pi/(1-r^2)$ and $r \approx 1 - \pi/2\mathcal{F}$, since the cavity finesse $\mathcal{F}$ is high.

Finally, we produce the Pound-Drever-Hall error signal by mixing the reflected power down by $\sin\Omega t$. Near the cavity resonance, the error signal is approximately

$$\varepsilon \approx -\frac{4}{\pi}\sqrt{P_c P_s}\,\frac{\delta\omega_L}{\delta\nu} \tag{D.12}$$

This error signal is linear in $\delta\omega_L$, so we can feed it back to a feedback loop, such as a PID loop, to keep $|\varepsilon|$ small, and thus lock the laser frequency to the cavity mode frequency.

Figure D.1 shows a simulated PDH error signal. For an Ω that is large enough that, when ω_L is resonant with a cavity mode, but $\omega_L \pm \Omega$, the error signal has three prominent "wings:" one large middle one at the cavity resonance, and two smaller ones at $\omega_L \pm \Omega$. Near ω_L, the error signal is linear and has a negative slope [3] Hence, if ω_L drifts away from the cavity mode

[3]The error signal could have had a positive slope, had we mixed down with $-\sin(\Omega t)$, instead of $+\sin(\Omega t)$. But the PID feedback loop must take the correctly sloped error signal to lock the laser, or the feedback loop will push the laser frequency away from the cavity mode instead. By convention, the negative slope is the correct one.

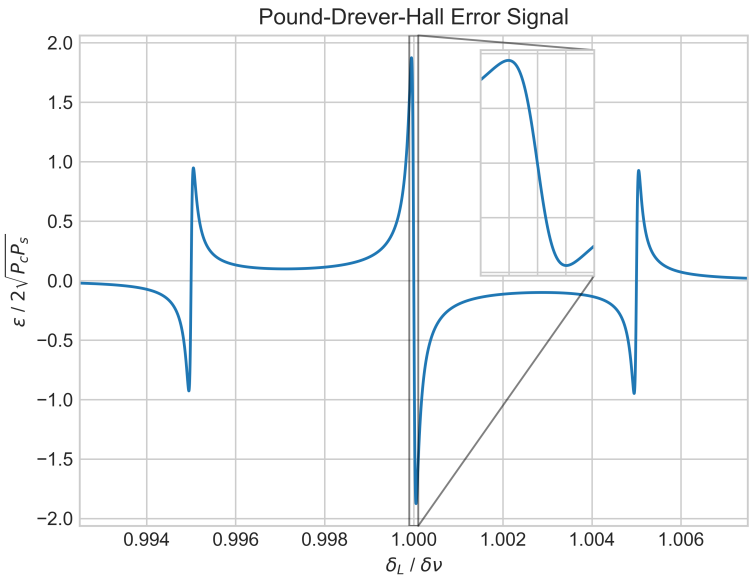

Figure D.1: Pound-Drever-Hall error signal. Simulated from the reflectivity coefficient, with $r_1 = .9997$ and $r_2 = .99998$, from $\Omega = 0.005\omega_c$, and from the imaginary part of Equation (D.9).

in the positive direction, ε is negative and linear in the deviation $\delta\omega_L$. Similarly, if the drift is negative from the cavity mode, ε is positive. Either way, ε counters the drift in laser frequency away from the cavity mode, and thus if ε is kept to zero, the laser is locked to a cavity mode.

Appendix E

Metric Expansions near EP's

E.1 Expansions near EP_2

Consider the matrix

$$J + \delta J = \begin{pmatrix} 0 & 1 & 0 \\ 0 & 0 & 1 \\ x & y & 0 \end{pmatrix}; x, y \in \mathbb{C} \tag{E.1}$$

and its characteristic polynomial

$$c_{x,y}(\lambda) = \lambda^3 - \lambda y - x \tag{E.2}$$

where x and y are the complex Jordan-Arnol'd control parameters (as discussed in Section 2.5). Its discriminant polynomial is

$$D(x, y) = 4y^3 - 27x^2 \tag{E.3}$$

In this section, we show that, with a small perturbation ε to x and y, that two of the solutions λ_1, λ_2, λ_3 of the characteristic polynomial vary as $\sqrt{\varepsilon}$, and the other varies as ε. We also show that the discriminant

$$D(\lambda_1, \lambda_2, \lambda_3) = \big((\lambda_1 - \lambda_2)(\lambda_2 - \lambda_3)(\lambda_3 - \lambda_1)\big)^2 \tag{E.4}$$

varies as ε. This is important to the data analysis, because in the data analysis (Section 6.3.1), we use the fact that the discriminant varies linearly away from an EP_2 in order to see that the phase of the discriminant winds by 2π around an EP_2 point, as opposed to $2\pi n$ for some different integer value of n.

First, we discuss Cardano's formula [119] for the solution of a cubic polynomial

$$t^3 + pt + q = 0. \tag{E.5}$$

[1] We can write

$$C = \sqrt[3]{-\frac{q}{2} + \sqrt{\frac{q^2}{4} + \frac{p^3}{27}}} \tag{E.6}$$

[2] Then a solution is

$$\lambda_1 = C - \frac{p}{3C}. \tag{E.7}$$

The other two solutions are obtained by multiplying one term by one primitive cube root of unity, $\frac{-1\pm i\sqrt{3}}{2}$, and the other term by the other primitive cube root of unity, $\frac{-1\mp i\sqrt{3}}{2}$. More explicitly, this is

$$\begin{aligned} \lambda_2 &= \frac{-1 \pm i\sqrt{3}}{2} C - \frac{-1 \mp i\sqrt{3}}{2} \frac{p}{3C} \\ \lambda_3 &= \frac{-1 \mp i\sqrt{3}}{2} C - \frac{-1 \pm i\sqrt{3}}{2} \frac{p}{3C} \end{aligned} \tag{E.8}$$

Now, suppose that the parameters x and y are such that they are near an EP_2 point in the (x, y) parameter space, that is, that

$$27x^2 - 4y^3 \approx 0 \tag{E.9}$$

We can consider a complex-valued perturbation ε to the Jordan-Arnol'd parameters x and y. First, we can apply the perturbation to x ($|\varepsilon| \ll |x|$):

$$x \mapsto x + \varepsilon \tag{E.10}$$

Now, we identify $q = -(x + \varepsilon)$ and $p = -y = -3(x/2)^{2/3}$ in Cardano's formula (E.5), and get

$$C = \sqrt[3]{\frac{x+\varepsilon}{2} + \sqrt{\frac{(x+\varepsilon)^2}{4} - \frac{y^3}{27}}} \tag{E.11}$$

[1] This is a *depressed cubic* polynomial, but any cubic polynomial $az^3 + bz^2 + cz + d = 0$ can be brought to the form of a depressed cubic polynomial by the substitution $z = t - b/(3a)$.

[2] To avoid ambiguity in the choice of branch cut for the square and cube roots, for a complex number $z = re^{i\theta}$, we define $\sqrt[3]{z} = \sqrt[3]{r}e^{i\theta/3}$, and $\sqrt{z} = \sqrt{r}e^{i\theta/2}$, where $\theta \in (-\pi, +\pi]$. This is the principal value of these root functions.

Using Taylor expansions, we can approximate C as

$$\begin{aligned} C &\approx \sqrt[3]{\frac{x+\varepsilon}{2}+\sqrt{\frac{x\varepsilon}{2}}} \\ &= \left(\frac{x}{2}\right)^{1/3}\sqrt[3]{1+\frac{\varepsilon}{x}+\sqrt{\frac{2\varepsilon}{x}}} \\ &\approx \left(\frac{x}{2}\right)^{1/3}\left[1+\frac{1}{3}\left(\frac{\varepsilon}{x}+\sqrt{\frac{2\varepsilon}{x}}\right)-\frac{1}{9}\left(\frac{\varepsilon}{x}+\sqrt{\frac{2\varepsilon}{x}}\right)^2\right] \\ &\approx \left(\frac{x}{2}\right)^{1/3}\left[1+\frac{1}{3}\sqrt{\frac{2\varepsilon}{x}}+\frac{1}{9}\frac{\varepsilon}{x}\right] \end{aligned} \tag{E.12}$$

Similarly, we can approximate $1/C$ as

$$\begin{aligned} \frac{1}{C} &\approx \left(\frac{x}{2}\right)^{-1/3}\sqrt[-3]{1+\frac{\varepsilon}{x}+\sqrt{\frac{2\varepsilon}{x}}} \\ &\approx \left(\frac{x}{2}\right)^{1/3}\left[1-\frac{1}{3}\left(\frac{\varepsilon}{x}+\sqrt{\frac{2\varepsilon}{x}}\right)+\frac{2}{9}\left(\frac{\varepsilon}{x}+\sqrt{\frac{2\varepsilon}{x}}\right)^2\right] \\ &\approx \left(\frac{x}{2}\right)^{-1/3}\left[1-\frac{1}{3}\sqrt{\frac{2\varepsilon}{x}}+\frac{1}{9}\frac{\varepsilon}{x}\right] \end{aligned} \tag{E.13}$$

We put (E.12) and (E.13) into (E.7):

$$\lambda_1 \approx 2\sqrt[3]{\frac{x}{2}}+\frac{2}{9}\frac{\varepsilon}{x}\sqrt[3]{\frac{x}{2}} \tag{E.14}$$

Thus, this root λ_1 grows linearly in ε. On the other hand, we also put (E.12) and (E.13) into (E.8) to get

$$\begin{aligned} \lambda_2 &\approx -\left(\frac{x}{2}\right)^{1/3}+i\left(\frac{x}{2}\right)^{1/3}\sqrt{\frac{2\varepsilon}{3x}} \\ \lambda_3 &\approx -\left(\frac{x}{2}\right)^{1/3}-i\left(\frac{x}{2}\right)^{1/3}\sqrt{\frac{2\varepsilon}{3x}} \end{aligned} \tag{E.15}$$

and see that these grow as $\sqrt{\varepsilon}$, which is faster than $\mathcal{O}(\varepsilon)$ near $\varepsilon = 0$. Finally, we can put (E.14) and (E.15) into (E.4):

$$\begin{aligned} D &\approx \left(\frac{x}{2}\right)^{2/3}\left(\left(3+\frac{2}{9}\frac{\varepsilon}{x}-i\sqrt{\frac{2\varepsilon}{3x}}\right)\left(3+\frac{2}{9}\frac{\varepsilon}{x}+i\sqrt{\frac{2\varepsilon}{3x}}\right)2i\sqrt{\frac{2\varepsilon}{3x}}\right)^2 \\ &= \left(\frac{x}{2}\right)^{2/3}\left(\left(\left(3+\frac{2}{9}\frac{\varepsilon}{x}\right)^2+\frac{2\varepsilon}{3x}\right)2i\sqrt{\frac{2\varepsilon}{3x}}\right)^2 \\ &\approx \left(\frac{x}{2}\right)^{2/3}\left(-\frac{72}{3x}\right)\varepsilon \end{aligned} \tag{E.16}$$

and so D grows linearly in the perturbation ε to x.

For completeness, we can also consider a complex-valued perturbation ε to y ($|\varepsilon| \ll |y|$):

$$y \mapsto y + \varepsilon \tag{E.17}$$

Then C (E.6) becomes

$$\begin{aligned} C &= \left(\frac{x}{2} + \sqrt{\frac{x^2}{4} - \frac{(y+\varepsilon)^3}{27}}\right)^{1/3} \\ &\approx \left(\frac{x}{2} + i\frac{y\sqrt{\varepsilon}}{3}\right)^{1/3} \\ &= \left(\frac{x}{2}\right)^{1/3}\left(1 + \frac{i2y}{3x}\sqrt{\varepsilon}\right)^{1/3} \\ &\approx \left(\frac{x}{2}\right)^{1/3}\left[1 + \frac{i2y}{9x}\sqrt{\varepsilon} + \left(\frac{2y}{9x}\right)^2\varepsilon\right] \\ &= \left(\frac{y}{3}\right)^{1/2}\left[1 + i\sqrt{\frac{\varepsilon}{3y}} + \frac{\varepsilon}{3y}\right] \end{aligned} \tag{E.18}$$

Similarly, we can approximate $1/C$ as

$$\begin{aligned} \frac{1}{C} &\approx \left(\frac{x}{2}\right)^{-1/3}\left(1 + \frac{i2y}{3x}\sqrt{\varepsilon}\right)^{-1/3} \\ &\approx \left(\frac{x}{2}\right)^{-1/3}\left[1 - \frac{i2y}{9x}\sqrt{\varepsilon} - 2\left(\frac{2y}{9x}\right)^2\varepsilon\right] \\ &= \left(\frac{y}{3}\right)^{-1/2}\left[1 - i\sqrt{\frac{\varepsilon}{3y}} - \frac{2\varepsilon}{3y}\right] \end{aligned} \tag{E.19}$$

Plugging (E.18) and (E.19) into (E.7), we get

$$\lambda_1 = \left(\frac{y}{3}\right)^{1/2}\left[2 - \frac{\varepsilon}{3y}\right] \tag{E.20}$$

so we again have a root that grows linearly in ε. Similarly, we plug (E.18) and (E.19) into (E.8):

$$\begin{aligned} \lambda_2 &\approx \left(\frac{y}{3}\right)^{1/2}\left[-\frac{\varepsilon}{3y} - 2i\sqrt{\frac{\varepsilon}{y}}\right] \\ \lambda_3 &\approx \left(\frac{y}{3}\right)^{1/2}\left[-\frac{\varepsilon}{3y} + 2i\sqrt{\frac{\varepsilon}{y}}\right] \end{aligned} \tag{E.21}$$

We see then that, in contrast to the case with (E.10), with the case in (E.17), that these eigenvalues have terms that grow in ε as well as in $\sqrt{\varepsilon}$. For small enough values of ε, the square-root terms dominate the linear terms in λ_2 and λ_3. However, when we compute the discriminant (E.4), by plugging in (E.20) and (E.21), we get

$$D \approx -\frac{16}{y}\varepsilon \tag{E.22}$$

which is linear in ε.

Thus, this appendix shows that, for any complex-valued perturbations ε to x or y, that the eigenvalues grow as either ε or $\sqrt{\varepsilon}$, and the discriminant D grows linearly in ε. [3]

E.2 Expansions near EP_3

In this section, we now consider perturbations of x and y when x and y are both near zero, i.e. the control space defined by x and y is near an EP_3. In addition to the discriminant (E.4), we also examine the d_3 metric

$$d_3 = |\lambda_1 - \lambda_2| + |\lambda_2 - \lambda_3| + |\lambda_3 - \lambda_1| \tag{E.23}$$

First, suppose that $y = 0$ and $x = \varepsilon$, for some "small" complex value of ε. Then C (E.6) becomes

$$C = \sqrt[3]{\frac{\varepsilon}{2} + \sqrt{\frac{\varepsilon^2}{4}}} = \sqrt[3]{\varepsilon} \tag{E.24}$$

In Equation E.7, $p = -y = 0$, so

$$\lambda_1 = \sqrt[3]{\varepsilon} \tag{E.25}$$

The other two roots (Equations E.8) are

$$\begin{aligned} \lambda_2 &= \left(\frac{-1 + i\sqrt{3}}{2}\right) \sqrt[3]{\varepsilon} \\ \lambda_3 &= \left(\frac{-1 - i\sqrt{3}}{2}\right) \sqrt[3]{\varepsilon} \end{aligned} \tag{E.26}$$

The discriminant (E.4) is then

$$D = \left(i\sqrt{3}\sqrt[3]{\varepsilon}\left(\frac{-3 - i\sqrt{3}}{2}\right)\sqrt[3]{\varepsilon}\left(\frac{3 - i\sqrt{3}}{2}\right)\sqrt[3]{\varepsilon}\right)^2 = -27\varepsilon^2 \tag{E.27}$$

so the value of D grows as ε^2 near EP_3. d_3 becomes

$$\begin{aligned} d_3 &= \left(\left|\frac{-3 + i\sqrt{3}}{2}\right| + \left|i\sqrt{3}\right| + \left|\frac{-3 - i\sqrt{3}}{2}\right|\right) \left|\sqrt[3]{\varepsilon}\right| \\ &= 3\sqrt{3}\left|\sqrt[3]{\varepsilon}\right| \end{aligned} \tag{E.28}$$

so d_3 grows as $|\sqrt[3]{\varepsilon}|$.

[3] Of course, to show this result for D, it suffices to expand $D = 4y^3 - 27x^2$ when x or y near EP_2 is perturbed by ε: for $x \mapsto x+\varepsilon$, we get $D \approx 4y^3 - 27x^2 - 54x\varepsilon = -54x\varepsilon$, and for $y \mapsto y+\varepsilon$, we get $D \approx 4y^3 + 12y^2\varepsilon - 27x^2 = 12y^2\varepsilon$.

Now, suppose that $x = 0$ and $y = \varepsilon$ is the perturbation. Then C (E.6) becomes

$$\begin{aligned} C &= \sqrt[3]{\sqrt{-\frac{\varepsilon^3}{27}}} \\ &= \sqrt{-\frac{\varepsilon}{3}} \\ &= i\sqrt{\frac{\varepsilon}{3}} \end{aligned} \tag{E.29}$$

Then λ_1 (E.7) is

$$\lambda_1 = i\sqrt{\frac{\varepsilon}{3}} + \frac{\varepsilon}{3i\sqrt{\varepsilon/3}} = 0 \tag{E.30}$$

and the other two roots are

$$\begin{aligned} \lambda_2 &= -2\sqrt{\varepsilon} \\ \lambda_3 &= +2\sqrt{\varepsilon} \end{aligned} \tag{E.31}$$

The discriminant is

$$D = 16\varepsilon^3 \tag{E.32}$$

and d_3 is

$$d_3 = 8\left|\sqrt{\varepsilon}\right| \tag{E.33}$$

so d_3 grows as $|\sqrt{\varepsilon}|$.

Thus, near EP_3, the discriminant D has a smaller sensitivity to perturbations in x and y, being of sensitivity ε^2 and ε^3. The triple difference d_3 grows as $|\sqrt{\varepsilon}|$ and $|\sqrt[3]{\varepsilon}|$.

Appendix F

Outlier Filter Implementation

Below is an efficient Python implentation of the outlier filter algorithm discussed in Section 6.4.1:

```
import numpy as np
from scipy.ndimage import median_filter

# Zm contains the experimental data
# load_experimental_data is some subroutine that loads the data
Zm = load_experimental_data()

size=5 # specifies the number of pixels used in the filter
s=6 # specifies the IQR parameter

def get_outlier_mask(arr, size, s):
    """
    Helper routine;
    arr -- input array of shape (I,J)
    size -- the length of each side of the grid
         over which a pixel is determined to be an outlier
    s -- the interquartile range

    Returns mask: a mask array which is of shape (I,J)
    where the (i,j) entry is
        0 if the (i,j) entry of arr is not flagged as an outlier
        1 if the (i,j) entry of arr is flagged as an outlier
    """
    I = arr.shape[0]
    J = arr.shape[1]
    mask = np.zeros_like(arr, dtype=int)

    for i in range(I):
        for j in range(J):
```

```
30              val = arr[i,j]
31              sub_arr = arr[max(0,i-size//2):min(I-1,i+size//2+1),
32                            max(0,j-size//2):min(J-1,j+size//2+1)]
33              Q1 = np.percentile(sub_arr,25)
34              Q3 = np.percentile(sub_arr,75)
35              IQR = Q3 - Q1
36              mask[i,j] = ~((Q1-s*IQR < val) & (val < Q3+s*IQR))
37
38      return mask
39
40  Zm_mask = get_outlier_mask(np.abs(Zm), size, s)
41
42  Zm_median_filter = (
43      median_filter(np.real(Zm), size) +
44      1j*median_filter(np.imag(Zm), size)
45  )
46
47  # Zmo is a copy of the Zm data, which will have
48  # the outlier pixels replaced by the entries in Zm_median_filter
49  Zmo = np.copy(Zm)
50  Zmo[np.where(Zm_mask)] = Zm_median_filter[np.where(Zm_mask)]
```

This implementation of the outlier rejection filter algorithm is efficient for our experimental data sets because we used a package-built median filter implementation, and we were careful in constructing the outlier-detection subroutine. This implementation of the median filter is built into SciPy [92, scipy.ndimage.median_filter], so it is already well-built. As for our custom-built `get_outlier_mask` subroutine, the for-loop in the `get_outlier_mask` subroutine is only $\mathcal{O}(n^2)$ in space complexity, where n is the input array size. This is because, in line 31, where `sub_arr` is assigned, the routine does not create a copy of the 5×5 entries in the input array, but only uses a reference to those entries. The rest of the `get_outlier_mask` subroutine has only $\mathcal{O}(1)$ complexity. Thus, this implementatio of `get_outlier_mask` has $\mathcal{O}(n^2)$ space-complexity, which is fine for our 2D arrays. The time-complexity is $\mathcal{O}(n^2 size)$, since in lines 31-34, we iterate over the input array entries, and further iterate over the entries of `sub_arr` to compute `Q1` and `Q3`. But since `size` is less than `n`, which has values of 15 to 35 for most of our slices (and since `size` is left at 5 for all slices), we can drop the time complexity to $\mathcal{O}(n^2)$.

Appendix G

Braid Coloring Algorithm

In Section 6.1, we describe the process of extracting eigenvalues in the space of control parameters (δ, P_1, P_2, P_3). Still, the fit routine can return the parameters for each Lorentzian in any order. This is not an issue for calculating the discriminant (Equation (6.48)), the eigenvector indicator (Equation (6.50)), or the triple degeneracy (Equation (6.34)), since these quantities do not vary when the eigenvalues are permuted. However, to see eigenvalue braids, we must place the eigenvalues in the natural order of the braid. If the step size is fine enough, we use a "coloring algorithm" to color the eigenvalue braids such that they follow the natural braids.

For instance, suppose that the eigenvalues are given by functions

$$\lambda_1(s) = e^{2\pi i s} + 2 \tag{G.1a}$$

$$\lambda_2(s) = 0.5e^{2\pi i s} + 4 \tag{G.1b}$$

$$\lambda_3(s) = 0 \tag{G.1c}$$

for $s \in [0, 1]$. Then suppose that, at each value of s they are the eigenvalues of some spectra, which were extracted by a fit function. The fit function does not take s as an input, so it does not care about the smooth path that the braids take as a function of s. Figure G.1a shows a sample possible output of the fit function.

To sort the output of the fit function from Figure G.1a, we can use a "coloring algorithm" to sort the eigenvalues between each increment in s. Namely, at the ith value of s, s_i, the coloring algorithm seeks to minimize the quantity

$$Q_i = \sum_{m=1}^{3} |\lambda_m(s_i) - \lambda_m(s_{i-1})|^2 \tag{G.2}$$

This minimization is done over all choices of permutations of $(\lambda_1(s_i), \lambda_2(s_i), \lambda_3(s_i))$.

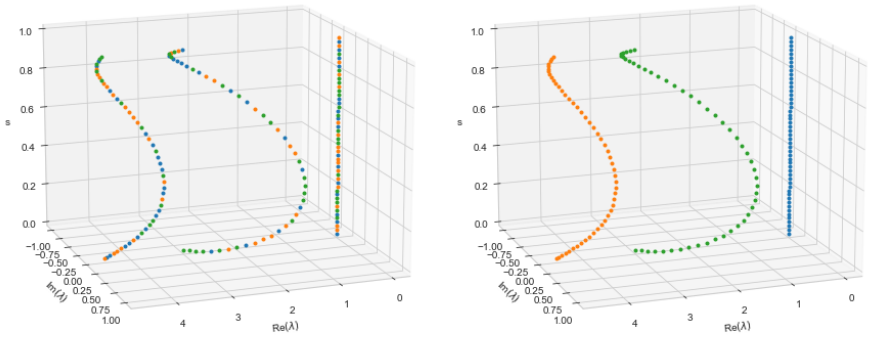

(a) (b)

Figure G.1: The results of applying the coloring algorithm to sort the eigenvalues along their braids.

An implementation of this algorithm in Python is given below:

```
def coloring_algorithm(y):
  """
  The data has shape (len, 3),
  where the 0 axis is time, and the 1 axis is the ith eigenvalue.
  This algorithm "colors" the three braids by
  sorting the 1 axis such that axis 0 traces out
  continuous paths.
  """
  y1, y2, y3 = y.T
  coloring_indices = [[0,1,2]]
  perms = [[0,1,2],
      [0,2,1],
      [1,0,2],
      [1,2,0],
      [2,0,1],
      [2,1,0]]
  for i in range(len(ys)-1):
    coloring_perm = perms[np.argmin(np.sum(
      np.abs(ys[i+1, perms] - ys[i, coloring_indices[i]])**2, axis=1))]
    coloring_indices.append(coloring_perm)

  coloring_indices = np.array(coloring_indices, dtype=int)

  y = np.take_along_axis(np.stack([y1,y2,y3], axis=-1), coloring_indices, axis=1)
  return y
```

In Figure G.1b, we see that this algorithm colors the strands such that they clearly follow continuous curves. This is very helpful in visually identifying braids.

References

[1] Yogesh S. S. Patil, Judith Höller, Parker A. Henry, Chitres Guria, Yiming Zhang, Luyao Jiang, Nenad Kralj, Nicholas Read, and Jack G. E. Harris. *Measuring the knot of degeneracies and the eigenvalue braids near a third-order exceptional point*. 2021. arXiv: 2112.00157 [physics.optics].

[2] John R. Taylor. *Classical Mechanics*. University Science Books, 2005.

[3] Herbert Goldstein, Charles Poole, and John Safko. *Classical Mechanics*. Third Edition. Addison-Wesley.

[4] Andrew Zangwill. *Modern Electrodynamics*. 1st Edition. Cambridge University Press, 2012.

[5] Jun J. Sakurai and Jim Napolitano. *Modern Quantum Mechanics*. Addison-Wesley, 2011.

[6] Haitan Xu, David Mason, Luyao Jiang, and Jack G. E. Harris. "Topological energy transfer in an optomechanical system with exceptional points". In: *Nature* 537 (July 2016), 80–83. DOI: https://doi.org/10.1038/nature18604.

[7] J. Doppler, A. Mailybaev, and J. Böem. "Dynamically encircling an exceptional point for asymmetric mode switching". In: *Nature* 537 (2016), pp. 76–79. DOI: https://doi.org/10.1038/nature18605.

[8] T. Gao, E. Estrecho, K. Y. Bliokh, T. C. H. Liew, M. D. Fraser, S. Brodbeck, M. Kamp, C. Schneider, S. Höfling, Y. Yamamoto, F. Nori, Y. S. Kivshar, A. G. Truscott, R. G. Dall, and E. A. Ostrovskaya. "Observation of non-Hermitian degeneracies in a chaotic exciton-polariton billiard". In: *Nature* 526 (2015), pp. 554–558. DOI: https://doi.org/10.1038/nature15522. URL: https://www.nature.com/articles/nature15522.

[9] John Milnor. *Singular Points of Complex Hypersurfaces*. Princeton University Press, 1968.

[10] G. Gamow. "Zur Quantentheorie des Atomkernes [On the Quantum Theory of the Atomic Nucleus]". In: *Zeitschrift für Physik* 51 (3-4 Mar. 1928), pp. 204–212. DOI: 10.1007/BF01343196.

[11] Ramy El-Ganainy, Konstantinos G. Makris, Mercedeh Khajavikhan, Ziad H. Musslimani, Stefan Rotter, and Demetrios N. Christodoulides. "Non-Hermitian physics and PT symmetry". In: *Nature Physics* 14 (2018), pp. 11–19. DOI: https://doi.org/10.1038/nphys4323.

[12] M. Berry. "Physics of Nonhermitian Degeneracies". In: *Czechoslovak Journal of Physics* 54 (2004), pp. 1039–1047. DOI: https://doi.org/10.1023/B:CJOP.0000044002.05657.04. URL: https://link.springer.com/article/10.1023/B:CJOP.0000044002.05657.04.

[13] Tosio Kato. *Perturbation Theory for Linear Operators*. Second Edition. Springer, 1980.

[14] Robert Gilmore. *Catastrophe Theory for Engineers*. Wiley, 1981.

[15] V. I. Arnold. "On Matrices Depending on Parameters". In: *Russian Mathematical Surveys* 26.2 (Apr. 1971), pp. 29–43. DOI: 10.1070/RM1971v026n02ABEH003827.

[16] Mohammad Ali-Miri and Andrea Alù. "Exceptional points in optics and photonics". In: 4.6422 (Jan. 2019). DOI: 10.1126/science.aar7709. URL: https://www.science.org/doi/10.1126/science.aar7709.

[17] Weijian Chen, Şahin Kaya Özdemir, Guangming Zhao, Jan Wiersig, and Lan Yang. "Exceptional points enhance sensing in an optical microcavity". In: *Nature* 548 (2017), pp. 192–196. DOI: 10.1038/nature23281. URL: https://www.nature.com/articles/nature23281.

[18] Jan Wiersig. "Review of exceptional point-based sensors". In: *Photon. Res.* 8.9 (Sept. 2020), pp. 1457–1467. DOI: 10.1364/PRJ.396115. URL: http://www.osapublishing.org/prj/abstract.cfm?URI=prj-8-9-1457.

[19] Zhenya Dong, Zhipeng Li, Fengyuan Yang, Cheng-Wei Qiu, and John S. Ho. "Sensitive readout of implantable microsensors using a wireless system locked to an exceptional point". In: *Nature Electronics* 2 (2019), pp. 335–342. DOI: 10.1038/s41928-019-0284-4. URL: https://www.nature.com/articles/s41928-019-0284-4.

[20] Hoi-Kwan Lau and Aashish A. Clerk. "Fundamental limits and non-reciprocal approaches in non-Hermitian quantum sensing". In: *Nature Communications* 9.4320 (2018). DOI: 10.1038/s41467-018-0647. URL: https://www.nature.com/articles/s41467-018-06477-7.pdf.

[21] Yasutomo Ota, Kenta Takata, Tomoki Ozawa, Alberto Amo, Zhetao Jia, Boubacar Kante, Masaya Notomi, Yasuhiko Arakawa, and Satoshi Iwamoto. "Active topological photonics". In: *Nanophotonics* (2020). DOI: https://doi.org/10.1515/nanoph-2019-0376. URL: https://www.degruyter.com/document/doi/10.1515/nanoph-2019-0376/html.

[22] W. P. Su, J. R. Schrieffer, and A. J. Heeger. "Solitons in Polyacetylene". In: *Phys. Rev. Lett.* 42 (25 1979), pp. 1698–1701. DOI: 10.1103/PhysRevLett.42.1698. URL: https://link.aps.org/doi/10.1103/PhysRevLett.42.1698.

[23] Marcel Klett, Holger Cartarius, Dennis Dast, Jörg Main, and Günter Wunner. "Relation between $\mathcal{PT}$-symmetry breaking and topologically nontrivial phases in the Su-Schrieffer-Heeger and Kitaev models". In: *Phys. Rev. A* 95 (5 2017), p. 053626. DOI: 10.1103/PhysRevA.95.053626. URL: https://link.aps.org/doi/10.1103/PhysRevA.95.053626.

[24] B. Bahari, A. Ndao, F. Vallini, A. El Amili, and B. Kanté Y. Fainman. "Nonreciprocal lasing in topological cavities of arbitrary geometries". In: *Science* 358.6363 (Oct. 2017), pp. 636–640. DOI: https://doi.org/10.1126/science.aao4551. URL: https://www.science.org/doi/10.1126/science.aao4551.

[25] Kohei Kawabata, Ken Shiozaki, Masahito Ueda, and Masatoshi Sato. "Symmetry and Topology in Non-Hermitian Physics". In: *Phys. Rev. X* 9 (4 2019), p. 041015. DOI: 10.1103/PhysRevX.9.041015. URL: https://link.aps.org/doi/10.1103/PhysRevX.9.041015.

[26] M. Naghiloo, M. Abbasi, Yogesh N. Joglekar, and Kater W. Murch. "Quantum state tomography across the exceptional point in a single dissipative qubit". In: *Nature Physics* 15.12 (Dec. 2019), pp. 1232–1236. DOI: https://doi.org/10.1038/s41567-019-0652-z.

[27] Maryam Abbasi, Weijian Chen, Mahdi Naghiloo, Yogesh N. Joglekar, and Kater W. Murch. *Topological quantum state control through exceptional-point proximity*. 2022. arXiv: 2108.05365 [quant-ph].

[28] Q. Zhong, S.K. Ozdemir, A. Eisfeld, A. Metelmann, and R. El-Ganainy. "Exceptional-Point-Based Optical Amplifiers". In: *Phys. Rev. Applied* 13 (1 Jan. 2020), p. 014070. DOI: 10.1103/PhysRevApplied.13.014070. URL: https://link.aps.org/doi/10.1103/PhysRevApplied.13.014070.

[29] Sid Assawaworrarit, Xiaofang Yu, and Shanhui Fan. "Robust wireless power transfer using a nonlinear parity–time-symmetric circuit". In: *Nature* 546 (2017), pp. 387–390. DOI: https://doi.org/10.1038/nature22404. URL: https://www.nature.com/articles/nature22404/.

[30] André Kurs, Aristeidis Karalis, Robert Moffatt, J. D. Joannopoulos, Peter Fisher, and Marin Soljačić. "Wireless Power Transfer via Strongly Coupled Magnetic Resonances". In: *Science* 317.83 (July 2007). DOI: 10.1126/science.1143254. URL: http://www2.lns.mit.edu/fisherp/83.pdf.

[31] H. Xu, D. Mason, Luyao Jiang, and J. G. E. Harris. *Topological dynamics in an optomechanical system with highly non-degenerate modes*. 2017. arXiv: 1703.07374 [physics.optics].

[32] Haitan Xu, Luyao Jiang, A. A. Clerk, and Jack G. E. Harris. "Nonreciprocal control and cooling of phonon modes in an optomechanical system". In: *Nature* 568 (Apr. 2019), pp. 65–69. DOI: https://doi.org/10.1038/s41586-019-1061-2.

[33] David Mason. "Dynamical Behavior near Exceptional Points in an Optomechanical System". Jack Harris Laboratory. PhD thesis. Yale University, 2018.

[34] Judith Höller, Nicholas Read, and Jack G. E. Harris. "Non-Hermitian adiabatic transport in spaces of exceptional points". In: *Physical Review A* (3 Sept. 2020), p. 032216. DOI: 10.1103/PhysRevA.102.032216.

[35] Sheldon Axler. *Linear Algebra Done Right*. 3rd Edition. Springer, 2015.

[36] Sergei Treil. *Linear Algebra Done Wrong*. Brown University, 2017.

[37] Paul R. Halmos. *Finite-Dimensional Vector Spaces*. Second Edition. Dover Publications, Inc., 2017.

[38] Herstein. *Abstract Algebra*. 3rd Edition. Prentiss-Hall Inc., 1996.

[39] Lawrence E. Spence Stephen H. Friedberg Arnold J. Insel. *Linear Algebra*. 4th Edition. 2002.

[40] Richard K. Guy John H. Conway. *The Book of Numbers*. 1st Edition. Springer-Verlag New York, 1996.

[41] Marco Taboga. *Jordan Chain*. Lectures on matrix algebra. 2021. URL: https://www.statlect.com/matrix-algebra/Jordan-chain.

[42] D.J.H. Garling. *Galois Theory and Its Algebraic Background*. Second Edition. Cambridge University, 2021, pp. 123–4.

[43] James R. Munkres. *Topology*. Second Edition. Pearson, 2013.

[44] Allen Hatcher. *Algebraic Topology*. Cornell University, 2001.

[45] *trivial group*. URL: https://ncatlab.org/nlab/show/trivial+group.

[46] David S. Dummit and Richard M. Foote. *Abstract Algebra*. 3rd Edition. John Wiley and Sons, Inc., 2004.

[47] E. Artin. *Theory of Braids*. Vol. 48. 1. 1946.

[48] Robert Ghrist. "Configuration Spaces, Braids, and Robotics". In: *Lecture Note Series, Institute for Mathematical Sciences* 19 (2009), pp. 263–304. DOI: 10.1142/9789814291415_0004. URL: https://www.worldscientific.com/doi/abs/10.1142/9789814291415_0004.

[49] Dale Rolfsen. "Configuration Spaces, Braids, and Robotics". In: *Lecture Note Series, Institute for Mathematical Sciences* 19 (2009), pp. 1–30. DOI: 10.1142/9789814291415_0001. URL: https://www.worldscientific.com/doi/suppl/10.1142/7550/suppl_file/7550_chap01.pdf.

[50] Todd Rowland and Eric W. Weisstein. *Algebraic Variety*. From Mathworld - A Wolfram Web Resource. URL: https://mathworld.wolfram.com/AlgebraicVariety.html.

[51] Victor Guillemin and Alan Pollack. *Differential Topology*. Prentice-Hall, Inc., 1974.

[52] Markus Aspelmeyer, Tobias J. Kippenberg, and Florian Marquardt. "Cavity optomechanics". In: *Rev. Mod. Phys.* 86 (4 Dec. 2014), pp. 1391–1452. DOI: 10.1103/RevModPhys.86.1391. URL: https://link.aps.org/doi/10.1103/RevModPhys.86.1391.

[53] Stig Stenholm. "The semiclassical theory of laser cooling". In: *Rev. Mod. Phys.* 58 (3 1986), pp. 699–739. DOI: 10.1103/RevModPhys.58.699. URL: https://link.aps.org/doi/10.1103/RevModPhys.58.699.

[54] Harold J. Metcalf and Peter van der Straten. *Laser Cooling and Trapping*. Springer-Verlag New York, Inc., 1999. DOI: https://doi.org/10.1007/978-1-4612-1470-0.

[55] M. H. Anderson, J. R. Ensher, M. R. Matthews, C. E. Wieman, and E. A. Cornell. "Observation of Bose-Einstein Condensation in a Dilute Atomic Vapor". In: *Science* 269.5221 (July 1995), pp. 198–201. DOI: https://doi.org/10.1126/science.269.5221.198.

[56] B. D. Cuthbertson, M. E. Tobar, E. N. Ivanov, and D. G. Blair. "Parametric back-action effects in a high-Q cyrogenic sapphire transducer". In: *Review of Scientific Instruments* 67 (1996), pp. 2435–2442. DOI: https://doi.org/10.1063/1.1147193.

[57] A. Dorsel, J. D. McCullen, P. Meystre, E. Vignes, and H. Walther. "Optical Bistability and Mirror Confinement Induced by Radiation Pressure". In: *Phys. Rev. Lett.* 51 (17 1983), pp. 1550–1553. DOI: 10.1103/PhysRevLett.51.1550. URL: https://link.aps.org/doi/10.1103/PhysRevLett.51.1550.

[58] A. F. Pace, M. J. Collett, and D. F. Walls. "Quantum limits in interferometric detection of gravitational radiation". In: *Phys. Rev. A* 47 (4 1993), pp. 3173–3189. DOI: 10.1103/PhysRevA.47.3173. URL: https://link.aps.org/doi/10.1103/PhysRevA.47.3173.

[59] URL: https://ligo.org/detections.php.

[60] B. P. Abbott et al. "Observation of Gravitational Waves from a Binary Black Hole Merger". In: *Phys. Rev. Lett.* 116 (6 2016), p. 061102. DOI: 10.1103/PhysRevLett.116.061102. URL: https://link.aps.org/doi/10.1103/PhysRevLett.116.061102.

[61] C. D. Brown, Y. Wang, M. Namazi, G. I. Harris, M. T. Uysal, and J. G. E. Harris. *Characterization of Levitated Superfluid Helium Drops in High Vacuum*. 2021. arXiv: 2109.05618 [cond-mat.other].

[62] Charles Daryl Brown II. "Optical, Mechanical and Thermal Properties of Superfluid Liquid Helium Drops Magnetically-Levitated in Vacuum". Jack Harris Laboratory. PhD thesis. Yale University, 2019.

[63] Yogesh S. S. Patil, Jiaxin Yu, Sean Frazier, Yiqi Wang, Kale Johnson, Jared Fox, Jakob Reichel, and Jack G. E. Harris. *Measuring High-Order Phonon Correlations in an Optomechanical Resonator*. 2022. arXiv: 2201.07340 [quant-ph].

[64] Mitchell James Underwood III. "Cryogenic Optomechanics with a Silicon Nitride Membrane". Jack Harris Laboratory. PhD thesis. Yale University, 2016.

[65] D.F. Walls and Gerard J. Milburn. *Quantum Optics*. 2nd Edition. Springer, 2008.

[66] M. J. Collett and C. W. Gardiner. "Squeezing of intracavity and traveling-wave light fields produced in parametric amplification". In: *Phys. Rev. A* 30 (3 Sept. 1984), pp. 1386–1391. DOI: 10.1103/PhysRevA.30.1386. URL: https://link.aps.org/doi/10.1103/PhysRevA.30.1386.

[67] C. W. Gardiner and M. J. Collett. "Input and output in damped quantum systems: Quantum stochastic differential equations and the master equation". In: *Phys. Rev. A* 31 (6 June 1985), pp. 3761–3774. DOI: 10.1103/PhysRevA.31.3761. URL: https://link.aps.org/doi/10.1103/PhysRevA.31.3761.

[68] Shanhui Fan, Şükrü Ekin Kocabaş, and Jung-Tsung Shen. "Input-output formalism for few-photon transport in one-dimensional nanophotonic waveguides coupled to a qubit". In: *Physical Review A* 82 (6 Dec. 2010), p. 063821. DOI: 10.1103/PhysRevA.82.063821. URL: https://web.stanford.edu/group/fan/publication/Fan_PRA_82_063821_2010.pdf.

[69] C. W. Gardiner and P. Zoller. *Quantum Noise: A Handbook of Markovian and Non-Markovian Quantum Stochastic Methods with Applications to Quantum Optics*. Third Edition. Springer, 2004.

[70] Luyao Jiang. "Nonreciprocal Dynamics in a Cryogenic Optomechanical System". Jack Harris Laboratory. PhD thesis. Yale University, 2020.

[71] Max Born and J. Robert Oppenheimer. "Zur Quantentheorie der Molekeln [On the Quantum Theory of Molecules]". In: *Annalen der Physik* 389.20 (1927). (In German), pp. 457–484. DOI: https://doi.org/10.1002/andp.19273892002. eprint: https://onlinelibrary.wiley.com/doi/pdf/10.1002/andp.19273892002. URL: https://onlinelibrary.wiley.com/doi/abs/10.1002/andp.19273892002.

[72] David J. Griffiths. *Introduction to Quantum Mechanics*. Second Edition. n.b., the discussion on the adiabatic approximation was removed from the third edition. Pearson Education, 2005.

[73] *ATP30 Model User's Manual, 1322-005, Rev. A0*. 2015.

[74] *ATL160+ Models User's Manual, 1321-002, Rev. A0*. 2017.

[75] D. Lee, M. Underwood, D. Mason, A. B. Shkarin, S. W. Hoch, and J. G. E. Harris. "Multimode optomechanical dynamics in a cavity with avoided crossings". In: *Nature Communications* 6.6232 (2015). DOI: https://doi.org/10.1038/ncomms7232.

[76] M. Underwood, D. Mason, D. Lee, H. Xu, L. Jiang, A. B. Shkarin, K. Børkje, S. M. Girvin, and J. G. E. Harris. "Measurement of the motional sidebands of a nanogram-scale oscillator in the quantum regime". In: *Phys. Rev. A* 92 (6 Dec. 2015), p. 061801. DOI: 10.1103/PhysRevA.92.061801. URL: https://link.aps.org/doi/10.1103/PhysRevA.92.061801.

[77] R. W. P. Drever, J. L. Hall, F. V. Kowalski, J. Hough, G. M. Ford, A. J. Munley, and H. Ward. "Laser Phase and Frequency Stabilization Using an Optical Resonator". In: *Applied Physics B.* 31 (2 June 1983), pp. 97–105. DOI: 10.1007/BF00702605.

[78] Eric D. Black. "An introduction to Pound–Drever–Hall laser frequency stabilization". In: *American Journal of Physics* 69.1 (2001), pp. 79–87. DOI: 10.1119/1.1286663. eprint: https://doi.org/10.1119/1.1286663. URL: https://doi.org/10.1119/1.1286663.

[79] Thorlabs. *Thorlabs PDA36A Si Switchable Gain Detector User Guide*. URL: https://www.thorlabs.com/drawings/c68906d3c2577581-96BF6AF3-9CBE-0B74-B70B64E04B7BD350/PDA36A-Manual.pdf.

[80] Guido Van Rossum and Fred L. Drake. *Python 3 Reference Manual*. Scotts Valley, CA: CreateSpace, 2009. ISBN: 1441412697.

[81] Zurich Instruments. *HF2 User Manual*. Version 21.02.0. Feb. 2021. URL: https://docs.zhinst.com/pdf/ziHF2_UserManual.pdf.

[82] Union College. *A Cube Unfolded*. URL: http://www.math.union.edu/~dpvc/talks/2001-04-28.HRUMC/cube-unfolded.html.

[83] Magnus J. Wenninger. *Polyhedron Models*. Cambridge University Press, 1971.

[84] Michael Friedman. *A History of Folding in Mathematics: Mathematizing the Margins*. Science Networks. Historical Studies, 2018, p.8. ISBN: 978-3-319-72486-7. DOI: https://doi.org/10.1007/978-3-319-72487-4.

[85] *Unfolding the Tesseract*. URL: https://unfolding.apperceptual.com/.

[86] Duncan Sommerville. *Introduction to the Geometry of N Dimensions*. Reprint 1958. Dover Books, 1929, p. 100.

[87] John W. Tukey. *Exploratory Data Analysis*. Addison-Wesley, 1977.

[88] Richard Szeliski. *Computer Vision: Algorithms and Applications*. Springer, July 2021. URL: https://szeliski.org/Book.

[89] Rob Fergus. *Image Filtering*. Courant Institute of Mathematical Sciences, New York University. URL: https://cs.nyu.edu/~fergus/teaching/vision/3_filtering.pdf.

[90] Patrice Delmas and Burkhard Wuensche. *Gaussian Filtering*. The University of Auckland, New Zealand. 2016. URL: https://www.cs.auckland.ac.nz/courses/compsci373s1c/PatricesLectures/Gaussian\%20Filtering_1up.pdf.

[91] Eric W. Weisstein. *Gaussian Function*. From Mathworld - A Wolfram Web Resource. URL: https://mathworld.wolfram.com/GaussianFunction.html.

[92] Pauli Virtanen, Ralf Gommers, Travis E. Oliphant, Matt Haberland, Tyler Reddy, David Cournapeau, Evgeni Burovski, Pearu Peterson, Warren Weckesser, Jonathan Bright, Stéfan J. van der Walt, Matthew Brett, Joshua Wilson, K. Jarrod Millman, Nikolay Mayorov, Andrew R. J. Nelson, Eric Jones, Robert Kern, Eric Larson, C J Carey, İlhan Polat, Yu Feng, Eric W. Moore, Jake VanderPlas, Denis Laxalde, Josef Perktold, Robert

Cimrman, Ian Henriksen, E. A. Quintero, Charles R. Harris, Anne M. Archibald, Antônio H. Ribeiro, Fabian Pedregosa, Paul van Mulbregt, and SciPy 1.0 Contributors. "SciPy 1.0: Fundamental Algorithms for Scientific Computing in Python". In: *Nature Methods* 17 (2020), pp. 261–272. DOI: 10.1038/s41592-019-0686-2.

[93] *SciPy v1.7.0, scipy.ndimage.convolve*. URL: https://docs.scipy.org/doc/scipy/reference/generated/scipy.ndimage.convolve.html.

[94] *SciPy v1.7.0, scipy.ndimage.gaussian_filter*. URL: https://docs.scipy.org/doc/scipy/reference/generated/scipy.ndimage.gaussian_filter.html.

[95] *Wolfram Research (2008), GaussianFilter, Wolfram Language Function*. URL: https://reference.wolfram.com/language/ref/GaussianFilter.html.

[96] Eric W. Weisstein. *Second Derivative Test*. URL: https://mathworld.wolfram.com/SecondDerivativeTest.html.

[97] M. Abramowitz and I. A. Stegun. *Handbook of Mathematical Functions with Formulas, Graphs, and Mathematical Tables*. 9th Printing. Dover, 1972, p. 14.

[98] G.B. Thomas Jr. and R. L. Finney. *Calculus and Analytic Geometry*. 8th Edition. Addison-Wesley, 1992, pp. 881–891.

[99] Charles R. Harris, K. Jarrod Millman, Stéfan J van der Walt, Ralf Gommers, Pauli Virtanen, David Cournapeau, Eric Wieser, Julian Taylor, Sebastian Berg, Nathaniel J. Smith, Robert Kern, Matti Picus, Stephan Hoyer, Marten H. van Kerkwijk, Matthew Brett, Allan Haldane, Jaime Fernández del Río, Mark Wiebe, Pearu Peterson, Pierre Gérard-Marchant, Kevin Sheppard, Tyler Reddy, Warren Weckesser, Hameer Abbasi, Christoph Gohlke, and Travis E. Oliphant. "Array programming with NumPy". In: *Nature* 585 (2020), 357–362. DOI: 10.1038/s41586-020-2649-2.

[100] *PhaseUnwrap — Wolfram Research Repository*. URL: https://resources.wolframcloud.com/FunctionRepository/resources/PhaseUnwrap.

[101] Lars V. Ahlfors. *Complex Analysis*. Third Edition. McGraw-Hill Inc., 1979, p. 19.

[102] Manfredo P. do Carmo. *Differential Geometry of Curves and Surfaces*. Revised & Updated Second Edition. Dover Publications, 2016, p. 231.

[103] Frank S. Crawford. "Elementary examples of adiabatic invariance". In: *American Journal of Physics* 58 (4 1990), pp. 337–344. DOI: 10.1119/1.16166. eprint: https://aapt.scitation.org/doi/10.1119/1.16166.

[104] George E. Uhlenbeck. "¡i¿Paul Ehrenfest, Collected Scientific Papers¡/i¿. Martin J. Klein, Ed. Introduction by H. B. G. Casimir. North-Holland, Amsterdam; Interscience, New York, 1959. 632 pp. $13.75." In: *Science* 131.3408 (1960), pp. 1204–1204. DOI: 10.1126/science.131.3408.1204.a. eprint: https://www.science.org/doi/pdf/10.1126/science.131.3408.1204.a. URL: https://www.science.org/doi/abs/10.1126/science.131.3408.1204.a.

[105] M. V. Berry. "Quantal Phase Factors Accompanying Adiabatic Changes". In: *Proceedings of the Royal Society of London. Series A, Mathematical and Physical Sciences* 392.1802 (1984), pp. 45–57. ISSN: 00804630. URL: http://www.jstor.org/stable/2397741.

[106] A. C. Aguiar Pinto, M. C. Nemes, J. G. Peixoto de Faria, and M. T. Thomaz. "Comment on the adiabatic condition". In: *American Journal of Physics* 68.10 (Oct. 2000), pp. 955–958. DOI: 10.1119/1.1285944. arXiv: quant-ph/9912030 [quant-ph].

[107] Barry R. Holstein. "The adiabatic theorem and Berry's phase". In: *American Journal of Physics* 57.12 (1989), pp. 1079–1084. DOI: 10.1119/1.15793. eprint: https://doi.org/10.1119/1.15793. URL: https://doi.org/10.1119/1.15793.

[108] Gheorghe Nenciu and G. Rasche. "On the adiabatic theorem for nonself-adjoint Hamiltonians". In: *Journal of Physics A* 25 (1992), pp. 5741–5751.

[109] M V Berry and R Uzdin. "Slow non-Hermitian cycling: exact solutions and the Stokes phenomenon". In: *Journal of Physics A: Mathematical and Theoretical* 44.43 (2011), p. 435303. DOI: 10.1088/1751-8113/44/43/435303. URL: https://doi.org/10.1088/1751-8113/44/43/435303.

[110] Raam Uzdin, Alexei Mailybaev, and Nimrod Moiseyev. "On the observability and asymmetry of adiabatic state flips generated by exceptional points". In: *Journal of Physics A: Mathematical and Theoretical* 44.43 (2011), p. 435302. DOI: 10.1088/1751-8113/44/43/435302. URL: https://doi.org/10.1088/1751-8113/44/43/435302.

[111] Thomas J. Milburn, Jörg Doppler, Catherine A. Holmes, Stefano Portolan, Stefan Rotter, and Peter Rabl. "General description of quasiadiabatic dynamical phenomena near exceptional points". In: *Phys. Rev. A* 92 (5 2015), p. 052124. DOI: 10.1103/PhysRevA.92.052124. URL: https://link.aps.org/doi/10.1103/PhysRevA.92.052124.

[112] C. Dembowski, H.-D. Gräf, H. L. Harney, A. Heine, W. D. Heiss, H. Rehfeld, and A. Richter. "Experimental Observation of the Topological Structure of Exceptional Points". In: *Phys. Rev. Lett.* 86 (5 2001), pp. 787–790. DOI: 10.1103/PhysRevLett.86.787. URL: https://link.aps.org/doi/10.1103/PhysRevLett.86.787.

[113] Dries Sels and Anatoli Polkovnikov. "Minimizing irreversible losses in quantum systems by local counterdiabatic driving". In: *Proceedings of the National Academy of Sciences* 114.20 (2017), E3909–E3916. ISSN: 1091-6490. DOI: 10.1073/pnas.1619826114. URL: http://dx.doi.org/10.1073/pnas.1619826114.

[114] M V Berry. "Transitionless quantum driving". In: *Journal of Physics A: Mathematical and Theoretical* 42.36 (2009), p. 365303. DOI: 10.1088/1751-8113/42/36/365303. URL: https://doi.org/10.1088/1751-8113/42/36/365303.

[115] D. Guéry-Odelin, A. Ruschhaupt, A. Kiely, E. Torrontegui, S. Martínez-Garaot, and J. G. Muga. "Shortcuts to adiabaticity: Concepts, methods, and applications". In: *Rev. Mod. Phys.* 91 (4 2019), p. 045001. DOI: 10.1103/RevModPhys.91.045001. URL: https://link.aps.org/doi/10.1103/RevModPhys.91.045001.

[116] Hugo Ribeiro and Florian Marquardt. *Accelerated Non-Reciprocal Transfer of Energy Around an Exceptional Point*. 2021. arXiv: 2111.11220 [quant-ph].

[117] A. Emmanouilidou, X.-G. Zhao, P. Ao, and Q. Niu. "Steering an Eigenstate to a Destination". In: *Phys. Rev. Lett.* 85 (8 2000), pp. 1626–1629. DOI: 10.1103/PhysRevLett.85.1626. URL: https://web2.ph.utexas.edu/~niugroup/article/lett851626.pdf.

[118] S. Ib'anez, Sofia Martínez-Garaot, Xi Chen, E. Torrontegui, and Juan Gonzalo Muga. "Shortcuts to adiabaticity for non-Hermitian systems". In: *Physical Review A* 84 (2011), p. 023415.

[119] *Cardano Formula – Encyclopedia of Mathematics*. URL: https://encyclopediaofmath.org/index.php?title=Cardano_formula.